

CSDL-R-2065

APPLICATION OF LINEAR PROGRAMMING TO COORDINATED  
MANAGEMENT OF JETS AND AEROSURFACES FOR  
AEROSPACE VEHICLE CONTROL

by

Joseph A. Paradiso

November 1988



**The Charles Stark Draper Laboratory, Inc.**

555 Technology Square  
Cambridge, Massachusetts 02139

CSDL-R-2065

# **Application of Linear Programming to Coordinated Management of Jets & Aerosurfaces for Aerospace Vehicle Control**

By

Joseph A. Paradiso

November, 1988

## **ABSTRACT**

An actuator selection procedure is presented which uses linear programming to optimally specify bounded aerosurface deflections and jet firings in response to differential torque and/or force commands. A six-axis vehicle controller is developed to drive the actuator selection and track the desired state of a vehicle model adapted from Space Shuttle aerodynamic data during constant altitude and re-entry simulations. Tests are presented that demonstrate intrinsic actuator decoupling, dynamic response to actuator reconfiguration, dynamic upper bound and objective specification, and hybrid jet/aerosurface capability. The objective calculation is adapted to realize several goals; ie. discourage large aerosurface deflections, encourage use of certain aerosurfaces (speedbrake, body flap) as a function of vehicle state, minimize drag, contribute to translational control, and adjust the balance between jet firings and aerosurface activity during hybrid operation. Simulations are also performed to examine the effects of mismodelling due to aerodynamic jet interaction, gusts, and systematic errors in measured vehicle state. An extension of this framework is proposed that includes thrust-vector control of propulsive actuators, allowing the selection procedure to manage the ascent of a hypersonic vehicle.

# Table of Contents

|   |     |
|---|-----|
| 1) Introduction.....                                      | 1   |
| 2) The Linear Selection.....                              | 4   |
| 2.1) Overview.....  | 4   |
| 2.2) Linear Programming & Simplex Adaptations.....        | 9   |
| 2.3) General Formulation of Objective Function.....       | 17  |
| 2.4) Implementation.....                                  | 21  |
| 3) Vehicle and Actuator Models.....                       | 24  |
| 3.1) Overview.....  | 24  |
| 3.2) Definition of Vehicle Model.....                     | 24  |
| 3.3) Adaptation of Shuttle Aerodynamic Data.....          | 30  |
| 3.4) Incorporation of RCS Jets.....                       | 49  |
| 3.5) Thrust-Vector Control Applied to Vehicle Ascent..... | 55  |
| 4) Vehicle Controllers.....                               | 59  |
| 4.1) Overview.....  | 59  |
| 4.2) The Rotational and Translational Controllers.....    | 60  |
| 4.3) Actuator-Dependent Objective Contributions.....      | 70  |
| 5) Simulation Examples.....                               | 72  |
| 5.1) Overview.....  | 72  |
| 5.2) Constant Altitude Rotational Maneuvers.....          | 74  |
| 5.3) Examples of Direct Lift Control.....                 | 97  |
| 5.4) Re-entry Simulations.....                            | 102 |
| 5.5) Response to Modelling Error.....                     | 156 |
| 6) Conclusions.....                                       | 173 |
| <i>Acknowledgements</i> .....                             | 176 |
| <i>List of References</i> .....                           | 177 |

# 1) Introduction

The complex missions and demanding environment considered for tomorrow's generation of aircraft and aerospace vehicles will impose increasingly formidable challenges on candidate control schemes. These vehicles will require control laws that can utilize the full potential of all available actuators in order to adapt quickly to changing vehicle characteristics, while maintaining stringent constraints on vehicle state. A prime example is the National Aerospace Plane (NASP), which is intended to perform as an aircraft from takeoff through at least the initial portion of its ascent. At extreme altitudes, aerosurfaces become ineffective; hence the vehicle must be controlled as a spacecraft, via reaction control jets (ie. RCS) and propulsive thrust vector control. The sequence reverses upon descent, where the RCS is initially needed to stabilize the vehicle, with a gradual transition to aerodynamic control after the aerosurfaces gain sufficient authority. Throughout the atmospheric flight, propulsive and thermal considerations impose strict constraints on vehicle angle-of-attack and aerosurface deflection.

Control systems partially addressing this challenge have been developed to manage re-entry of the Space Shuttle[1]. In order to handle the transition from RCS to aerodynamic control as dynamic pressure increases, the current Shuttle autopilot uses several different control strategies which are sequentially applied at different points during the descent.

Managing each of a group of actuators with independent control logic can result in reduced vehicle controllability and efficiency. Because aerospace vehicles such as the NASP need to combine the actions of various types of actuators during both ascent and descent in order to cope with variations in dynamic pressure and air-breathing engine operating characteristics, they will require a highly coordinated actuator management scheme. An adaptive hybrid control strategy is needed that is capable of extracting maximum performance from each actuator family (in solo performance or concerted

operation) and optimally reconfiguring during evolution of the vehicle environment and after hardware failures. Such reliability will be flight-critical, as even a transient degradation in control at high Mach number could result in loss of the vehicle.

A CSDL-developed method based upon linear programming has produced a highly adaptable fuel-optimal jet selection[2], which has been successfully flight-tested[3] onboard the Shuttle Orbiter. These concepts have been revised and extended[4,5] to incorporate Control Moment Gyroscopes (CMGs) into the selection process. Much of the technology developed to manage jets and CMGs is applicable to the problem of controlling hypersonic aircraft and aerospace vehicles such as the NASP. The capability of selecting the angular displacements of nonlinear bidirectional actuators while minimizing an objective function and enforcing limits on travel (as was demonstrated[6] for CMGs) can also be used for aerosurface control. Small gimballed displacements must be specified to incrementally re-direct engine nozzles on ascent and provide thrust-vector control; techniques developed to steer double-gimballed CMGs[5] and magnetically gimballed gyros[7] may be adapted to handle such systems under the linear programming scheme. An aerospace vehicle traveling at high altitude also requires RCS firings to maintain control when the authority of the aerosurfaces is limited; the application of linear programming to jet selection has already been demonstrated[3]. By dynamically adjusting objective factors, upper bounds, and failure flags associated with each set of actuators, the linear program can adaptively determine efficient and effective policies of actuator usage. Since all available actuators are considered together in a common "pool", the linear program has the ability to select and blend the action of various types of effectors (ie. jets, aerosurfaces, propulsion), resulting in true "hybrid control".

Previous aircraft control efforts[8] have employed a pseudoinverse solution to linearly map desired body torques into aerosurface commands. Such methods can provide control laws with intrinsic longitudinal/lateral actuator decoupling, yet the conventional pseudoinverse calculation lacks the capabilities provided by linear programming to impose hard constraints on actuator usage and establish actuator preference via an objective function. Incorporating features such as these in pseudoinverse and conventional schemes would imply careful tuning and adaption of the control laws, which may become less feasible after actuator failures and reconfiguration, leading to potentially degraded performance. Linear programming retains the benefit of intrinsic actuator decoupling, while providing the control logic the ability to dynamically specify the preferred actuator behavior and limit actuator displacement.

An additional benefit of this approach is the potential of coordinating both translational and rotational vehicle response, simply by extending the order of actuator

activity vectors (ie. measures of vehicle response to specific actuator motion) to also account for translational degrees of freedom. In this fashion, small corrections to the flight path can be accommodated by allowing the selection to specify actuator lift and drag while maintaining full rotational control. Because this control scheme can account for all degrees of freedom simultaneously, it is intrinsically able to compensate for coupled translational and rotational response to actuator deflection.

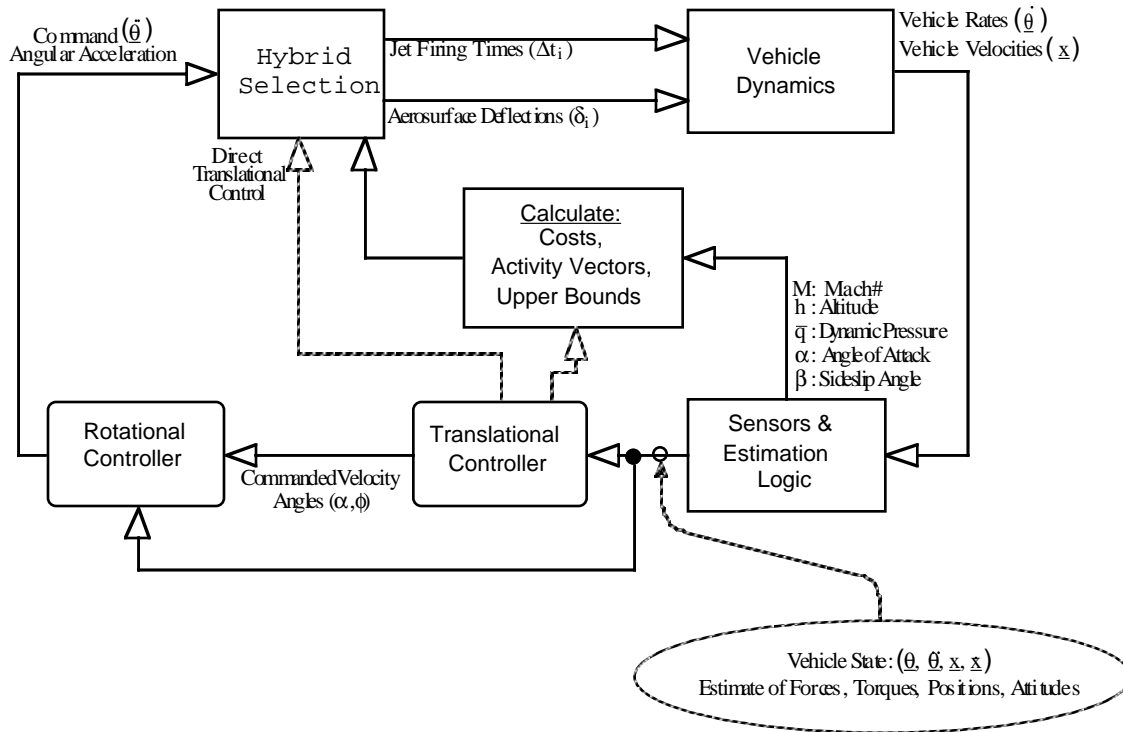
The activity summarized in this report has demonstrated the application of hybrid actuator management techniques to the control of aerospace vehicles. An algorithm capable of adapting to known changes in dynamic pressure, actuator constraints, and vehicle status is used to select a blend of jets and aerosurfaces to dynamically provide maximum control capability. The utility of this approach is demonstrated in a set of constant altitude and re-entry simulations which depict the response of the hybrid control scheme to a variety of challenging situations and constraints. Simulations are also performed to attain a coarse look at the effects of vehicle/environment mismodelling under such a scheme; effects arising from aerodynamic jet interaction, random "gusts" (ie. errors in dynamic pressure), and errors in vehicle state are examined. A means of selecting thrust-vector commands is introduced, potentially enabling the hybrid control scheme to manage a NASP-type vehicle during powered ascent.

## 2) The Linear Selection

### 2.1) Overview

Fig. 1 shows a diagram depicting the means by which a hybrid selection procedure can be integrated into an aerospace plane (ie. NASP) flight control package. A collection of aero sensors, inertial measurement units (IMUs), etc., along with appropriate estimation algorithms and software, is assumed to provide a dynamic measurement of the vehicle state (attitudes, rates position, velocity) and environment (forces, torques, aerosurface/jet authorities, dynamic pressure, etc.). These quantities are used to continually update parameters for the linear selection; ie. aerosurface activity vectors (estimate of instantaneous torque/force control authorities), costs (objective penalizations per actuator), and upper bounds (maximum allowed deflections per control step). In order to compensate for aerodynamic effects, activity vectors for jets may also be periodically updated as a function of vehicle state (at orbital altitude, the net jet thrust is nearly constant, thus the "vacuum" jet activity vectors need only be calculated once).

The estimate of vehicle position and velocity is compared with a set of desired values in a translational controller, which generates commanded velocity attitude (angle of attack [ $\alpha$ ] and bank [ $\phi$ ]; sideslip [ $\beta$ ] is generally held at zero), which will correct the net force on the vehicle. The translational control logic is also able to input a translational force-change command directly to the hybrid selection (leftmost dotted line in Fig. 1), allowing the actuators themselves to directly deliver the requested force difference. One must bear in mind, however, that the aerosurfaces and jets are only capable of restricted translational authority, due to the limited aerosurface area and constraints on available jet thrust and fuel. The primary mode of translational control is via adjustment of vehicle attitude (ie.  $\alpha, \phi$ ), causing the airframe to rotate with respect to the relative wind direction. The aerodynamic force components (ie. lift, drag, side force) change appreciably



*HYBRID CONTROL SCHEME AS APPLIED TO AEROSPACE VEHICLE*

**Figure 1**

with airframe attitude, providing considerable control authority. During ascent of proposed aerospace vehicles such as the NASP, however, vehicle attitude may be tightly constrained by operational requirements (ie. airflow through the propulsion system may impose restrictions on  $\alpha$ ). In these cases, it may be advantageous to command the aerosurfaces for translational trim while holding constant velocity attitude (ie. modulate lift at constant  $\alpha$ ). Provided that there are sufficient independent aerosurfaces available to maintain simultaneous rotational control, this option may prove practical, as will be demonstrated in Sec. 5.3.

Whenever a translational force-change command is applied directly to the hybrid selection, as sketched above, the selection procedure will try to produce a set of actuator commands that realize the request exactly (in the instantaneously linearized model). As translational requests grow in magnitude, the actuators will encounter increasing difficulty in answering them. When the actuator response begins to saturate, the error in requested vs. realized effect becomes considerable, degrading any simultaneous rotational control that

is also attempted. In order to avoid this pitfall, translational control may be applied indirectly to the actuators via the objective function (rightmost dotted line in Fig. 1). Under this scheme, the cost of using a particular actuator is determined by its translational authority. Actuators respond to answer a 3-axis rotational command, but the redundancy in the actuator system is exploited such that actuators are used in a fashion that yields the desired translational effect. One sacrifices the ability of commanding precise translational response under this technique; the actuator selection is informed to "answer this rotational command, but try and do it in such a fashion as to give that translational effect". This strategy may be exploited to intrinsically minimize actuator drag, or to incorporate an actuator assist into an outer velocity attitude ( $\alpha, \phi$ ) translational loop (examples are shown in Secs. 5.2 & 5.4).

The options sketched above are special features provided by the hybrid selection to deliver direct actuator translational control. The standard method of adjusting translation of an aircraft, however, is to change its velocity attitude. This is denoted in Fig. 1 by the arrow connecting the translational and rotational control logic; the translational control law calculates a desired  $\alpha$  and  $\phi$  that yields the commanded force change ( $\beta$  is kept zero). The rotational controller compares this attitude command with an estimate of current attitude (and rate), generating a requested angular acceleration ( $\ddot{\theta}$ ) which is input to the hybrid selection.

The "hybrid selection" package executes a linear program to determine the optimal mix of bounded aerosurface deflections, jet firings, and thrust-vector gimbal commands that yield the commanded vehicle response. An estimate of the rotational & translational authorities of all actuators (termed "activity vectors") is scanned during the selection process. Each actuator possesses at least one associated objective coefficient, upper bound, and failure flag that determine its desirability, authority limit, and availability (respectively). This allows one to dynamically adjust the mix of different actuators appearing in the solution. For example, one can make the cost of forward jets more expensive as the vehicle descends (discouraging their use), eventually failing them altogether (for aerodynamic considerations) after altitude drops below a pre-determined threshold. Dynamic adjustment of actuator objective and bound factors is applied extensively, as discussed in the succeeding sections of this text. The ability to dynamically impose objectives, bounds, and reconfiguration upon the actuator selection is a unique and extremely useful feature of the hybrid selection procedure.

The control loop is closed in Fig. 1 through the vehicle dynamics; actuator activity and environmental acceleration change the vehicle state, which is sensed, estimated, and

updated before being passed again to the translational/rotational control logic, then on to a new hybrid selection.

One must note that each selection is only instantaneously optimal. Actuators are assumed to be linear in their decision variable. Jet torques are assumed to be linear with duty cycles (errors are introduced via discretization), aerosurface force & torque authorities are assumed to be proportional to deflection (large deflections can exhibit considerably nonlinear response, especially at low  $\alpha$ ), and acceleration change is assumed to be proportional to thrust-vector gimbal commands (this is a rotation, hence the acceleration components change trigonometrically). Although methods have been developed to aid in aerosurface linearization (see Sec. 2.4), the actuator authorities are essentially approximated to leading order. In addition, actuator effect is considered only at the current vehicle attitude; as the airframe rotates between selections, the velocity angles change, perturbing assumed aerosurface authorities and environmental accelerations, also in a somewhat nonlinear fashion.

Coping directly with these nonlinearities is not feasible in real time, and may not prove very useful in the face of an uncertain aerodynamic environment. Instead, this "linearized" selection is iterated periodically as the aerosurface and vehicle states change. Such repeated linear "stepping" is conventional in today's aircraft autopilots; ie. the Shuttle entry DAP iterates linearized control loops at rates approaching 25 Hz[1].

In the simulations presented in Sec. 5, a control update rate of 1.5 Hz was found to provide adequate stability and limit perturbation due to non-linearities. In the presence of increased modelling uncertainty, estimation effects, and a less benign vehicle environment, however, a higher repetition rate might be needed. This should be possible to achieve; a linear program has already been cycled at up to 12.5 Hz as an experimental jet selection onboard the Shuttle Orbiter[3].

Recent advances in control theory, such as external linearization[9], provide a framework for transforming non-linear systems into equivalent linear systems, enabling linear control laws to achieve better performance than encountered with the leading-order "tangent" approximation detailed above. Similar techniques have been applied to aircraft controllers[10], and could potentially be used with a linear programming selection as well; ie. the selection would be wrapped around a linearizing transformation and would select activity vectors in equivalent linear coordinates (effective methods of dealing with redundancy in the control transformation have been developed in Ref. [11]). This framework is not pursued here; a simple control scheme is developed that is designed primarily for demonstrating the hybrid selection. Additional effort in adapting advanced

control theory to actuator selection schemes of this type is a promising subject for future efforts.

In most conventional aircraft autopilots, particular aerosurfaces are dedicated to controlling specific coordinates (ie. the body flap has its own pitch loop, the rudder manages yaw, etc.). Custom logic is often introduced to decouple actuators that possess simultaneous authority in several axes, and specific aerosurfaces are often used in pre-determined ways to compensate classical aircraft instabilities. This can sometimes reduce efficiency and control margin, especially in the case of failures. As depicted in Fig. 1, however, the hybrid selection logic does not explicitly dedicate aerosurfaces to pre-specified coordinates and decoupling strategies. The input command is a 3 (rotation only) to 6 (full rotation & translation) element column vector specifying the desired vehicle acceleration change. The linear selection uses the actuator authorities modelled in the activity vectors (with an estimate of the vehicle mass and inertias) to decouple actuator response. The mode of particular actuator usage may be encouraged and/or enforced by adjusting the bounds, objective factors, and failure flags used by the selection; all activity vectors are considered together in a common "pool", however, and none are explicitly dedicated to specific control strategies. Although this benefit of "intrinsic decoupling" is also exhibited by pseudoinverse procedures[8], they lack the ability to influence individual actuator usage via bounds and objective functions, which prove to be exceedingly advantageous, as will be shown later in this document.

The 1-normed optimization (sum of absolute values) solved by the linear program has been noted[12] to often exhibit a "noisy" and discontinuous solution history when constraints and objective factors are smoothly varied. This has been attributed to "vertex switching" of the solution, whereby the linear program frequently converges to different currently-optimal solutions represented by distinct vertices of the hyperpolyhedron defined by the constraints in decision-variable space. A small change in the constraints or objective can result in a switch to another vertex, representing a totally different solution. When linear programming was applied to the CMG steering problem, this effect could produce frequent spikes in the gimbal rate profiles, leading to inefficiency and noisy response. By running the CMGs differentially (ie. solving for a *change* of gimbal rates needed to yield a *change* in net torque), this "switching" of gimbal rates could be penalized directly and attenuated[12].

The aerospace vehicle controller (Fig. 1), however, is naturally constructed in this differential framework. Changes in aerosurface deflections (relative to their current angles) are produced in response to an acceleration-change request. The objective minimization performed by the linear program tends to specify solutions with minimal aerosurface

deflection change (except in cases with negative objective coefficients), yielding smooth aerosurface response. When jets or other "impulsive" actuator families are used with aerosurfaces in "hybrid" maneuvers, the aerosurface motion can be rougher (ie. aerosurfaces are moved abruptly to compensate off-axis jet thrust when jets start firing, and are returned afterward), but such action is relevant under these conditions, and may be minimized by making aerosurfaces relatively more expensive to use in hybrid maneuvers.

The 1-normed optimization seems to yield satisfactory performance in controlling a vehicle with aerosurfaces, as will be shown in Chapter 5. The minimum 2-norm (sum of squares) solution, however, is generally less sensitive to perturbations in the constraints and objectives. A scheme has been applied in Ref. [11] to solve a quadratic program with bounded decision variables; although such a method might be incorporated into the hybrid selection scenario to yield smoother response, the increase in required computation may prove problematic for frequent real-time iteration. Linear programming may also be adapted to optimize in other norms (ie.  $\infty$ -norm, see Ref. [11]), usually at the expense of increased computation. Again, the simpler 1-normed linear program presently employed in the hybrid controller is well-suited to this problem and seems to yield satisfactory results.

## **2.2) Linear Programming & Simplex Adaptations**

The linear programming problem solved by the hybrid selection implemented in Fig. 1 may be summarized as:

*Minimize:*

$$1) \quad Z = \sum_{j=1}^N c_j |x_j|$$

Subject to:

$$2) \quad \begin{aligned} & \text{a) } \sum_{j=1}^N \underline{A}_j x_j = \underline{\Delta R} \\ & \text{b) } -U_j^- \leq x_j \leq U_j^+ \end{aligned}$$

Where:

- $N$  = # of actuators available to system  
 $c_j$  = Cost factor associated with actuator #j  
 $U_j^\pm$  = Upper/Lower bounds associated with actuator #j  
 $\underline{A}_j$  = Activity vector representing authority of actuator #j  
 $x_j$  = Decision variable denoting action of actuator #j  
 $\underline{\Delta R}$  = Requested vehicle acceleration change

Eq. 2a is the equality constraint. It is a vector equation representing an under-determined system of  $M$  scalar equations ( $M$  = # of controlled axes; ie. dimension of  $\underline{A}_j$  and  $\underline{\Delta R}$ ) in  $N$  unknowns. Eq. 2b is an inequality constraint expressing independent upper and lower bounds on the allowed range of the decision variables  $x_j$ . Although Eq. 2b could contribute another  $2N$  equations in  $2N$  unknowns to the system (via the addition of "slack variables"[13]), the "upper bounding simplex method"[14] allows the limits of Eq. 2b to be considered without augmenting the order of the problem stated in Eq. 2a.

Eq. 1 is the linear objective function that is minimized in the solution to the linear program; it essentially defines a weighted 1-norm in the space of decision variables  $x_j$ . The solution values of  $x_j$  denote the selected amounts of corresponding actuator action (ie. change in aerosurface deflection). Limits on actuator usage may be imposed independently by clamping positive and negative decision values by their corresponding bounds ( $U_j^\pm$ ). The activity vectors in this framework, ( $\underline{A}_j$ ), denote the instantaneous acceleration change produced by each actuator per unit decision value  $x_j$ . The  $\underline{\Delta R}$  is the input acceleration change command; Eq. 2a essentially states that the sum of all actuator activity in any solution must realize the input command. The activity and command vectors ( $\underline{A}_j$  and  $\underline{\Delta R}$ )

are dimensioned to the number of independent control axes ( $M$ , as introduced above). For rotational control only,  $M=3$ ; as translational degrees of freedom are added,  $M$  ranges from 4 to 6. In the software constructed for this effort, activity vectors and simplex-based linear programming algorithms are structured to assume either  $M=3$  (rotation only) or  $M=6$  (full rotation & translation). A simple scheme, described below, was devised to release simplex control of selected axes, allowing  $M$  to effectively possess intermediate values. The actual calculation of activity vectors is customized for each type of actuator, as will be presented in Chapter 3.

The simplex procedure solves a linear program by successively modifying a solution to the constraints of Eqs. 2 through discrete exchanges of candidate activity vectors. If the problem is properly posed, each activity vector exchange improves (ie. increases or decreases, in accordance with the optimality protocol) the evaluation of the objective function, until the optimum is reached. The explicit imposition of upper bounds (per Eq. 2b) enables simplex to introduce as many activity vectors (ie. actuators) into the solution as needed to optimally attain the input command. Simplex is started with an arbitrary solution to Eqs. 2 (potentially "artificial" with non-physical "imaginary" activity vectors). The first simplex exchanges substitute actual activity vectors for any imaginary startup vectors; all subsequent exchanges work on an actual solution to the constraints of Eqs. 2 to improve the objective evaluation.

The logic used to solve the linear program is very similar to the upper-bounded revised simplex algorithm detailed in Sec. 2.4 of Ref. [5]. The flow charts given in Figs. 4 through 8 of Ref. [5] may be taken to describe the simplex procedure applied here, with a few minor changes, as outlined below.

A very simple modification enables simplex to solve a problem of lower dimension without reducing the rank of the basis, activity vectors, and related calculations. A boolean vector "**AX CTL**" is created with parallel dimension to the activity vectors ( $\underline{A}_j$ ) and input request ( $\underline{\Delta R}$ ). Axes retaining full control consideration under simplex have their corresponding "**AX CTL**" set to "ON", ignored axes set their "**AX CTL**" to "OFF". When forming the identity matrix to use as the starting basis for simplex ( $[\mathbf{B}]$  in Fig. 4 of Ref. [5]), diagonal elements corresponding to ignored axes (flagged by their **AX CTL** component set "OFF") are zeroed. This enables all matrix operations used in the exchange and pivoting logic to retain accuracy in the over-dimensioned system. All such zero columns and corresponding zero rows of the basis are retained after each exchange operation (Fig. 8 of Ref. [5]), and because the basis is never actually inverted during simplex, its singular nature at full-rank is never bothersome. An additional modification, however, must be performed to the simplex "**Exclude**" loop (Fig. 6 of Ref. [5]) to prevent

numerical difficulty. When looping over the basis ( $L = 1$  to  $N$ ), to select an activity vector for exclusion, any basis vectors corresponding to an uncontrolled coordinate must be ignored. This is readily accommodated in the logic of Fig. 6 of Ref. [5] by inserting another decision diamond immediately below the  $L$  "Do" loop, that checks the value of  $\mathbf{AX CTL}(L)$  and skips out to "NEXT  $L$ " if it is "OFF", thus averting the **Exclude** tests, which would "blow up" upon encountering a zero basis vector.

Additional changes to the simplex structure were needed to accommodate dynamic RCS constraints and aid in compensating aerosurface nonlinearity. The shuttle jets are organized into "clusters", which, in turn, are grouped into "pods". Because of fuel flow and hardware-related constraints, the number of jets allowed to fire per pod is limited. The simplex procedure has been modified, as discussed below, to avoid violation of these constraints.

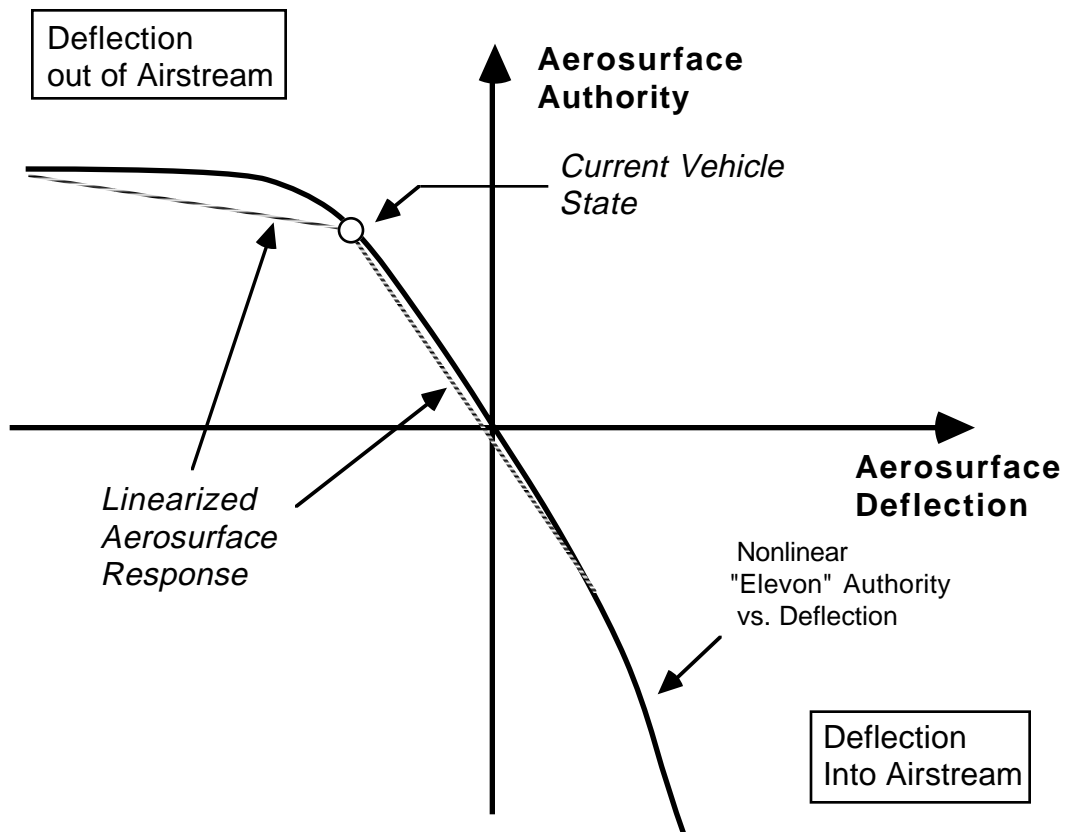


**Figure 2: Potential Elevon Nonlinearity**

Significant nonlinearity can be associated with aerosurface deflection. Moving an aerosurface "down" into the airstream can yield a significantly higher authority than deflecting it "up" into a shadowed region (the magnitude of this effect depends on the vehicle  $\alpha$  and Mach number). An extreme case is shown in Fig. 2, which gives a plot of "elevon" authority vs. deflection. The nonlinearity and "saturation" in the shadowed region (at left) is obvious. If the current vehicle state approaches the "knee" of the curve, as in Fig. 2, one can see that the linearized aerosurface authority (ie. slope of lines in Fig. 2) is very different between significant positive and negative deflections. If one retains the same activity vector for both senses of aerosurface deflection (as was justified for CMGs in Ref. [5]), significant errors can be introduced into the simplex solution. In order to avoid this calamity, the simplex procedure of Ref. [5] was also modified to consult different activity vectors for positive and negative aerosurface deflections.

The logic of the original simplex software used in Ref. [5] is coarsely diagrammed in Fig. 3. Each box corresponds to an entire diagram in Ref. [5]. Note that *all* available activity vectors are considered in the "**Invite**" loop. The activity vector with the largest Cost Gradient (ie. yielding most objective benefit) is selected to enter the solution. It is used in the "**Exclude**" loop to determine the basis elements (if any) that can be removed, and in the "**Decide**" tree to choose the simplex operation to pursue (simplex pivot, simplex pivot & upper bound substitution, or upper bound substitution). Note that the "**Invite**" and "**Exclude**" loops are entirely separate here; all activity vectors are first scanned in "**Invite**" before the basis is examined in "**Exclude**".

The logic has been changed in the simplex package adapted for use in this effort, as can be noted in Fig. 4. The **Invite** and **Exclude** loops have essentially been merged here. Every activity vector possessing a positive Cost Gradient is checked in **Exclude** and **Decide**; the activity vector producing the largest cost improvement (under the operation determined in **Decide**) is invited into the basis or upper-bounded. This implies that the basis must be examined with every activity vector available for invitation, significantly increasing the required computational burden. One does benefit, however, in that simplex seems to often converge more rapidly under this formalism. By specifying the detailed simplex operation for each candidate, the particular activity vector is invited that yields the largest cost decrease. This contrasts with the previous technique of inviting the "most promising" activity vector based on its Cost Gradient, which might not descend as steeply to the optimal solution. The simplex applied in Ref. [2] also merges its **Invite** and **Exclude** loops in this fashion. Note that much of Fig. 4 represents an expansion of the **Invite** loop. The presentation is still at a high level; much greater detail can be found in Sec. 2.4 of Ref. [5].

# Simplex Overview (Logic of Ref. 5)

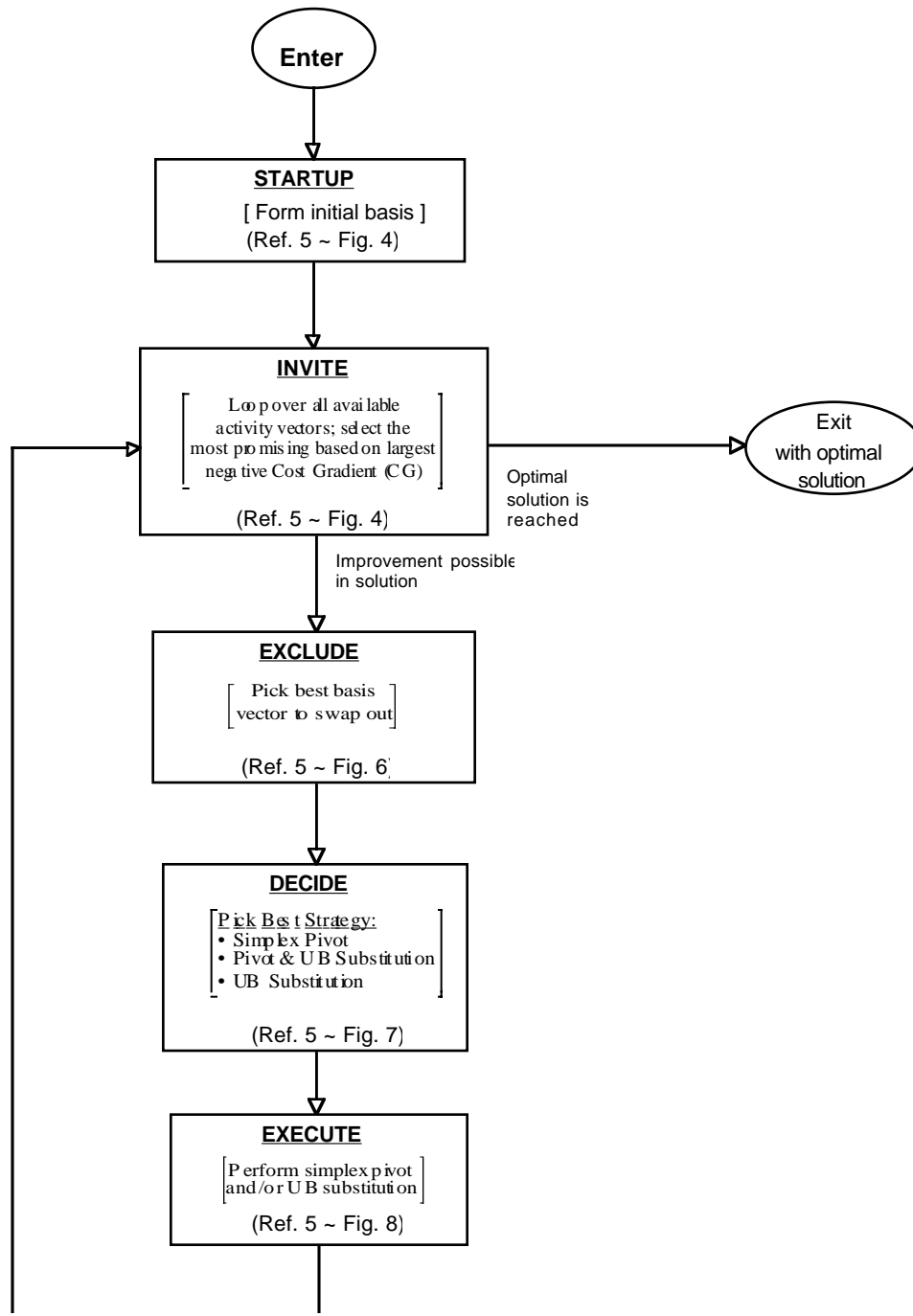


Figure 3



The conditional branch "diamonds" at the lower portion of Fig. 4 were inserted to meet the maximum jets-per-pod constraint and incorporate dual activity vectors for positive and negative aerosurface deflection, as introduced earlier. The logic flow splits into two basic paths, depending upon the outcome of the **Decide** operation. If a simplex pivot is selected (indicating that an activity vector will leave the solution as the invited vector is admitted), the leftmost path is pursued. Here, the invited vector is ignored if it is a jet from a pod that is already full (and the outgoing activity vector is not also from that pod), or if it is an aerosurface which is opposite in sense to an activity vector already in the solution (and the opposing activity vector is not selected to be pivoted out of the basis). The right-hand path is taken when the **Decide** operation selects an upper bound & pivot combination or upper-bound substitution (indicating that an activity vector will not be leaving the solution). The logic in this path is identical, except for the lack of a check on the outgoing activity vector (since there is no outgoing activity vector here).

The above conditions are needed to avoid solutions specifying simultaneous forward/backward aerosurface deflections or an over-abundance of jets firing per pod. Their imposition dictated the re-structuring of the simplex process to merge the **Invite** and **Exclude/Decide** loops; since the detailed solution is investigated for every invited activity vector, all solutions can be evaluated during **Invite**, and any violating these constraints can be culled from consideration.

A difficulty may arise from this means of incorporating constraints into simplex, in that the linear programming problem is being dynamically modified as it is solved. Such effects did indeed precipitate in the results of Ref. [7], where a bound on the quadrature sum of two decision variables that was incorporated in this fashion could prevent the simplex pivoting chain from always reaching the optimal solution.

The situation should be substantially better here. Consider first the aerosurface condition. The positive and negative activity vectors for each aerosurface should generally be oriented in approximately opposite directions. Because of the need to retain linear independence and minimize cost projection, simplex, by itself, will generally tend to allow only one paired activity vector at a time. If, in the course of solving the constrained problem, it becomes advantageous to switch deflection sign, simplex still has a path available; it can pivot the activity vector in question out of the solution, then invite its opposite-sign companion in on the next iteration. Since both of these operations will apply control authority in roughly the same direction and exhibit similar Cost Gradients, their sequential application will be chosen, when needed, by simplex.

The maximum jets-per-pod constraint, however, could pose more of a problem. If simplex was faced with a large request that immediately caused a pod to saturate, other jets

in that pod, which may prove more beneficial to introduce after the solution has evolved somewhat, are effectively prohibited from firing unless one of the original jets is pivoted out (there is not necessarily any "opposite sign" effect to aid us here, as existed with aerosurfaces). The practical severity of this difficulty is diminished somewhat, in that pods will generally fill promptly only in the case of excessively large commands, which should not often occur. In addition, most jets sharing the same pod should have nearly equivalent costs, thus simplex may not gain much optimality by replacing a jet in the solution with another from the same pod. Solutions exhibiting a lack of optimality through this constraint will still be valid, although perhaps some fraction less efficient than ultimately possible.

In any future application of this work, the effects of such dynamic constraints on the simplex process should be examined more quantitatively. Alternative means of solving such constrained problems in a more rigorous fashion should be investigated. The method of Fig. 4, however, is quite straightforward, and has been seen to aptly respond to the objective function while maintaining all constraints, as will be demonstrated in Chapter 5.

A few further remarks are in order concerning the relation of Fig. 4 to the logic detailed in Ref. [5]. In Ref. [5], each CMG gimbal had only one activity vector (yet still two objective coefficients), due to the reflection symmetry of the instantaneous gimbal rotation. In the current case, this symmetry has been removed, hence we now have two activity vectors per aerosurface, constrained as in Fig. 4. Each of the corresponding decision variables are bounded at zero and either  $U^+$  or  $U^-$  (as appropriate; Eq. 2b). In order to accommodate direct specification of duty cycles, jets are now also upper-bounded (as detailed in Sec. 3.4). An additional comment must be made on the interpretation of the upper-bound substitution (**UBS**) algorithm presented in Fig. 8 of Ref. [5]. In a combination pivot/UBS operation, the recombination vector  $\underline{T}$  must be calculated with respect to the *new* basis (after the pivot operation); the original  $\underline{T}$  (as calculated in Fig. 6 of Ref. [5]) is not appropriate. A few typographical errors may have crept into the diagrams of Ref. [5] (ie. the " $L_{out}$ " in the "**Update  $\underline{X}$** " block of the **PIVOT** logic in Fig. 8 is nonsensical; it should read " $\underline{X}_j$ "), but they are otherwise intact.

### **2.3) General Formulation of Objective Function**

The objective function minimized by simplex (Eq. 1) is a sum of weighted cost contributions having a general form analogous to Eq. 30 of Ref. [5]. Terms are included to

penalize deflection angle and avoid maximum deflection limits (ie. "stops"). Since CMG-style singular states are not a problem for the system considered here (due to relatively tight limits on available deflection, manipulation of the actuator configuration can not directly cause the aerosurface Jacobian to lose rank), related terms (ie. the CMG anti-lineup term) are omitted. In analogy to Eq. 30 of Ref. [5], we now have:

$$\begin{aligned}
 & \text{a) } c_j = K_{\text{jet}}(j) \quad (\text{Activity vector } \#j \text{ corresponds to RCS jet}) \\
 3) & \\
 & \text{b) } c_{j,s} = K_0(j) + K_A F_{\text{Angle}}(j,s) + K_S G_{\text{Stops}}(j,s) + K_T V_{\text{Translation}}(j,s) + \\
 & \quad \quad \quad K_Q Q_{\text{Specific}}(j,s) \\
 & \quad \quad (\text{Activity vector } \#j \text{ corresponds to aerosurface [or thrust-vector gimbal])
 \end{aligned}$$

The objective penalization of RCS jets is given by a single term,  $K_{\text{jet}}$ . This factor is different for various sets of jets (ie. use of forward jets is penalized more heavily, since they can appreciably perturb entry aerodynamics), and altitude-dependent (jets are made more expensive as the vehicle descends, and are eventually prohibited altogether at low altitude). The  $K_{\text{jet}}$  factors are generally significantly higher than average aerosurface costs, in order to discourage jet firings except where absolutely necessary. Tests examining the effects of the relative jet/aerosurface cost balance are given in Chapter 5.

The cost calculation for dynamic actuators (such as aerosurfaces or thrust-vector gimbals) is, however, more complicated, and includes terms from several sources. The leading term,  $K_0$ , is a bias which dictates the general desirability of using a particular actuator. If  $K_0$  is relatively large, the actuator will be avoided in a solution (where possible), with its participation increasing as  $K_0$  drops. The  $F_{\text{Angle}}$  and  $G_{\text{Stops}}$  functions act to penalize deflection. Although aerosurfaces (and, perhaps, limited-range thrust-vector gimbal systems) do not suffer from effects that degrade the authority of one actuator with advancing deflection of another (as plagues the nested gimbal system of the double-gimballed CMG world; ie. Sec. 3.2 of Ref. [5]), one would generally like to keep them (in the absence of other considerations) near their trim positions. This is encouraged for small & moderate deflections through the  $F_{\text{Angle}}$  function, which adds an amplitude into the objective penalizing simplex solutions that increase deflection angles:

$$4) \quad F_{\text{Angle}}(j,s) = \begin{cases} |\delta_j| & \text{If rotation "s" increases } |\delta_j| \\ 0 & \text{Otherwise....} \end{cases}$$

Deflection increments which increase the magnitude of net deflection angle  $|\delta_j|$  are assigned a cost contribution in direct proportion to the current value of  $|\delta_j|$ . Deflections which decrease  $|\delta_j|$  are given no cost contributions via  $F_{\text{Angle}}$ . Rotations that increase the deflection angle thus become linearly more expensive as the angle grows. Solutions involving the activity vector and decision variables that bring  $|\delta_j|$  back to zero accordingly become increasingly favored as  $|\delta_j|$  rises.

If an actuator is pinned against a hard "stop", a degree of freedom is essentially lost to the selection algorithm (the actuator can then only be moved in one direction; ie. off the stop). In addition, thermal and hinge-moment constraints may create regions near the extremes of actuator deflections that should be avoided whenever possible. Although the upper bounds of Eq. 2b may be imposed to absolutely prevent actuator motion past stop boundaries, an objective function that increases rapidly as an actuator nears its limit could slow or inhibit actuator motion before maximum deflection is reached.

The  $G_{\text{Stops}}$  cost contribution signals such a "warning" to the selection procedure as an actuator nears its limit. In contrast to the linear form of  $F_{\text{Angle}}$ ,  $G_{\text{Stops}}$  contributes a nearly insignificant amount to the objective if the gimbal is removed from its stop (allowing the other terms in Eq. 3b to act unimpeded), but increases rapidly after the gimbal has approached to within a pre-set distance from the stop location. The form of  $G_{\text{Stops}}$  chosen to be applied here can be expressed:

$$5) \quad G_{\text{Stops}}(j,s) = \begin{cases} \Lambda(\delta_j) & \text{If rotation "s" moves actuator toward stop} \\ 0 & \text{Otherwise....} \end{cases}$$

$$\text{Where: } \Lambda(\delta_j) = \tan \left[ \frac{\pi}{2} \left( (1 - \zeta) \left[ \frac{\delta_j}{\delta_{\text{Stop}_j}} \right] + \zeta \right) \right] - \tan \left( \frac{\pi}{2} \zeta \right)$$

$$\zeta = \text{"Steepness" parameter; } 0 < \zeta < 1$$

The function  $\Lambda$  has a small value for low  $\delta_j$ , however, as  $\delta_j/\delta_{\text{Stop}}$  approaches unity,  $\Lambda$  diverges asymptotically to infinity. One may control the "breakpoint" at which  $\Lambda$  diverges by adjusting the " $\zeta$ " parameter in Eq. 5. For large  $\zeta$ , the function begins to contribute at lower  $\delta$  and slowly diverges as  $\delta$  increases. If  $\zeta$  is brought below 0.9,  $\Lambda$  begins to diverge more sharply at higher  $\delta_j$ , until for  $\zeta \rightarrow 0$ ,  $\Lambda(\delta_j)$  can approximate a delta function peaking when actuator #j is against its stop.  $\Lambda(j)$  is plotted for several values of  $\zeta$

in Fig. 5 (the variation of steepness with  $\zeta$  is quite obvious). The "intermediate" curve with  $\zeta = 0.93$  is the  $\Lambda$  function generally used in the examples of Chapter 5; this corresponds to a "breakpoint" in aerosurface deflection at  $\delta_{\text{Break}} \approx 0.75 \delta_{\text{Stop}}$ .

Eq. 5 is essentially the same as Eq. 32 of Ref. [5], which was used to avoid CMG stops. A set of typographical errors, however, crept into Eq. 32 and Sec. 3.3 of Ref. [5]; these have been corrected in the discussion presented here.

## ***Stops Penalty Function for Several Different Steepness Values***

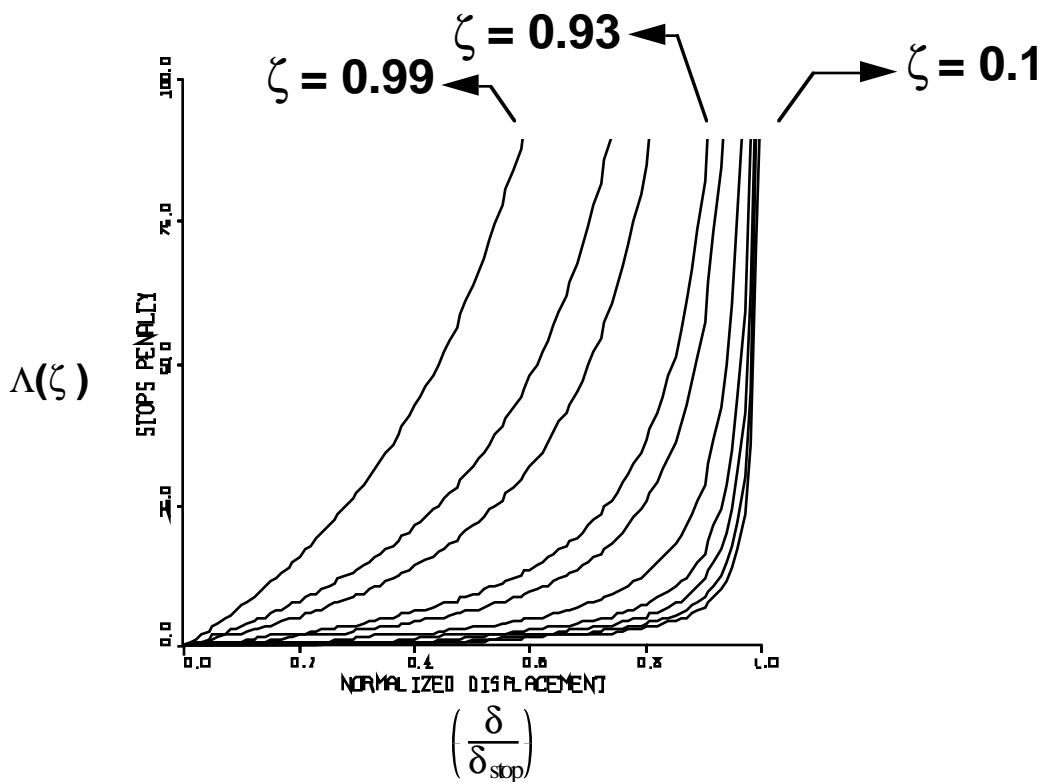


**Figure 5**

If the rotation "s" brings an actuator toward a stop, the objective contribution will be proportional to  $\Lambda$ . No such contribution will be added to the objective coefficient if an actuator has unlimited freedom or if rotation "s" will remove it from a stop. If an actuator has neared its stop, the function  $\Lambda$  will contribute appreciably, and solutions which rotate the actuator away from the stop are heavily favored in contrast to those which move it

closer. The form of  $\Lambda$  in Eq. 5 may be simplified (one can use several divergent functions); it was set up in its present realization to facilitate modifications during testing. Both functions  $F_{\text{Angle}}$  and  $G_{\text{Stops}}$  attempt to minimize deflection angles, but the "steep"  $G_{\text{Stops}}$  contribution works primarily at large  $\delta_j$ , whereas the function  $F_{\text{Angle}}$  has effect at smaller  $\delta_j$ .

The two remaining terms in Eq. 3b were not introduced in Ref. [5].  $V_{\text{Translation}}$  denotes a function which enables translational control to be applied through the objective function. The form of this function is detailed in Sec. 4.2.  $Q_{\text{Specific}}$  denotes objective contributions which are specific to individual actuators; the application of these functions is discussed in Sec. 4.3.

Upper bounds (Eq. 2b) are imposed on the decision variables of all actuators. Since their calculation is customized for each type of actuator, details will be given in the discussion of particular device models developed in Chapter 3.

## **2.4) Implementation**

In order to better accommodate actuator characteristics and cope with nonlinear response, the hybrid selection procedure has been buffered with a front end that further addresses large aerosurface deflections. Because of the nonlinearity inherent in aerosurface response, simplex solutions specifying large aerosurface deflections may be significantly inaccurate. Three or more "linearized" aerosurfaces participating in a three-axis maneuver often balance the action of one actuator against another to yield a net effect. Even with only small errors in the knowledge of each actuator response, the relative error in the conglomerate solution can still be sizable.

Upper bounds impose a clamp on deflection of each aerosurface; by unilaterally reducing bounds, one limits how far aerosurfaces can travel per control step, thus reducing nonlinear distortion in the solution. If bounds are reduced excessively, however, the aerosurface response to standard commands will be "stunted", and jets will be wastefully called in to augment their action.

Clearly, a compromise must be made between large aerosurface deflections (with nonlinear effect) and tightly bounded aerosurface deflections (with frequent jet firings). The choice taken in this endeavor has been to leave reasonable room for aerosurface deflection in the upper bound definition (fast actuators are allowed to slew at their

maximum rates [see Table 1] allotting them a large authority margin), while breaking up large commands (which yield wide deflections) into a series of smaller components.

The software developed for this study accomplishes this by checking each simplex solution for an aerosurface deflection change exceeding a pre-set factor  $\delta_{\max}$ . When this occurs, the input command is broken into chunks scaled by a factor of  $\delta_{\max}$  divided by the maximum deflection change specified in the solution. These pieces are sequentially fed to simplex, yielding a string of smaller deflection increments. The aerosurface angles and linearized activity vectors are updated after each selection. If, in the course of solving these sub-commands, jets are required or another aerosurface deflection-change surpasses  $\delta_{\max}$  (per selection), the process is aborted, and the original simplex response to the full command is used. If, on the other hand, all sub-selections were satisfactory, their deflection-changes are summed, yielding a (hopefully) more accurate aerosurface solution.

Although this process is computationally inefficient, it is not often invoked ( $\delta_{\max}$  is generally set at over  $4^\circ$ ). Other methods may offer a superior means of answering this situation; ie. the control update rate could be increased (diminishing the deflection-change per step), or command magnitudes could be limited before simplex is invoked.

Another condition that could involve additional postprocessing of selection results can occur in hybrid jet/aerosurface maneuvers. Extensive investigation of hybrid jet/CMG spacecraft maneuvering was presented in Sec. 4.3 of Ref. [5]. The jet/aerosurface case is fortunately somewhat simpler; aerosurfaces (particularly the elevons) generally have much higher relative bandwidth and authority (in the flight regime considered here) than did the double-gimballed CMGs of Ref. [5]. An exception exists about the yaw axis, however, where the vehicle defined in Chapter 3 has negligible aerosurface authority at high angle-of-attack. The problem naturally decouples; jets are introduced in this case to handle yaw, while aerosurfaces clean up the residual and handle other coordinates. Since the hybrid situation is more accommodating for aerosurfaces than it was for CMGs, the simplex solution may be used as-is in hybrid operations, and the relative action of jets and aerosurfaces can be managed in a single selection through appropriate manipulation of objective factors and upper bounds.

This simple strategy seems to be adequate, and is applied in all of the examples shown in Chapter 5. Earlier tests, however, employed additional logic imported from Ref. [5] (upon which much of this software was originally based) to supervise hybrid maneuvers. Simplex selections, under this plan, are first attempted with jets inhibited. This produces solutions that "squeeze out" as much pure aerosurface response as possible. If imaginary vectors remain in the solution to the linear program, simplex has indicated that the aerosurfaces are unable to yield the required response alone. Another selection is then

performed and implemented with jets available and reduced upper bounds (preventing excessive "flailing" of aerosurfaces as the jet firing policy changes).

This "second" hybrid selection is potentially wasteful of computation time, and (as hinted above) seems to be unneeded here. Although more control of the jet/aerosurface mix is provided by the dual selection, a single selection with properly-adjusted objectives and bounds should provide adequate solutions for both pure and hybrid maneuvers.

Relative selection preferences may be established between different aerosurfaces (or jets) by appropriately adjusting their  $K_0$  and  $K_A$  values. This is exploited in the tests of Chapter 5 to generally discourage deflection of certain aerosurfaces and firing of specific jet families. Adjusting this cost balance may also be used to discourage selection of large contributions by sensitive "high-authority" actuators (which may be prone to estimation errors). If an actuator possesses a significantly larger authority, it may be made proportionally more expensive, resulting in an "even" distribution of command realization across all participating effectors, and a potentially more accurate solution. Creative construction of the objective formulation and upper bounds provides ample opportunity for developing effective approaches to managing the characteristics of diverse actuators.

Because it has not been implemented in simulations, discussion of thrust-vector control has been omitted in this section. The principles applied here, however, may be readily extended. Non-linearities in thrust-vector rotation will probably not be as problematic, due to limited gimbals range and potentially slower gimbals response. If needed, large gimbals displacements could also be broken up into a sequence of sub-selections (or similar logic applied). If the thrust-vectoring bandwidth is much lower than that of the RCS system (or aerosurface array), the allowed thrust-vector gimbals response per control step can be limited with tight upper bounds; in extreme cases, a hybrid re-selection (as introduced above) can be performed to re-assign bounds and objectives that are better suited to the situation. As usual, the relative preference of all actuator families is specified through the objective function. A slowly-gimballing thrust-vector system may be an ideal candidate for a negative cost factor, projected in a direction to offload the aerosurfaces. Provided that the aerosurfaces have higher bandwidth, they will respond promptly to null disturbances. The thrust-vector gimbals will move more slowly (as reflected in their tight upper bounds), but, if given a negative cost (favoring motion that offloads aerosurfaces), the thrust vector will be selected at each control iteration until its activity gradually allows the aerosurfaces to again approach trim (or maximally unload). This technique was used to manage body flap activity in the simulated vehicle, as detailed in Sec. 4.3.

## **3) Vehicle and Actuator Models**

### **3.1) Overview**

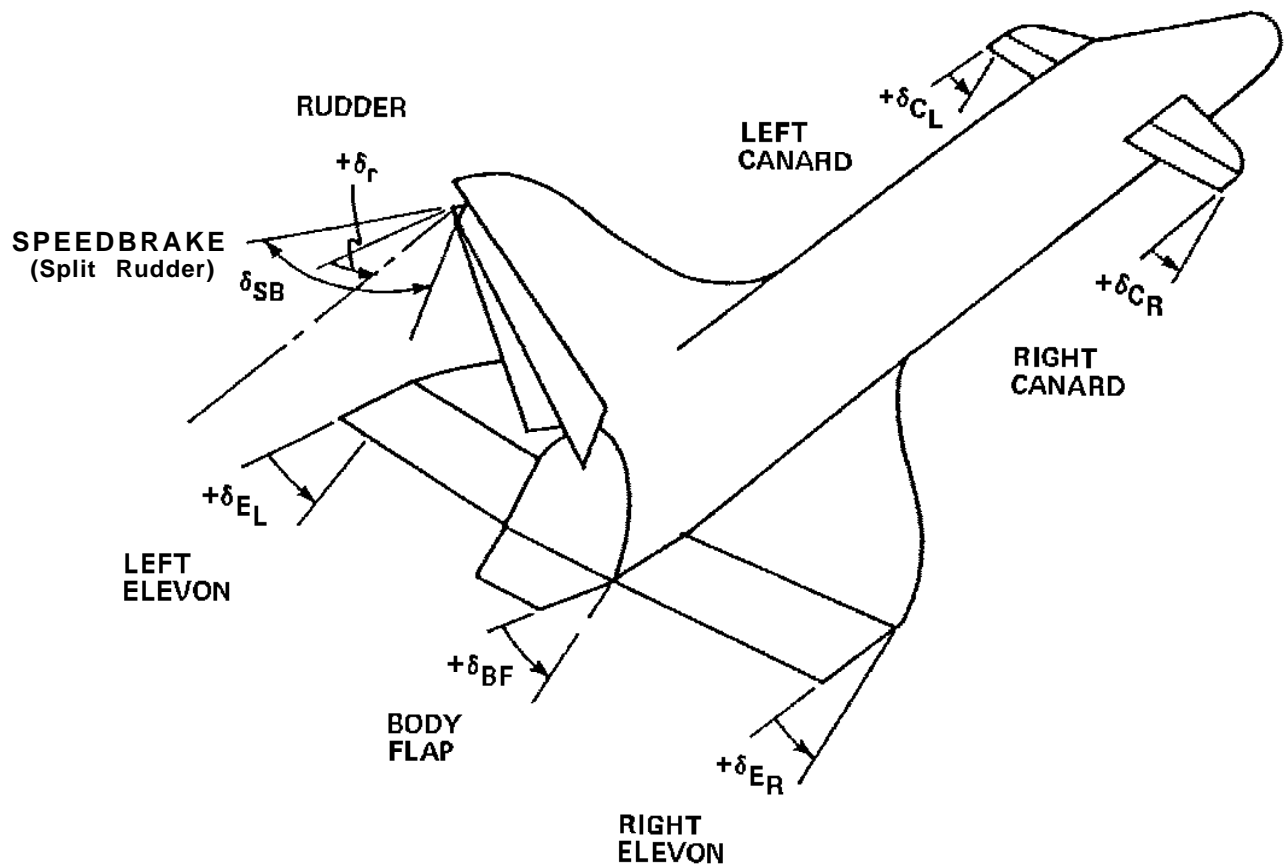
This chapter introduces the particular vehicle model used in the simulations of Chapter 5. Details are presented on the adaptation of Space Shuttle re-entry data to produce airframe aerodynamic response and aerosurface authorities. The RCS jet configuration is defined, and RCS aerodynamic interaction is investigated. A model of thrust-vector control is developed, and methods are proposed for hybrid management of hypersonic vehicle ascent. Detailed calculations are given for activity vectors and upper bounds needed to incorporate each type of actuator into the hybrid selection.

### **3.2) Definition of Vehicle Model**

Due to the current lack (in the unclassified literature) of a detailed airframe/aerosurface model for proposed aerospace vehicles such as the NASP, simulations conducted during this study have adopted a model based on the standard Space Shuttle aerosurface and jet configurations as defined for re-entry. This has enabled a hybrid selection to be immediately tested and developed with a readily-available, fully determined, and well-understood vehicle model. The software and experience thus accumulated can eventually be applied to other models (ie. NASP) after the emergence of candidate vehicle definitions.

The Shuttle-derived vehicle defined in these tests is assumed to possess seven controllable aeroactuators. Two elevons a body flap, a rudder, and a speedbrake are incorporated as conventionally defined[16], with parameters summarized in Table 1. Two canards were added to the model as a means of increasing the alternatives available to the actuator selection. Although the

canards are not needed for conventional 3-axis attitude control, tests which attempt simultaneous actuator control of rotational and translational vehicle states require the extra degrees of freedom. A diagram depicting the location of the seven aerosurfaces is given in Fig. 6. Positive elevon, canard, and body flap deflections are defined as moving down into the airflow at positive angle of attack, as portrayed in Fig. 6.



## Modelled Aerosurface Locations and Sign Conventions

**Figure 6**

**Table 1: Maximum Aerosurface Angles and Slew Rates**

| <u>Aerosurface</u>   | <u>Maximum Range (ie. Stop Locations)</u> | <u>Slew Rate</u> |
|----------------------|---|------------------|
| Left & Right Elevons | -35° → 20°                                | 20 °/sec.        |
| Left & Right Canards | -10° → 10°                                | 20 °/sec.        |
| Body Flap            | -11.7° → 22.5°                            | 1.3 °/sec.       |
| Rudder*              | -22.8° → 22.8°                            | 10 °/sec.        |
| Speedbrake*          | 0° → 87.2°                                | 5 °/sec.         |

\*: The maximum allowed Rudder deflection is decreased for large Speedbrake deflections, and the maximum allowed Speedbrake deflection is decreased for large Rudder deflections (see Eq. 6).

The inner and outer panels of left & right elevons are assumed to always deflect equally (as is the convention during Shuttle entry), forming a single effective elevon on each side of the vehicle. Recent studies[15] indicate that differential deflection of inboard and outboard elevon panels can provide a means of controlling vehicle yaw at high angle of attack (where the rudder is ineffective), reducing the need for jet firings. The hybrid selection is entirely capable of specifying this; indeed, differential deflection would be performed automatically to answer yaw, if inboard & outboard panels were separately available to the linear program. Because the vehicle model used here does not provide for independent inner/outer elevon control, this capability can not be demonstrated in these results. A similar effect is possible, however, by differentially deflecting the elevons and canards; the linear program is, in fact, seen to exploit this possibility for additional yaw authority, as will be demonstrated in Chapter 5.

Since the Space Shuttle lacks canards, their control contribution is approximated by scaling the reaction to an equivalent deflection of the corresponding elevon by -1 in pitch (since these canards are assumed to be placed considerably forward of the vehicle CG) and by 0.1 in roll, yaw, and translational forces (primarily due to their smaller aerosurface area). Admittedly, the analogy between canards and elevons is a crude one; canards would have considerable effect on the airstream (perturbing the aerodynamics of the body and other aerosurfaces considerably), and effectors placed at the rear of the airframe (ie. elevons) would encounter different shadowing phenomena and exhibit substantially different authorities than any canards mounted forward. Heat

loads on forward canard surfaces could also become excessive at high Mach number. These considerations are ignored in this model; this elementary formulation is intended only for demonstrating the performance of the hybrid selection & control procedure with an additional set of aeroactuators.

The speedbrake on the Shuttle vehicle is realized by a split rudder; both surfaces open symmetrically under speedbrake deflection (see Figs. 6 & 7). Because of their correlated operation, the maximum allowed rudder deflection can depend on the current speedbrake angle (and vice-versa). This is summarized in the constraints below (see Ref. [16]):

- a)    **If**     $\delta_{SB} > 64.14^\circ \implies |\delta_r|_{(max)} = 54.88^\circ - \frac{\delta_{SB}}{2}$   
       **Else**    $|\delta_r|_{(max)} = 22.8^\circ$
- 6)    b)    **If**     $|\delta_r| > 11.28^\circ \implies \delta_{SB(max)} = 2 (54.88^\circ - |\delta_r|)$   
       **Else**    $\delta_{SB(max)} = 87.2^\circ$

A graphical representation of Eqs. 6 is presented in Figure 7.

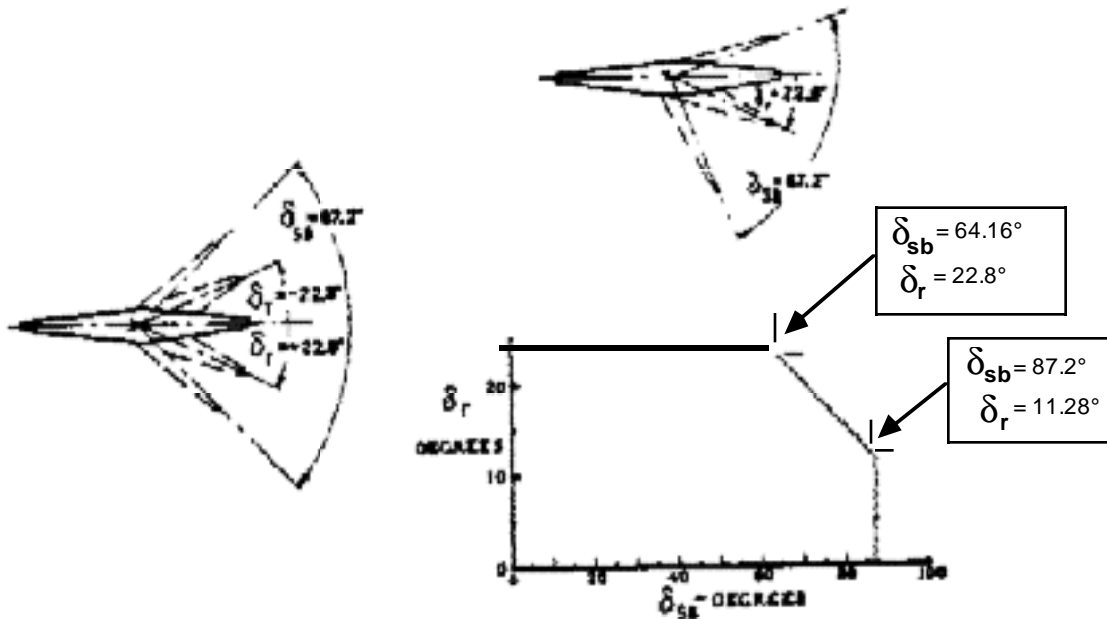
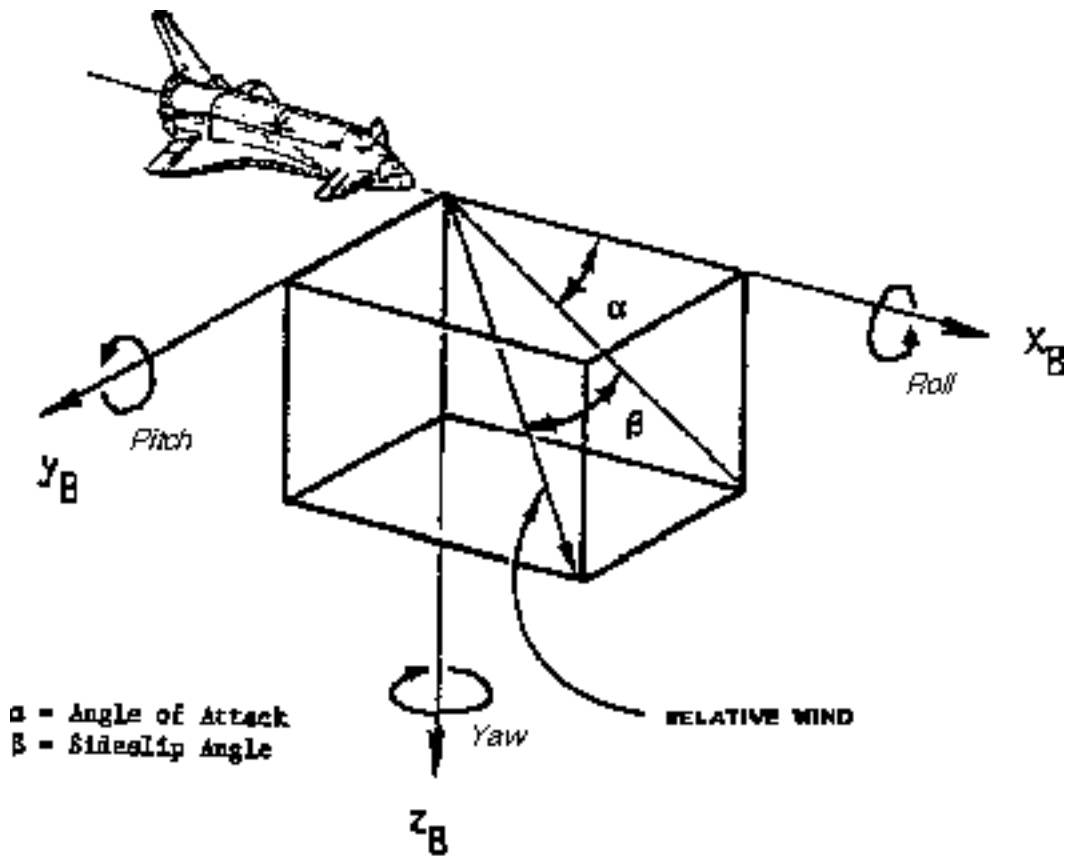


**Figure 7 : Speedbrake/Rudder Definition & Constraints**

The maximum allowed rudder ( $\delta_r$ ) and speedbrake ( $\delta_{SB}$ ) deflections (circa Eq. 6) are used in bounding the decision variables for these actuators in the linear program (Eq. 2b). This might introduce problems with selection of large deflections; ie. a rudder and speedbrake initially at trim would be allowed to simultaneously deflect up to the full  $22.8^\circ$  and  $87.2^\circ$  (respectively), as strictly forbidden by Eqs. 6. Aerosurfaces are never allowed to deflect so far in a single control step, however; maximum slew rates generally impose upper limits appreciably more severe than Eq. 6 until a stop is approached, at which time the high "stops" cost (Eq. 5) acts to additionally slow aerosurface advance. If an attempt is nonetheless made to pass a limit imposed by Eq. 6, the vehicle model halts the advancing aerosurface at its current  $\delta_{(max)}$ , and does not allow it to advance further in future selections (until at least one of the aerosurfaces is pulled back). The rudder & speedbrake are the only actuators that are correlation-bounded in this fashion; all others have independent bounds, as summarized in Table 1.



Definition of  $\alpha$  and  $\beta$

**Figure 8**

Most control calculations and related discussions employ the velocity coordinate frame, as defined in Figs. 8 & 9. Velocity attitudes are referred to the "relative wind" direction, which is assumed parallel to the vehicle velocity in these simulations (which are mainly performed at high Mach number). Vehicle angular accelerations are computed around body axes (ie. roll, pitch, yaw); these are respectively defined to be directed along  $+\hat{x}_B, +\hat{y}_B, +\hat{z}_B$  axes (as listed in Fig. 8). The velocity angles are signed such that a positive pitch rotation (in body axes) at zero sideslip increases  $\alpha$ , a positive yaw rotation (at zero angle of attack) decreases  $\beta$ , and a positive roll rotation (at zero angle of attack & sideslip) increases  $\phi$ . Forces are provided in stability axes, which remove the  $\alpha$  rotation to direct "lift" force along the local vertical (in the absence of bank) and "drag" along local horizontal. Forces in body coordinates may be obtained by rotating the stability-axis components by  $-\alpha$  about the  $\hat{y}_B$  axis.

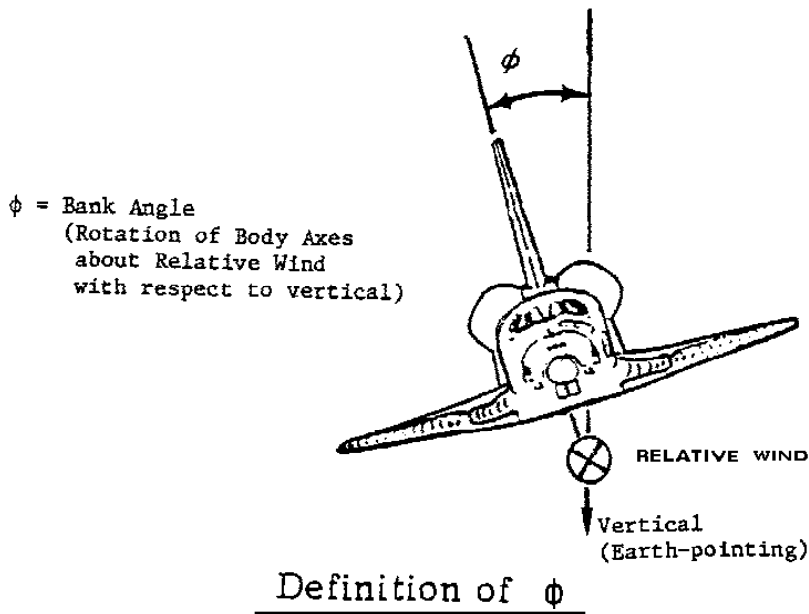


**Figure 9**

All of these frames are used in the environment & control software. Attitude control is performed relative to the velocity frame (although the hybrid selection accepts rotational commands in body coordinates). Translational control is performed relative to a static set of inertial axes, although resultant attitude commands are issued to the rotational controller in velocity coordinates. The hybrid selection accepts direct translational commands in the stability frame.

Confusion between vectors defined in these various frames is minimized by maintaining a matrix of body axes (ie.  $\hat{x}_B, \hat{y}_B, \hat{z}_B$ ) as a basis defined in inertial coordinates. Transformation from inertial to body axes is accomplished by multiplying an inertial vector by this matrix; multiplication by its inverse accomplishes the reverse operation. This basis is updated in accordance with the integrated body rates at each environment time-step, thus the orientation of body axes is continuously defined in inertial coordinates. The vehicle velocity (ie. relative wind) is also altered by integrated translational force; a velocity vector is maintained in inertial coordinates, and used with the inertial definition of body axes to derive velocity angles. Vehicle velocity is also integrated to form a 3-axis inertial position vector. All simulations assume rigid body dynamics; effects due to flexure and structural properties are not considered.

### **3.3) Adaptation of Shuttle Aerodynamic Data**

Aerodynamic coefficients describing the forces and torques exerted on the airframe as a function of vehicle attitude, Mach number, and aerosurface deflection were constructed from the extensive data base created for the Draper Statement Level Simulator (SLS) package[17]. In order to avoid the complexity[18] of interfacing the SLS environment directly to the hybrid controller, a network of data points was taken from the SLS that describes the aerodynamic action on the vehicle at various attitudes, airspeeds, and actuator deflections within the Shuttle operational envelope. An efficient multi-dimensional interpolation procedure is then invoked by the hybrid controller to consult this table of sampled data and estimate the aerodynamic forces, torques, and aerosurface authorities at the current vehicle state.

Aerodynamic coefficients have been tabulated[16,19] for the Space Shuttle entry scenario under a range of velocity attitudes, actuator deflections, and airspeeds. The set of coefficients used here are defined in the aerodynamic continuum region, with the value of the hypersonic viscosity parameter ( $v'_\infty$ ) under 0.005 (ie. altitude generally under 120,000 ft.). Although the examples presented in Chapter 6 actually extend somewhat into the viscous interaction region (initial altitude in entry simulations is usually 170,000 ft.), continuum aerodynamics are still used. Since the major purpose of these tests is to investigate hybrid controller application, any small errors introduced by approximations of this sort will bear little relevance.

The aerodynamic coefficients evaluated for a given vehicle state are summed and scaled to form vehicle forces and torques, as defined in Ref. [17] and adapted below:

### Torque Equations:

$$\begin{aligned} \tau_{\text{Roll}} &= \bar{q} S_w b \left[ C_l + \left( \Delta C_{l_{\beta(\text{SB})}} + \Delta C_{l_{\beta(\text{e})}} \right) \beta + C_{l_{\delta(\text{r})}} \delta_r + C_{l_{\delta(\text{a})}} \delta_a \right] \\ 7) \quad \tau_{\text{Pitch}} &= \bar{q} S_w c \left[ C_m + \Delta C_{m(\text{e})} + \Delta C_{m(\text{SB})} + \Delta C_{m(\text{BF})} \right] \\ \tau_{\text{Yaw}} &= \bar{q} S_w b \left[ C_n + \left( \Delta C_{n_{\beta(\text{SB})}} + \Delta C_{n_{\beta(\text{e})}} \right) \beta + C_{n_{\delta(\text{r})}} \delta_r + C_{n_{\delta(\text{a})}} \delta_a \right] \end{aligned}$$

### Force Equations:

$$\begin{aligned} F_{x_s} &= -\bar{q} S_w \left[ C_D + \Delta C_{D(\text{e})} + \Delta C_{D(\text{SB})} + \Delta C_{D(\text{BF})} \right] \\ 8) \quad F_{y_s} &= \bar{q} S_w \left[ C_y + \left( \Delta C_{y_{\beta(\text{SB})}} + \Delta C_{y_{\beta(\text{e})}} \right) + C_{y_{\delta(\text{r})}} \delta_r + C_{y_{\delta(\text{a})}} \delta_a \right] \\ F_{z_s} &= -\bar{q} S_w \left[ C_L + \Delta C_{L(\text{e})} + \Delta C_{L(\text{SB})} + \Delta C_{L(\text{BF})} \right] \end{aligned}$$

### Where:

$C_l, C_m, C_n$  = Untrimmed airframe moment coefficients (roll, pitch, yaw)

$\Delta C_{l_{\beta(\text{SB})}}, \Delta C_{n_{\beta(\text{SB})}}$  = Sideslip increment in roll, yaw moment coefficients due to speedbrake deflection

$\Delta C_{l_{\beta(\text{e})}}, \Delta C_{n_{\beta(\text{e})}}$  = Sideslip increment in roll, yaw moment coefficients due to elevator deflection

$C_{l_{\delta(\text{r})}}, C_{n_{\delta(\text{r})}}$  = Derivatives (roll, yaw) due to rudder deflection

$C_{l_{\delta(a)}}, C_{n_{\delta(a)}} =$  Derivatives (roll, yaw) due to aileron deflection

$\Delta C_{m(e)}, \Delta C_{m(SB)}, \Delta C_{m(BF)} =$  Increment in pitching moment coefficient due to elevon, speedbrake, body flap deflections

$C_D, C_y, C_L =$  Untrimmed force coefficients (drag, side, lift)

$\Delta C_{D(e)}, \Delta C_{D(SB)}, \Delta C_{D(BF)} =$  Increment in drag force coefficient due to elevon, speedbrake, body flap deflections

$\Delta C_{D(e)}, \Delta C_{D(SB)}, \Delta C_{D(BF)} =$  Increment in lift force coefficient due to elevon, speedbrake, body flap deflections

$\Delta C_{y_{\beta(e)}}, \Delta C_{y_{\beta(SB)}} =$  Sideslip increment in side force coefficient due to elevon, speedbrake, body flap deflections

$C_{y_{\delta(r)}}, C_{y_{\delta(a)}} =$  Side force derivatives due to rudder, aileron deflection

$\delta_{(e)} = \frac{1}{2} (\delta_{E_L} + \delta_{E_R}) =$  "Elevator" deflection

$\delta_{(a)} = \frac{1}{2} (\delta_{E_L} - \delta_{E_R}) =$  "Aileron" deflection

$\delta_{(r)} =$  Rudder deflection

$\bar{q} =$  Dynamic Pressure

$\beta =$  Sideslip angle

$S_w =$  Reference wing area = 2690 ft<sup>2</sup>

$b =$  Wing span = 78 ft.

$\bar{c} =$  Mean aerodynamic chord = 39.6 ft.

Although the left and right elevons are both composed of inner and outer panels in the actual Orbiter, both panels are forced to deflect identically, thus:

$$\delta_{E_{R(\text{inner})}} = \delta_{E_{R(\text{outer})}} \equiv \delta_{E_R}$$

$$\delta_{E_{L(\text{inner})}} = \delta_{E_{L(\text{outer})}} \equiv \delta_{E_L}$$

The torque equations (7) are written in body axes, while the force equations (8) are expressed in stability coordinates. Ground effect and landing gear terms have been omitted from these relations. The rate-dependent increments to Eq. 7 have also been dropped in order to minimize size of required data files. Eqs. 7 & 8 simplify considerably in the viscous interaction region (as seen in Ref. [17]), but their continuum form is appropriate for the majority of test trajectories considered here. Application of both viscous and continuum calculations would require storage of even more data, hence only continuum aerodynamics are used.

The vehicle center of gravity (CG) assumed for these tests is the "Moment Reference Center", about which all data of Ref. [19] are calculated. This is defined[16] to be located at (1076.7", 0.0", 375.0") in Fabrication ("Shuttle") Coordinates[20], corresponding to (35.28', 0.0', -2.08') in Orbiter Coordinates[20] used by the OEX Autopilot[2]. Although it is not applied, provision has been made in the software to account for a displaced center of gravity. Torques derived from Eq. 7 are corrected by moments induced from forces of Eq. 8 acting about the shifted CG:

$$9) \quad \underline{\tau}' = \underline{\tau}_{(\text{Eq. 7})} - (\underline{X}_{\text{CG}} - \underline{X}_{\text{MRC}}) \times \underline{F}_{(\text{Eq. 8})}$$

Where:

$\underline{X}_{\text{CG}}$  = Center of gravity coordinates

$\underline{X}_{\text{MRC}}$  = Moment Reference Center (above text)

$\underline{\tau}'$  = Torque at displaced center of gravity

The Shuttle aerodynamic data is accessed by the SLS "AEROFIT" routine[17], which is a program written in the MAC language that performs a multi-dimensional linear interpolation between the archived data values of Ref. [19]. AEROFIT accepts the Shuttle state as an input (Mach #,  $\alpha$ ,  $\beta$ ,  $\delta_{\text{SB}}$ ,  $\delta_{\text{BF}}$ ,  $\delta_{E(L)}$ ,  $\delta_{E(R)}$ ) are used in the continuum portion of vehicle entry) and approximates all aerodynamic coefficients needed in Eqs. 7 & 8. An off-line data formatter has been constructed to call AEROFIT for several possible state combinations, forming a "grid" in the Shuttle state variables. The actual sampling grid used in the simulations of Chapter 5 is summarized in Table 2.

Note that the rudder deflection,  $\delta_r$ , is not included for variation in Table 2. This is because the rudder, being at the rear of the vehicle, does not affect any of the aerodynamic coefficients in Eqs. 7 & 8 (although this is not true of the speedbrake). In order to reduce the size of the resultant data table, the rudder was kept at trim and its coefficients were stored at each sampled point. Since the aerodynamic accelerations only rotate with bank ( $\phi$ ), bank is not included as a dependent aerodynamic variable.

**Table 2: Sampling of Shuttle Aerodynamic Data**

| <u>State Parameter</u> | <u>Sampled Variations</u>          |
|------------------------|------------------------------------|
| Mach #                 | 0.2, 0.6, 1.0, 1.5, 4.0, 7.0, 10.0 |
| $\alpha$               | 5°, 10°, 15°, 20°, 25°, 30°        |
| $\beta$                | -10°, 0, 10°                       |
| $\delta_{E(L)}$        | -30°, -15°, 0, 15°, 30°            |
| $\delta_{E(R)}$        | -30°, -15°, 0, 15°, 30°            |
| $\delta_{BF}$          | -11°, 0, 11°, 22°                  |
| $\delta_{SB}$          | 0, 45°, 90°                        |

The AEROFIT routine was invoked to produce the "C" factors needed in Eqs. 7 & 8 for all combinations of state values possible in Table 2. The resultant aerodynamic forces and torques (unnormalized by the leading factors:  $\bar{q}$ , s, b, & c) are stored in a data file along with the rudder coefficients,  $C_{l_{\delta(r)}}$ ,  $C_{n_{\delta(r)}}$ ,  $C_{y_{\delta(r)}}$ . This produces a file that contains 37,800 records, each containing a 6-vector (force/torque) and 3 scalars (rudder coefficients).

This file could be reduced somewhat by removing dependent variables from redundant variations; ie. since elevon and body flap deflections seem to have little effect on each other's authority, every combination of Mach #,  $\alpha$ ,  $\beta$ ,  $\delta_{SB}$  could append separate variations of  $\delta_a^{aileron}$ ,  $\delta_e^{elevator}$ , and  $\delta_{BF}$  (ie. vary only one of these at a time, keeping the others at trim). The elimination of cross-dependence between these three variables will result in a 5,292-record file, producing an 85% reduction of needed file space, assuming the sampling densities of Table 2. Additional simplifications (ie. assuming a symmetric vehicle and looking at only positive  $\beta$  displacement, or

identifying other decoupling possible in the mutual dependencies between Mach#,  $\alpha$ ,  $\beta$ , and  $\delta_{SB}$ ) could lead to further decrease in file size.

These modifications, however, will break the symmetry between the variations of Table 2, complicating look-up logic that indexes the resultant data file. Since the file space and memory requirements needed to hold the aerodynamic data were not constrained on the computer system used for these studies, the brute-force approach was chosen, and *all* variations possible in Table 2 were sampled. If necessary in any eventual implementation, the required data storage could readily be reduced by instituting decoupling strategies similar to those sketched above.

The points in Table 2 were chosen to cover the Shuttle operational envelope (where the data of Ref. [19] is defined) and best fit nonlinear actuator response with linear interpolation. Airspeed is sampled densely about Mach 1, and more sparsely out to Mach 10, where the data of Ref. [19] ends (simulations, however, start at Mach 12, using an extrapolation). All other variables are stepped uniformly. Angle of attack is varied between  $5^\circ$  and  $30^\circ$  (spanned by the simulations of Chapter 5), sideslip (which is held near zero) is sampled between  $\pm 10^\circ$ , and the speedbrake is taken closed, half-open, and fully deployed.

The extremes of some parameters in Table 2 (ie. elevon deflection) extend slightly out of their Shuttle limits (quoted in Table 1). This is done to symmetrize the sampling intervals while keeping sampled points near spots where the data generally changes slope. Since AEROFIT performs a linear extrapolation outside of its data definition, these extensions will have little effect.

Figs. 10 & 11 show the elevator pitching moment coefficient (ie.  $C_{m(e)}$  in Eq. 7) from the data of Ref. [19], plotted continuously as a function of elevator deflection at  $\alpha = 25^\circ$  &  $\alpha = 10^\circ$ . The nonlinear character of the curves is evident as they cross from positive to negative deflection, and eventually shelve when the aerosurface is shadowed by the airframe (more noticeable at low  $\alpha$ , where shadowing is encountered sooner). The curves tend to form two "clusters" (one at low and another at high Mach number), with lower relative authority at high airspeed. Analogous plots for the body flap are given in Figs. 12 & 13, where a similar nonlinearity can be observed (the body flap has a more limited negative swing, thus the plateau is less obvious). Note the lower values of  $C_m$  for the body flap; the data of Ref. [19] indicate nearly a factor of 10 reduction in authority over the full range of deflection (this is closer to a factor of 3 at equal angles), presumably due to the body flap's lower surface area (remember that this is *elevator* deflection, composed of inner & outer surfaces deflecting simultaneously on *both* sides of the vehicle).

Figs. 14 & 15 show a similar set of  $C_m$  plots for the elevon (elevon deflections are considered to be inner and outer panels deflecting together on *one* side of the vehicle, as modelled in Tables 1 & 2) and body flap at intermediate Mach number (5) and  $\alpha$  ( $18^\circ$ ). The sampled points are plotted over the curves, and lines are drawn between them to indicate a linear interpolation. The nonlinear aerosurface response is seen to be adequately fit by this approximation.

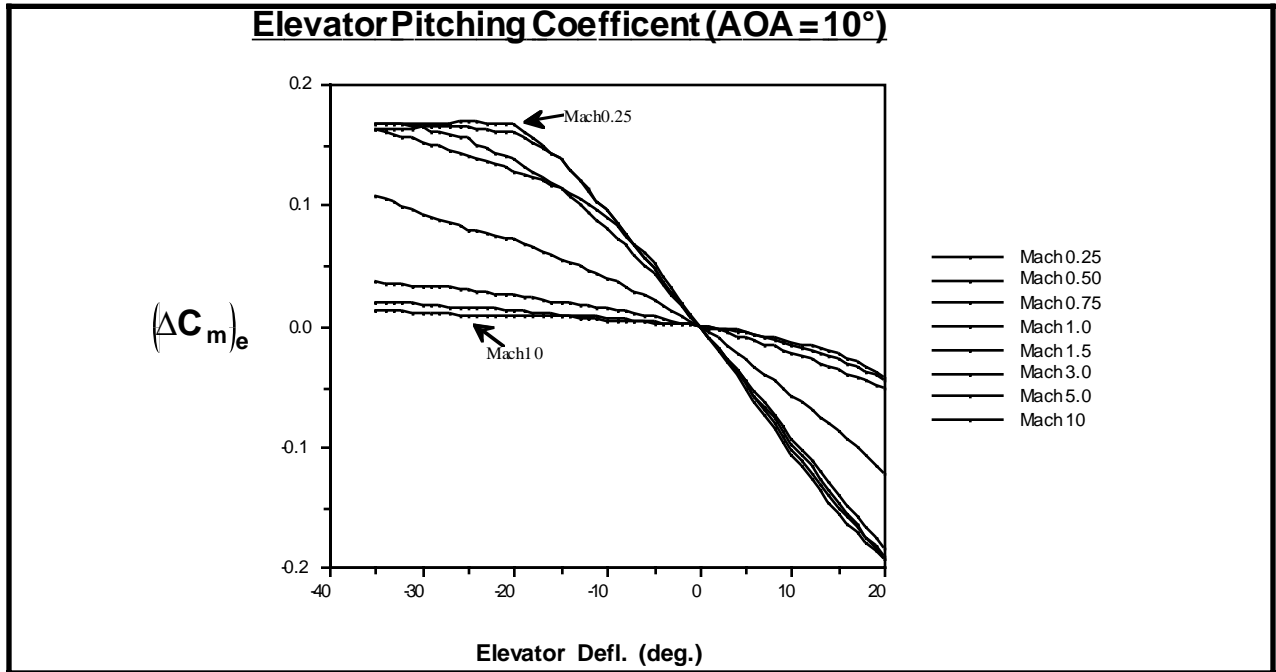


Figure 10

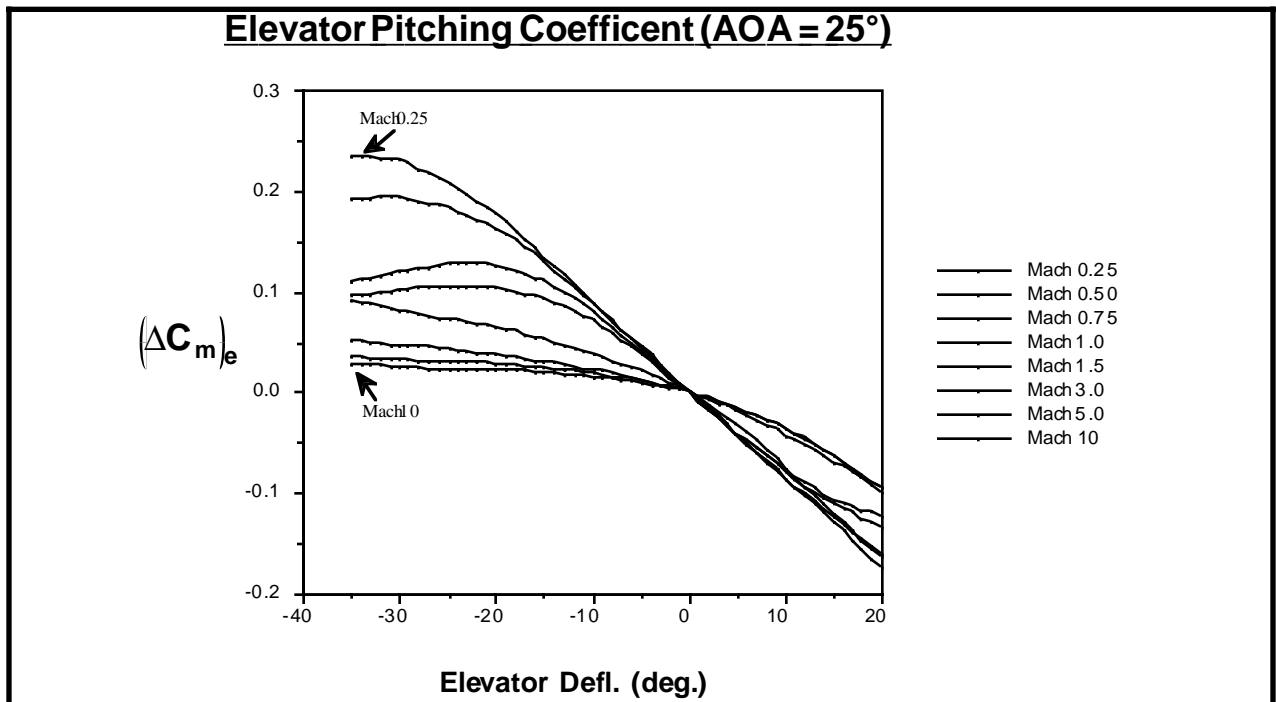
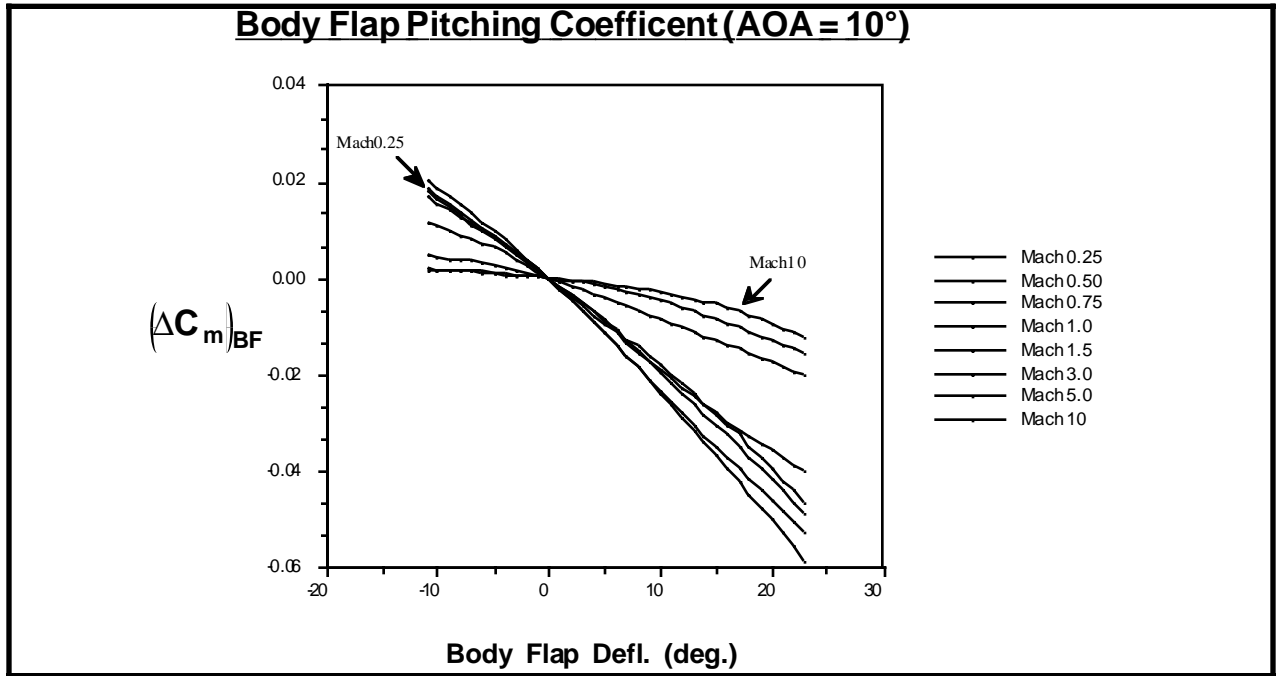
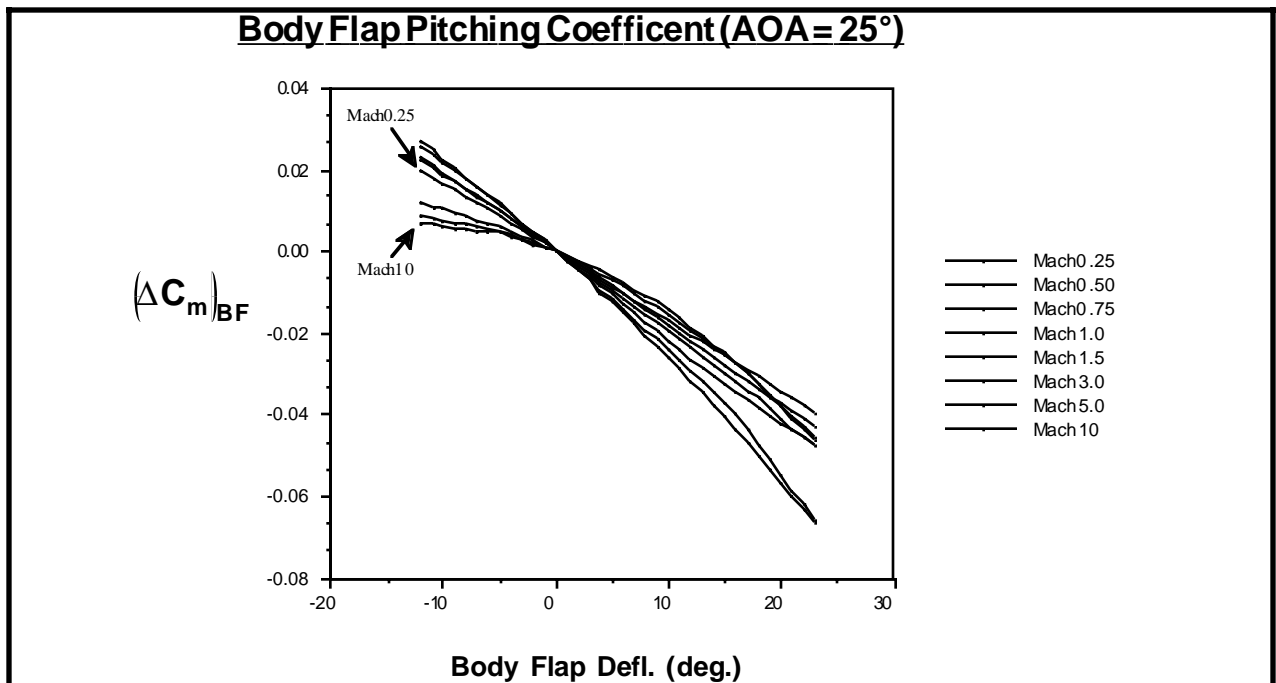


Figure 11



**Figure 12**



**Figure 13**

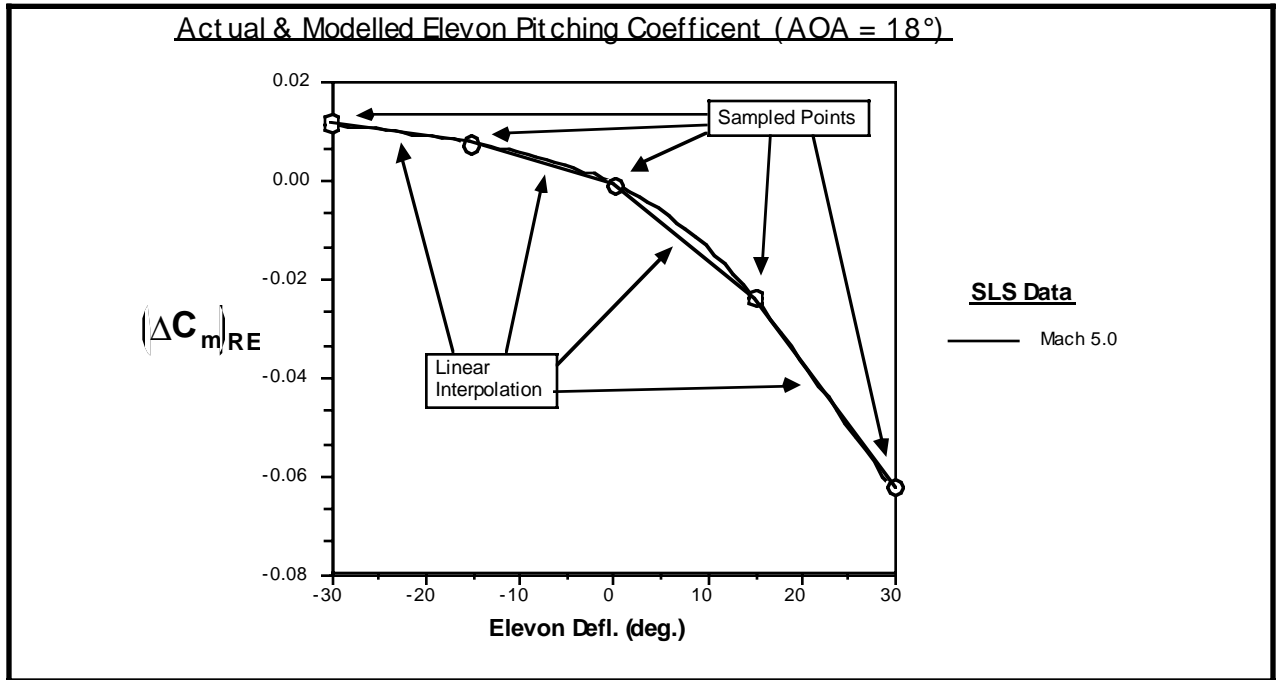


**Figure 14**

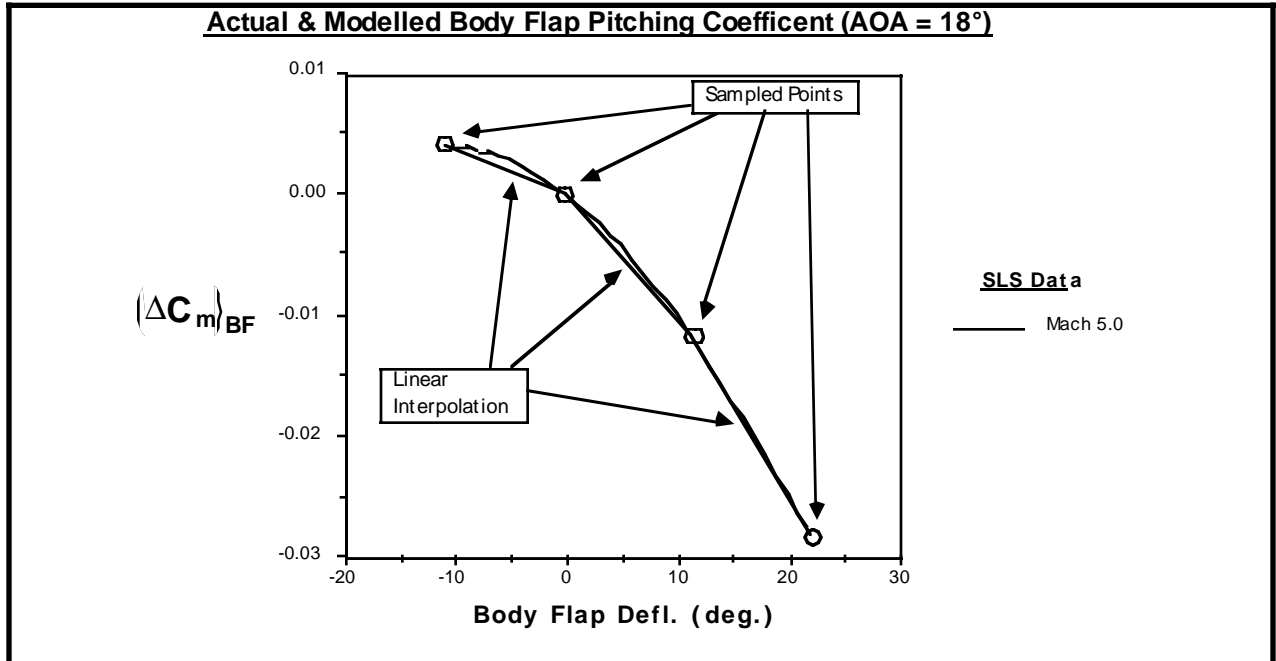


**Figure 15**

The speedbrake deflection is scaled such that the data will be relative to the "Rudder Hinge Line" (RHL; Ref. [17]). This can not be done with the rudder, however, since its deflection is not considered in the variations of Table 2. The rudder data is thus relative to the "Fuselage Reference Line" (FRL), and should be also scaled into RHL coordinates by any application that employs the standards of Ref. [17].

The data table generated via the above procedure need be produced only once by an "off-line" MAC front-end to the SLS package. The resulting file is read each time the vehicle control & simulation software is initialized. The aerodynamic data file begins with a header that lists the parameter variations used (such as in Table 2), giving simulations the ability to automatically configure to any grid spacing or variation protocol.

Aerodynamic accelerations & authorities are calculated by indexing this data with the current vehicle state, ordered as: (Mach #,  $\alpha$ ,  $\beta$ ,  $\delta_{E(R)}$ ,  $\delta_{E(L)}$ ,  $\delta_{BF}$ ,  $\delta_{SB}$ ,  $\delta_{C(R)}$ ,  $\delta_{C(L)}$ ,  $\delta_r$ ). The extra parameters ( $\delta_{C(R)}$ ,  $\delta_{C(L)}$ ) represent canard deflections (Fig. 6), while the other variables represent quantities defined in our Shuttle model. The ensuing discussion assumes " $\Psi$ " to represent the 9-element vehicle sub-state (as listed above with  $\delta_r$  removed), and " $\vartheta$ " to denote a 7-element truncated state (with both canards and rudder removed), which can directly index the aerodynamic data base created through Table 2. Unfortunately, the MAC-based AEROFIT routine can not be efficiently invoked from the selection, control, & simulation package (written in the Shuttle's HAL language). A special on-line interpolation procedure, more suited to the needs and application of this effort, was developed to read this data base and estimate the vehicle aerodynamic response.

The on-line table interpolation routine (referred to as "AEROCALC") first finds the point (termed " $\vartheta_0$ ") in the sampling grid closest to the input state " $\vartheta_1$ ". Next, each coordinate of  $\vartheta_0$  is independently perturbed by one sampling step in the positive and negative directions (leaving other coordinates untouched) to form two sets of seven states pointing at the vehicle responses to adjustment of each state variable. These states will be termed " $\vartheta_{0_{x(n)}}^{\pm}$ ", where n refers to the state being perturbed (one out of seven), and the " $\pm$ " superscript indicates the direction of variation. If a coordinate of  $\vartheta_0$  is at an extreme of the sampling grid, however, it will not be able to perturb in one direction (either + or -). In these cases, the sign of perturbation is reversed to point back into the table (causing both positive and negative  $\vartheta_{0_{x(n)}}^{\pm}$  vectors to be the same for this n), and an extrapolation will be automatically be performed for points lying outside the bounds on this coordinate.

Using the values of the 9 parameters (6 rotational & translational acceleration components, 3 rudder coefficients) stored at  $\vartheta_0$ , the gradient of vehicle response can be calculated:

$$10) \quad \left[ \nabla \underline{\mathbf{G}} \right] \Big|_{\underline{\vartheta}_0} = \left( \frac{\underline{\mathbf{G}} \Big|_{\underline{\vartheta}_{0x(n)}^\pm} - \underline{\mathbf{G}} \Big|_{\underline{\vartheta}_0}}{\left( \underline{\vartheta}_{0x(n)}^\pm \right)_n - \left( \underline{\vartheta}_0 \right)_n} \right)_{n=1 \rightarrow 7}$$

Where  $\underline{\mathbf{G}} \Big|_{\underline{\vartheta}}$  represents the 9-component vehicle response at state  $\underline{\vartheta}$ .

The above gradient may be considered to represent the Jacobian of vehicle response (9-component) with variation in vehicle state  $\underline{\vartheta}$  (7-component). The parenthesized expression in Eq. 10 defines a column vector in this Jacobian that reflects the change in vehicle response with respect to state variable "n". Each Jacobian "column" is actually made from either of two vectors, depending on the sign ( $\pm$ ) of state displacement. When calculating vehicle response, the signs are selected such that each state component (n) is perturbed (where possible) in the direction of the input state  $(\underline{\vartheta}_1)_n$ .

Since all points  $\underline{\vartheta}$  in Eq. 10 are discretized at sampled vertices (Table 2),  $\nabla \underline{\mathbf{G}} \Big|_{\underline{\vartheta}_0}$  may be readily calculated. A linear estimate of the vehicle response at the input state  $\underline{\vartheta}_1$  can then be obtained:

$$11) \quad \left( \underline{\mathbf{G}} \Big|_{\underline{\vartheta}_1} \right)_0 = \underline{\mathbf{G}} \Big|_{\underline{\vartheta}_0} + \left[ \nabla \underline{\mathbf{G}} \right] \Big|_{\underline{\vartheta}_0} \underline{\Delta \vartheta}_0$$

Where:  $\underline{\Delta \vartheta}_0 = \underline{\vartheta}_1 - \underline{\vartheta}_0$

Varying the state variables independently, as in the Jacobian of Eq. 10, is not entirely appropriate when applied to a coarsely sampled nonlinear manifold, as exists in this case. Ideally, one would like to account for all possible variations, since the values of  $\underline{\mathbf{G}}$  may not change solely as predicted by  $\nabla \underline{\mathbf{G}}$  in Eq. 10. This will lead to calculation of 127 9-component vectors; surely an inconvenience, even in the presence of significant computation resources. A somewhat inaccurate, yet much simpler scheme has been adopted to aid in accounting for this effect. In addition to calculating  $\underline{\mathbf{G}}$  and  $[\nabla \underline{\mathbf{G}}]$  from the closest sampled point ( $\underline{\vartheta}_0$ ), these quantities are also calculated (per the method of Eqs. 10 & 11) using a point ( $\underline{\vartheta}_1$ ), which displaces each state coordinate from  $\underline{\vartheta}_0$  by one sampling grid step in the direction of  $\underline{\vartheta}_1$ . If  $\underline{\vartheta}_0$  is outside the grid in any coordinate (or if  $\underline{\vartheta}_1$  is within  $1/3$  of the sampling interval from  $\underline{\vartheta}_0$  in that coordinate), the corresponding component is not changed in  $\underline{\vartheta}_1$ , and the value in  $\underline{\vartheta}_0$  is retained. One may think of the input state  $\underline{\vartheta}_1$  as surrounded by a hyper-polyhedron with vertices corresponding to sampled states. The

closest vertex is  $\underline{\vartheta}_0$  and the most distant is  $\underline{\vartheta}_1$ . The relationship between  $\underline{\vartheta}_I$ ,  $\underline{\vartheta}_0$ , and  $\underline{\vartheta}_1$  is illustrated graphically for a 3-dimensional state space in Fig. 16, where state axes are denoted by  $(x_1, x_2, x_3)$  (with tildes for  $\underline{\vartheta}_1$  coordinates).  $R_0$  and  $R_1$  correspond to  $\underline{\Delta}\underline{\vartheta}_0$  (from Eq. 11) and  $\underline{\Delta}\underline{\vartheta}_1$ .

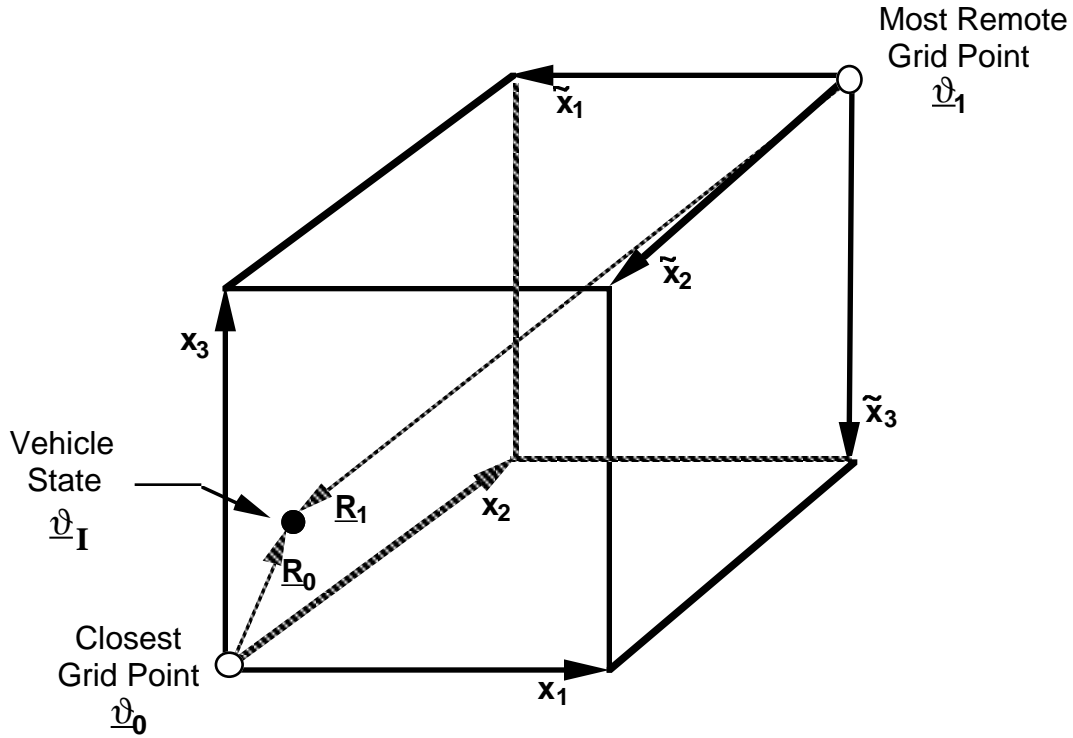


**Figure 16: 3D Analog to 7-Dimensional State Interpolation**

A set of points  $\underline{\vartheta}_{1x(n)}^{\pm}$  may be calculated at  $\underline{\vartheta}_1$ , enabling  $[\underline{\nabla}\underline{G}]|_{\underline{\vartheta}_1}$  and  $(\underline{G}|_{\underline{\vartheta}_1})_1$  to be calculated as described in Eqs. 10 & 11. A weighted sum of the results at  $\underline{\vartheta}_0$  and  $\underline{\vartheta}_1$  is made in Eq. 12 to arrive at an estimate for the vehicle response at  $\underline{\vartheta}_I$ .

$$12) \quad \underline{G} \Big|_{\underline{\vartheta}_I} = \frac{1 - z_0}{z_0 + z_1} \left( \underline{G} \Big|_{\underline{\vartheta}_I} \right)_0 + \frac{z_1}{z_0 + z_1} \left( \underline{G} \Big|_{\underline{\vartheta}_I} \right)_1$$

Where:

$$z_i = \left( \sum_{n=1}^9 \frac{\Delta\Psi_{i(n)}}{\Delta S_{(n)}} \right)^2$$

$S_n$  = Sampled grid spacing for variable n

$\Delta\Psi_{i(n)}$  = n'th component of  $\underline{\Delta\Psi}_i$  (i = 0 or 1)

Although the above relation usually gives much more weight to the closer vertex (due to the squaring of  $z_i$ ), the opposite vertex contributes when the 9-component vehicle state ( $\underline{\Psi}_i$ ) approaches being evenly split between  $\underline{\Psi}_0$  and  $\underline{\Psi}_1$  in several simultaneous coordinates. Note that the sum for  $z_i$  also extends over the canard deflections, thus we use " $\Psi$ " here as opposed to " $\vartheta$ ". Canards assume the sampling limits ( $S_n$ ) defined for their respective elevons.

Canards have been omitted from most of the above discussion. The  $\underline{G} \big|_{\underline{\vartheta}_1}$  is still a basic Shuttle response, ignoring the canard augmentation. Canards are incorporated by replacing the elevon deflections by corresponding canard deflections in the truncated vehicle state vectors  $\underline{\vartheta}$ , and employing the methods of Eqs. 10  $\rightarrow$  12 to calculate a  $\underline{G}_c \big|_{\underline{\vartheta}_{I(c)}}$ . Eqs. 10  $\rightarrow$  12 are also applied with elevon deflections zeroed to calculate the vehicle response at elevon trim,  $\underline{G}_t \big|_{\underline{\vartheta}_{I(t)}}$ . Their difference yields a differential response to canard deflection (assuming the effect of our crude "canard" model is decoupled from the elevons). This canard contribution is weighted to account for the smaller canard surface area (and location forward of the vehicle center of gravity), and summed into the  $\underline{G} \big|_{\underline{\vartheta}_1}$  to form a vehicle-plus-canards response:

$$13) \quad \underline{\tilde{G}} \big|_{\underline{\Psi}_I} = \underline{G} \big|_{\underline{\vartheta}_I} + [W_c] \left( \underline{G}_c \big|_{\underline{\vartheta}_{I(c)}} - \underline{G}_t \big|_{\underline{\vartheta}_{I(t)}} \right)$$

$[W_c]$  is a 9 x 9 diagonal matrix with the element corresponding to pitch torque,  $[W_{c(2,2)}]$ , set to -1 and all others set to 0.1. The vectors ( $\underline{\vartheta}_{I(c)}$ ,  $\underline{\vartheta}_{I(t)}$ ) are 7-component substates assuming the canard deflections (c) or zero (t) to be respectively substituted for elevon deflections.

The rudder is still not included in the above effect, although the rudder coefficients were carried into the last three elements of  $\underline{\tilde{G}} \big|_{\underline{\Psi}_I}$ . These coefficients are used to form a torque/force

vector according to the rudder contribution in Eqs. 7 & 8, then scaled by the rudder deflection and

summed with the first six components of  $\tilde{\underline{G}} \Big|_{\underline{\Psi}_I}$  (denoted  $\underline{G} \Big|_{\underline{\Psi}_I}$ ), to form the complete vehicle response:

$$14) \quad \left( \underline{F} \Big|_{\underline{\Psi}_{In}} \right)_{tot} = \tilde{\underline{G}} \Big|_{\underline{\Psi}_{In}} + \underline{A}_R \delta_r$$

$$\text{Where: } \underline{A}_R = \begin{bmatrix} C_{\alpha \delta_r} \\ 0 \\ C_{n \delta_r} \\ \text{-----} \\ 0 \\ C_{y \delta_r} \\ 0 \end{bmatrix} \quad \frac{\text{Torque}}{\text{Force}}$$

In addition to providing the torques & forces on the vehicle, AEROCALC also generates the estimates of aerosurface authorities needed by the linear selections. The authorities for the first 7 state variables (ie.  $\underline{\vartheta}$ ) are given by the first 6 elements of the vectors in the Jacobian  $[\nabla \underline{G}]^\pm$ . In order to account for the opposite-vertex phenomenon, the Jacobians calculated at  $\underline{\vartheta}_0$  and  $\underline{\vartheta}_1$  are combined as in Eq. 12. Two Jacobians are actually produced, corresponding to positive and negative deflections about  $\underline{\vartheta}_1$ , thus providing the bipolar activity vectors used by the simplex selection.

Canard authorities are generated via the elevon-substitution method proposed in the discussion of Eq. 13. When calculating  $\underline{G}_c \Big|_{\underline{\vartheta}_1}$ , a Jacobian was constructed that specified canard authorities (in place of elevons). The Jacobian columns corresponding to canards (ie. "elevons") can be scaled by  $[\underline{W}_c]$  of Eq. 13, and used as canard torque/force-change authorities. The rudder authority is readily provided by the vector  $\underline{A}_R$ , as constructed in Eq. 14. Since rudder deflection is not included in the aerodynamic state variation, only one value of  $\underline{A}_R$  is calculated; it represents rudder authority in both directions of displacement.

The procedure described above constitutes the core of the routine AEROCALC that provides torques, forces, and aerosurface authorities to the control, simulation, and selection

routines. After initial tests, however, it became evident that additional adaptation was needed to account for the combined effects of sampling granularity and nonlinearity.

Because of the coarse sampling grid, the slope of the linear approximations to actuator authority can be quite different in each interval (see Figs. 14 & 15). As one traverses this curve, the slope changes abruptly after each sampled point. This is not the case for the actual data, which changes in a continuous fashion. Problems can thus be created in situations where an actuator state (ie. elevon deflection) is located slightly to one side of a sampled value. If the selection chooses to move the actuator past this point, the estimate of its authority, which was only "valid" in the small region between the current state and sampled point, can be appreciably in error. An attempt has been made to account for this by "smearing" the activity vector corresponding to deflection toward the sampled point with its counterpart (in the same direction) located immediately opposite the sampled point, as formalized below:

### **Define:**

$\rho$  = Maximum normalized displacement from nearest sampled point ( $x_n$ ) to do smear. The allowed range of  $\rho$  is  $0 \rightarrow 1$ , and it is typically used at  $1/3$ .

$$x_n = \left| \frac{(\Psi_I)_n - (\Psi_0)_n}{\Delta S_n} \right| = \text{(Normalized distance to nearest point for state n)}$$

**IF** Deflection sign (Sg) moves actuator toward nearest sampled point in coordinate n [ie.  $(\Psi_0)_n$ ] and  $x_n < \rho$ , **THEN:**

$$15) \quad [\nabla \underline{\Psi}]_n^{sg} = \left( \frac{x_n}{\rho} \right) [\nabla \underline{\Psi}]_n^{sg} \Big|_{\underline{\Psi}_I} + \left( 1 - \frac{x_n}{\rho} \right) [\nabla \underline{\Psi}]_n^{sg} \Big|_{(\underline{\Psi}_{I_{[opp]}})_n}$$

$\underline{\Psi}_{I_{[opp]}} = \underline{\Psi}_I$ , except for component n, which is reflected about  $(\Psi_0)_n$

The above expression for  $[\nabla \underline{\Psi}]_n^{sg}$  denotes the n'th actuator authority (ie. Jacobian vector) in direction "sg"; the symbol " $\underline{\Psi}$ " here denotes a 6-component torque/force including rudder effect. The first term right of the equality is the standard aerosurface authority vector that was calculated according to the methods described in the previous text. The second term denotes the actuator authority with its n'th state component displaced to the opposite side of the closest

sampling vertex  $\underline{\Psi}_0$ . Eq. 15 produces actuator authorities which gradually change as sampling vertices are approached, reducing inaccurate simplex solutions arising from this effect.

Another problematic artifact stems from vehicle states located midway between sampled vertices. As the state changes, it eventually becomes closer to one vertex than another, and the proximity point  $\underline{\vartheta}_0$  abruptly switches. This has particular effect with angle of attack and Mach number. Since these quantities influence all torques, forces, and authorities, a vertex switch in one of these coordinates can cause an appreciable step in all output parameters. Mach number and  $\alpha$  are also varied continuously in most tests attempted in Chapter 6; this effect can lead to large spikes in the results at points where vertices switch.

Although the introduction of the opposite vertex per Eq. 12 may aid in smearing out this step, the contribution is not significant in this case; we're considering changes in only one or two simultaneous state variables here, while Eq. 12 was constructed to contribute only when all state entries approach their sampling midpoint together. Since the parameters most susceptible to this problem are Mach number and  $\alpha$ , a solution was adopted that incrementally smeared the calculated torques, forces, and authorities about the midpoint of their sampling intervals. This is detailed below for  $\alpha$ :

### **Define:**

$[\mathbf{P}] \big|_{\underline{\Psi}_{In}}$  = Aerodynamic parameters (torques, forces authorities at input state; ie., results of Eq. 10 → 15 and related discussion)

$$\Delta\alpha = \alpha - \alpha_{mid}$$

$\alpha_{mid}$  = Value of  $\alpha$  at midpoint of current sampling interval

$\Delta\alpha_s$  = Sampling step over  $\alpha$

$\sigma_\alpha$  = Normalized smearing width in  $\alpha$  (= 0.25)

**IF**  $\left| \frac{\Delta\alpha}{\Delta\alpha_s} \right| < \sigma_\alpha$  **THEN:**

$$[\mathbf{P}] \big|_{\underline{\Psi}_\alpha} \equiv [\mathbf{P}] \big|_{\underline{\Psi}_I[\alpha = \alpha_{in} - 2 \Delta\alpha]}$$

16)

**Calculate:**

(Again, use Eqs. 10 → 15)

$$[\mathbf{P}] \big|_{\underline{\Psi}_{smear}} = q [\mathbf{P}] \big|_{\underline{\Psi}_\alpha} + (1 - q) [\mathbf{P}] \big|_{\underline{\Psi}_I}$$

$$\text{Where: } q \equiv \frac{1}{2} \left[ 1 - \frac{\Delta\alpha}{\Delta\alpha_s \sigma_\alpha} \right]$$

Performing the above smear whenever  $\alpha$  is within  $\pm 1/4$  of the sampling interval from the sampling midpoint effectively removes vertex-switching spikes from the  $\alpha$ -profile. The same operation is performed over Mach number; if one replaces " $\alpha$ " with "Mach #" in the above discussion, Eq. 16 also describes the appropriate process ( $\sigma$  is also chosen at 0.25 for Mach smears). The technique summarized in Eq. 16 is portrayed graphically in Fig. 17.

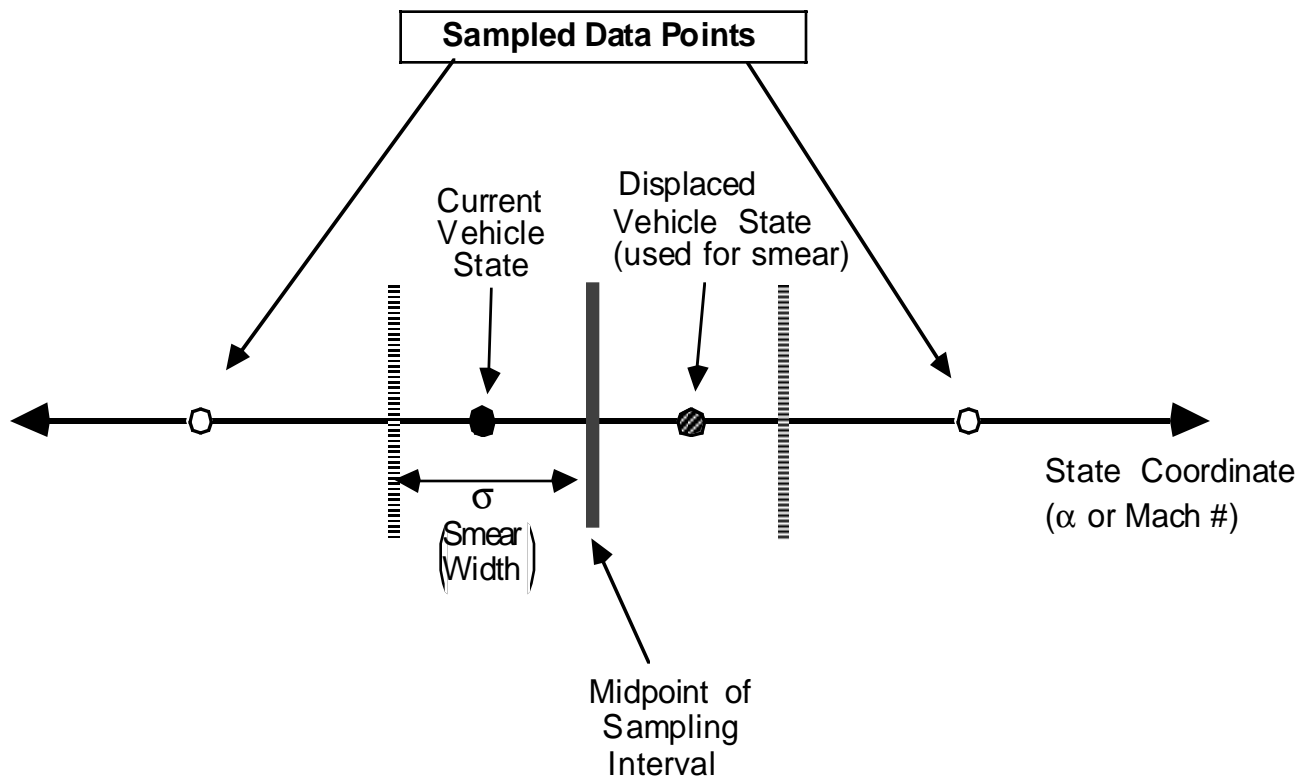


**Figure 17: Aerodynamic State Smearing**

This latter mid-point smearing procedure is structured as a pair of software shells surrounding the core AEROCALC logic; the inner shell calls AEROCALC twice to do the  $\alpha$  smear (if needed), while the outer shell calls the inner shell twice to do the Mach smear (if needed). If the vehicle state is close to its midpoint in both  $\alpha$  and Mach #, up to four calls to AEROCALC can



The speed of sound, used to determine Mach number, varies nonlinearly with altitude, assuming values from 900 to slightly over 1100 ft/sec. A table-lookup/interpolation scheme (based on the data of Ref. [24]) is used to evaluate sound velocity as a function of altitude estimate.

The force & torque output from the aerodynamic interpolation (and related smearing) is scaled to become dimensional using the dynamic pressure of Eq. 17 and Shuttle parameters ( $S_W$ ,  $b$ ,  $c$ ) defined in Eqs. 7 & 8. The interpolated torque-change authorities (termed  $\underline{d\tau}_i$ ) are multiplied by the inverse vehicle inertia matrix to form decoupled accelerations, and combined with the interpolated force-change authorities ( $\underline{dF}_i$ ) to form 6-component activity vectors:

$$19) \quad \underline{A}_i^{\pm} = \begin{bmatrix} [\mathbf{I}]^{-1} \underline{d\tau}_i^{\pm} \\ \hline \frac{1}{M} \underline{dF}_i^{\pm} \end{bmatrix}$$

Where:       $[\mathbf{I}]$  = Estimate of vehicle inertia matrix  
                    $M$  = Estimate of vehicle mass  
                    $\underline{d\tau}_i^{\pm}$  = Torque authority of actuator # $i$  in the  $\pm$  direction  
                    $\underline{dF}_i^{\pm}$  = Force authority of actuator # $i$  in the  $\pm$  direction

Note that the index "i" here runs only over the *actuators* in the vehicle state " $\underline{\Psi}$ ". Since they are not selectable control parameters, the first three elements in  $\underline{\Psi}$  (ie. Mach #,  $\alpha$ ,  $\beta$ ) do not possess corresponding activity vectors.

Upper bounds are imposed on the aerosurface decision variables to restrict deflection at each control step, enabling direct enforcement of maximum displacement limits (ie. "stops"), incorporating maximum slew rates, and generally limiting allowed aerosurface control authority. An expression for upper bound calculation is given below that addresses all of these concerns:

$$20) \quad U_i^{\pm} = \min \left\{ \begin{array}{l} \pm L_i \\ \delta_{\text{Stop}(i)}^{\pm} - \delta_i \\ \frac{\pm \dot{\delta}_{\text{max}(i)}}{\Delta t_c} \end{array} \right.$$

The upper expression in Eq. 20 is a generic clamp on allowed deflection change per control step. The current software employs one value of "L" for all aerosurfaces. L is generally set to  $\pm 10^\circ$  for all selections. The middle expression is the angle between the current aerosurface deflection and the maximum "stop limit" (in the appropriate " $\pm$ " direction). This limits the absolute deflection angle, and prevents the linear selection from providing a deflection change that places an aerosurface beyond its allowed range.  $\delta_{\text{Stop}(i)}^\pm$  may be varied dynamically, allowing the restriction on aerosurface deflections to evolve during ascent or entry. The bottom expression in Eq. 20 represents the maximum deflection possible per control time step ( $\Delta t_c$ ). This limits the participation of various aerosurfaces in the solution in order to account for the different slew rates attainable by each actuator. Simulated aerosurfaces are moved at their maximum rates, as given in Table 1; these values are used as  $\delta_{\text{max}(i)}$  in Eq. 20. The quantity in Eq. 20 with the smallest magnitude is chosen as the bound on aerosurface #i in the direction " $\pm$ ".

### **3.4) Incorporation of RCS Jets**

Jets are defined as continuous torque actuators under the selection framework. The jet accelerations (angular & translational for up to 6-DOF control) are used as activity vectors, in correspondence with the conventions pursued in Refs. [2] and [5]. The jet decision variables ( $x_j$ ), however, are now defined to be jet duty cycles (as opposed to jet firing times, as was the case in the previous efforts). These range from  $0 \rightarrow 1$ , and define the fraction of maximum jet acceleration needed to realize the input command. The continuous duty-cycles are realized by discrete jet firings in the environment software. The ratio of average jet *on* times to *off* times is made proportional over the control update interval to the corresponding duty cycles (discretized, however, by the minimum jet firing times). By setting upper bounds to unity for jet decision variables (and lower bounds to zero through the intrinsic "feasibility" constraint), simplex will solve directly for jet duty cycles in response to an acceleration-change input command. In summary:

$$21) \quad \underline{A}_{j(\text{jet})} = \begin{bmatrix} [\mathbf{I}]^{-1} \underline{r}_j \times \underline{T}_j \\ \hline \frac{1}{M} \underline{T}_j \end{bmatrix} \quad : \quad \text{Jet Activity Vector}$$

$$x_{j(\text{jet})} = D_j = \text{Jet duty cycle} \quad : \quad \text{Jet Decision Variable}$$

Where:       $[\mathbf{I}]$  = Spacecraft Inertia Matrix  
                    $\underline{r}_j$  = Position of jet #j relative to the vehicle Center of Mass  
                    $\underline{T}_j$  = Thrust of jet #j  
                    $M$  = Vehicle Mass

$$22) \quad U_{(\text{jet})}^+ = 1.0 \quad : \quad \text{Jet Bounds}$$

$$U_{(\text{jet})}^- = 0 \quad :$$

Because the current jet acceleration is not considered when computing the commanded acceleration change, simplex will solve for *absolute* jet duty cycles (ranging from  $0 \rightarrow 1$ ), rather than *changes* to ongoing duty cycles. This is discussed further in Chapter 4.

The jet driver in the vehicle environment software produces jet pulses whenever the running ratio of net jet-on time to elapsed time falls below the commanded duty cycle. Quantitatively:

**Define:**

$$23) \quad \mathcal{R}_j \Big|_{N_t} = \frac{0.5 + \sum_{k=1}^{N_t} J_j(k)}{N_t}$$

$N_t$  = Number of minimum jet-pulse cycles that have elapsed since commanded jet duty cycle was established.

$$J_j(k) = \begin{cases} 1 & \text{- If jet \#j was firing during time cycle \#k} \\ 0 & \text{- Otherwise} \end{cases}$$

23)

**Iff**  $\mathcal{R}_j|_{N_t} < D_j$  **then** Fire jet #j this cycle

After each hybrid selection, the ratios  $\mathcal{R}_j$  in Eq. 23 are propagated for jets commanded with a non-zero duty cycle  $D_j$ . The  $\mathcal{R}_j$  are updated with each minimum jet-pulse interval. The current software assumes restrictions similar to those imposed on the Shuttle Orbiter[25], which allows a minimum jet pulse of 80 msec. until the vehicle drops below an altitude of 125,000 ft., at which point a 320 msec. minimum firing is required. Ref. [25] also indicates a minimum jet duration of 4 sec. below 70,000 ft.; since these studies seldom use jets under this altitude, this condition is not imposed. In order to eliminate initial transients,  $\mathcal{R}_j$  is initialized to 0.5 on its first cycle after a simplex selection has been performed and new duty cycles have been specified.

As time elapses, the actual "discretized" jet firings commanded through the logic of Eq. 23 will reflect the selected duty cycles. At extreme times  $N_t$ , truncation error may begin to affect the accuracy of  $\mathcal{R}_j$ ; this effect, however, is not significant over the maximum jet policy duration allowed in these tests (jet & control update intervals under 1 second are generally used).

The scheme detailed in Eq. 23 produces the finest resolution of commanded duty cycles that the minimum jet pulsing interval will allow. This, however, can sometimes cause excessive jet chatter; ie. a 50% duty cycle (the worst case) will cause a jet to be cycled on and off with alternating iterations of Eq. 23. By artificially increasing the minimum allowed interval, jets will stay on longer and "chatter" less, although at a resulting loss in accuracy. The method of Eq. 23 is adequate for introducing discretization effects into our simulations; implementation onboard an actual vehicle, however, may require the addition of some "hysteresis" to reduce jet chatter.

In addition to the dynamic constraints on minimum jet firings outlined above, jet costs and failure flags are continually adjusted as the vehicle changes altitude. A jet-inhibit protocol for vehicle entry has been adapted from the Shuttle procedures of Ref. [25] and assumed here. Above 400,000 ft., all jets are available. Below this altitude, all forward jets are "failed", except for a select group (F1F, F1L, F3L, F3U, F2U, F1D, F2R, R2D in Shuttle nomenclature), and these are also made unavailable after the vehicle drops below 125,000 ft. (forward jets can appreciably perturb the vehicle aerodynamics). Below 165,000 ft., all vehicle aft jets are inhibited, except for the side-firing yaw jets, thus (combined with the forward jet condition), only aft yaw jets are

available below 125,000 ft. All jets are removed from selection when the vehicle descends below 45,000 ft.

During most of the entry phase, a large portion of Shuttle jets are made unavailable by the attitude constraints defined above. This can appreciably speed the simplex process; as opposed to considering the full 44-jet array during each iteration, simplex need only examine a considerably reduced subset. The logic of Ref. [26] reduced the jet select problem by grouping jets into similar "clusters" that are picked via simplex, thereafter imposing constraints and distributing firings among cluster members. Because of our dynamic attitude constraints and torque-request command format, it was more convenient to structure the current jet selection to manage individual jets. As noted above, with re-entry constraints imposed, this problem simplifies and becomes quite tractable.

The cost coefficients of various jet families were made to increase before they were removed from selection, incrementally discouraging their participation until they were totally inhibited. The actual logic used is specified below:

**Define:**

$$\begin{aligned}
 h' &= 400,000 \text{ ft.} - h \\
 C_{\infty} &= \text{Constant "vacuum" jet cost} \\
 C_1 &= 5 \\
 C_0 &= C_{\infty} \left( 1 + C_1 \frac{h'}{300,000} \right) \quad [\text{for } h < 400,000 \text{ ft.}]
 \end{aligned}$$

$$C_{F_j} = C_0 \left( 1 + C_1 \frac{h'}{235,000} \right) \quad : \quad \textit{Forward Jets}$$

$$24) \quad C_{A0_j} = C_0 \left( 1 + C_1 \frac{h'}{275,000} \right) \quad : \quad \textit{Aft Jets (not Yaw)}$$

$$C_{AY_j} = C_0 \quad : \quad \textit{Aft Jets (Yaw)}$$

Eqs. 24 increase the cost of all jets as altitude decreases below 400,000 ft., with expense accruing faster for jets "failed" at higher altitudes. The simulations performed in Chapter 5 show

considerable effect from this cost partitioning. The cost functions defined above can be readily adapted to reflect any desired jet preference.

Primarily because of plume interaction with aerodynamic flow and plume expansion under finite ambient pressure, atmospheric jet firings can produce effects differing significantly from identical firings performed in a vacuum. The corrected jet moments & forces can be expressed[16]:

$$\begin{aligned} \underline{\tau}_j &= K_{RCS}(h) \underline{\tau}_{0j} + \bar{q} S_w [W_\tau] (\underline{\Delta C}_{(\tau)} + \underline{\Delta C}_{(\tau)_e} + \underline{\Delta C}_{(\tau)_{BF}}) \\ \underline{E}_j &= K_{RCS}(h) \underline{E}_{0j} + \bar{q} S_w [R] [W_F] (\underline{\Delta C}_{(F)} + \underline{\Delta C}_{(F)_e} + \underline{\Delta C}_{(F)_{BF}}) \end{aligned} \quad (25)$$

Where:

$$[W_t] = \begin{bmatrix} b & 0 & 0 \\ 0 & c & 0 \\ 0 & 0 & b \end{bmatrix}$$

$$[W_F] = \begin{bmatrix} -1 & 0 & 0 \\ 0 & 1 & 0 \\ 0 & 0 & -1 \end{bmatrix}$$

[ R ] = Rotation from stability coordinates into frame in which  $\underline{E}_0$  is defined (ie. body or inertial axes).

$\underline{\tau}_{0j}, \underline{E}_{0j}$  are the vacuum torque and force from jet #j.

$\underline{\Delta C}$ 's are vectors of jet interaction coefficients (defined for each jet family).

b, c,  $S_w$  are Shuttle parameters defined with Eqs. 7 & 8.

The leftmost terms in Eqs. 25 denote a uniform attenuation in jet thrust with altitude (ie. ambient pressure), expressed by the function  $K_{RCS}$ . A coarse fit to the data of Ref. [16] has resulted in:

$$K_{RCS} = 1 - e^{-h/26,000} \quad [h > 30,000 \text{ ft.}]$$

26)

$$K_{RCS} = 0.64 \quad \text{Otherwise...}$$

The rightmost terms in Eqs. 25 model aerodynamic jet interaction. Since they are defined to be analogous to the airframe relations of Eqs. 7 & 8, they must be similarly normalized. Forces must be rotated into standard coordinates, and torques must be corrected per Eq. 9 if the vehicle center of gravity is displaced from the Moment Reference Center. Three "ΔC" vectors are consulted in each relation; one base coefficient, and elevon & body flap dependent increments. The ΔC vectors are defined independently for each variation on jet placement and direction (ie. left side-firing, right down-firing, etc.). They are nonlinear functions of  $\alpha$ , elevon & body flap deflection (the latter two dependencies are summarized in the "e" and "BF" increment terms of Eqs. 25), and "momentum ratio", as defined[16] below:

$$\text{Momentum Ratio} \equiv \frac{\phi_j}{\phi_\infty} = 0.1543 \frac{n_{(\text{Jet\_Type})}}{\bar{q}}$$

27)

Where:  $n_{(\text{Jet\_Type})} = \# \text{ of jets (of particular type) simultaneously firing}$

Momentum ratios are calculated separately for each jet type (ie. left side-firing, etc.). They are used to determine the ΔC's (again, for each jet type), which can be summed in Eq. 25.

The interaction data tabulated in Ref. [16] has been laboriously fit "by eye" to various intuitive functions (performing a computer interpolation of SLS data, as in Sec. 3.3, would be an even more arduous task), thereby making an approximate model of Shuttle jet interaction available to the simulation software. Since it is assumed that altitude data will always be available onboard an actual vehicle, the attenuation factor  $K_{RCS}$  (Eq. 26) is incorporated into the environment software and activity vector calculation (Eq. 21). It is much more difficult to account for the interaction data, since the momentum ratio depends on the number of jets firing, which is a result of the jet selection itself, and is not known in advance. Various strategies, however, may be attempted to account for interaction effects in the selection & control procedure. Since most ΔC interaction functions seem to "plateau" at high momentum ratios, jets may be forced to fire in pairs or triads, such that the momentum ratio will always be saturated. This will generate a more predictable effect

that could be folded into the activity vector model of actuator authority. Another strategy of incorporating aerodynamic jet interaction might entail estimation logic; ie. a simplex jet response could be corrected after its initial interaction effect can be calculated or measured.

The plume impingement terms[16] are not included in the jet model of Eq. 25. They are already relatively small on-orbit, and their effect decreases with increasing static pressure (ie. decreasing altitude), thus impingement is vastly eclipsed by the vacuum response and interaction corrections in the altitude regime considered here.

Most test of Chapter 5 ignore interaction effects and assume the ideal "vacuum" jet response used in the activity vectors of Eq. 21. The "Mismodelling" section (5.5), however, examines the effect of the interaction terms presented in Eq. 25.

### **3.5) Thrust-Vector Control Applied to Vehicle Ascent**

Because the aerodynamic data base of our Shuttle-derived model is not defined for an ascent corridor (low  $\alpha$ , high  $\bar{q}$ ), no attempts are made at performing ascent simulations. Although techniques of thrust-vector control have been introduced in the previous discussion, main propulsion systems are not used during an unpowered re-entry, thus thrust vectoring has not been included in the vehicle model or hybrid selection presented here. A few suggestions, however, are made in this section to indicate how future efforts may integrate a thrust-vector system into the hybrid selection.

Vectoring of main propulsive engines may be described as a controlled rotation of their thrust direction:

$$28) \quad \underline{T}' = T[R] \hat{T}_c = T \left( \hat{T}_c \cos \theta + \hat{\sigma} \times \hat{T}_c \sin \theta \right)$$

Where:

- [R] = Gimbal rotation matrix
- $T$  = Thrust magnitude
- $\hat{T}_c$  = Unit vector in direction of current thrust
- $\hat{\sigma}$  = Unit vector along thrust rotation axis
- $\theta$  = Rotation angle about thrust rotation axis
- $\underline{T}'$  = Rotated thrust vector

Specification of an activity vector for the vehicle propulsive system (in response to an acceleration-change command) requires the time derivative of Eq. 28:

$$29) \quad \frac{d\mathbf{T}'}{dt} = \dot{T}(\hat{\mathbf{T}}_c \cos \theta + \hat{\boldsymbol{\sigma}} \times \hat{\mathbf{T}}_c \sin \theta) + T(-\dot{\hat{\mathbf{T}}}_c \sin \theta + \hat{\boldsymbol{\sigma}} \times \hat{\mathbf{T}}_c \cos \theta)\dot{\theta}$$

As in the CMG case, we consider a contact rotation, and linearize by retaining only leading-order contributions:

$$30) \quad \frac{d\mathbf{T}'}{dt} = \dot{T}(\hat{\mathbf{T}}_c) + T(\hat{\boldsymbol{\sigma}} \times \hat{\mathbf{T}}_c)\dot{\theta}$$

The first term in Eq. 30 represents the authority of a fixed thruster, as expressed in Sec. 3.4 for RCS jets (where  $\dot{T}$  was replaced by a variable duty-cycle). The second term is due to controlled rotation of the thrust vector. These terms may be separately inserted into Eq. 21 to form activity vectors for a single-step controller responding to acceleration-change commands. The equations listed below assume that a current estimate of the main propulsion's contribution is included in the commanded acceleration change.

$$31) \quad \underline{\mathbf{A}}_{(T)} = \left[ \begin{array}{c} [\mathbf{I}]^{-1} \mathbf{r}_j \times \hat{\mathbf{T}}_c \\ \hline \frac{1}{M} \hat{\mathbf{T}}_c \end{array} \right] T_{\max} \quad : \text{Activity Vector}$$

$$\Delta \mathbf{x}_{(T)} = \text{Change in Throttle Setting} \quad : \text{Decision Variable}$$

[ The absolute throttle setting,  $x_{(T)}$ , ranges (0 → 1) ]

$$32) \quad \underline{\mathbf{A}}_{(V)} = \left[ \begin{array}{c} [\mathbf{I}]^{-1} \mathbf{r}_j \times (\hat{\boldsymbol{\sigma}} \times \hat{\mathbf{T}}_c) \\ \hline \frac{1}{M} (\hat{\boldsymbol{\sigma}} \times \hat{\mathbf{T}}_c) \end{array} \right] T_c \quad : \text{Activity Vector}$$

$$\mathbf{x}_{(V)} = \Delta \boldsymbol{\theta} = \text{Angular gimbal displacement} \quad : \text{Decision Variable}$$

Where:  $\mathbf{r}$  = Position of propulsion nozzle relative to the vehicle CM

$T_{\max}$  = Peak thrust of propulsion system

$T_c$  = Current Thrust Magnitude =  $x_T T_{\max}$

Eq. 31 defines an activity vector modelling the translational & rotational acceleration change resulting from adjustment of net engine thrust. It's decision variable is the change in throttle setting. In order to prevent large changes per control step (reflecting finite throttle slew, reducing coupling between Eqs. 31 & 32, and generally limiting allowed use of thrust adjustment), small upper & lower bounds can closely sandwich the current throttle setting. Maximum thrust can be hard-imposed by assuming an upper limit on  $x_{(T)}$  of unity, and using the difference  $(1 - x_{(T)})$  as the worst-case upper bound on  $\Delta x_{(T)}$ . Assigning a worst-case lower bound of  $-x_{(T)}$  to  $\Delta x_{(T)}$  will prevent negative thrust values from occurring. If throttling is to be discouraged, its objective factor may be set to a large positive value; if the throttle is desired to be increased or decreased, the corresponding objective coefficient can be made negative.

Eq. 32 describes the translational & rotational acceleration change that results from incremental thrust-vector rotation. The rotation is assumed to be about a fixed (or instantaneous) gimbal axis  $\hat{\sigma}$ , and the decision variable is the angular gimbal displacement  $\Delta\theta$ . In actual systems, the thruster gimbal may be given two degrees of freedom. If one assumes a double gimbal (ie. an inner & outer gimbaled Euler-suspended system), the analysis performed for double-gimbaled CMGs in Sec. 2.5 of Ref. [5] may be applied nearly verbatim. Since the gimbal rotations locally decouple, two activity vectors are created for thrust-vector rotation; ie. one for each gimbal:

$$\underline{\mathbf{A}}_{(V)_{inner}} = \left[ \begin{array}{c} [\mathbf{I}]^{-1} \mathbf{r}_j \times (\hat{\sigma}_\gamma \times \hat{T}_c) \\ \hline \frac{1}{M} (\hat{\sigma}_\gamma \times \hat{T}_c) \end{array} \right] T_c$$

33)

$$\underline{\mathbf{A}}_{(V)_{outer}} = \left[ \begin{array}{c} [\mathbf{I}]^{-1} \mathbf{r}_j \times (\hat{\sigma}_\delta \times \hat{T}_c) \\ \hline \frac{1}{M} (\hat{\sigma}_\delta \times \hat{T}_c) \end{array} \right] T_c$$

$$\begin{aligned}
X_{(V)_{inner}} &= \Delta\gamma = \text{Inner gimbal displacement} \\
X_{(V)_{outer}} &= \Delta\delta = \text{Outer gimbal displacement}
\end{aligned}$$

Simplex may point the thrust vector as desired by choosing  $\Delta\gamma$  and  $\Delta\delta$  appropriately. Upper bounds may be imposed to limit gimbal displacement, thereby avoiding angles commanded past "stop" limits (which may be quite conservative for thruster gimbals), accounting for peak gimbaling rates, and generally limiting authority to reduce effects of nonlinearity & coupling. Objective functions may be devised to avoid stops, minimize gimbal angles, and encourage or discourage particular rotations (singular states may not be a problem here due to the limited gimbal freedom). Since the format of the system in Eq. 33 is entirely derived from the concept of selecting double-gimbaled CMG displacement, much of the analysis performed in Ref. [5] will also apply to this problem.

Ref. [7] discusses a means of managing a magnetically gimbaled rotor system with a linear selection. If the inner & fixed-outer gimbal framework can not model the thrust-vector scheme under consideration, Ref. [7] introduces methods of selecting a two degree-of-freedom rotation without imposing any fixed gimbal axes. Two orthogonal "virtual" axes are defined at each selection to determine the net rotation of a vector (again, two angles are selected). Preliminary methods were proposed in Ref. [7] to limit the absolute rotation and bound the quadrature sum of both gimbal rates.

If throttling and/or thrust-vectoring are included with other actuators in a hybrid selection, a relative balance between all objective factors and upper bounds must be achieved in order to account for the differences in effective bandwidth & authority between the various actuator families, and limit effects of nonlinearity (and mutual actuator coupling). The capability of selecting an efficient mixture of jets and aerosurfaces has been attained by balancing bounds and cost factors in such a fashion; with further adaptation, the concepts introduced in this section may enable the main vehicle propulsion system to also be incorporated in a 6 degree-of-freedom hybrid actuator management procedure.

## 4) Vehicle Controllers

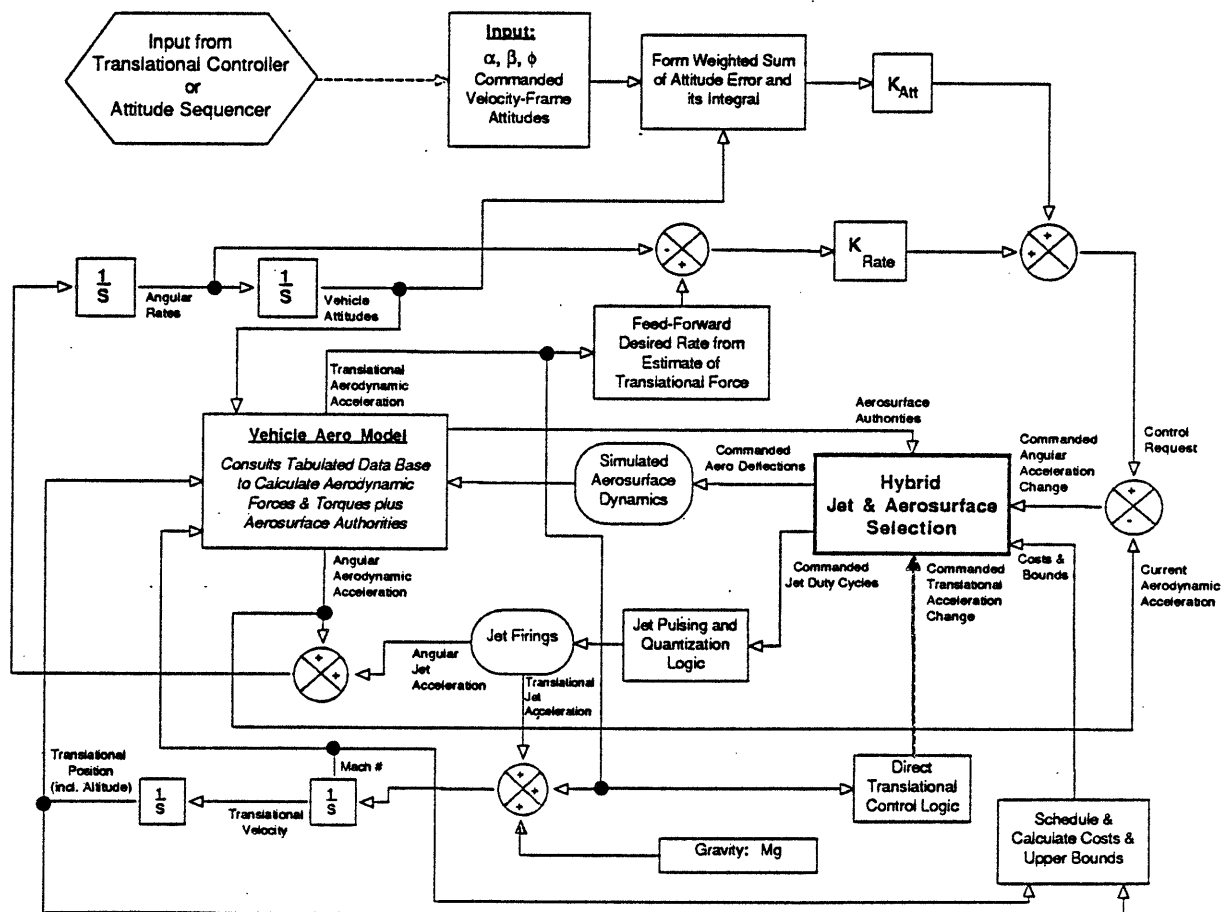
### 4.1) Overview

This chapter presents the control algorithms developed to drive the linear selection and vehicle simulation. A two-level control hierarchy is applied. At the highest level, a translational controller uses estimates of position errors to produce angle of attack and bank commands, which, at the lower level, are realized by a rotational controller. A coarse view of the overall control loop was given in Fig. 1 (Chapter 1), where the relationships between translational controller, rotational controller, and hybrid selection were defined.

Both control levels are based on variants of Proportional-Integral-Derivative (PID) compensators. In all cases, the control gains were chosen empirically to deliver the required vehicle response with adequate stability. Note that these controllers were constructed only to demonstrate the hybrid selection procedure. The actuator selection process may be easily amenable to other control schemes, thus a more complex procedure (ie. phase-plane logic[2], linearization schemes[9,10,11], etc.) may be used, in practice, to augment or replace these simple proportional loops. The vehicle assumed in these studies is considered to act as a rigid body. Flexible dynamics are not applied in either the control schemes or simulation dynamics.

The vehicle state and actuator authorities input to the control logic are generally taken directly from the output of the environment software. No model of sensor hardware or state estimator performance is inserted into the data flow. Some error, however, is naturally introduced through inherent aerodynamic nonlinearity (ie. data predicted via AEROCALC at a current  $\alpha$  can be somewhat different several timesteps later after  $\alpha$  changes). A quick investigation into the effect of estimation uncertainty is presented through a set of examples in Sec. 5.5 that examine the vehicle & controller response to random and systematic modelling errors. The design of adaptive state estimation and dynamic identification algorithms for a NASP-type aerospace vehicle will be the subject of future efforts[27].

This chapter concludes with a description of the re-entry scheduling logic driving the translational controller. Methods are outlined that bias the actuator objective factors to account for actuator scheduling, elevon unloading, and translational control.



**Velocity Frame Attitude Controller and 6-Axis Environment Model**

**Figure 18**

## **4.2) The Rotational and Translational Controllers**

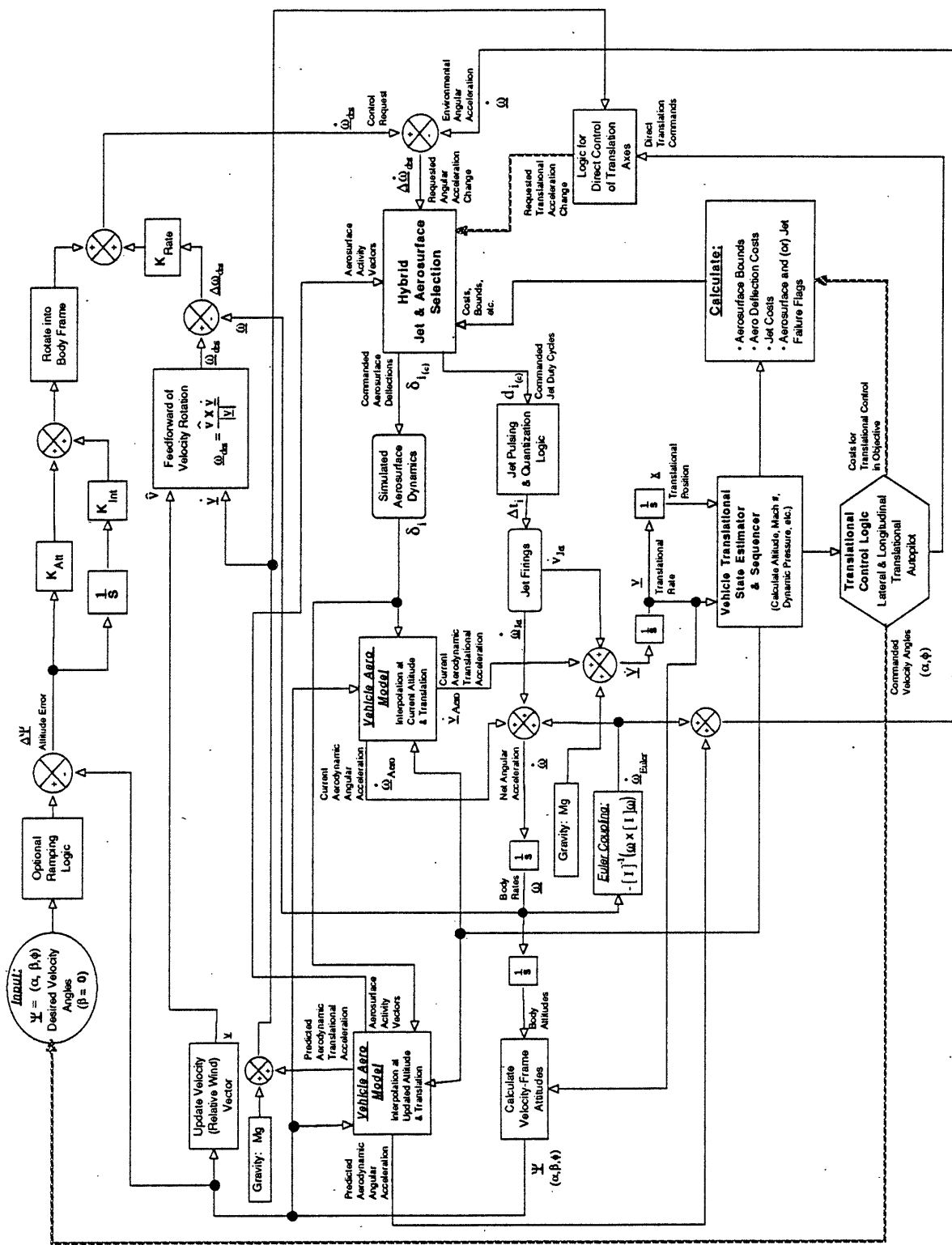
A block diagram depicting the overall structure of the vehicle rotational controller is given in Figure 18. Rotational control is performed in the velocity frame. A standard proportional-integral-derivative compensator responds to instantaneous attitude and rate errors, generating an

eigenaxis representing desired angular acceleration. This is transformed into body axes and subtracted from an estimate of the current vehicle angular acceleration (here output from the environment modelling routine, as noted above, but assumed to be derived from sensor data in an actual vehicle), then applied to the hybrid selection as an acceleration-change request. Note that a feedforward correction is applied to the desired vehicle rate, based upon the expected rotation of the velocity vector by estimated translational force. Translational commands may also be presented directly to the actuator selection as an acceleration-change request (depicted by the dotted line in Fig. 18).

The effects of any currently firing jets are not considered in the estimate of vehicle acceleration used in computing the commanded acceleration change. This causes the jet commands to be absolute; ie. all jets are initialized to be "off" at the start of each selection, and *absolute* duty cycles are specified when jets are required. If jet acceleration was considered when computing the commanded acceleration change, each selection would then calculate a set of relative duty cycles; ie. the *change* in jet duty cycle needed to attain the requested change in *net* acceleration. While this could be implemented under simplex, it is more convenient to specify absolute duty cycles, which are thus adopted here. In an actual vehicle that uses sensors (ie. accelerometers) to determine net vehicle disturbance, it may be more difficult to decouple the jet-related effects from other (ie. aerodynamic) sources (particularly with jet interaction effects). A modified approach may become necessary, ie. one could apply the default strategy to specify *relative* duty cycles in response to *net* acceleration change.

The vehicle aerodynamic model (ie. AEROCALC) accepts the aerosurface angles, vehicle velocity attitude, and vehicle altitude & Mach number as inputs; angular accelerations, translational accelerations, and aerosurface authorities are produced. The former two quantities are summed with the jet response and integrated in the succeeding simulation step (a hold is assumed here), to form updated vehicle angles, rates, velocities (Mach #), and positions (altitude), which are used in the next control iteration and actuator selection. The vehicle Mach number and altitude may also be used to schedule dynamic cost factors and upper bounds for the linear selection.

Figure 19 presents the rotational controller logic at a much higher level of detail. The major difference in structure here is the splitup of calls to AEROCALC (the "Vehicle Aero Model"). The first AEROCALC invocation (at right) calculates the aerodynamic accelerations at the current vehicle attitudes (where the hybrid selection was performed) with updated aerosurface deflections (the "Simulated Aerosurface Dynamics" ramp the aerosurface angles at their maximum rates, as were quoted in Table 1). These accelerations are then integrated to form updated rates & velocities, which are in turn integrated to form updated attitudes and positions. The second call to AEROCALC assumes this new state as an input; the resulting vehicle accelerations and aerosurface



Detailed Logic for Velocity Frame Attitude Controller and 6-Axis Environment Model

Figure 19

authorities are presented to the vehicle controller and hybrid selection, respectively, for application in the next control step.

As detailed in Fig. 19, the predicted rotation of the vehicle velocity vector (through action of aerodynamic and gravitational forces) is fed-forward as the desired vehicle rate, in order to aid in tracking the commanded velocity angles. The expression for desired vehicle rate is:

$$34) \quad \underline{\omega}_{ds} = \frac{\hat{\underline{v}} \times \dot{\underline{v}}}{|\underline{v}|}$$

Where:

- $\hat{\underline{v}}$  = Unit vector along vehicle velocity
- $\dot{\underline{v}}$  = Net translational acceleration
- $|\underline{v}|$  = Airspeed

The current & predicted angular accelerations are also corrected for expected Euler coupling of the vehicle rates. The proportional attitude control law can be expressed:

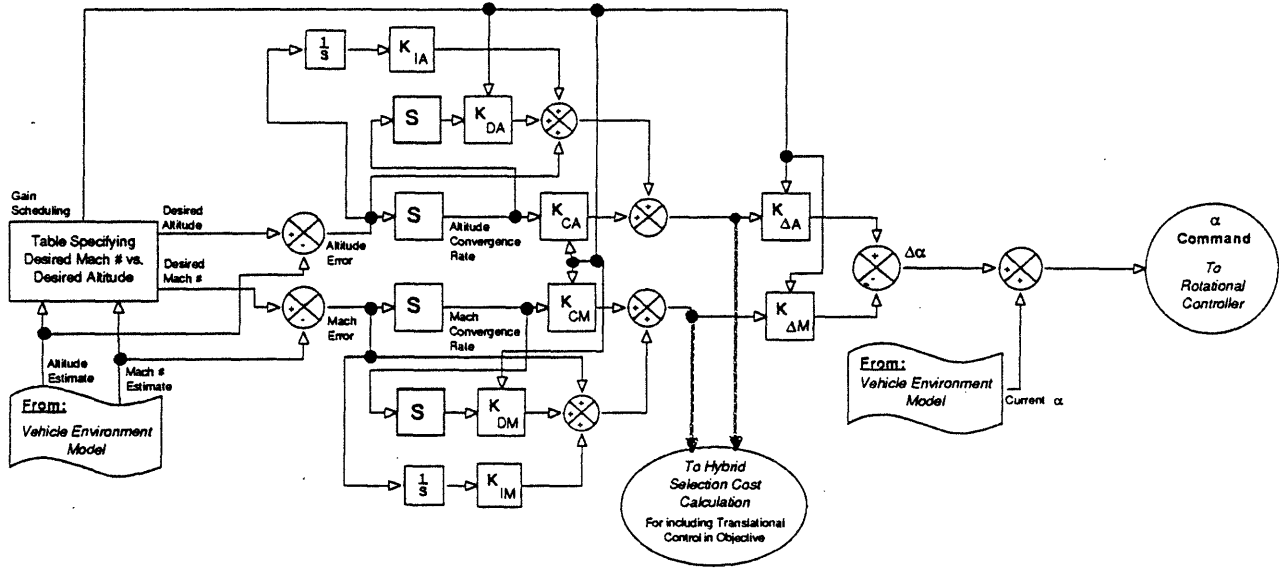
$$35) \quad \Delta \dot{\underline{\omega}}_{des} = [R_{V \rightarrow B}] \left[ [K_{Int}] \int (\underline{\psi}_{des} - \underline{\psi}) dt + [K_{Att}] (\underline{\psi}_{des} - \underline{\psi}) \right] + [K_{Rate}] (\underline{\omega}_{des} - \underline{\omega}) - \dot{\underline{\omega}}_{Pred}$$

Where:

- $\underline{\psi}, \underline{\psi}_{des}$  = Vehicle velocity angles (current, desired).
- $\underline{\omega}, \underline{\omega}_{des}$  = Vehicle body rates (current, desired).
- $\dot{\underline{\omega}}_{Pred}$  = Predicted vehicle aerodynamic & Euler accelerations in body frame (not including jet acceleration).
- $[R_{V \rightarrow B}]$  = Rotation; velocity frame to body axes.
- $[K_{Int}], [K_{Att}], [K_{Rate}]$  = Diagonal weighting matrices; Elements given in Table 3.

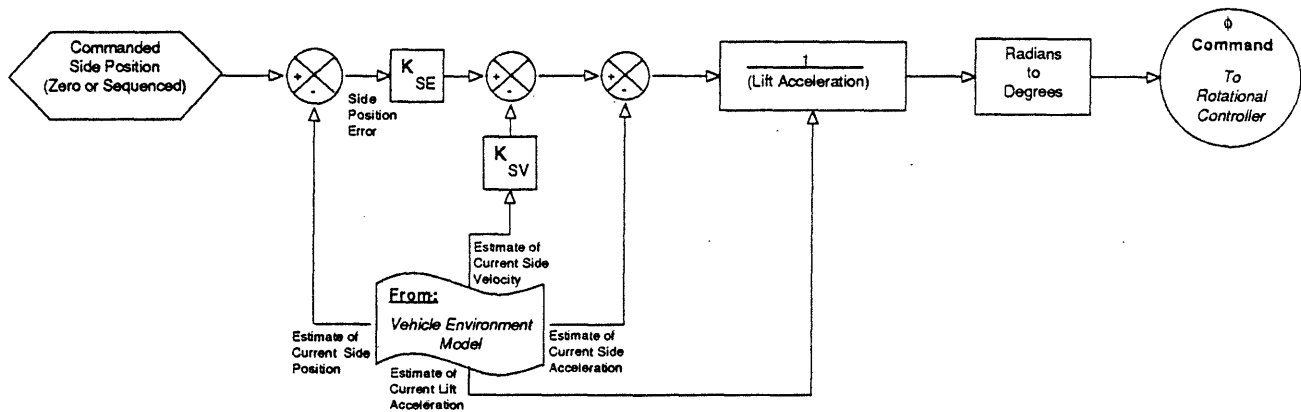
The translational controller is referenced in the small lozenge at the bottom of Fig. 19. Changes in  $\alpha$  and  $\phi$  are commanded in response to translational error ( $\beta$  is held at zero). An optional linear ramp buffers the commanded attitudes to smooth sharp steps (arising from sequenced attitude commands which replace the translational controller in certain tests) that can needlessly engage jets in the selected actuator response.

A proportional control scheme is also employed to govern vehicle translation in re-entry simulations. Separate control loops are defined for longitudinal and lateral translation dynamics. These are individually detailed below in Figs. 20 and 21 (respectively).



Longitudinal Translation Controller

Figure 20



Lateral Translation Controller

Figure 21

The lateral logic determines a desired side acceleration ( $\ddot{y}$ ) resulting from errors in side position, velocity, and current acceleration. Assuming that a bank maneuver results in a leading-order rotation of the vehicle lift force, a commanded bank angle is calculated by scaling the desired side acceleration by an estimate of current aerodynamic lift acceleration ( $\ddot{z}$ ).

The desired longitudinal vehicle state is determined from a Mach number vs. altitude re-entry profile. The relative vertical position errors are summed with a derivative plus integral compensator (weighted by an altitude-dependent set of gains), and used to determine a commanded change in angle of attack ( $\alpha$ ). Since the control variable is the *change* of  $\alpha$  (not absolute  $\alpha$ ), the second derivative of altitude (and/or airspeed) must be included to damp the vehicle response. The longitudinal errors can also be input to the selection's objective function, as discussed below with the presentation of Eq. 38.

The translational control laws can be summarized:

Longitudinal Controller

$$36) \quad \Delta\alpha_{\text{cmd}} = \left[ K_{IA} \int (\Delta h) dt + K_{CA}(h) (\dot{\Delta h}) + K_{DA}(h) (\ddot{\Delta h}) + \Delta h \right] K_{\Delta A}(h) \\ - \left[ K_{IM} \int (\Delta M) dt + K_{CM}(h) (\dot{\Delta M}) + K_{DM}(h) (\ddot{\Delta M}) + \Delta M \right] K_{\Delta M}(h)$$

Lateral Controller

$$37) \quad \phi_{\text{cmd}} = \left( \frac{180^\circ}{\pi} \right) \frac{[K_{SE} \Delta y - K_{SV} \dot{y} - \ddot{y}]}{\ddot{z}}$$

Where:

|  |   |                             |
|--|---|-----------------------------|
| $\Delta h = h_{\text{des}} - h_{\text{estimated}}$ | : | <i>Altitude error</i>       |
| $\Delta M = M_{\text{des}} - M_{\text{estimated}}$ | : | <i>Mach error</i>           |
| $y =$  |   | Side position               |
| $\Delta y =$                                       |   | Error in side position      |
| $\ddot{z} =$                                       |   | Estimated lift acceleration |

The inclusion of translational effect into the cost function was defined by the " $V_{\text{Translation}}$ " function of Eq. 3b. This term can be defined to aid in longitudinal control, as stated below:

38)

$$V_0(i,\pm) = K_x \Delta D (\Delta_i^\pm)_4 - K_y \Delta L (\Delta_i^\pm)_6$$

$$V_{\text{Translation}}(i,\pm) = V_0(i,\pm) - K_{\text{min}}$$

Where:

- $\Delta D$  = Desired change in drag force
- $\Delta L$  = Desired change in lift force
- $\Delta_i^\pm$  = Activity vector for aerosurface #i in  $\pm$  direction
 

|                                  |
|----------------------------------|
| Component #4 = x-Acceleration    |
| Component #6 = z-Acceleration    |
| Defined in stability coordinates |
- $K_{\text{min}}$  = Minimum value of  $V_0(i,\pm)$  over all i  
 Added to keep  $V_{\text{Translation}}$  positive

Eq. 38 assigns a cost contribution to each aerosurface activity vector in proportion to its authority in drag and lift. Deflection is encouraged in a direction to produce the desired effect, with an "urgency" proportional to the magnitude of the requested change. Longitudinal control can be accommodated by setting  $\Delta L$  to the first term in Eq. 36 and  $\Delta D$  to the second term (with negative sign intact). A "minimum drag" bias can be injected into the objective per Eq. 38 by setting  $K_z$  to zero and  $\Delta D$  to -1. Eq. 38 could also provide lateral control by adding a third "y" term in a similar fashion. The  $K_{\text{min}}$  term is incorporated to keep the  $V_{\text{Translation}}$  factors positive (in an analogous fashion to the "B" bias term added to the anti-lineup cost described in Chapter 3 of Ref. [5]).

The velocity angle commands (Eqs. 36 & 37) attain translational control by commanding net vehicle attitude, employing the large resultant forces to gain a specific translational response. The objective method of Eq. 38 differs from this, in that it encourages aerosurface deflection to produce a gross translational effect. Eq. 38 is not a hard constraint, as it only expresses a "desire" for a translational force change. The order of simplex calculation, however, can be extended from pure 3-axis rotation (per the "AX\_CTL" flags discussed in Sec. 2.2) to form a hard constraint over any combination of translational axes. This evokes a precise translational response from the aerosurfaces, provided that the system has sufficient degrees of freedom available to simultaneously decouple the rotation. This method is termed "Direct Translational Control" in the block diagrams.

Since the separate aerosurfaces have much smaller authority than the full airframe, these techniques of direct translational control and objective manipulation per Eq. 38 are primarily useful for small translational trimming and (in the case of Eq. 38) achieving a generic effect (such as minimizing actuator drag). Eqs. 36 & 37 must be employed for large-authority translation.

Typical control gains used in Eqs. 35, 36, & 37 are summarized in the tables below:

**Table 3: Controller Gains**

**a) Rotational Controller**

| Axis     | $K_{Int}$ (sec <sup>-3</sup> ) | $K_{Att}$ (sec <sup>-2</sup> ) | $K_{Rate}$ (sec <sup>-1</sup> ) |
|----------|--------------------------------|--------------------------------|---------------------------------|
| $\alpha$ | .002                           | .14                            | .08                             |
| $\beta$  | .010                           | .20                            | .08                             |
| $\phi$   | .004                           | .30                            | .08                             |

**b) Translational Controller**

Longitudinal Control:

| Parameter                       | h > 145,000 ft.      | 51,000 ft. < h < 140,000 ft. | h > 51,000 ft.       |
|---------------------------------|----------------------|------------------------------|----------------------|
| $K_{IA}$ (ft-sec) <sup>-1</sup> | $8.7 \times 10^{-8}$ | $8.7 \times 10^{-8}$         | $8.7 \times 10^{-8}$ |
| $K_{CA}$ (ft-sec) <sup>-1</sup> | 0.026                | 0.013                        | 0.013                |
| $K_{DA}$ (ft-sec) <sup>-1</sup> | 0.22                 | 0.021                        | 0.021                |
| $K_{AA}$ (deg.)                 | 1.00                 | 3.00                         | 1.75                 |
| $K_{IM}$                        | ---                  | ---                          | ---                  |
| $K_{CM}$                        | ---                  | ---                          | ---                  |
| $K_{DM}$                        | ---                  | ---                          | ---                  |
| $K_{AM}$                        | 0                    | 0                            | 0                    |

Lateral Control:

$$K_{SE} = 0.00038 \text{ ft}^{-1}$$

$$K_{SV} = 0.038 \text{ ft}^{-1}$$

Note that the Mach number loop of Eq. 36 was not used ( $K_{AM}$  is zeroed in Table 3). Since the desired altitude is made a function of Mach number, the altitude loop in Eq. 36 is independently sufficient, and the Mach loop is redundant. If one desires to inject translational control into the objective, however, both Mach number and altitude terms should be calculated and introduced into Eq. 38, since the drag and lift gradients might be substantially different for any given aerosurface.

Certain tests replace the longitudinal controller of Fig. 20 with an  $\alpha$  sequencer. In these cases,  $\alpha$  is generally commanded to vary between  $30^\circ$  and  $40^\circ$ , as a function of Mach number. The adopted  $\alpha$ -profile was taken from the Shuttle re-entry conventions[16], and is plotted in Fig. 22.

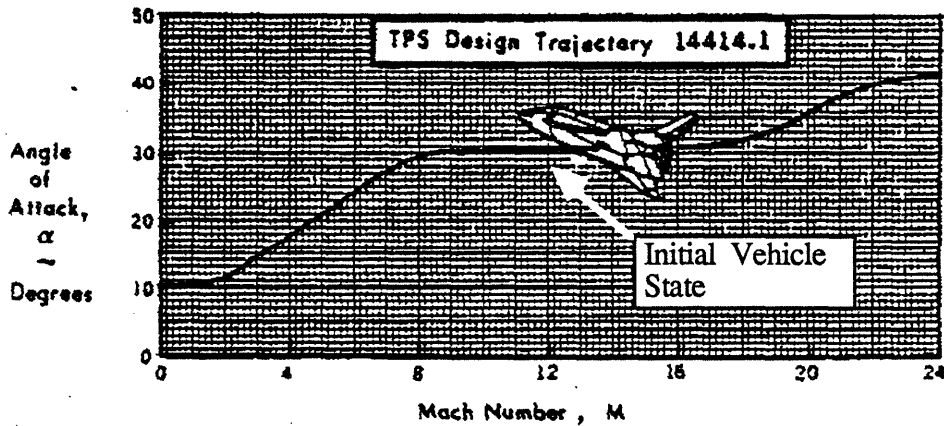


**Figure 22: Sequenced  $\alpha$  Entry Profile**

All other re-entry simulations automatically trim  $\alpha$  via Eq. 36. The altitude-vs.-Mach function used to drive the longitudinal translation controller was adapted from the Shuttle entry corridor defined in Ref. [28] and is plotted in Fig. 23. The target state is determined by a curve at the center of the plotted grey region.

Jet firings commanded under the proportional controller of Figs. 18-19 may be somewhat inefficient. The lack of hysteresis in this logic may invoke many small firings (provided that aerosurface control alone is inadequate) in response to small attitude errors. Conventional RCS control laws employ phase planes, or other means of imposing a deadband on vehicle response to eliminate small jet firings. Deadband limits could be imposed on the hybrid selection in a variety of ways. A phase-space approach has already been implemented with a linear programming jet selection[2,3]; such methods might be adapted to drive both jets and aerosurfaces through the hybrid selection. Solutions which indicate a necessity of jets could be modified (ie. a selection specifying short firings could be re-done with the unresolved coordinate removed via the AX\_CTL simplex flag, or the jet response could be ignored) as a function of vehicle state and

potential control error magnitude. Although initial work has begun to investigate these ideas, all simulations presented in Chapter 5 employ no jet hysteresis, except that intrinsic to the duty-cycle discretization of Eq. 23.

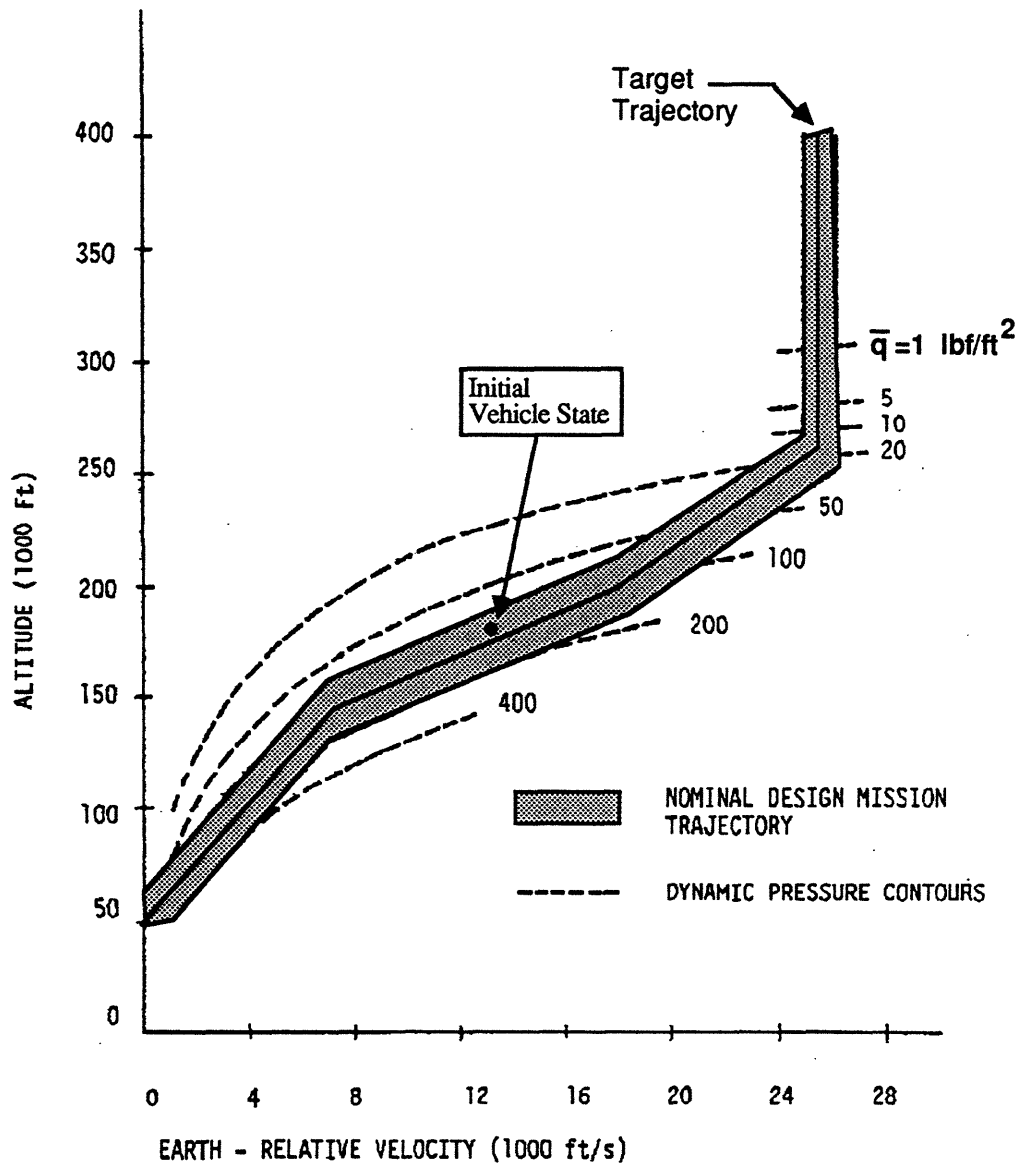


**Figure 23: Vehicle Re-entry Corridor**

### 4.3) Actuator-Dependent Objective Contributions

The ability to set independent objective coefficients for each aerosurface (and sign of deflection) has been exploited to tailor the action of the body flap and speedbrake to specific applications. A major function of the body flap during Shuttle re-entry is to reduce the elevator deflection. The objective function has been adapted here (through the " $Q_{\text{Specific}}$ " term of Eq. 3b) to aid in relieving the elevons & canards. Body flap deflections leading to reduced elevon/canard loads are assigned a negative cost value, which approaches zero and eventually goes positive for large body flap excursion. This encourages appropriate body flap deflection to be selected (thus yielding smaller elevon/canard angles) until its excursion becomes appreciable (causing the stops and deflection costs to contribute significantly, removing the negative body flap cost), or the elevons & canards return to trim.

In order to determine how the body flap will unload the other surfaces, a vector sum is taken of all elevon & canard activity vectors (rotation only is assumed) in the direction opposing their current deflection, weighted by the absolute values of their current deflection angles. This represents the net change in rotational acceleration that would be caused by returning these surfaces to trim. The dot product of this vector is then taken with the body flap activity vectors for + and - body flap deflection. The sign giving the most negative projection denotes the direction of body flap motion best unloading the elevons & canards. The cost factor for this sense of body flap rotation is given a negative amplitude (through  $Q_{\text{Specific}}$ ), thereby encouraging its selection.

The speedbrake has very limited authority across most of the regime studied in these tests, and (especially with the presence of canards) is not needed to complete commands. In order to adequately exhibit its use, however, a series of tests dynamically assigns the speedbrake a high negative cost to encourage its deflection.

A typical speedbrake vs. Mach # profile for Shuttle re-entry[16] is given in Fig. 24. One notes a fast ramp up to full deflection between Mach 10  $\rightarrow$  9, and a gradual return to trim below Mach 5. Actual Shuttle data[29] seems to follow this general scenario (with significantly more modulation).

The " $Q_{\text{Specific}}$ " cost contribution for the speedbrake was defined to model this profile in the relevant tests. In these cases, the  $Q_{\text{Specific}}$  corresponding to positive speedbrake deflection was defined to linearly ramp from zero to a large negative value as Mach number drops below 10. After the airspeed decreases below Mach 5, the negative cost on positive speedbrake deflection is brought to zero, and the cost on closing the speedbrake is ramped slightly negative. Tests that do not employ this scheduling technique assign relatively high values to " $K_0$ " and " $K_A$ " (Eq. 3b)

## 5) Simulation Examples

### 5.1) Overview

A series of examples is presented in this chapter to demonstrate the performance and illustrate the advantages & flexibility of the hybrid control approach. This chapter is divided into 4 sections. The first two examine sequenced attitude maneuvers performed at constant altitude, yielding a clear impression of hybrid controller performance in a simplified environment. The third section investigates vehicle re-entry, tracking a trajectory from 170,000 ft. @ Mach 12 through approximately 20,000 ft. @ Mach 0.5. At the higher altitudes (and larger  $\alpha$  values), both jets and aerosurfaces are required for vehicle control. At the lower altitudes (and smaller  $\alpha$  values), aerosurfaces are capable of maintaining control without jet assistance, and the vehicle can be managed conventionally as an unpowered aircraft. A major advantage of the linear programming approach (as demonstrated in the re-entry tests) is its ability of readily adapting to the changing aerodynamic conditions encountered across the entry trajectory; ie. a single control scheme can manage the vehicle through all aerodynamic regimes. A variety of vehicle reconfigurations, control options, and maneuver commands are attempted in these examples, and the resulting vehicle response is presented and analyzed. The final section of this chapter examines hybrid controller performance with errors introduced in the assumed vehicle, actuator, and aerodynamic models.

Typical controller gains used in these tests are listed in Table 3. All aerosurfaces are initially at trim, and sideslip is always commanded to remain zero. The vehicle state and environment were updated every 320 msec., control was applied every 640 msec., and aerosurfaces were moved at the standard rates given in Table 1 (with the corresponding stop limits). Jet costs (ie.  $C_{\infty}$  in Eq. 24) are typically set to be roughly 200 times more expensive than baseline aerosurface costs, thereby significantly discouraging jet firings. Jets are made available in all selections; the re-selection philosophy of Sec. 2.4 is not applied in any of these examples.

Typical values assumed by the "deflection" ( $K_A$ ) and "bias" ( $K_0$ ) cost factors defined in Eq. 3b are given in Table 4.

These cost factors are adjusted for certain examples, as outlined in the relevant test descriptions. The " $K_s$ " amplitude for the stops cost (in the units of Table 4) is set at 40, with breakpoint " $\zeta$ " (Eq. 5) at 0.93 for all surfaces except the body flap, which uses a  $\zeta$  of 0.90. The " $Q_{\text{Specific}}$ " term is adjusted for the body flap and speedbrake as outlined in Sec. 5.3. For the former,  $K_Q Q_{\text{Specific}}$  is set to a constant (-3) for the deflection that best offsets elevon & canard loads (it is zero in the opposite sense), and the deflection cost  $K_A$  is reduced to 0.01. In specific tests, the speedbrake employs the negative cost factor scheduling described in Sec. 4.3. Otherwise the speedbrake is set to be highly expensive, effectively discouraging its selection.

**Table 4: Relative Aerosurface Costs**

| Surface | $K_A$ (deg <sup>-1</sup> ) | $K_0$ |
|---------|----------------------------|-------|
| $E_R$   | 1.00                       | 0.05  |
| $E_L$   | 1.00                       | 0.05  |
| BF      | 10.                        | 0.10  |
| SB      | 20.                        | 1.0   |
| $C_R$   | 2.00                       | 0.05  |
| $C_L$   | 2.00                       | 0.05  |
| R       | 1.00                       | 0.05  |

The assumed vehicle mass and inertial properties are derived from Shuttle Orbiter data[3], and are given in Table 5. The vehicle center of gravity is assumed to reside at the "Moment Reference Center" defined in Sec. 3.2.

As described in Sec. 2.1, the control strategy applied here does not directly address the nonlinear nature of the vehicle, environment, and trajectory. Instead, a tangent "instantaneous" approximation is followed to maintain discrete control as seen by linearized actuators at the moment of each control update. This can instigate sensitivity to small perturbations in test parameters (indeed, the dependence on initial conditions in certain situations indicates a potential application of classical chaos theory; ie. quantities such as Lyapunov exponents[30] might be calculated to estimate the divergence rate of various actuator and state trajectories). As a result, perturbation to a

flight path or control/selection parameter at a certain point in the simulation can lead to immediate aerosurface deflection & jet firings which change the system such that it may perform differently later in the test. The function of the objective coefficients is to encourage (ie. "attract") certain types of actuator behavior, compensating for potential divergence in the discretized system. Because of of this effect, however, the response of tests run under different parameters may vary somewhat, even though the changed parameters may not yet have significant particular effect (ie. a small difference in aerosurface deflection specified by simplex may lead to a change in the chosen jet firing pattern, which, in turn, can instigate sideslip disturbance and lead to greater fuel usage later in the test). The characteristics of these results must thus be compared for their overall properties; ie. a certain change in parameters creates a response featuring larger negative aerosurface deflections, fewer jet firings, more canard usage, etc. Because of the different (potentially divergent) state trajectories followed under different examples, overly specific comparisons may not be meaningful.

**Table 5: Vehicle Mass & Inertias**

a) *Vehicle Inertia* (slug/ft<sup>2</sup>)

|       | Roll      | Pitch     | Yaw       |
|-------|-----------|-----------|-----------|
| Roll  | 883307.8  | -8119.8   | -247266.5 |
| Pitch | -8119.8   | 6748838.5 | -417.7    |
| Yaw   | -247266.5 | -417.7    | 7058013.0 |

b) *Vehicle Mass* = 5903.351 slugs

**5.2) Constant Altitude Rotational Maneuvers**

This series of examples does not integrate the effects of translational force on the vehicle, which is thus assumed to cruise at constant speed (Mach 8) and constant altitude (140,000 ft.), yielding a dynamic pressure of approximately 225 lb/ft<sup>2</sup> via the assumed atmospheric model.

Closed-loop translational control (circa Figs. 20 & 21) is disabled; instead, the attitude controller is driven by a series of sequenced angle of attack and bank commands (sideslip is commanded to remain zero).

Although the aerosurface deflections are all plotted to a common scale in this section, the axis limits in plots of elevon and body flap deflections are scaled to the peak range of deflections produced in these particular examples, and do not reflect the location of imposed stops. Jet firings (when they occur) are denoted by "x" marks printed above the curves in each plot. Jet accelerations are plotted to the same scale in all axes.

The first tests command a simple maneuver sequence. The simulations begin with an angle of attack ( $\alpha$ ) of  $15^\circ$ , and both bank ( $\phi$ ) and sideslip ( $\beta$ ) zero. All aerosurfaces are initially at trim (ie. zero deflection). The vehicle is commanded to ramp up in pitch to  $\alpha = 25^\circ$  at  $t = 3.1$  sec., after which  $10^\circ$  of bank are commanded, followed by a pitch-down to  $\alpha = 10^\circ$ , and ending with a return to zero bank. Sideslip is commanded to remain zero throughout the entire maneuver sequence, and all aeroactuators are assumed to be operational over the full 5-minute test duration. Translational control, drag, and speedbrake usage are not reflected in the computation of aerosurface costs; only deflection minimization and stops avoidance contributions are considered.

Aerosurface deflections are plotted in Fig. 25, velocity-frame attitudes are given in Fig. 26, and body rates are given in Fig. 27. Because of its excessively large cost, the speedbrake was not selected in any of these tests, thus its corresponding plot is omitted. The left and right aerosurface deflections are plotted together in the elevon and canard plots; the deflection angles of right aerosurfaces are drawn solid, while the left are dashed. Receipt of new maneuver commands are indicated by a triangle drawn on the x-axis.

Due to the delta-wing Shuttle configuration, the vehicle exhibits static pitch stability, thus is subject to a restoring moment in pitch that tries to reduce significant positive  $\alpha$  values. In order to stabilize the vehicle at  $\alpha = 15^\circ$ , rapid canard and body flap displacements were selected at the beginning of the test (recall that the test is initialized with the aerosurfaces at trim). The higher authority of canards moving into the airstream makes them more favorable for positive pitch maneuvers than the corresponding lower authority solution that moves elevons out of the airstream. The body flap's initial negative cost encourages its selection to unload the canards (which have opposite-sense pitching effect) until it also achieves significant deflection.

At  $t = 3.1$  sec., the pitch-up command is issued to reach  $\alpha = 25^\circ$ . Since the canards are already at significant deflection, the linear program finds it more efficient to deflect both elevons slightly negative (approximately  $0.15^\circ$ ) and stop slewing the body flap to achieve the positive pitch rate (because of the scale in this plot, this small elevon displacement is barely visible; it is indicated in the elevon plot of Fig. 25). This example employs a linear ramp between input commands (as introduced in Fig. 19), which significantly reduces the needed torque response.

As the vehicle starts to increase pitch, the net airframe pitch-down moment starts to slightly decrease (a characteristic of the Shuttle in the vicinity of Mach 10). As a result, the canards are actually pulled back and elevons are slightly extended to maintain the desired torque. Limited canard scissoring and rudder displacement are specified to cancel any  $\alpha$ -dependent sideslip disturbance caused as the vehicle changes pitch. The pitch-down moment begins to increase again after  $\alpha$  rises beyond  $20^\circ$ ; because the canards are already deflected to yield a positive pitch torque, the linear program now finds it more efficient to compensate by moving the elevons (which are near zero deflection) a degree or so in the negative direction, together with a small additional body flap increment.

The  $10^\circ$  bank command is issued at  $t = 61$  sec.; required roll torque is derived by scissoring the elevons and canards, while rudder pulses are selected to generate the needed yaw authority stabilize sideslip. Opposite-sign scissoring deflections and rudder pulses are commanded to start and stop the vehicle bank. Note that the canard model has a roll authority reduced relative to the elevons by an order of magnitude (due to their smaller surface area), yet their pitch authority remains equal (due to the long lever arm of canards placed forward of the vehicle CG). Canard scissoring thus produces a much smaller roll disturbance than identical elevon motion.

At  $t = 113$  sec., the vehicle is commanded to pitch down to  $\alpha = 10^\circ$ ; the needed rate is initially generated by commanding a small positive elevon displacement. As  $\alpha$  decreases, however, the net airframe pitch-down moment begins to build again, instigating positive canard displacement, negative elevon motion, and additional body flap excursion to maintain the desired pitch response (since the airframe pitch torque is considerably larger at  $\alpha = 10^\circ$  than at the initial  $15^\circ$  state, significantly larger aerosurface deflections are required to stabilize the vehicle). The command to restore bank angle is issued at  $t = 202$  sec.; this is mainly answered by small elevon scissoring to create roll and rudder deflection to handle yaw. Since the rudder authority is considerably higher at smaller  $\alpha$ , and less yaw component is included in a low- $\alpha$  bank, much smaller rudder deflections are adequate.

Velocity-frame angles are plotted for this test in Fig. 26 (the dashed lines represent attitude commands here; solid lines are the vehicle response). The angle of attack is seen to respond with the sequence  $15^\circ \Rightarrow 25^\circ \Rightarrow 10^\circ$  (as commanded), the requested  $10^\circ$  bank is smoothly achieved and removed, and sideslip disturbances caused by aerosurface/airframe coupling and non-linearities remain under  $0.2^\circ$ . The body rates (plotted in Fig. 27) needed to achieve commanded attitudes and compensate disturbances are achieved quite smoothly. Bank is a superposition of roll and yaw motion mixed as a function of  $\alpha$ , thus the yaw rate needed for the  $10^\circ$  bank is considerably smaller at  $\alpha = 10^\circ$  than at  $\alpha = 25^\circ$ ; this is evident from the asymmetry in the yaw rate profile.

### Example #1: Attitude Sequence, Nominal Case

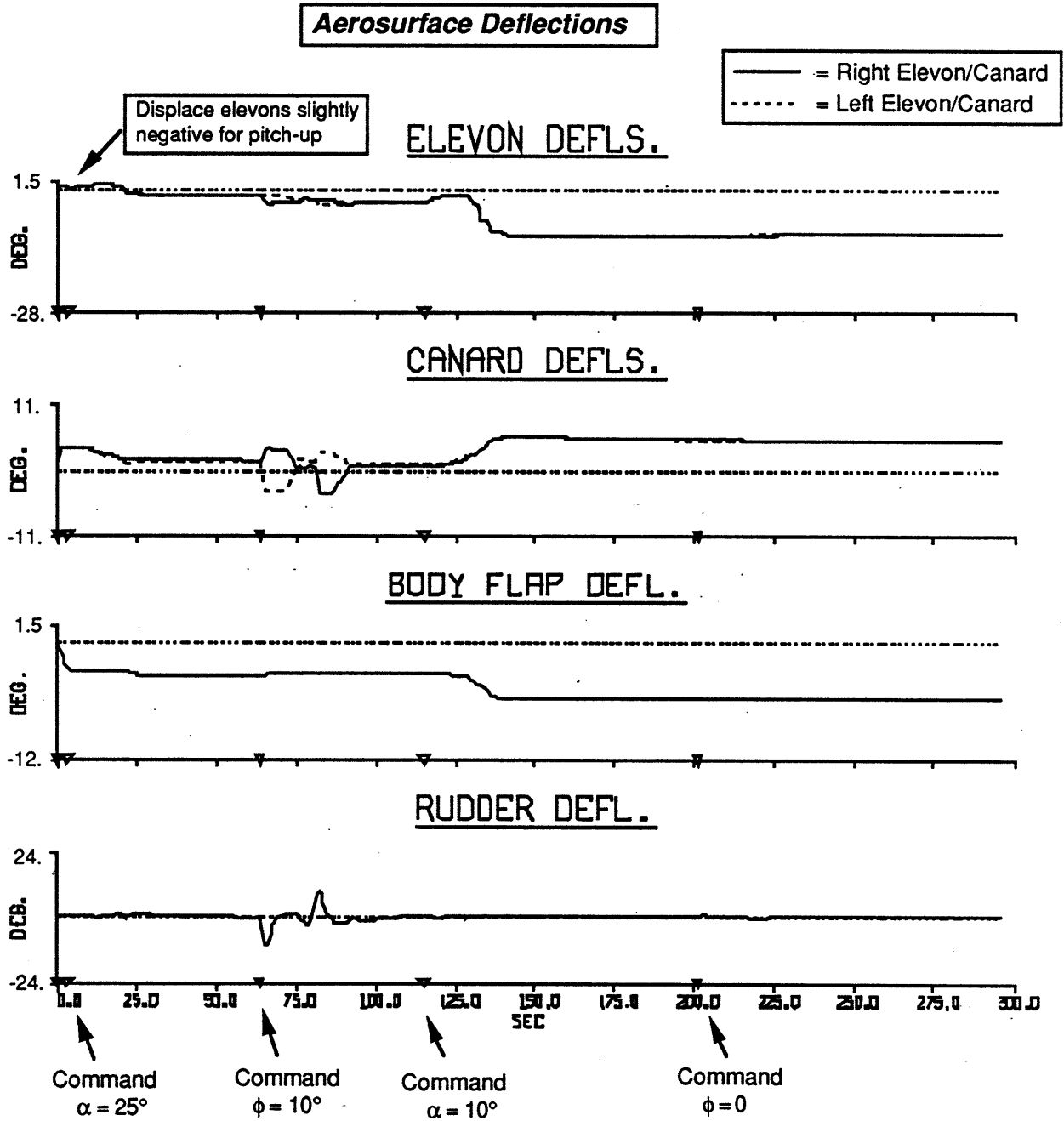
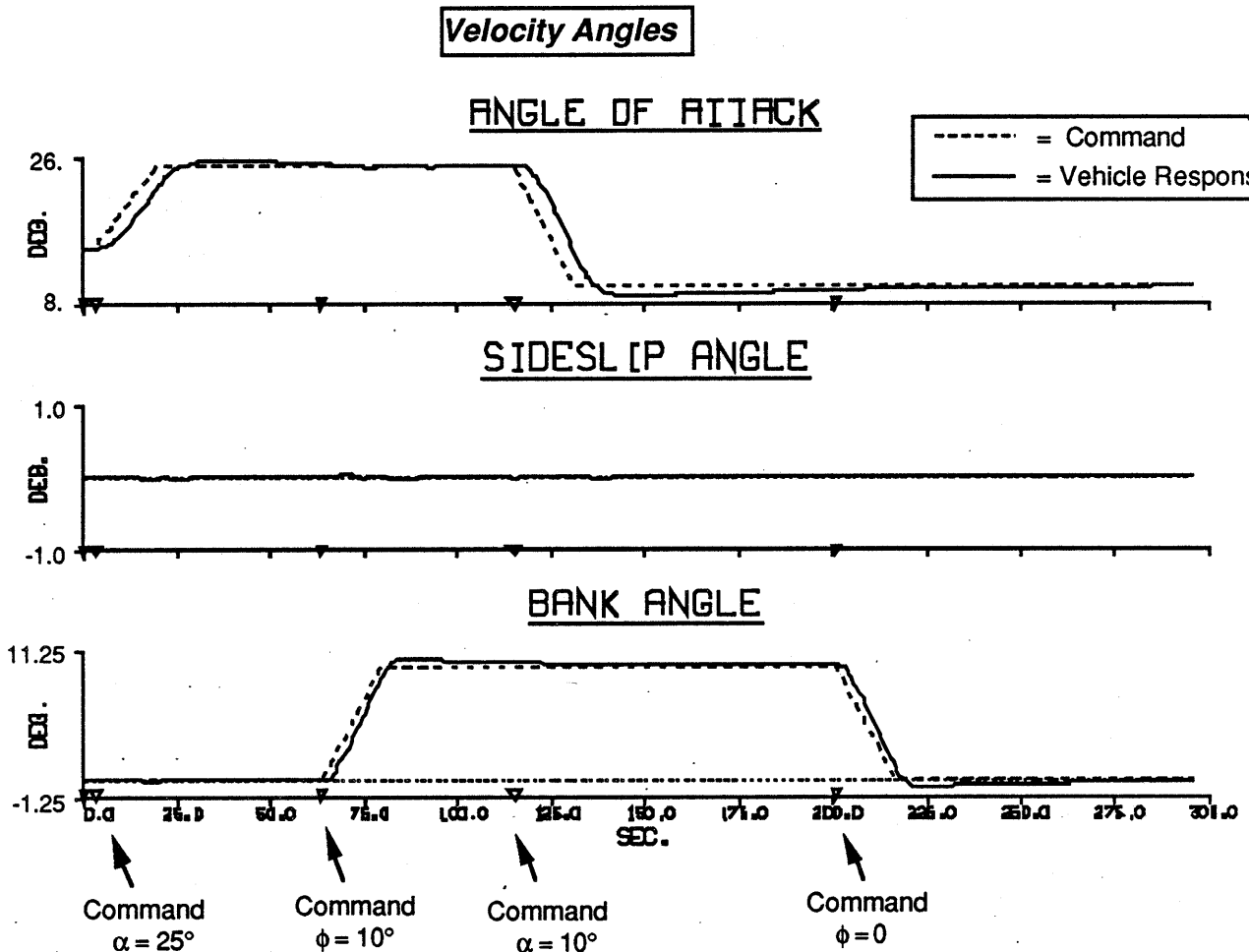


Figure 25

## Example #1: Attitude Sequence, Nominal Case



**Figure 26**

The elevon/canard scissoring in the second bank rotation is considerably smaller than that encountered earlier at  $\alpha = 25^\circ$ ; indeed, canard scissoring seems to be essentially absent in the latter case. If one examines the elevon/canard motion used to establish the bank angle, the reason becomes evident; the elevons and canards are scissored here to produce *opposing* roll torques (note the different deflections of solid and dotted curves in the canard & elevon plots of Fig. 25; the roll authority of the canards is the same sign as that of the elevons, although a factor 10 smaller). Canards are thus made to oppose elevons in roll in order to produce a small residual yaw torque, which is desperately needed to aid the rudder at high  $\alpha$ , where it is largely shadowed by the vehicle fuselage. This additional yaw torque is no longer required at smaller  $\alpha$ , hence the bank is performed exclusively with much smaller elevon scissoring and rudder pulsing.

## Example #1: Attitude Sequence, Nominal Case

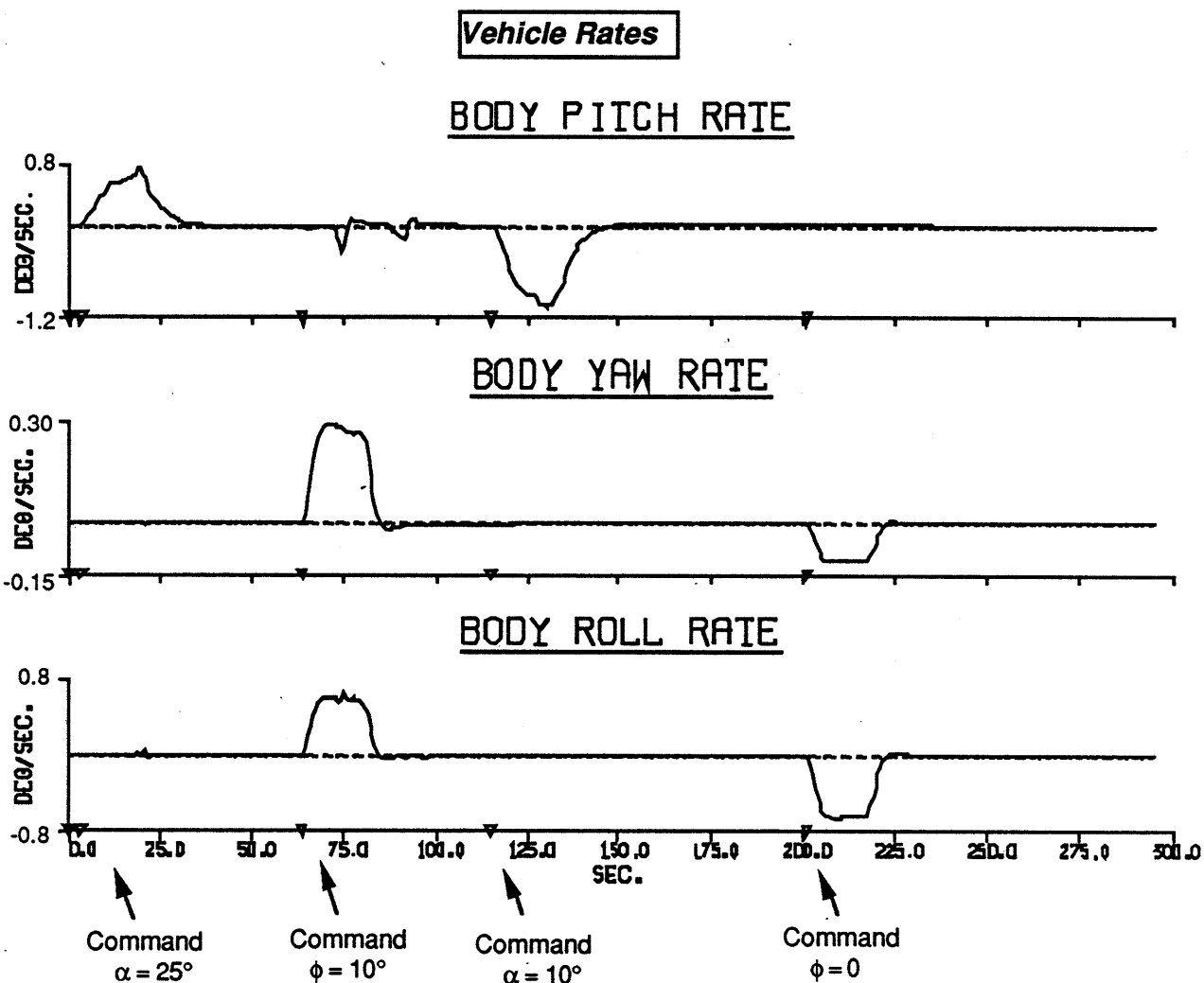


Figure 27

A major advantage of the linear programming approach is its ability to adapt the selection strategy and/or introduce additional actuators (ie. jets) to maintain vehicle control after actuator failures and reconfiguration. This property is illustrated in the next example, which is performed initially under conditions similar to the test of Figs. 24 → 26. After  $t = 25$  sec. (when the vehicle has stabilized at  $\alpha = 25^\circ$ ), both canards are "failed" (ie. frozen at constant angle and inhibited from further selection). Although the static aerosurface "freeze" is adopted as the standard failure mode in this study, alternate dynamic failure models (ie. "floating" uncontrolled aerosurfaces that feather

## Example #2: Attitude Sequence, Fail Canards

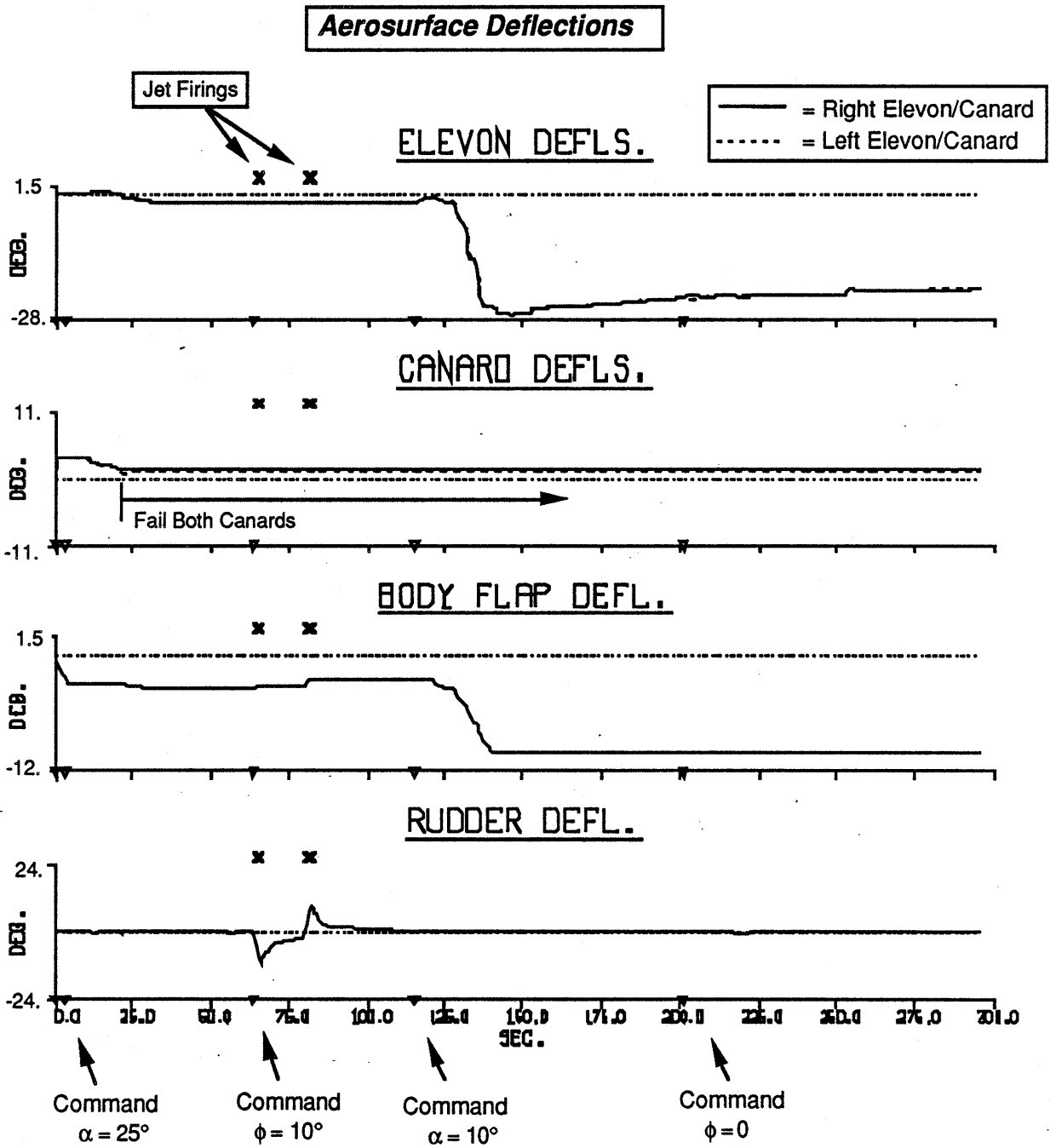


Figure 28

## Example #2: Attitude Sequence, Fail Canards

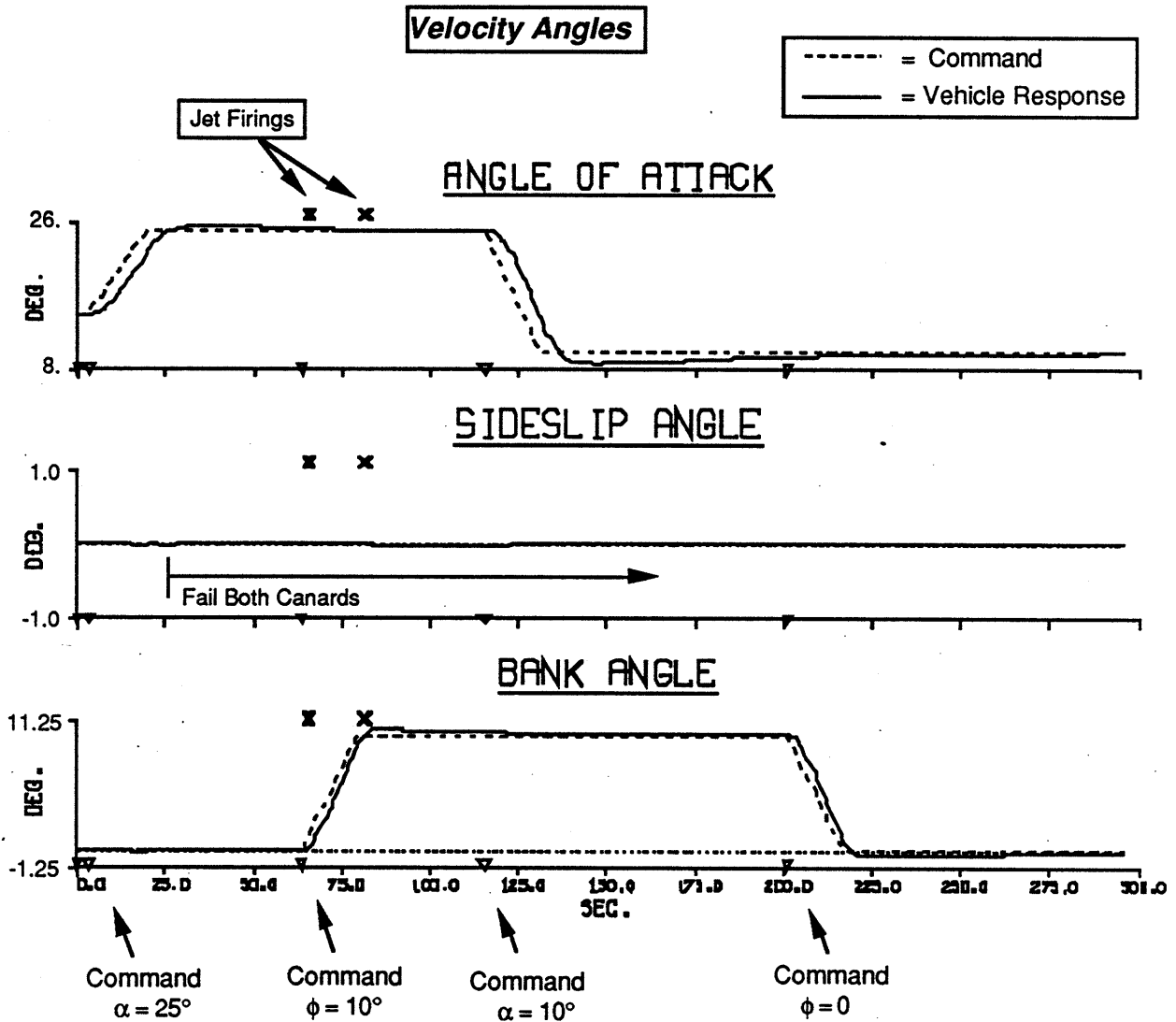
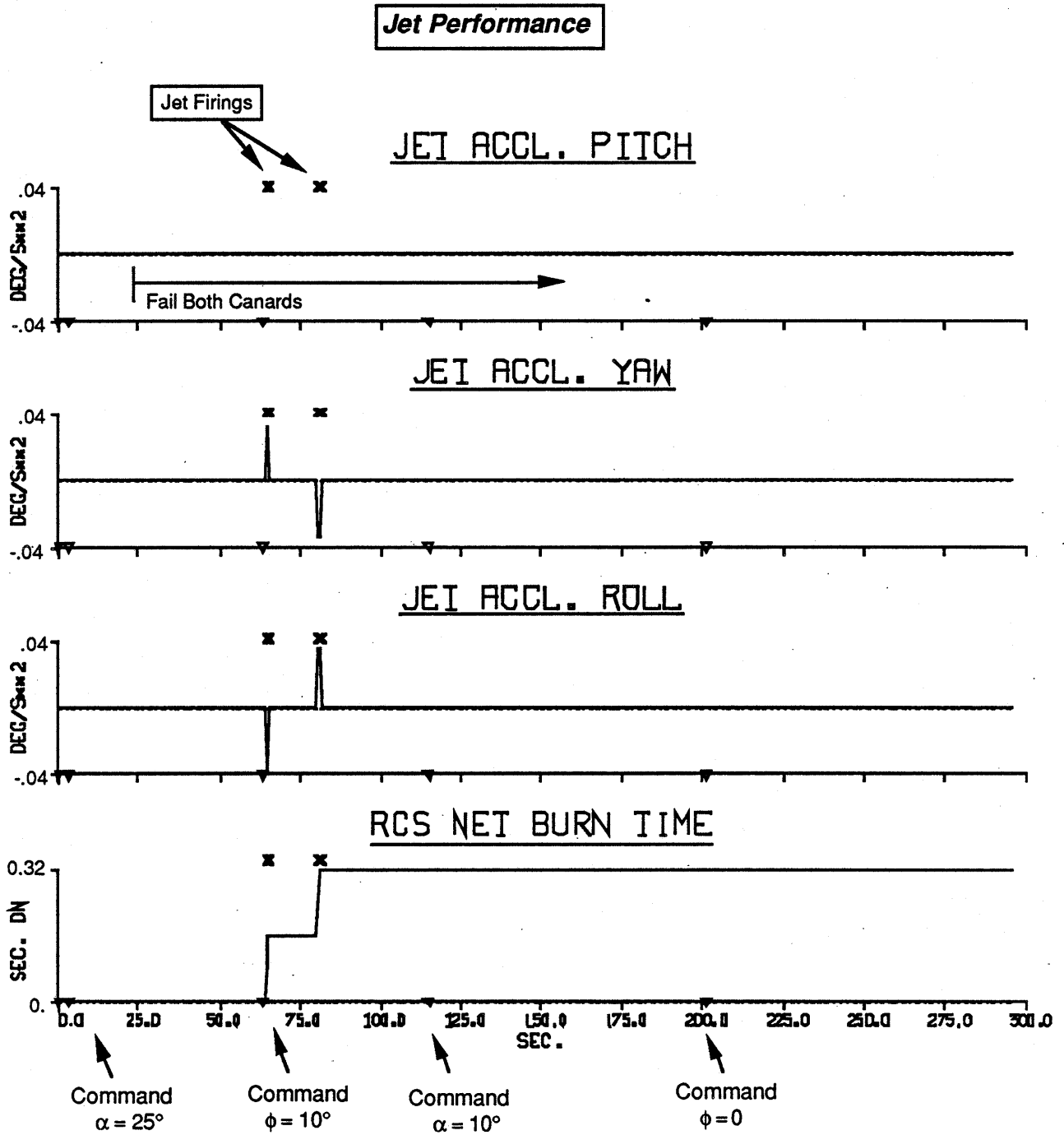


Figure 29

to minimize aerodynamic projection) may be accommodated by inhibiting the malfunctioning aerosurface from being selected, and adjusting the commanded torque change to compensate for its expected effect.

The aerosurface response (Fig. 28) is seen to be initially identical to that of Fig. 24. After the canards are failed, however, all pitch control must be performed exclusively by the elevons and body flap. With the lack of canard assistance, the elevons are now seen to be deflected much further in the negative sense (reaching roughly 80% of their maximum deflection) to null the

**Example #2: Attitude Sequence, Fail Canards**



**Figure 30**

aerodynamic imbalance after the pitch-down to  $\alpha = 10^\circ$ . This extreme elevon deflection also stresses the body flap, which has essentially been moved up to its stop in this example. Note that the elevons here have much less differential pitch authority at high negative deflection and low  $\alpha$ , as was plotted in Fig. 11. The canard assist was thus significant in the previous example (Fig. 25), since the canards can deflect in the positive sense (where their authority is much higher) to achieve the desired effect.

Although the velocity angles (Fig. 29) are seen to follow their familiar profiles, two brief jet firings (denoted by "x" plotted over the curves) are requested in order to augment rudder action in starting and stopping the vehicle bank at high  $\alpha$ . These are indeed fast lateral firings, as seen in Fig. 30. They arise from a simplex response to the reconfigured vehicle; in the original example (Fig. 25), the canards participated in the bank maneuver to react differentially against the elevons (ie. the "opposite" scissoring), thereby providing a small amount of additional yaw torque. With this channel now unavailable, simplex has introduced a pair of brief jet pulses (Fig. 30) to augment yaw. Now that the elevons and canards are not being differentially scissored, much less elevon response is needed for the initial bank. The jets selected in this example are side-firing aft thrusters. Side-firing forward jets, which give yaw authority with much less roll disturbance, are also available to the selection at this altitude, although they are made more expensive with decreasing altitude (per Eq. 24), due to induced aerodynamic disturbance. Because of their lower cost at the altitudes considered in this test, the aft jets are preferred; the associated roll disturbance is still small, and easily compensated by the elevons.

The next example uses the same attitude sequence, but fails both elevons after the initial bank maneuver (for  $t > 100$  sec.). All other actuators are assumed to remain operational over the full test duration. The initial aerosurface profile (Fig. 31) is identical to the nominal case (Fig. 25); differential elevon/canard scissoring is seen to overcome the need for a jet firing. When the pitch-down command is issued after  $t = 115$  sec., however, the canards must be pushed to considerably higher deflection in order to independently stabilize the  $\alpha$ -dependent pitch torque. Since the canards have reduced roll authority, the absence of elevons entails significantly greater canard scissoring after  $t = 200$  sec. to return the vehicle to zero bank. Velocity angles (Fig. 32) appear to adequately follow their commanded profiles.

The intrinsic optimization performed at each linear programming selection provides an opportunity to introduce other operational biases into the actuator management policy. The objective functions used in the previous examples worked only to minimize individual aerosurface deflections. The objective calculated in the next example, however, also contains a contribution (per the first term in Eq. 38) that encourages each aerosurface to move in the direction of minimum drag (such a strategy may be desirable if one wishes to minimize thermal loading of aerosurfaces). All actuators are assumed to be fully operational throughout this test.

### Example #3: Attitude Sequence, Fail Elevons

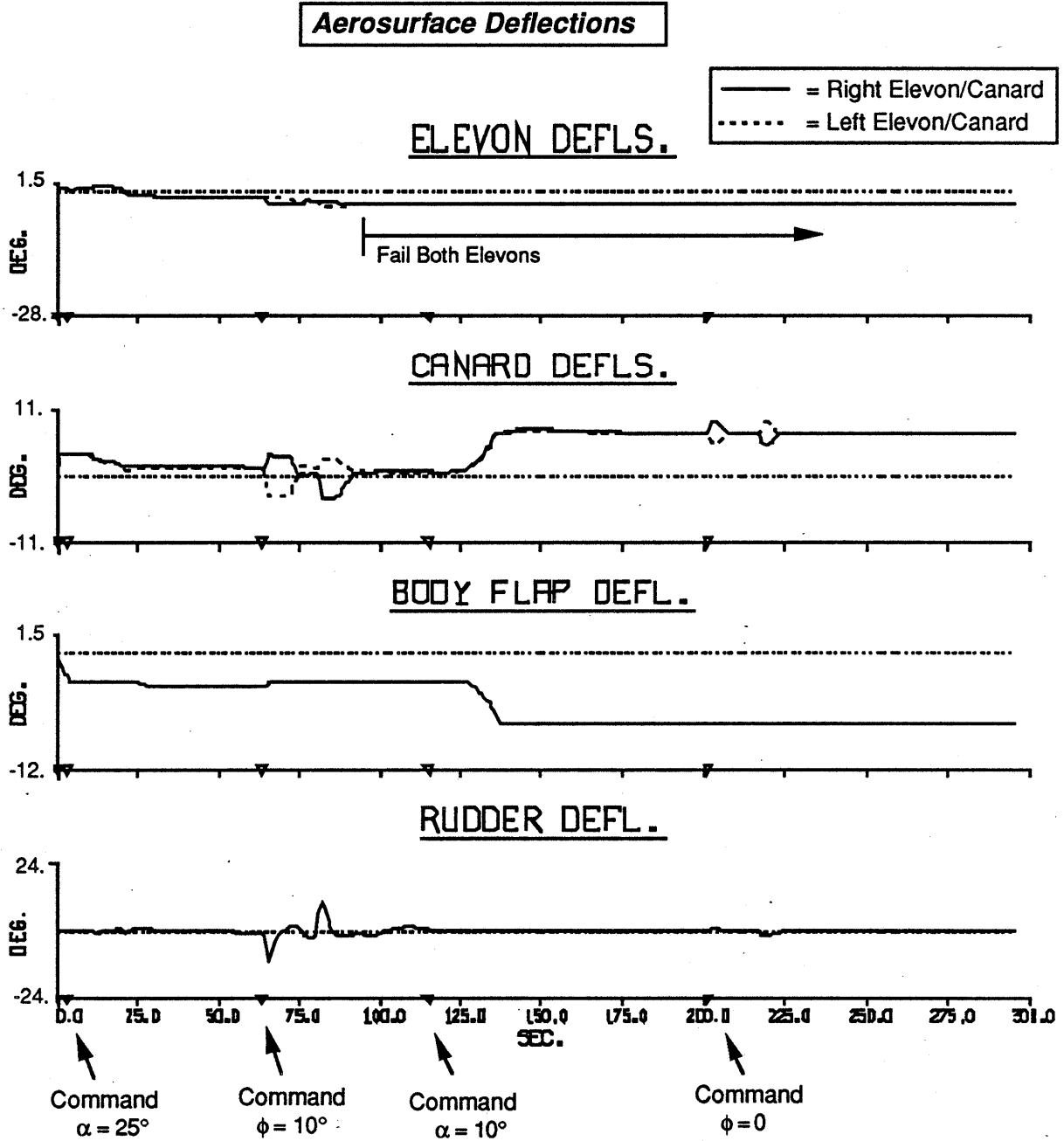
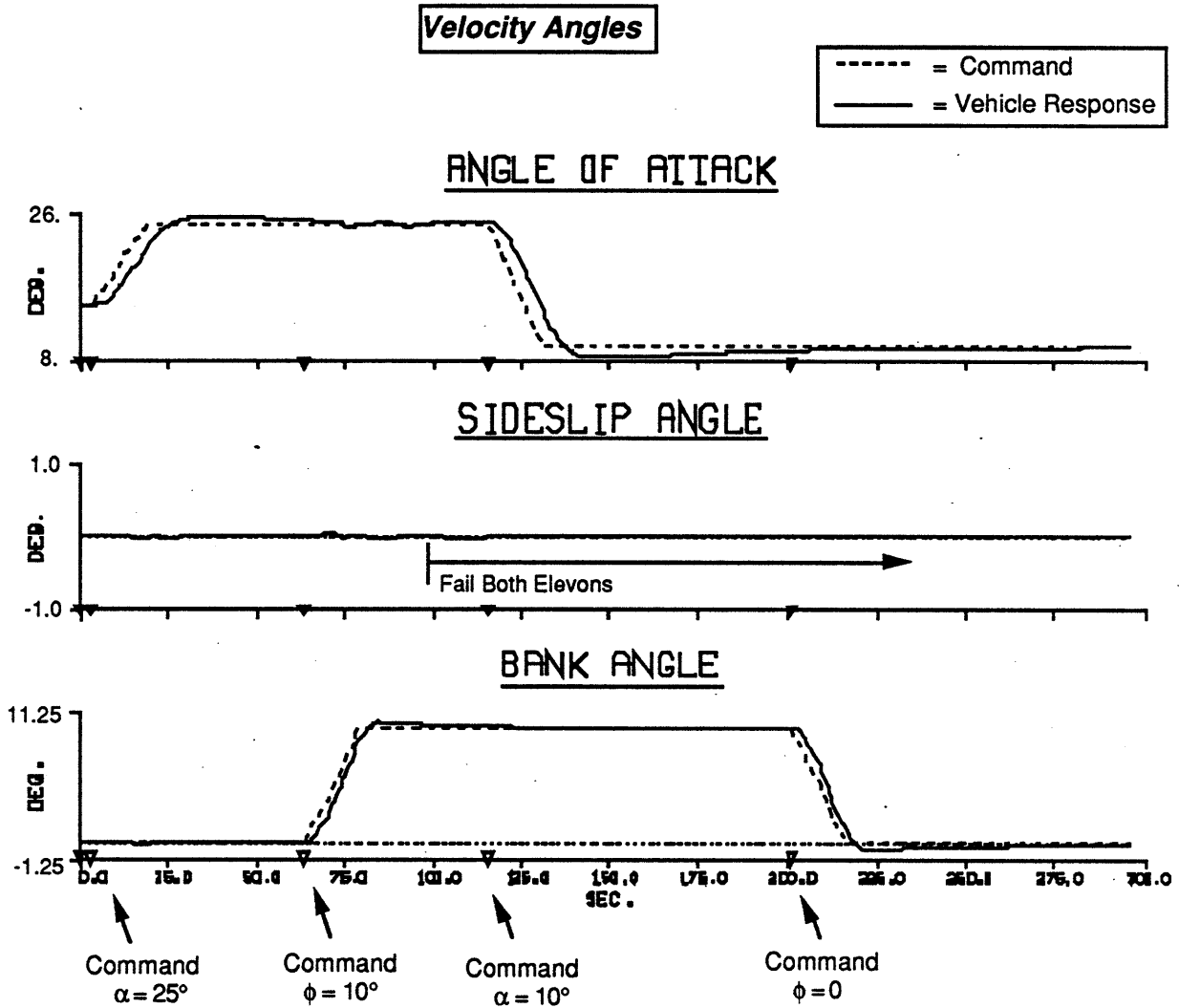


Figure 31

### Example #3: Attitude Sequence, Fail Elevons



**Figure 32**

Aerosurface deflections are shown in Fig. 33. The results are markedly different here; a strong preference is seen for negative elevon and canard displacement. This is exactly as expected, since negative deflection brings aerosurfaces out of the flow field, thereby reducing resultant drag effects.

The test again begins with an initial request to null the quiescent pitch-down body torque encountered at  $\alpha = 15^\circ$  with aerosurfaces at trim. In earlier examples, this was answered nearly exclusively with positive canard deflection. Now, however, the selected strategy involves

### Example #4: Attitude Sequence, Minimize Drag

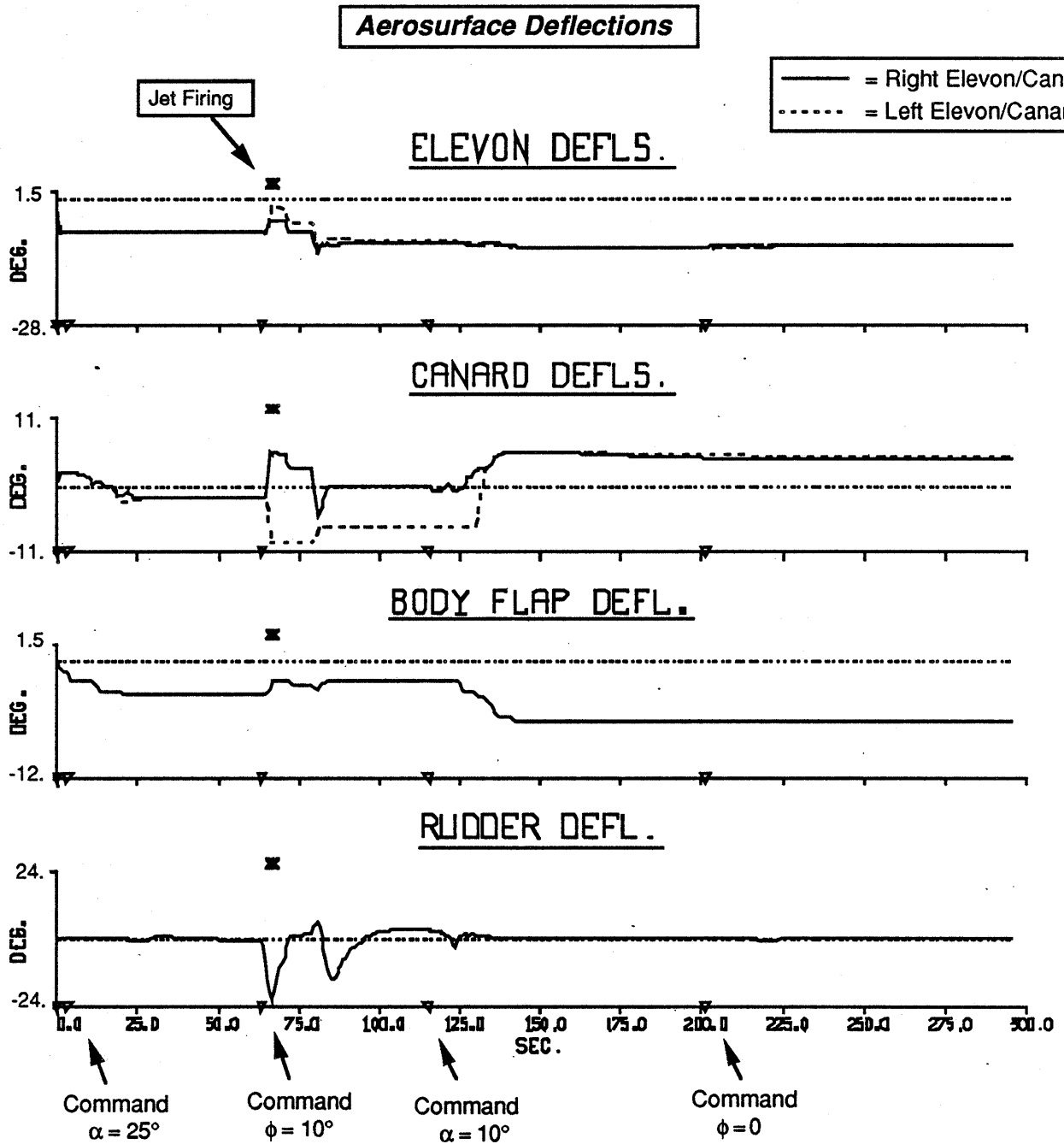


Figure 33

### Example #4: Attitude Sequence, Minimize Drag

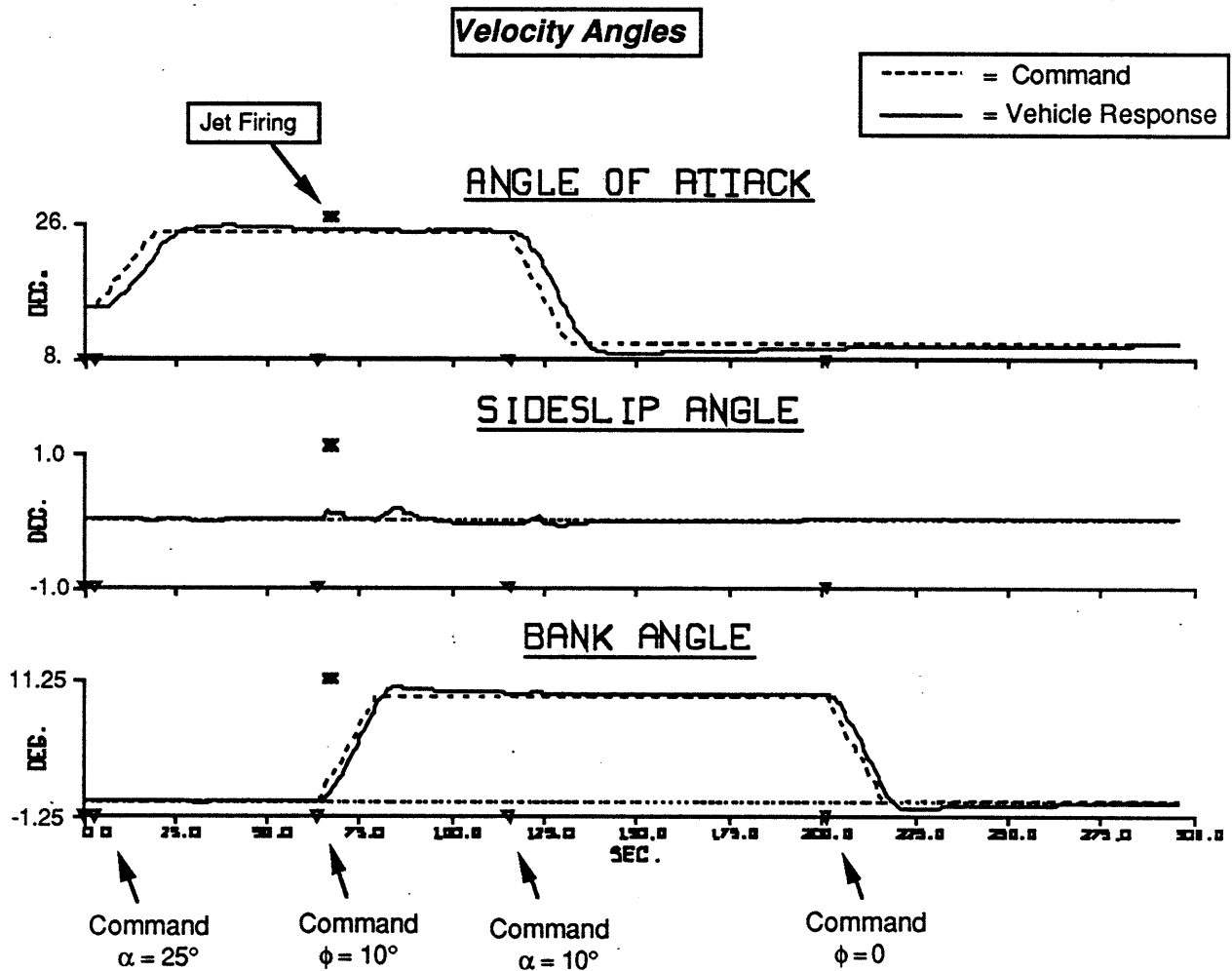


Figure 34

substantial negative elevon deflection. Because of their larger drag coefficients, moving the elevons negative can result in substantial cost savings. As the vehicle pitches up to  $\alpha = 25^\circ$ , the canards are also brought into negative deflection, yielding additional drag benefit; this is preferred over the equivalent solution involving positive elevon deflection, which would contribute considerable drag penalty. Substantial elevon/canard scissoring is attempted upon receipt of the  $10^\circ$  bank command, in order to stabilize yaw at high  $\alpha$ . With the aerosurfaces at these negative deflections, however, insufficient yaw torque could be developed (in spite of the extreme rudder deflection), and a brief set of lateral jet firings were requested (see Fig. 35).

# Example #4: Attitude Sequence, Minimize Drag

## Jet Performance

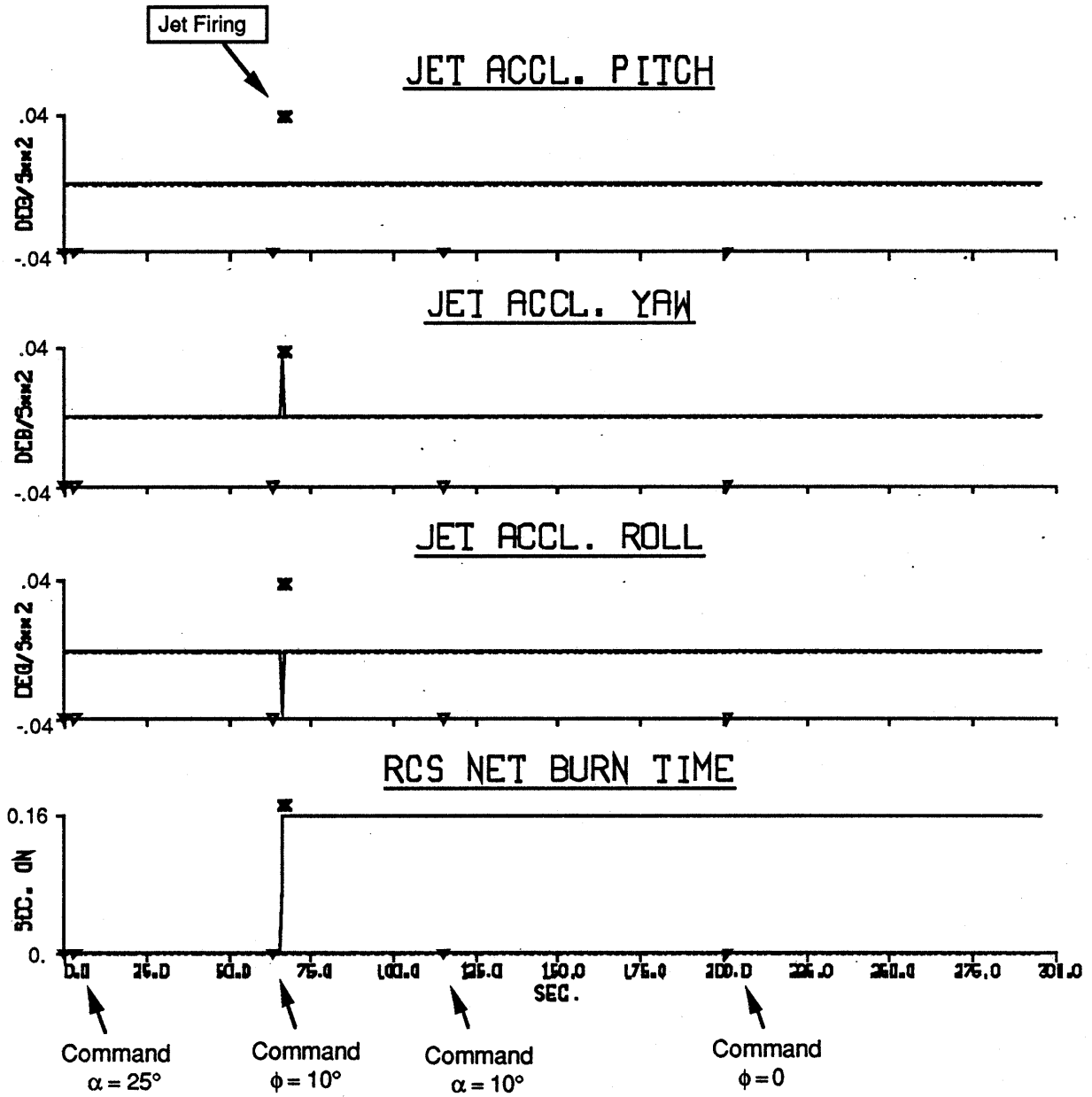


Figure 35

The drag cost contribution also acted to maintain the canard scissoring (compensated by small elevon scissoring and rudder deflection) after the bank was established; this cost structure favors large negative canard deflections. The pitch down to  $\alpha = 10^\circ$  required the canards to deflect positive; this strategy is not highly expensive (since the canards have a reduced drag coefficient in this model), and greatly aids in balancing pitch torques, since the elevon authority can decrease with negative deflection at low  $\alpha$ .

Velocity angles for this test responded as commanded (Fig. 34), and sideslip disturbances were kept minimal. The minimum-drag selection bias may be increased by weighting the drag minimization contribution more heavily in the objective calculation (Eq. 38), allowing it to override the deflection minimization and stops avoidance costs at even higher aerosurface angles, resulting in additional negative deflection.

The next test in this sequence assumes all aerosurfaces to be operational and retains the minimum-drag objective contribution used in the last example. The rudder, however, is now constrained to operate under a  $\pm 5^\circ$  maximum deflection (actuator stops may be re-defined at will under the linear programming scheme). The aerosurface response (Fig. 36) is identical to that of the previous test until the initial bank command is issued at  $t = 61$  sec. The rudder, which is needed here to stabilize yaw, is seen to approach its  $5^\circ$  limit (in both directions as the bank rate is established and removed), whereupon jet firings were introduced to gain additional authority (these are again yaw firings, as seen in Fig. 38). Additional canard action is also evident during the firings, presumably to cancel jet-induced roll disturbances and perhaps attain a small amount of additional aerosurface yaw authority. Jet firings aren't needed for the subsequent bank return due to the higher rudder authority at lower  $\alpha$ . The shape of the rudder deflection profile is affected by the stops amplitude of Eq. 5, which acts to discourage advance of the rudder close to its limits at  $\pm 5^\circ$ . Velocity angles are seen (Fig. 37) to follow their commands with minimal sideslip disturbance.

Because the "ramping" logic applied in the previous examples limited the magnitude of input commands by distributing them across several control cycles, the primary aerosurface response was dedicated to nulling  $\alpha$ -dependent evolution of the aerodynamic environment; the deflections needed to create control torques were comparatively small. In the next example, this ramping logic is removed, and the controller responds to the full step changes commanded in velocity angle. All aerosurfaces remain operational (with full deflection allowed), and the minimum-drag objective used in the last two examples is retained.

Prompt aerosurface impulses coupled with jet firings are noted in Fig. 39, producing a more immediate vehicle reaction, as seen in Fig. 40 (the vehicle response is now limited by the gains in the proportional attitude controller). Achieving this increase required the

### Example #5: Attitude Sequence, Clamp Rudder

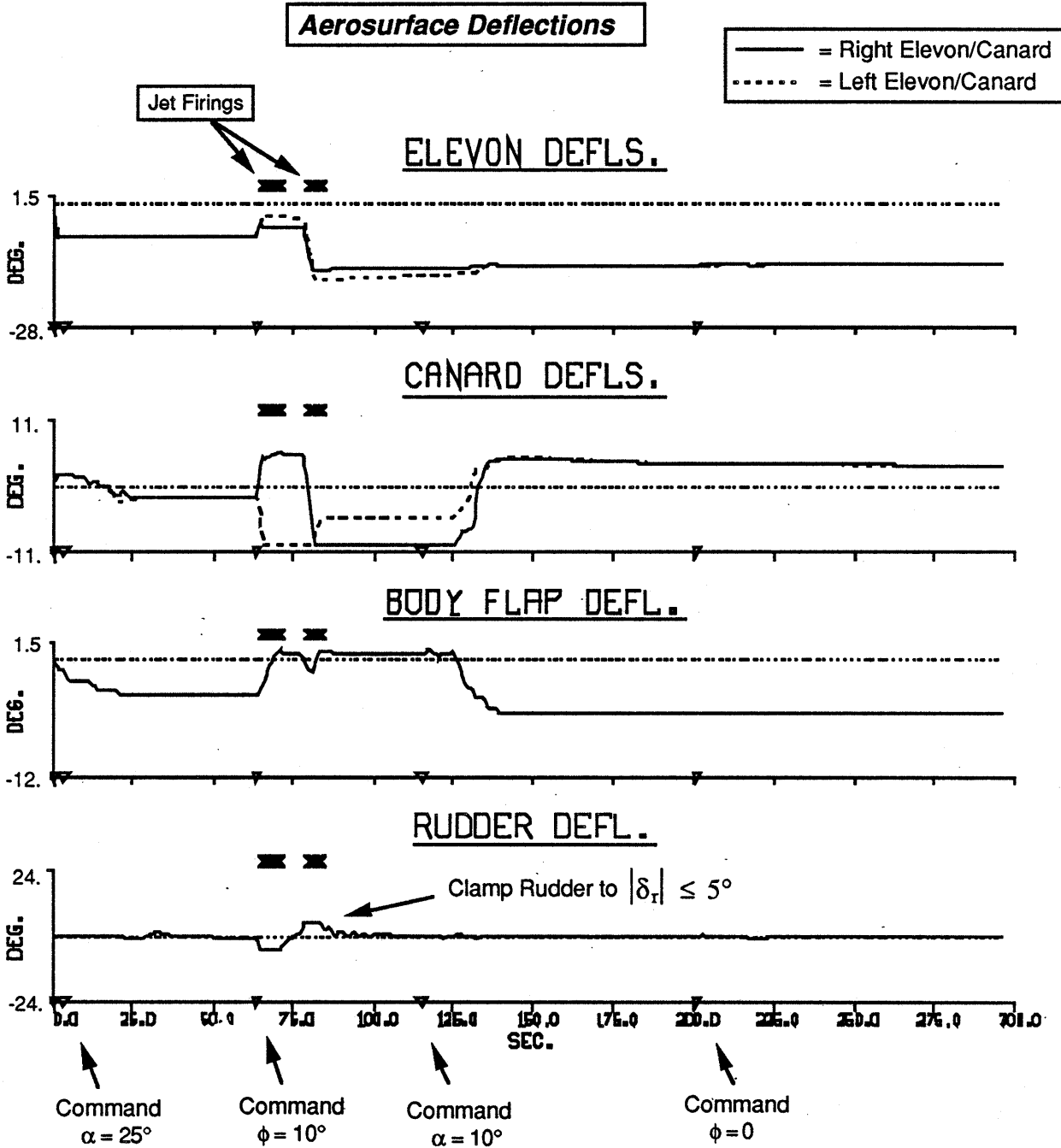


Figure 36

### Example #5: Attitude Sequence, Clamp Rudder

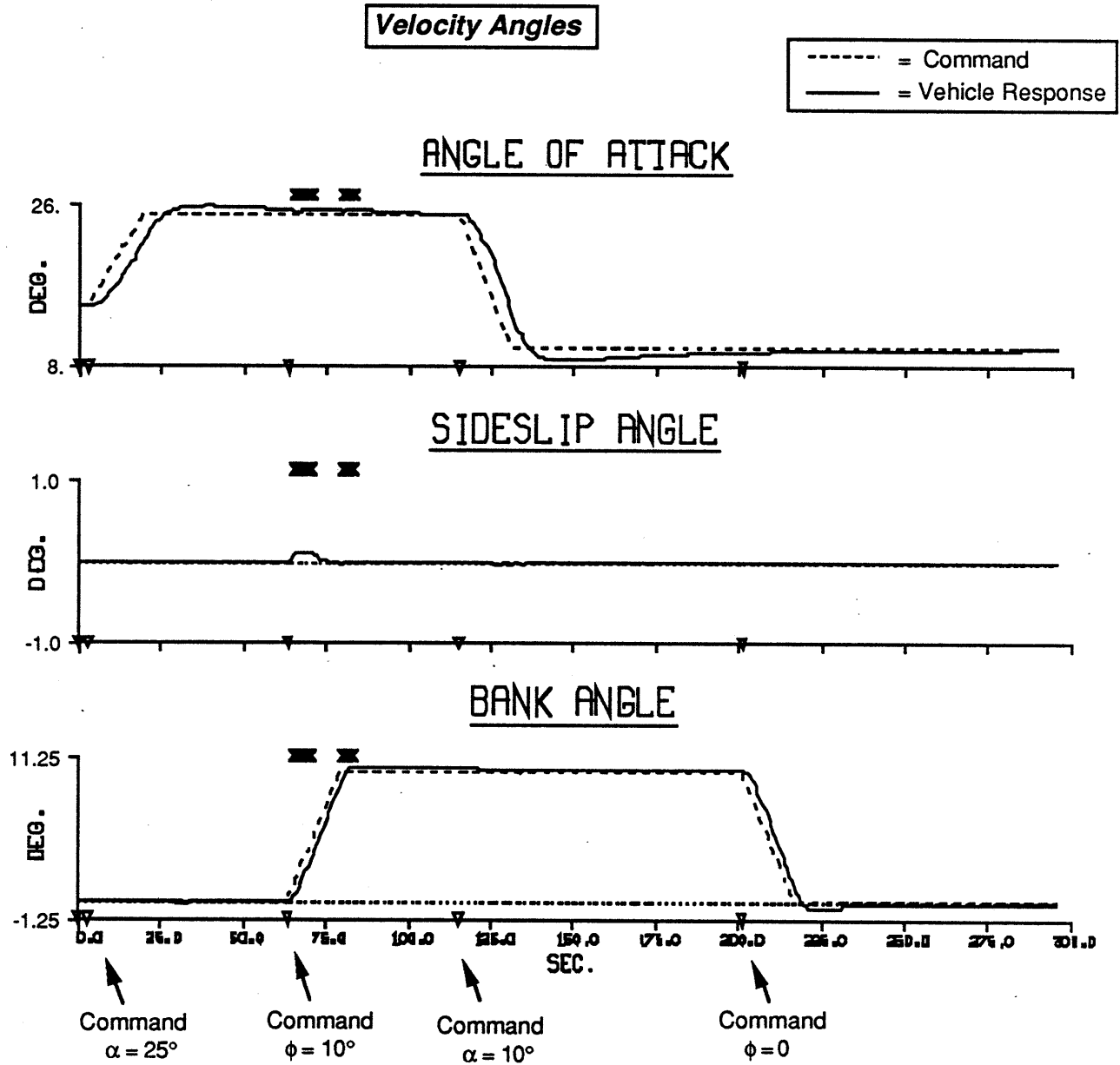


Figure 37

attainment of considerably higher vehicle rates. Although the aerosurface response (Fig. 39) is also seen to compensate changes in aerodynamic environment with  $\alpha$ , a greater transient activity occurs upon receipt of commands, as needed to create the large torques that build and remove these higher vehicle rates.

### Example #5: Attitude Sequence, Clamp Rudder

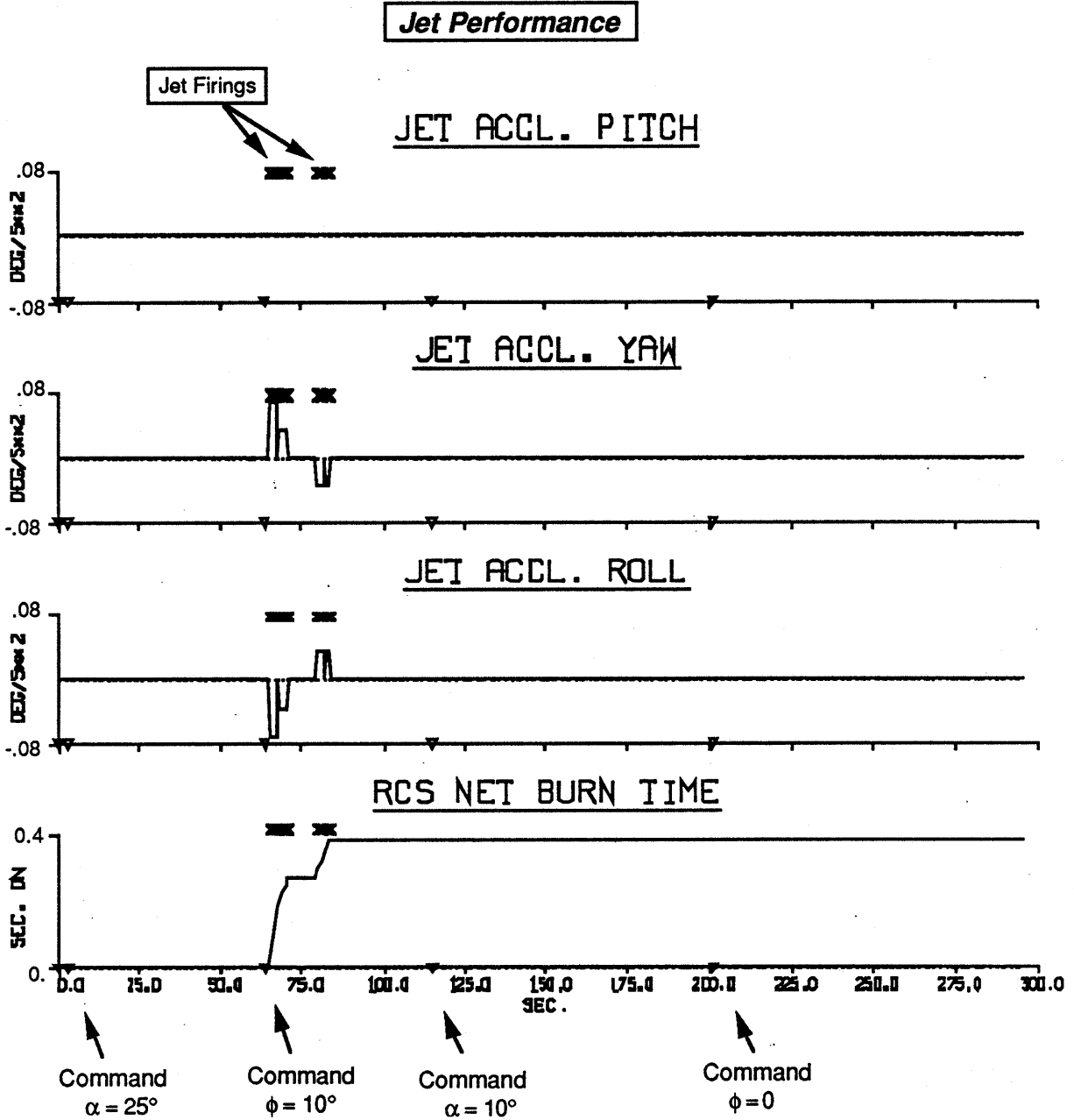


Figure 38

### Example #6: Attitude Sequence, Rapid Slew

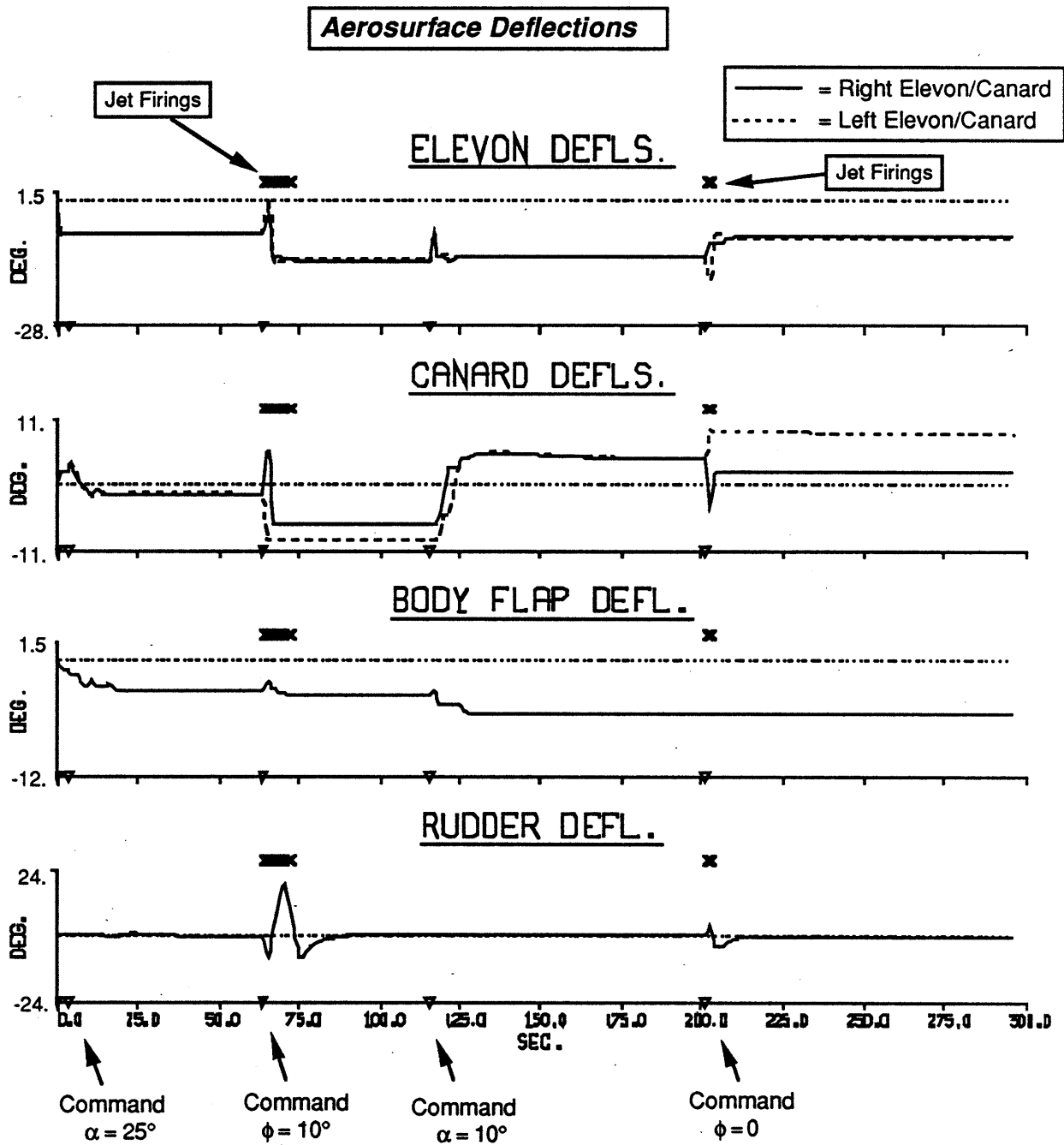
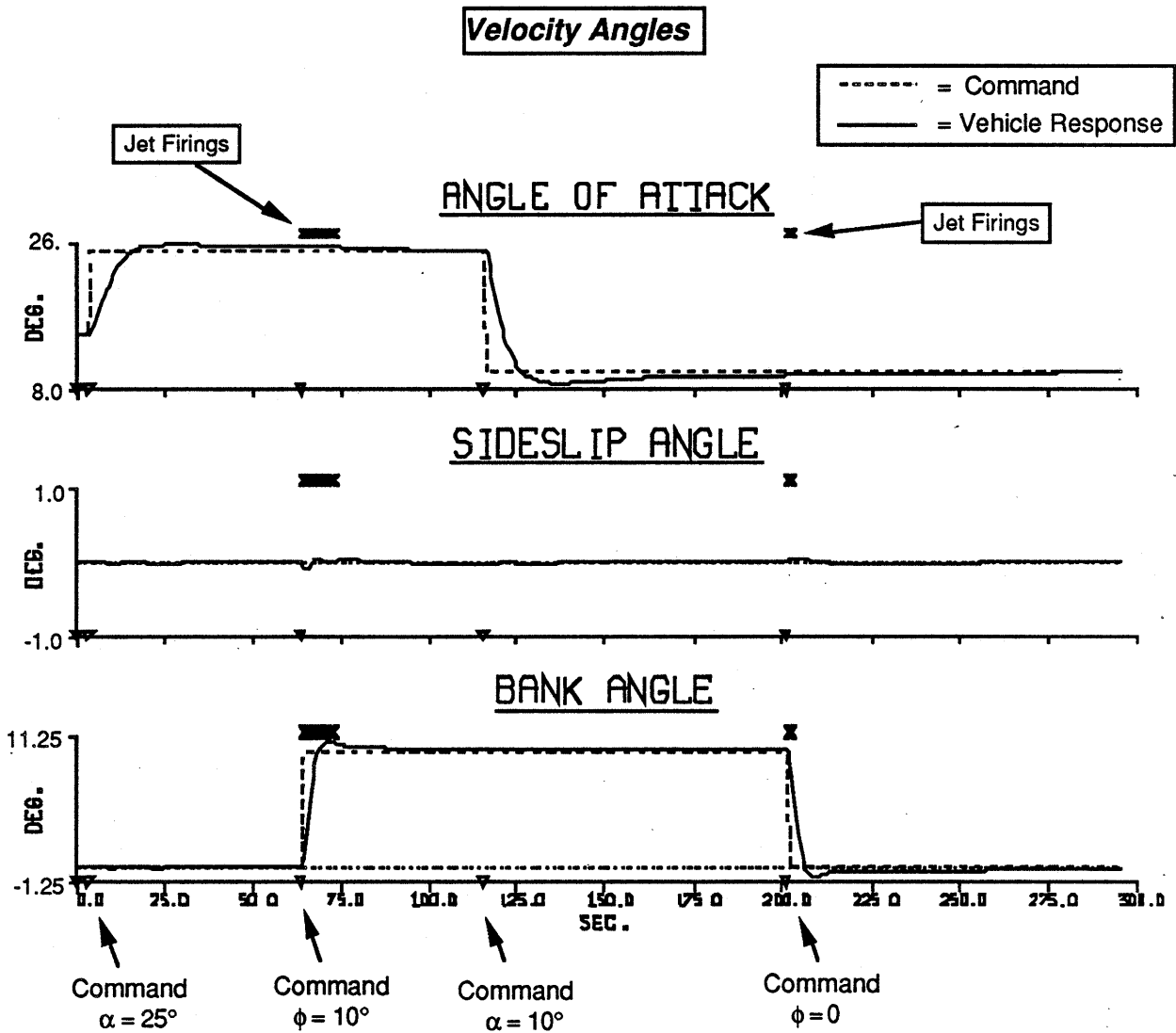


Figure 39

### Example #6: Attitude Sequence, Rapid Slew



**Figure 40**

Jet assistance is seen to be needed only at the points where bank commands are issued. The  $\alpha$  commands were realized exclusively through aerosurfaces. The plotted jet accelerations (Fig. 41) indicate that these firings were purely for roll/yaw effect (again, side-firing aft jets were picked here), as expected. Note that the later firing is much less intense (ie. briefer and involves fewer jets) than its predecessor. This is because it takes place at lower  $\alpha$ , where the rudder has much more authority, thus less jet augmentation is needed.

### Example #6: Attitude Sequence, Rapid Slew

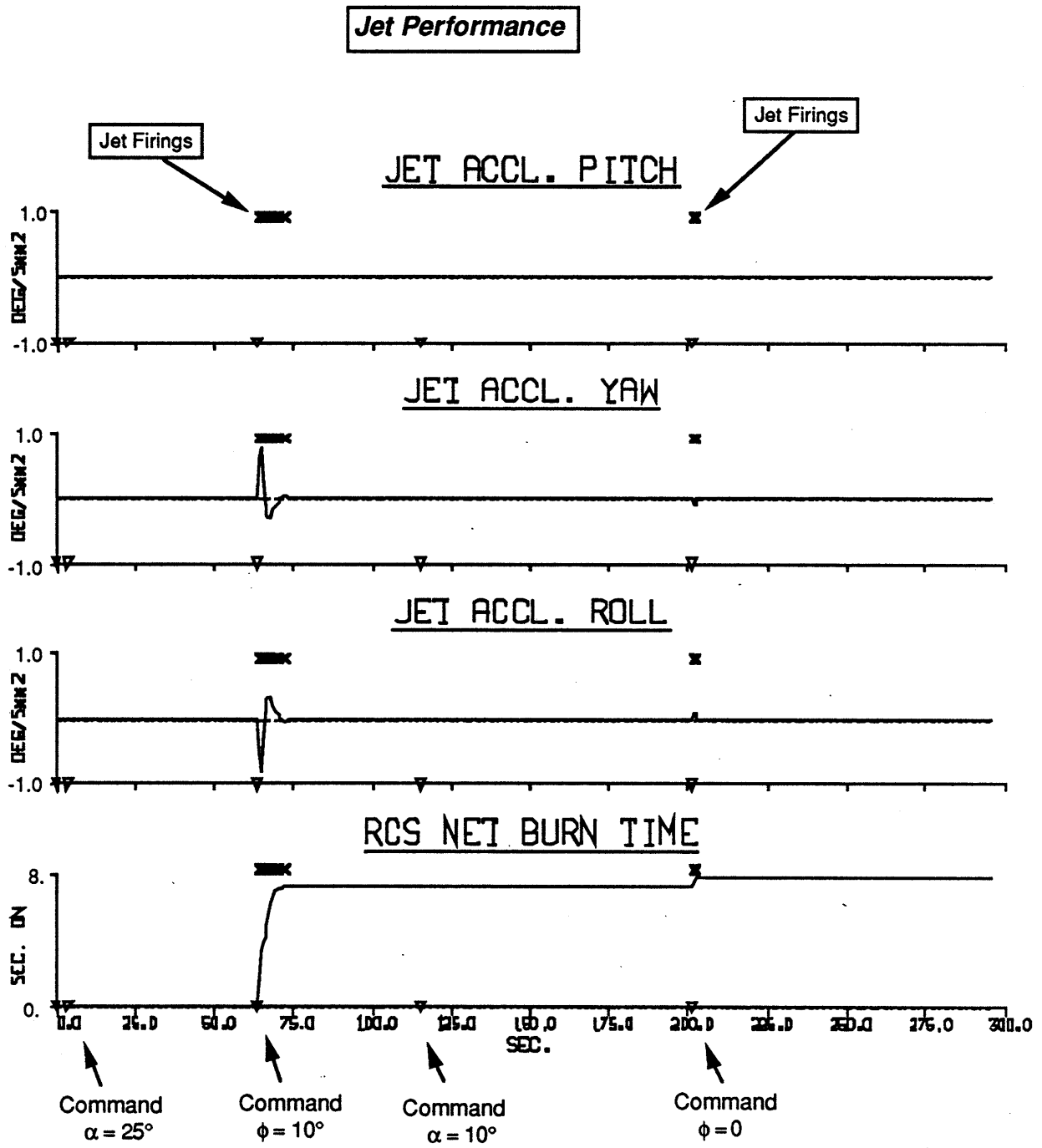


Figure 41

Although the requested accelerations are much higher in this example, extreme aerosurface activity is avoided. The upper bounds and balanced jet-to-aerosurface cost ratio defined in the hybrid selections encourage jet firings to replace frantic aerosurface deflection. This mix can be altered by adjusting the relative jet costs (or upper bounds on aerosurface response), as will be further examined in Sec. 5.3.

Notice, in Fig. 39, that the canards are left scissored at the conclusion of the test, with one remaining at relatively large deflection. Resultant roll/yaw torques are relatively minor, and are readily compensated by small rudder deflection with elevon scissoring. This is, however, a non-optimal configuration. The high canard deflection will evict a substantial stops cost contribution. The reason for this behavior may well reside in the abrupt nature of the commands answered in these examples. The large torque requests result in jet firings & fast aerosurface deflection, yet they are extraordinarily brief. This allows the system to "crystallize" into a high-cost state (some distant analogy may be made with convergence at non-optimal solutions during simulated annealing with rapid cooling; see Ref. [31]). Linear programming with mainly positive objective coefficients tends to result in a proportional response; ie. actuators are moved as little as possible to achieve small input requests. In this "benevolent" vehicle environment (with no vehicle disturbance outside of applied commands), torque requests are indeed minimal at the end of the test, allowing the canard to stay at large deflection. In a more realistic case (with continuous aerodynamic disturbance), or if negative-cost null motion were performed (as developed for CMGs in Ref. [5]), the wide canard deflection would be gradually reduced to relieve its cost penalty.

### 5.3) Examples of Direct Lift Control

The next set of examples demonstrates the ability of the linear program to intrinsically decouple actuator response along controlled axes. The vehicle is again assumed to cruise at constant altitude (125,000 ft.) and constant airspeed (Mach 8). The hybrid selection is now expanded, however, to include lift force (in stability axes), yielding direct 4-DOF (angle of attack, sideslip, bank, lift) actuator control. During the 160 sec. run, a 20° bank angle is established and removed. Two tests are presented; one controlling only vehicle rotation states, contrasted with another that also commands the vertical component of lift force to remain constant (resulting in a "flat" turn).

Actuator response is plotted for these cases in Figs. 42 and 44. Very little elevon, canard, or body flap deflection is evident in the 3-DOF example (Fig. 42). Bank is controlled primarily by rudder motion (for yaw) and small elevon/canard scissoring (for roll). An entirely different policy is pursued when lift force is also considered in the 4-DOF selection (Fig. 44). Considerable elevon, canard, and body flap deflection is now evident, presumably to neutralize the loss of vertical lift occurring during the bank maneuver. The vehicle state variables plotted in Figs. 43 & 45 indicate that this is indeed the case. In both tests, angle of attack is stabilized about 15°, sideslip stays near zero, and bank is seen to readily reach 20° and return to zero as commanded (the dashed curve represents the commanded state in these plots). A significant difference, however, is noted in the plots of vertical acceleration. A dip of approximately 4 ft/sec<sup>2</sup> occurred in the 3-DOF simulation (Fig. 43) due to rotation of the lift vector during the bank. This effect was compensated in the 4-DOF test (Fig. 45), where the lift disturbance was significantly attenuated by the additional aerosurface activity (the brief transient at the beginning of the test is due to the zero-deflection aerosurface initialization).

The ability to perform translational trim at constant angle of attack (as demonstrated above) may be very relevant for a NASP-type vehicle, where, for instance, tight restrictions on  $\alpha$  may be necessary to meet engine airflow requirements during ascent. Other unique flight modes can be explored via this technique of translational decoupling; ie.  $\alpha$  can be allowed to vary over a limited range, while the actuators intrinsically compensate changes in vertical lift to maintain level flight. Again, the small translational actuator authority (relative to the large aerodynamic forces exerted on the net airframe) may limit the useful range of this strategy; its primary application may be in applying a desired vernier "trim" to the vehicle state. Actuator translation may also be exploited via the objective formulation, as illustrated in Example #12 of Sec. 5.4.

### Example #7: Bank Sequence, No Vertical Lift Control

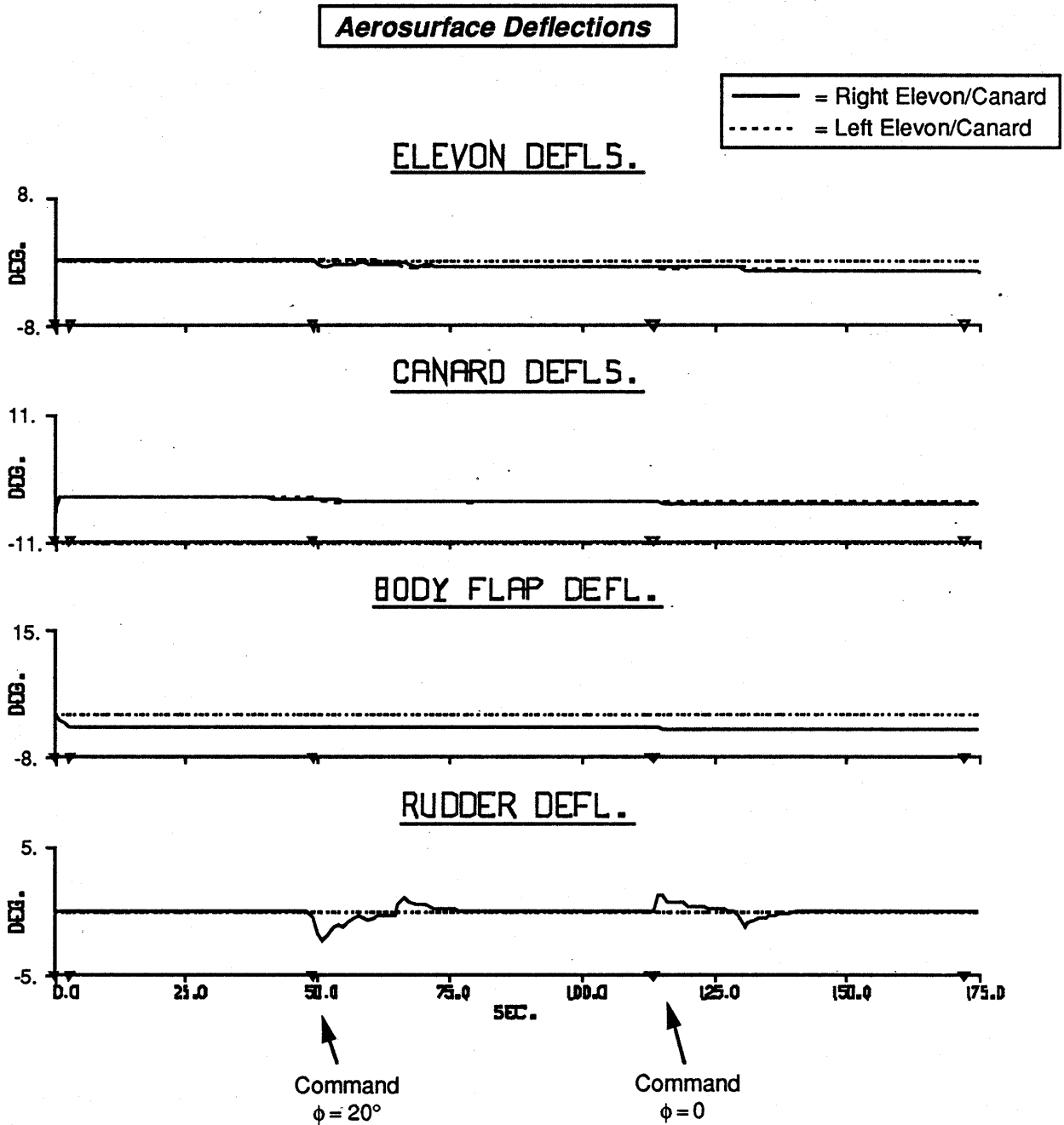


Figure 42

# Example #7: Bank Sequence, No Vertical Lift Control

## Velocity Angles & Vertical Acceleration

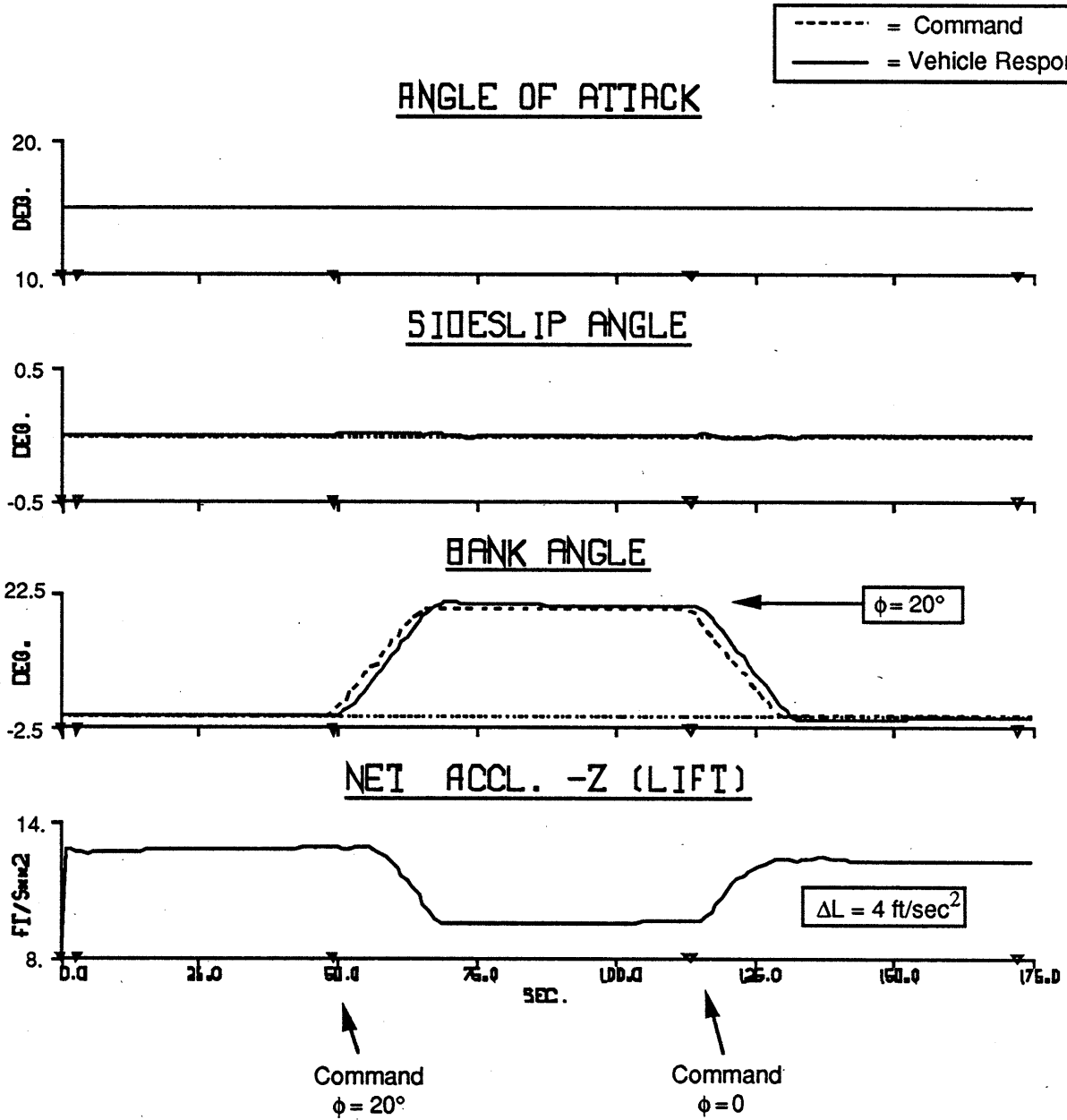


Figure 43

### Example #8: Bank Sequence, Hold Constant Vertical Lift

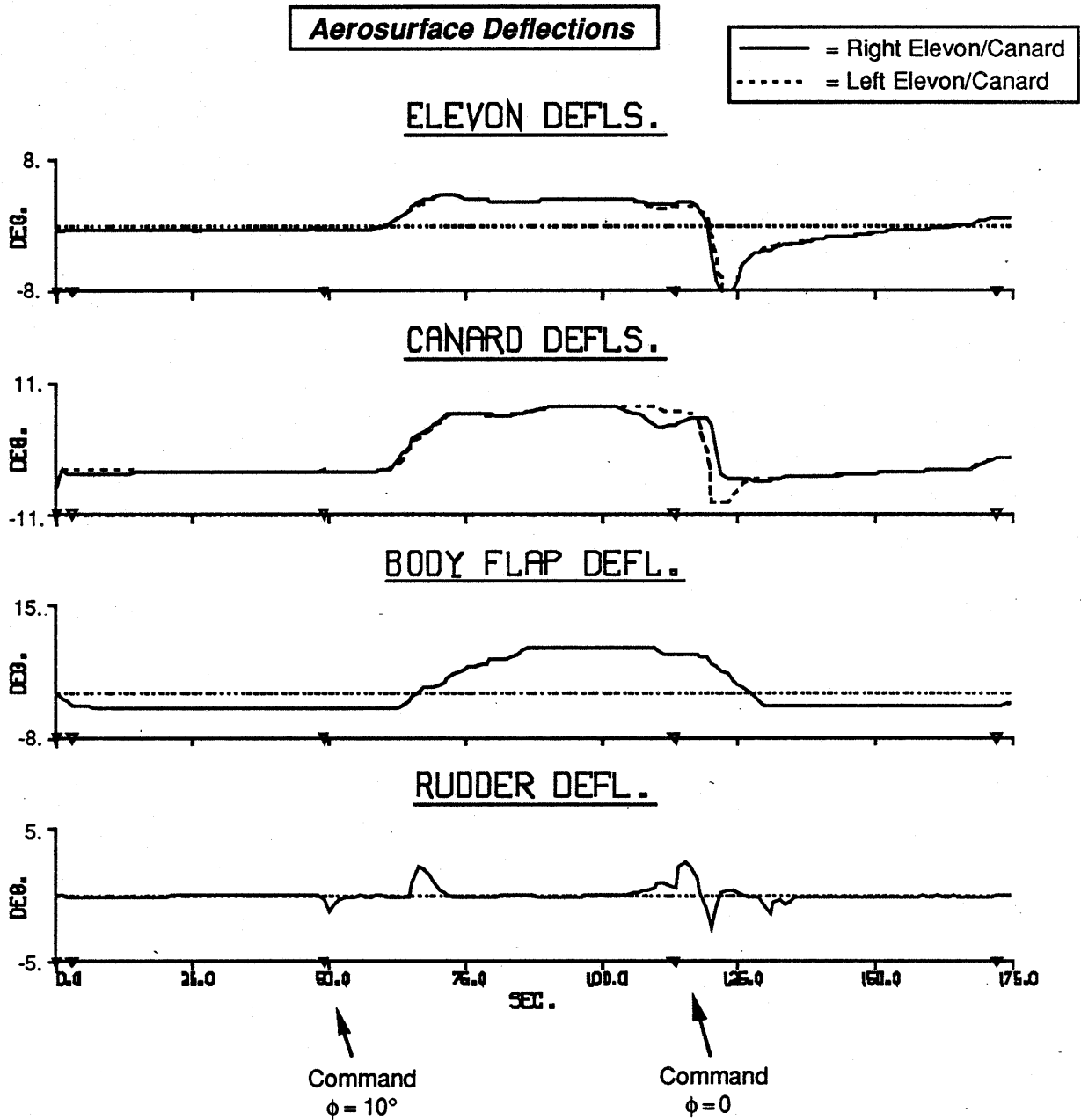


Figure 44

# Example #8: Bank Sequence, Hold Constant Vertical Lift

## Velocity Angles & Vertical Acceleration

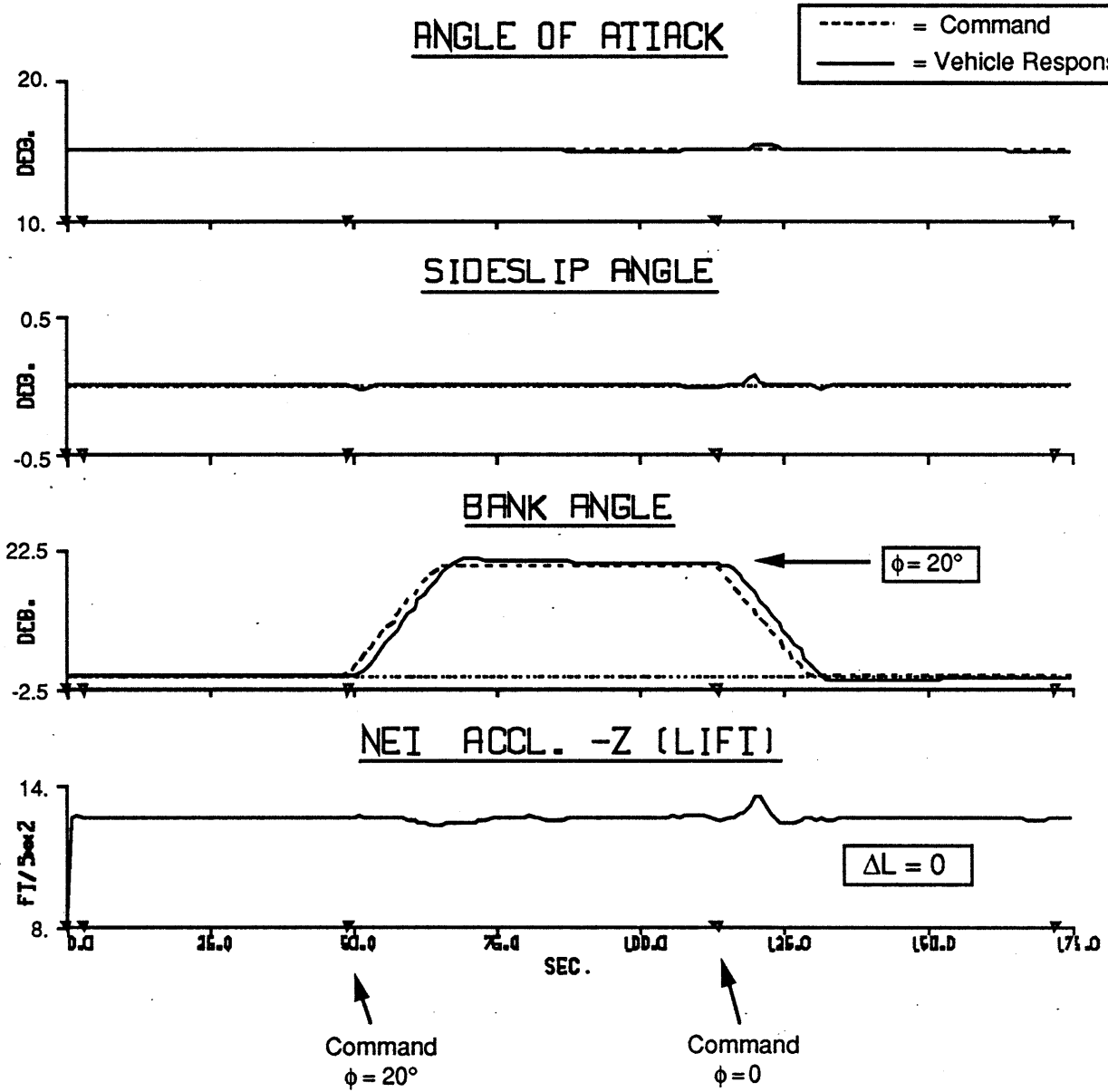


Figure 45

## 5.4) Re-entry Simulations

The examples examined in this section simulate a vehicle re-entry from 170,000 ft. at Mach 12 through approximately 20,000 ft. at 500 ft/sec. In addition to depending on angle of attack, sideslip, and aerosurface deflection, the vehicle environment and aerosurface authorities are now made to vary with vehicle altitude and airspeed (in accordance with Sec. 3.2). Modelled translational forces are now integrated in the vehicle environment in order to dynamically update the vehicle position and velocity. Angle of attack and vehicle bank are commanded via the translational controller of Figs. 20 & 21, or driven by an attitude sequencer following the  $\alpha$ -profile of Fig. 22. Sideslip is held at zero. Scheduled altitude vs. Mach data are obtained from Shuttle entry profiles (Sec. 4.2) for longitudinal control. Dynamic pressure varies between approximately 150  $\rightarrow$  360 lb/ft<sup>2</sup> throughout the re-entry. Aerosurface plots are now all scaled to their maximum allowed deflections. The speedbrake angle is not shown unless it is actually deflected.

The first test assumes the longitudinal controller to be driven by the sequenced  $\alpha$ -profile; the longitudinal translation feedback of Fig. 21 is disabled. The lateral control logic drives  $\phi$  to keep side position zero. A "nominal" vehicle status is assumed; ie. objective weights and upper bounds are at their standard values, and all actuators are operational throughout the simulation. Actuator drag and lift are not considered in the objective function; only angle & stops contributions are present.

Aerosurface deflections are shown in Fig. 46, jet accelerations in Fig. 47, and velocity attitudes in Fig. 48. The "x" marks drawn at left on these plots indicate that jets are required at high  $\alpha$ ; hybrid operation continues until  $\alpha$  drops below roughly 25°, and the rudder gains yaw authority. The vehicle is seen to precisely follow the commanded  $\alpha$  profile (the dashed curve representing the commanded  $\alpha$  state in Fig. 48 is almost completely overdrawn by the solid curve representing the vehicle response). Sideslip and bank are kept near zero, excepting the disturbance caused when passing through Mach 1 at roughly 720 sec. into the run, where the modelled vehicle aerodynamics are subject to rapid change.

The jet accelerations (Fig. 47) show primarily roll/yaw lateral firings (again, aft side-firing jets are preferred due to their lower cost, as in the previous section). Very limited aerosurface activity is evident during jet firings in Fig. 46, primarily because of the relatively low jet costs. Some elevon & canard deflection is performed (to balance pitch torques) and limited canard scissoring and rudder deflection are attempted for lateral control. This latter function is mainly performed via jet firings until the rudder attains sufficient authority. The granularity due to the minimum jet firing duration is highly significant in the jet response of Fig. 47, contributing to the

**Example #9: Re-Entry, Schedule  $\alpha$ : Low Jet Cost**

**Aerosurface Deflections**

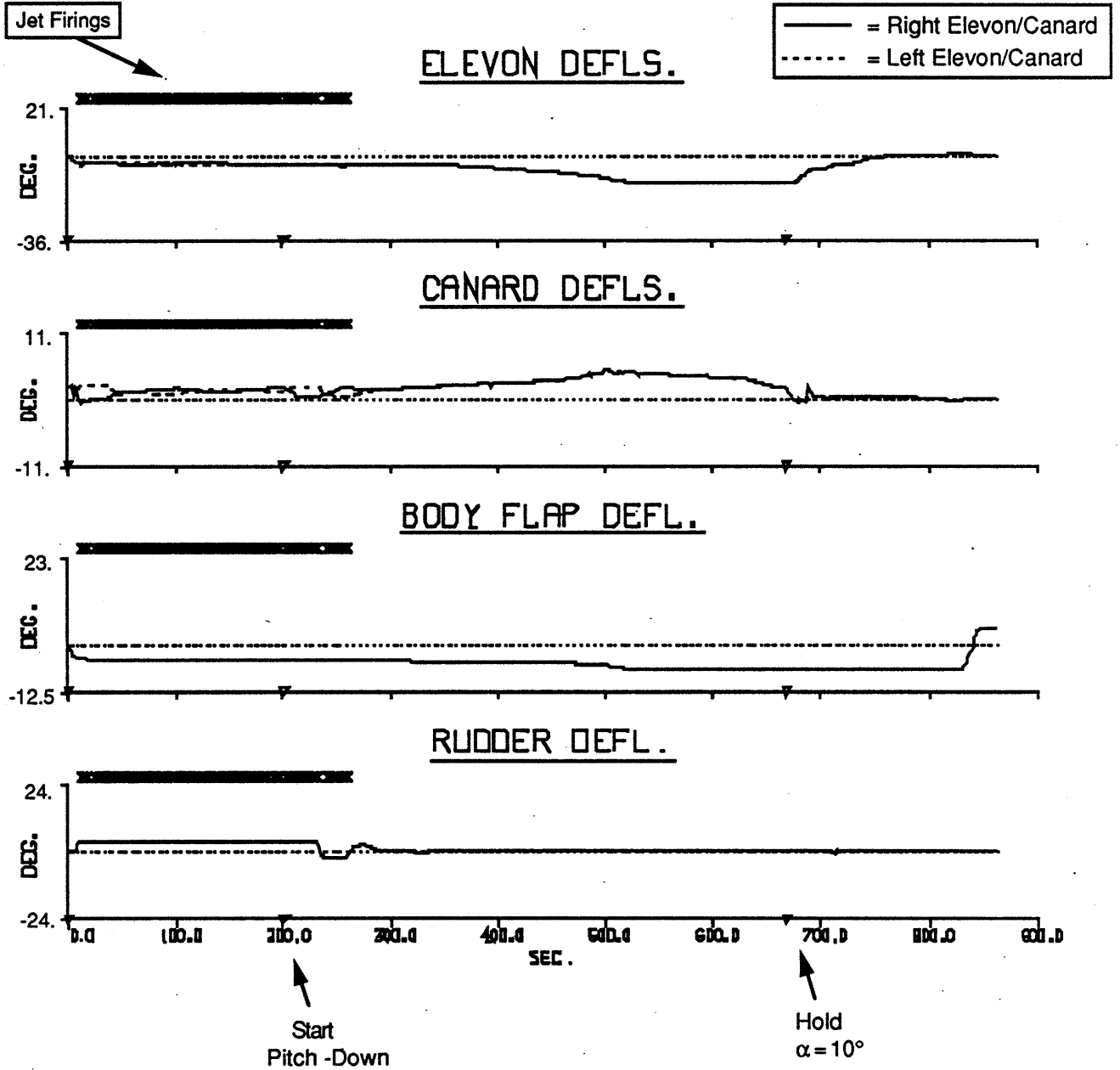


**Figure 46**

**Example #9: Re-Entry, Schedule  $\alpha$ : Low Jet Cost**

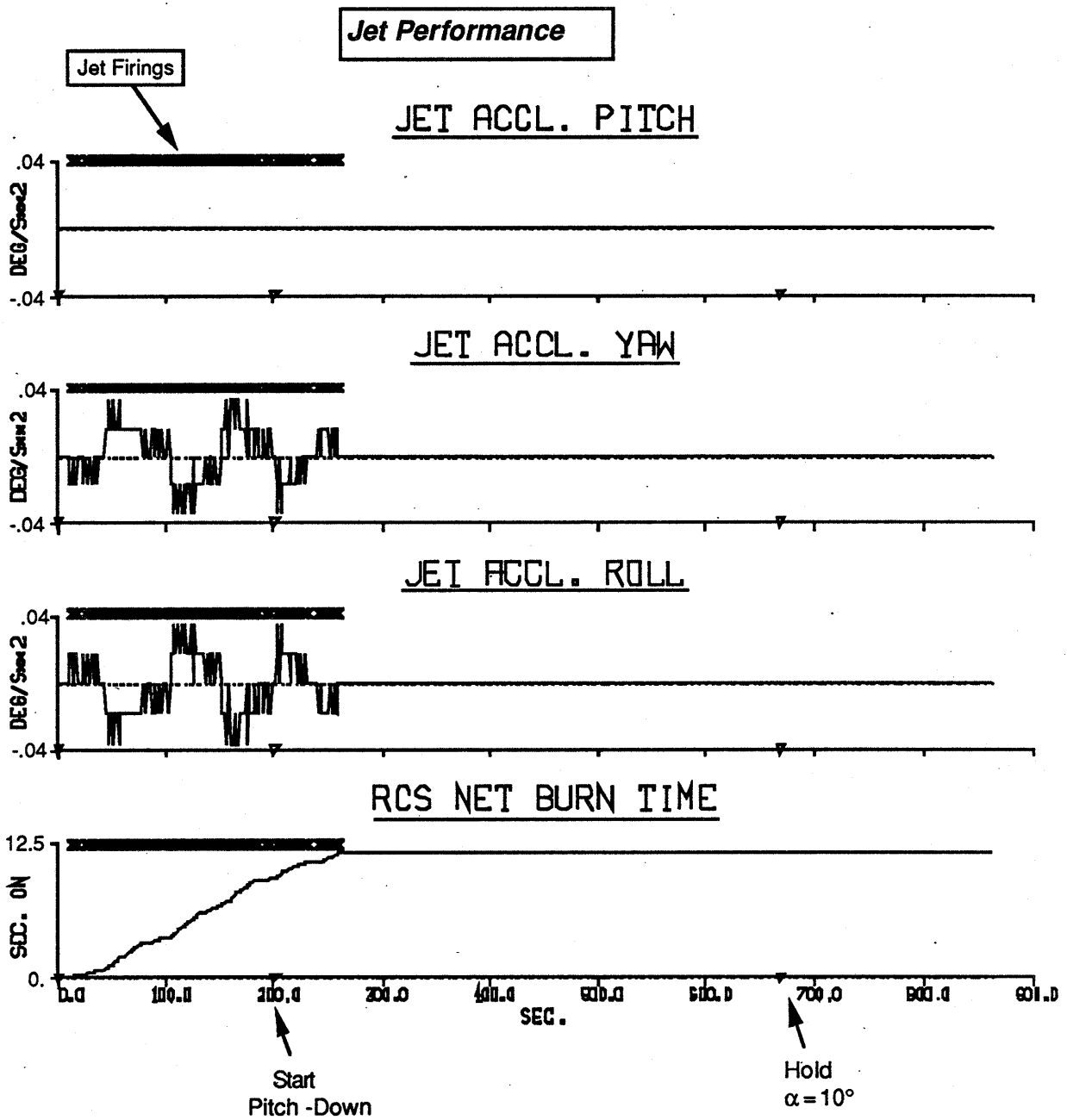


**Figure 47**

**Example #9: Re-Entry, Schedule  $\alpha$ : Low Jet Cost**

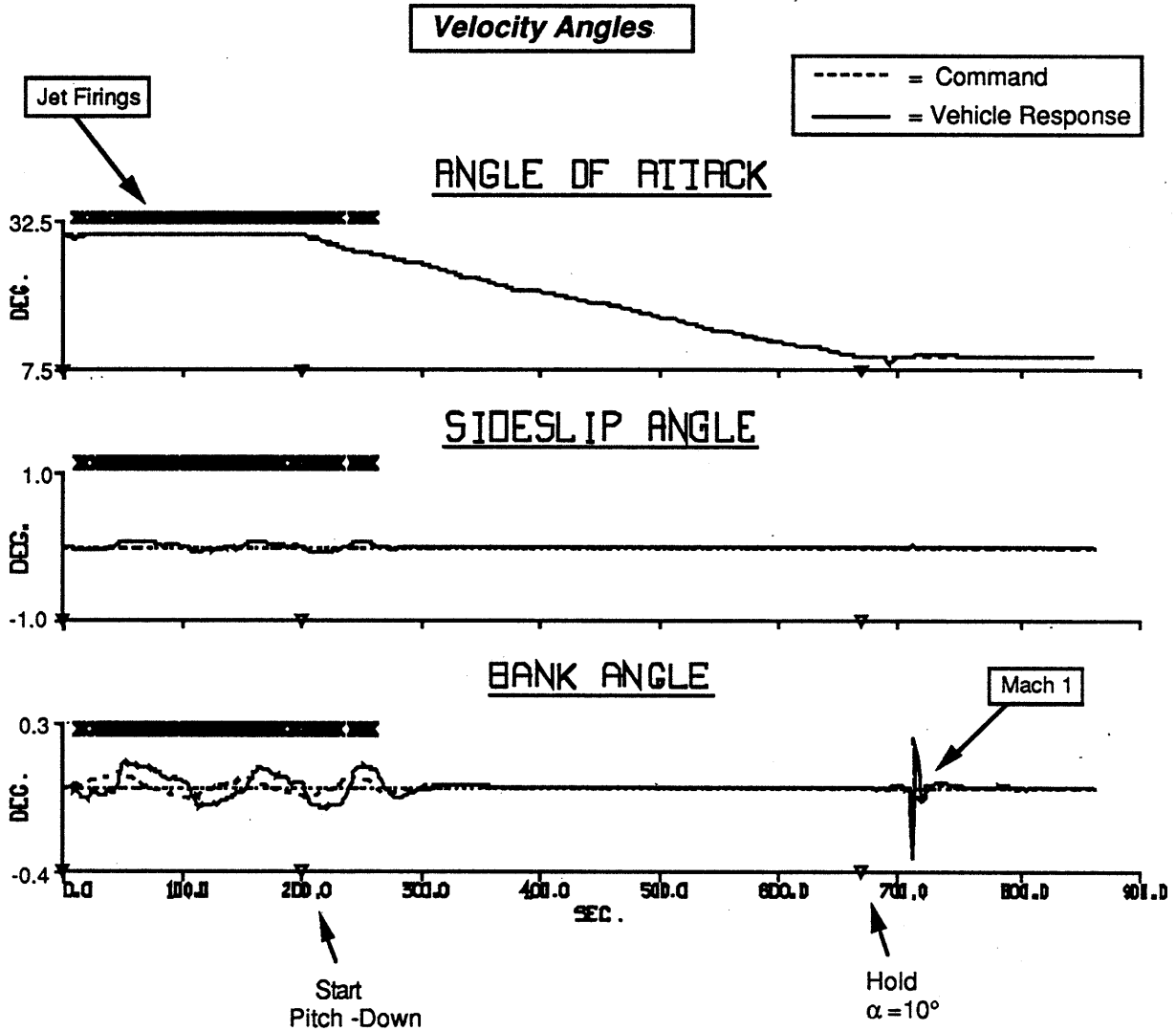


**Figure 48**

sideslip and bank limit cycling evident in Fig. 48 during the hybrid maneuver phase. Note that the pattern of jet firings plotted in Fig. 47 indicate a yaw limit cycle; by introducing hysteresis through a yaw phase-plane controller (proposed in Sec. 4.2), the multitude of small firings exhibited here could be replaced with fewer discrete firings of larger magnitude.

Aerosurfaces are seen to systematically deflect throughout the test to offset the gradual evolution in aerodynamic environment with changing  $\alpha$  and Mach number (excepting more rapid response needed during hybrid maneuvers and near Mach 1). Minimal aerosurface deflections are needed to start and stop the vehicle pitch-down at  $t = 200$  &  $t = 675$  sec. (the resultant  $\alpha$  rate is very small); most aerosurface activity evident in Fig. 46 is specified to dynamically compensate

**Example #9: Re-Entry, Schedule  $\alpha$ : Low Jet Cost**

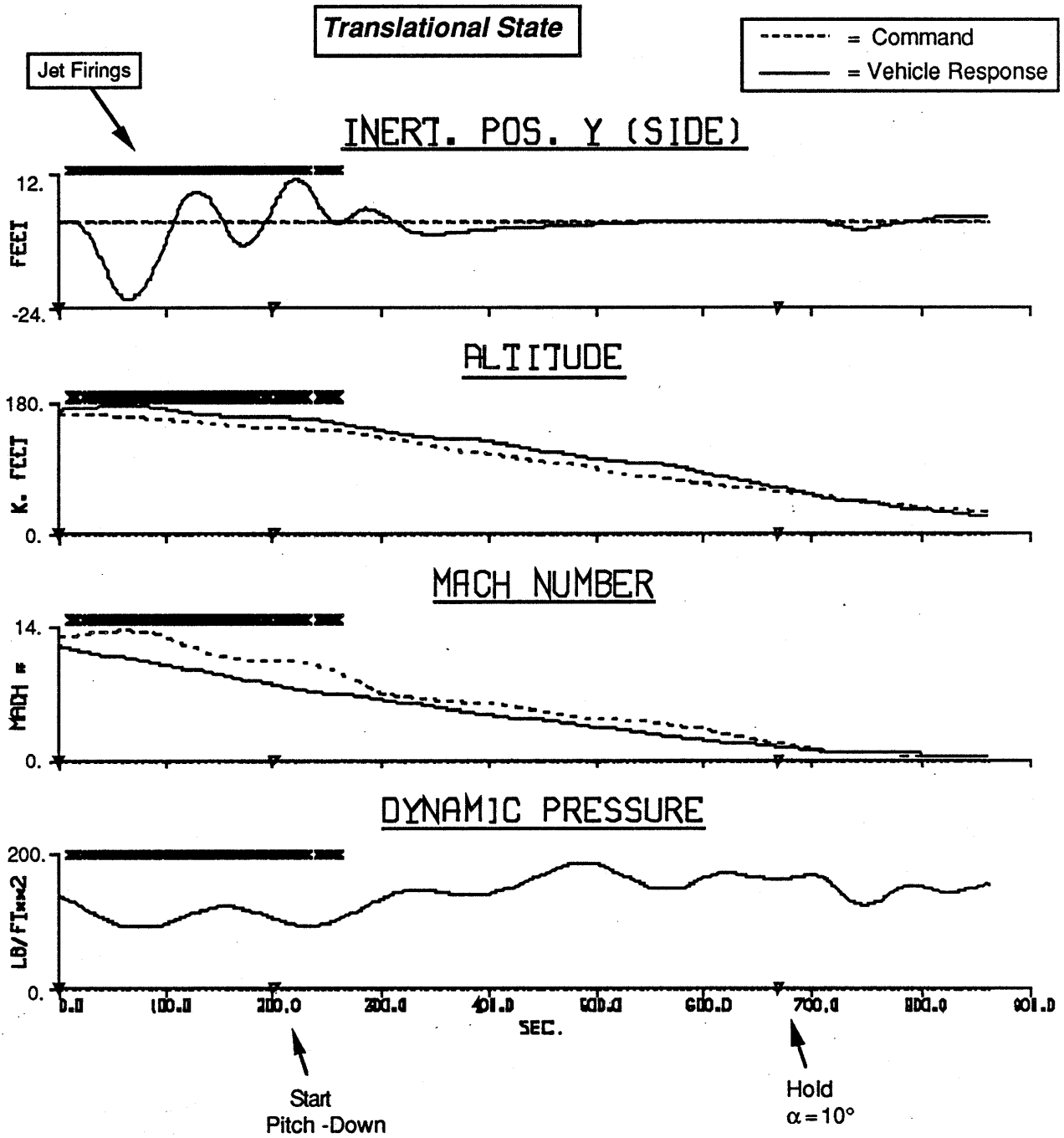


**Figure 49**

state-dependent body torques.

The body flap is seen to systematically deflect up in an effort to unload the elevons. Note the manner in which the body flap deflection switches sign in correspondence with the change in combined elevon and canard polarities at the conclusion of the test. Because the speedbrake was kept at zero deflection, its plot is not presented.

Translational quantities and dynamic pressure are plotted in Fig. 49. Altitude and Mach number are seen to smoothly decrease. The dotted line on these plots is the target state determined through the data of Fig. 23; since the translational controller is not engaged in this test, this state is not tracked. The small oscillations in altitude (hence also desired Mach # through Fig. 23) prevalent at the start of the test (ie. at high  $\alpha$ ) are due to excitation of the vehicle phugoid mode. Side position is seen to closely track zero, and the lateral controller rejects small disturbances encountered during hybrid maneuvers and during passage through Mach 1. Dynamic pressure is seen to slowly climb with descending altitude; the gradual variations are due to longitudinal oscillation driven by the phugoid effect.

The hybrid activity occurring in this test specified a minimal amount of aerosurface activity. The upper & lower bounds and objective factors imposed on the aerosurface decision variables prevented excessive displacement and "flailing" of aerosurfaces in hybrid solutions. The next two examples attempt to illustrate the control provided by the objective function over the participation of various actuators in hybrid maneuvers.

In the next test, aerosurface costs were increased (by roughly a factor of 5) relative to jet costs in hybrid maneuvers; otherwise conditions were identical. Results are plotted in Figs. 50-52.

Aerosurfaces are now seen to be significantly more involved in hybrid maneuvers (Fig. 50). The canard plot indicates that jets are used primarily for yaw control; the obvious canard scissoring during jet firings is an attempt to cancel jet roll residuals and glean additional yaw authority through elevon/canard differential aileron deflection. The coordination between canard scissoring and jet firings is evident when comparing aerosurface deflections in Fig. 50 with the lateral jet accelerations in Fig. 51 (again, mainly side-firing aft jets are chosen). In between jet firings, Fig. 50 indicates frenetic low-level elevon/canard/rudder activity in an attempt to balance yaw torques and maintain lateral control with marginal yaw authority. This was performed nearly exclusively with jets in the previous example, but aerosurfaces are now preferred due to their lower cost. This has indeed resulted in a potential saving of "fuel"; the net jet firing time is now roughly 30% lower than expended in the previous test. This fuel savings, however, comes at the price of a slightly noisy aerosurface response at high  $\alpha$ .

After  $\alpha$  is decreased later in the test, jets are no longer needed, and the aerosurface profile is very similar to the results of the previous example. Velocity angles (Fig. 52) follow commands, with sideslip remaining near zero and bank (affected slightly by the noisy high- $\alpha$  activity) being

**Example #10: Re-Entry, Schedule  $\alpha$ : Moderate Jet Cost**

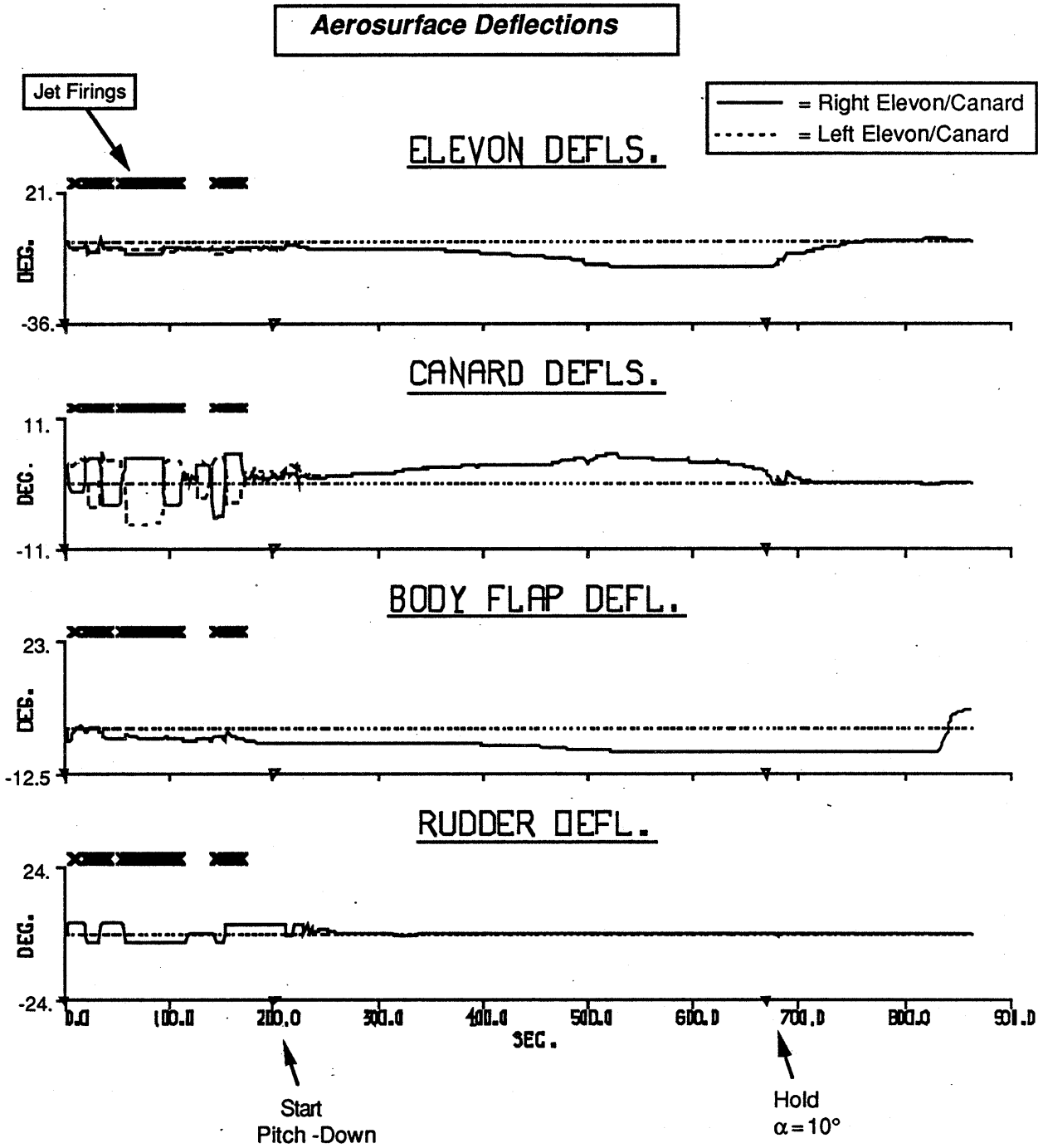


**Figure 50**

**Example #10: Re-Entry, Schedule  $\alpha$ : Moderate Jet Cost**

**Jet Performance**

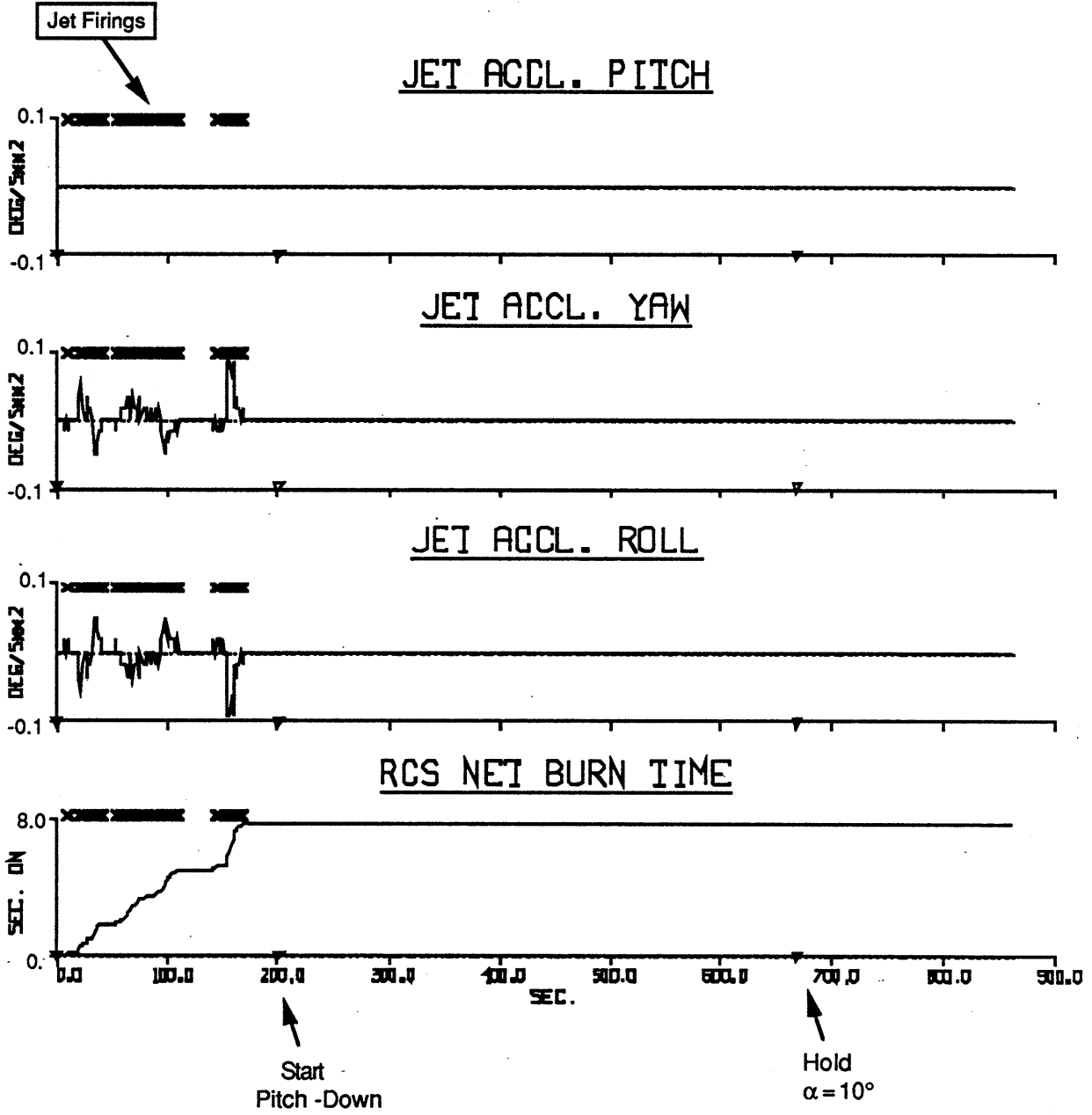


**Figure 51**

**Example #10: Re-Entry, Schedule  $\alpha$ : Moderate Jet Cost**

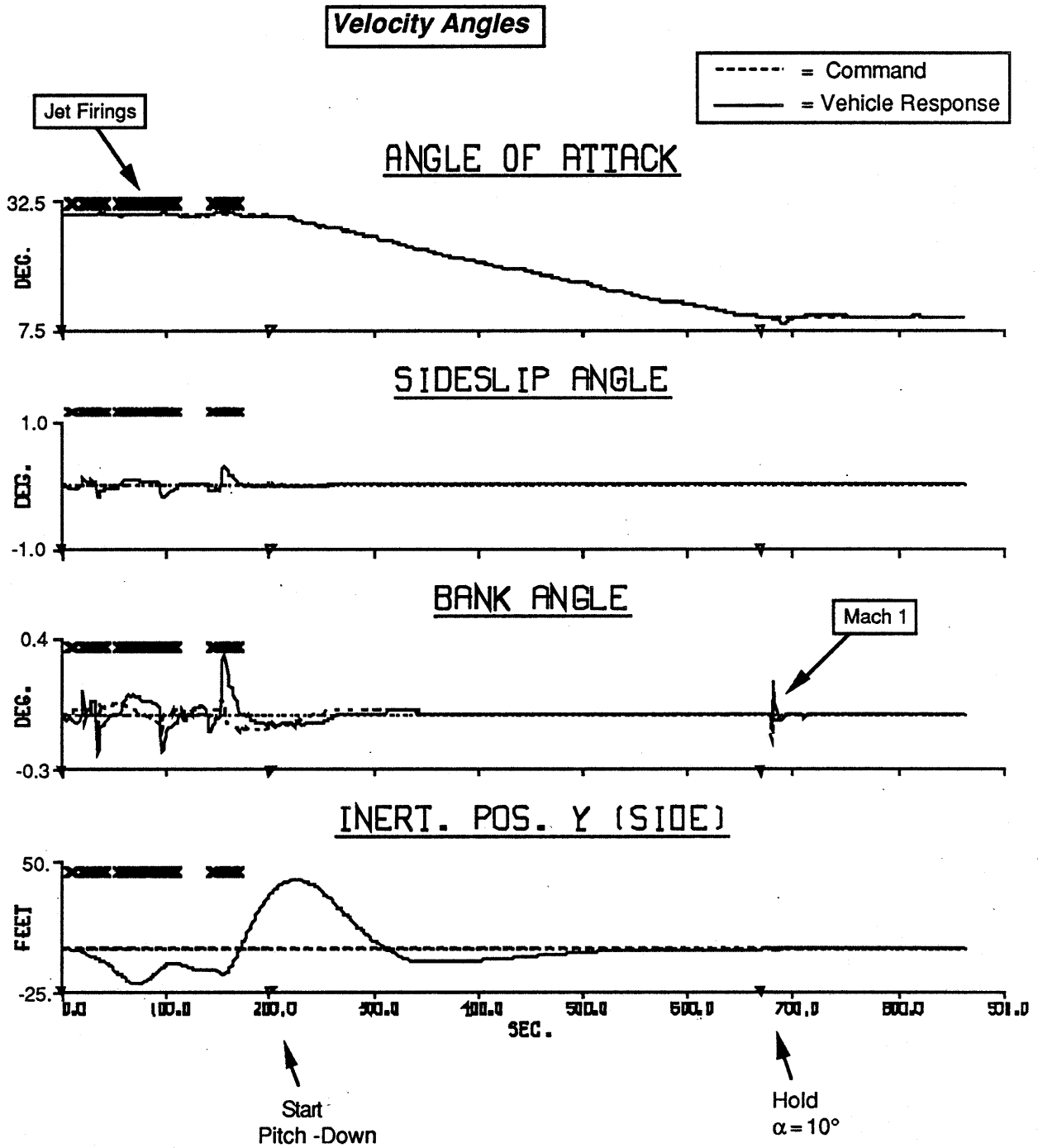


**Figure 52**

adjusted to null side position error (Fig. 52). The vehicle altitude, Mach #, and dynamic pressure behave similarly to the previous results (Fig. 49), thus are omitted in this example.

By further decreasing the relative aerosurface costs, the trend to substitute aerosurface activity for jet firings will continue. The next example is run under identical assumptions, except the jet costs are increased by a factor of 2500 over the values used in the previous test.

The aerosurface response, shown in Fig. 53, indicate that this is an extreme case. The lower cost of aerosurfaces has indeed increased their participation in hybrid maneuvers. Much more aerosurface activity is evident during jet firings; in fact, the rudder, elevons, and canards are often seen to approach maximum limits, in spite of the stops contribution of Eq. 5. Relative costs are sufficiently low to specify some speedbrake activity, as seen in Fig. 45 (this plot is not scaled to the speedbrake maximal spread of  $87.2^\circ$ ; this activity is still minimal). After jets cease firing and the rudder engages at lower  $\alpha$ , aerosurface activity is much calmer, and the remainder of the run is similar to the previous examples.

The jet torques plotted in Fig. 54 again indicate yaw firings. Since aerosurface participation is encouraged by virtue of their lower cost, one would expect reduced jet activity. This does not appear to be the case here; jets fire frequently, and the mean thrust levels are nearly an order of magnitude larger in this example. This is due to nonlinear aerosurface effects; a small yaw authority is attempted to be gleaned through large deflections (in the absence of jets), which produces a sizable error that eventually requires a significant jet firing to compensate. This inefficiency also leads to substantially increased fuel consumption (in comparison to the data of Figs. 47 & 51). Obtaining optimal hybrid performance with both actuator families is clearly a function of adjusting their objective factors and upper bounds to reflect their physical limitations and the accuracies of linear approximations.

Velocity angles and side position are plotted in Fig. 55. Aside from greater noise during the hybrid operation, the vehicle is seen to appropriately track the target state. The plots of longitudinal state and dynamic pressure are omitted, since their appearance is similar to the previous results (eg. Fig. 49).

In the next example, the longitudinal translation state error (ie. error in altitude and Mach #) is allowed to enter the vehicle cost calculation via Eq. 38. The needed lift and drag amplitudes were derived via the altitude and Mach errors only; the derivative and integral compensation terms in Eq. 36 were not considered in forming Eq. 38. The " $K_{\min}$ " factor in Eq. 38 has been reduced by 70% in this example to bring the costs of favorable aerosurface motion negative and entice selection of the corresponding activity vectors. The commanded  $\alpha$ -profile has been adapted slightly from the previous example to better track the desired longitudinal translation state. The vehicle is initialized at  $\alpha = 27^\circ$ , but is immediately commanded to hold  $\alpha = 20^\circ$  until the airspeed drops below Mach 9, at which point  $\alpha$  is commanded to gradually ramp down to  $\alpha = 10^\circ$  (as

**Example #11: Re-Entry, Schedule  $\alpha$ : High Jet Cost**

**Aerosurface Deflections**

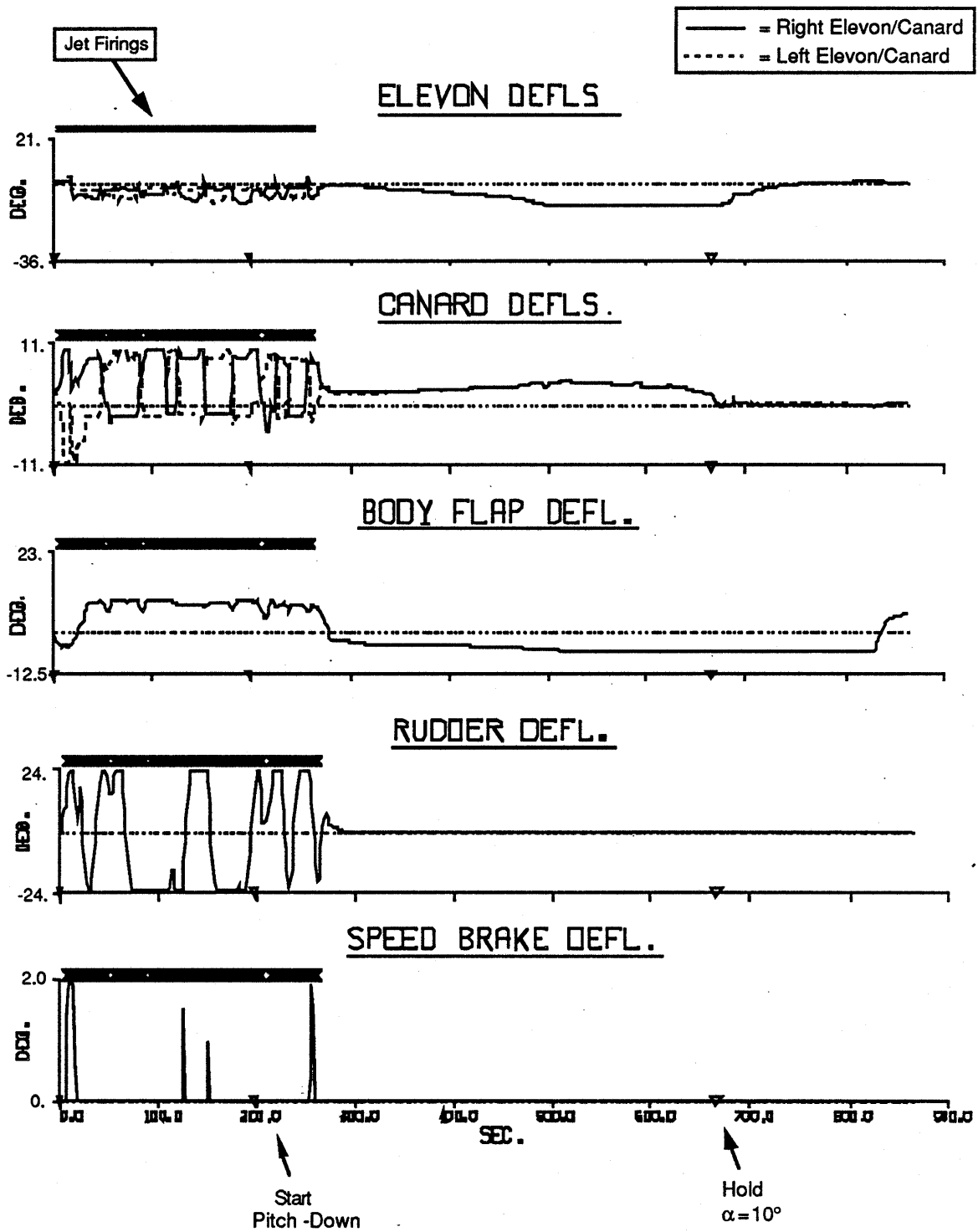


**Figure 53**

**Example #11: Re-Entry, Schedule  $\alpha$ : High Jet Cost**

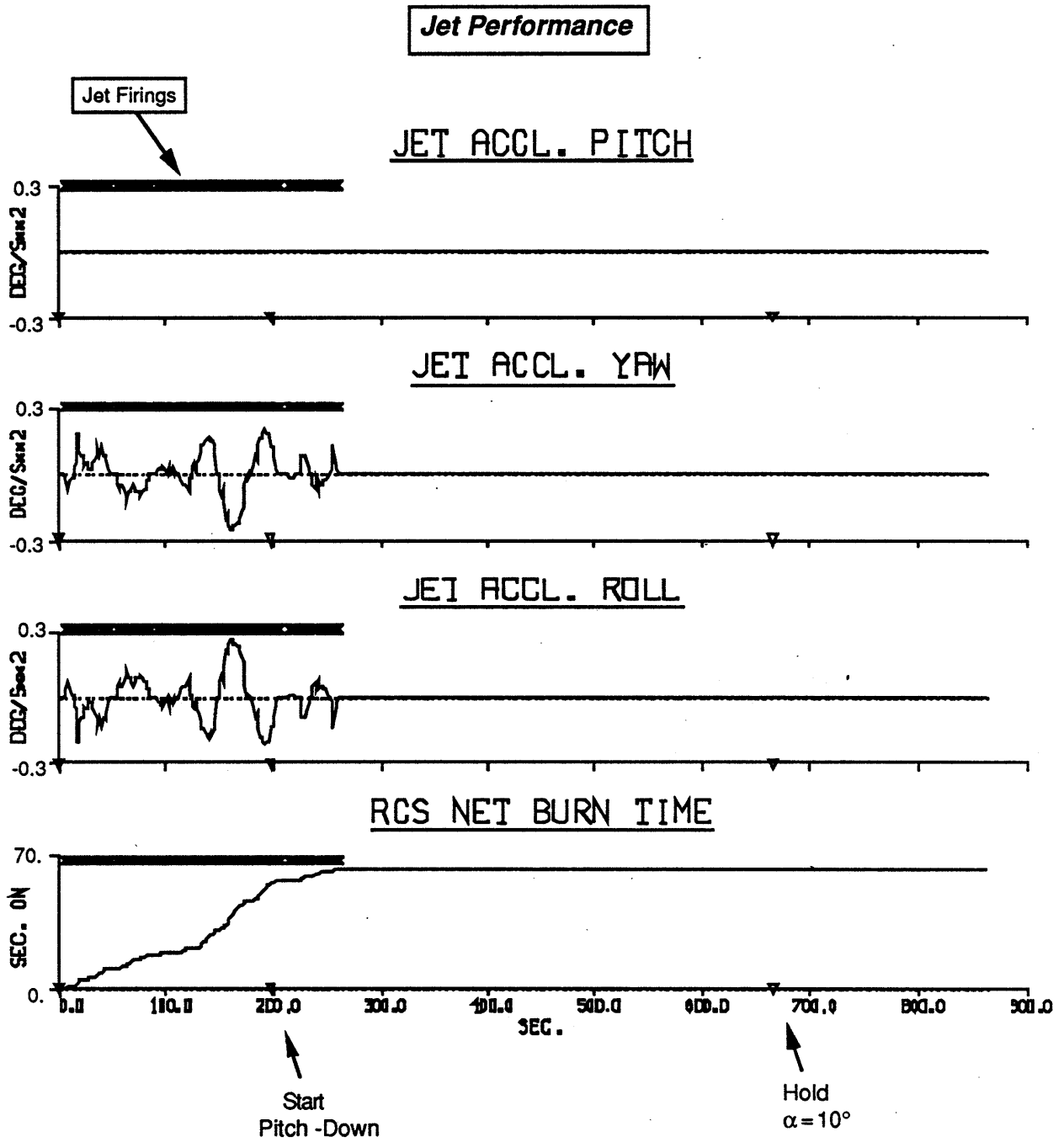


**Figure 54**

**Example #11: Re-Entry, Schedule  $\alpha$ : High Jet Cost**

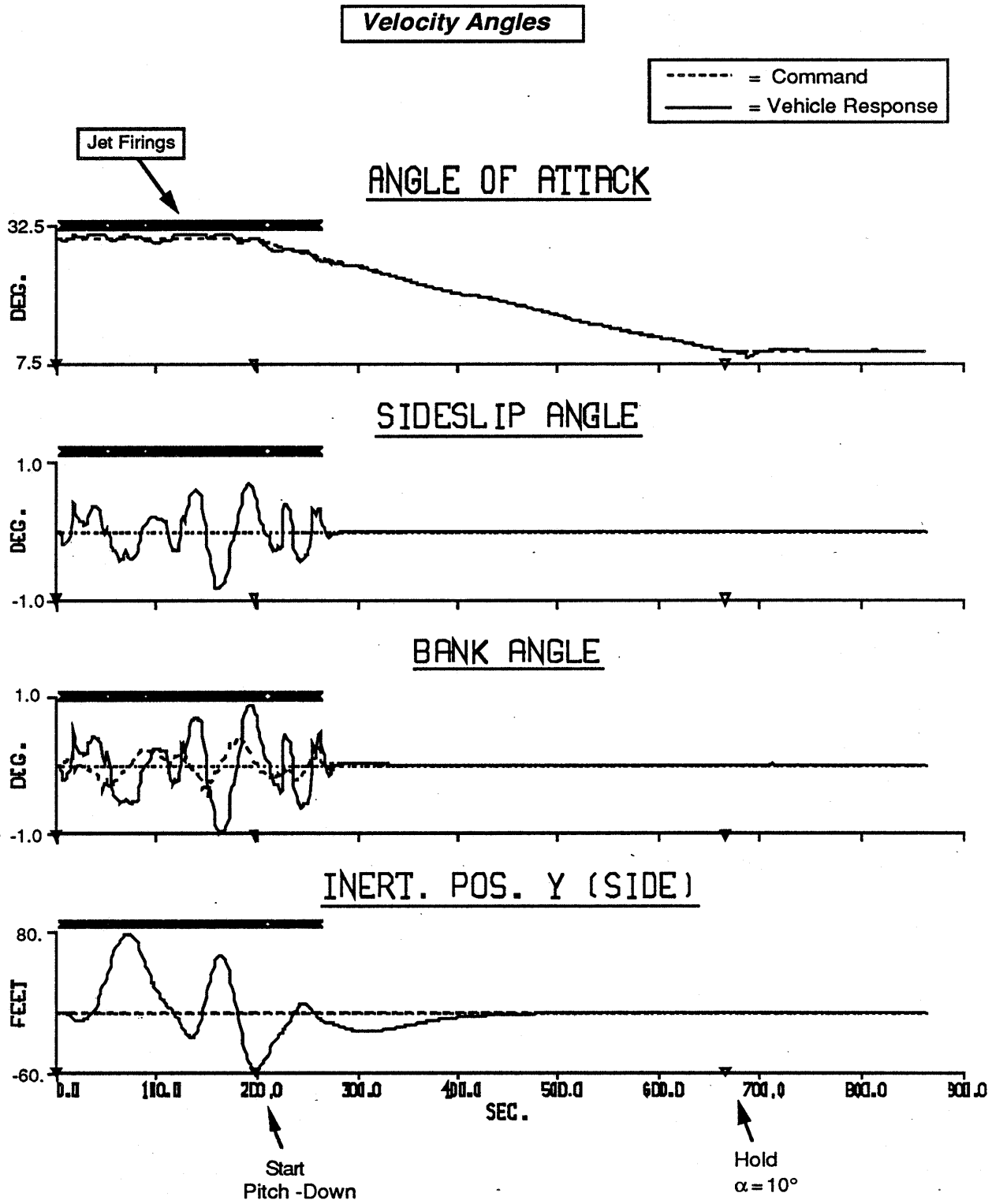


**Figure 55**

before). Jet costs were specified to agree with the "moderate" magnitude specified in Example #10, although the firing pattern will certainly be affected by the radically different actuator behavior expected in this test.

Aerosurface deflections are plotted in Fig. 56. The elevons, canards, and (to some extent) body flap are seen to discretely switch polarities several times during the run. The speedbrake is also used in this fashion later in the test. The velocity angles (Fig. 57) offer no clue to this behavior; the angle of attack is seen to track its revised profile (as outlined above), with small disturbances at the conclusion of the test caused by the frequent aerosurface shifts. Note that the pitch authority of the elevons & canards can become appreciably nonlinear at low  $\alpha$  (Fig. 11), and grows at low airspeed under constant  $\bar{q}$  (these trajectories generally exhibit limited  $\bar{q}$  variation; see Fig. 49). Such effects, together with the large  $\alpha$ -dependence of the airframe pitching moment at low  $\alpha$ , instigate a sensitivity to rapid & wide aerosurface impulses, hence lead to the  $\alpha$  disturbances seen at the end of the run in Fig. 57. Although some limited effect is introduced from the aerosurface cycling, sideslip & bank errors remain minimal throughout the flight.

The cause of the observed aerosurface behavior is resolved in the plots of longitudinal translation state (Fig. 58). The switches in actuator polarity are seen to correlate with sign changes in the longitudinal state error. When the vehicle is traveling too slowly and at too high an altitude, the aerosurfaces are encouraged to deflect negative (up away from the airstream) and lose lift while reducing drag. When the vehicle drops below its desired altitude and exceeds its desired airspeed, the aerosurfaces are encouraged to reverse behavior and deflect down (into the airstream) to gain lift and increase drag. The aerosurfaces alone, however, have relatively small translational authority; most of the cyclic behavior evident in Fig. 58 results from the vehicle phugoid (earlier in the run) and  $\alpha$  disturbances (later in the run). The aerosurface effect has nonetheless some significance. Figure 59 shows translational parameters resulting from a test run under identical assumptions without using objective-based translational control. A definite improvement is evident in the altitude and airspeed tracking with the translational objective active in Fig. 58.

The speedbrake usage arises from its beneficial projection onto the desired vehicle longitudinal state; it is selected after  $\alpha$  drops sufficiently for it to gain appreciable authority. Because of the lower  $\alpha$  at which most of this test takes place, the rudder has adequate authority to stabilize yaw without jet assistance, and lateral disturbances remain exceedingly small (the discrete steps in the side position plot of Fig. 58 arise from plot truncation error and don't reflect the actual vehicle behavior). Again, the net translational effect available from this strategy is somewhat limited (on this vehicle model), hence its primary use may be only in trimming small translational error. Investing additional effort into damping the objective response may result in a smoother aerosurface "switching" transition then seen in Fig. 56, and better stabilize longitudinal response.

**Example #12: Re-Entry, Schedule  $\alpha$ : Translational Objective**

**Aerosurface Deflections**

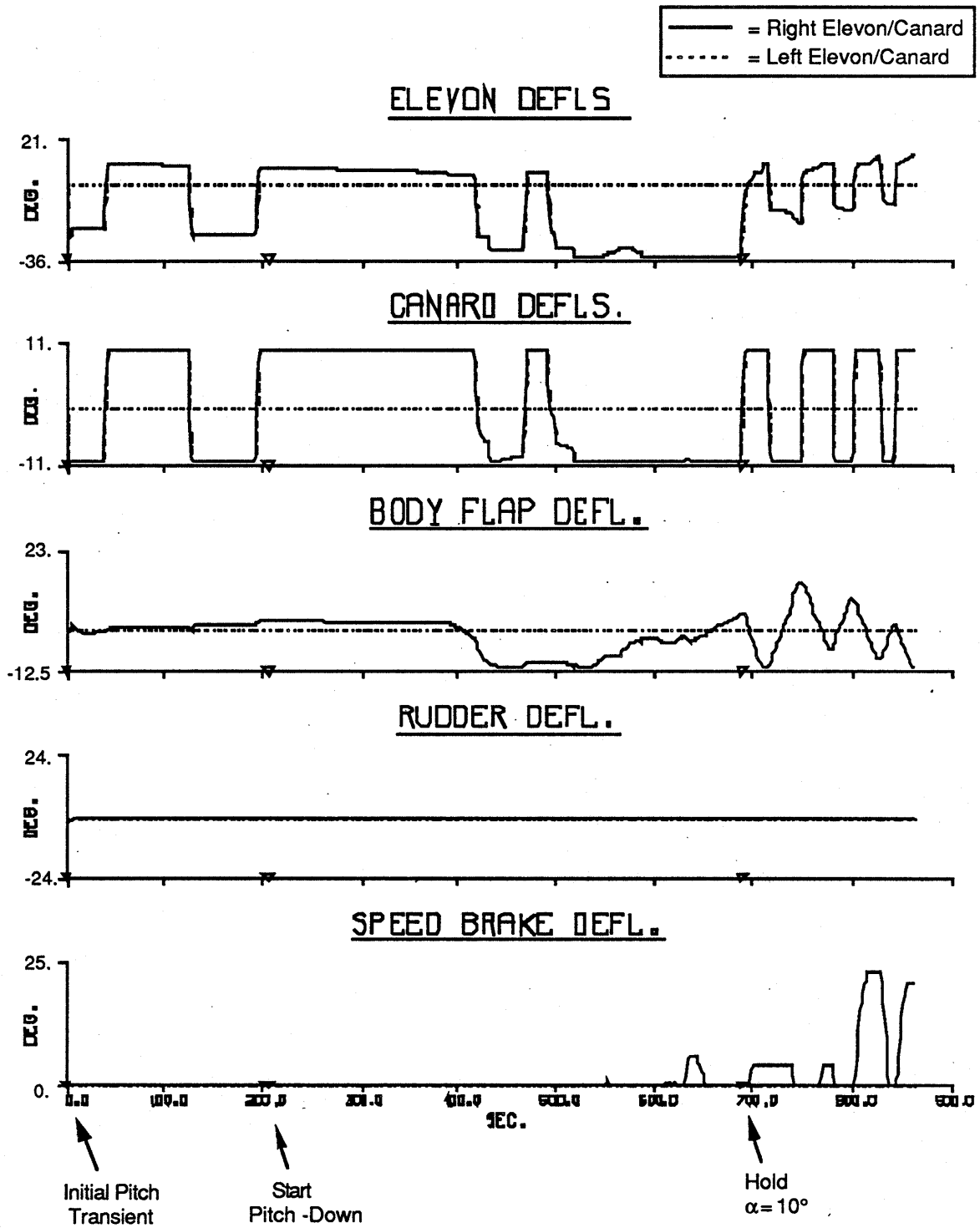


**Figure 56**

### Example #12: Re-Entry, Schedule $\alpha$ : Translational Objective

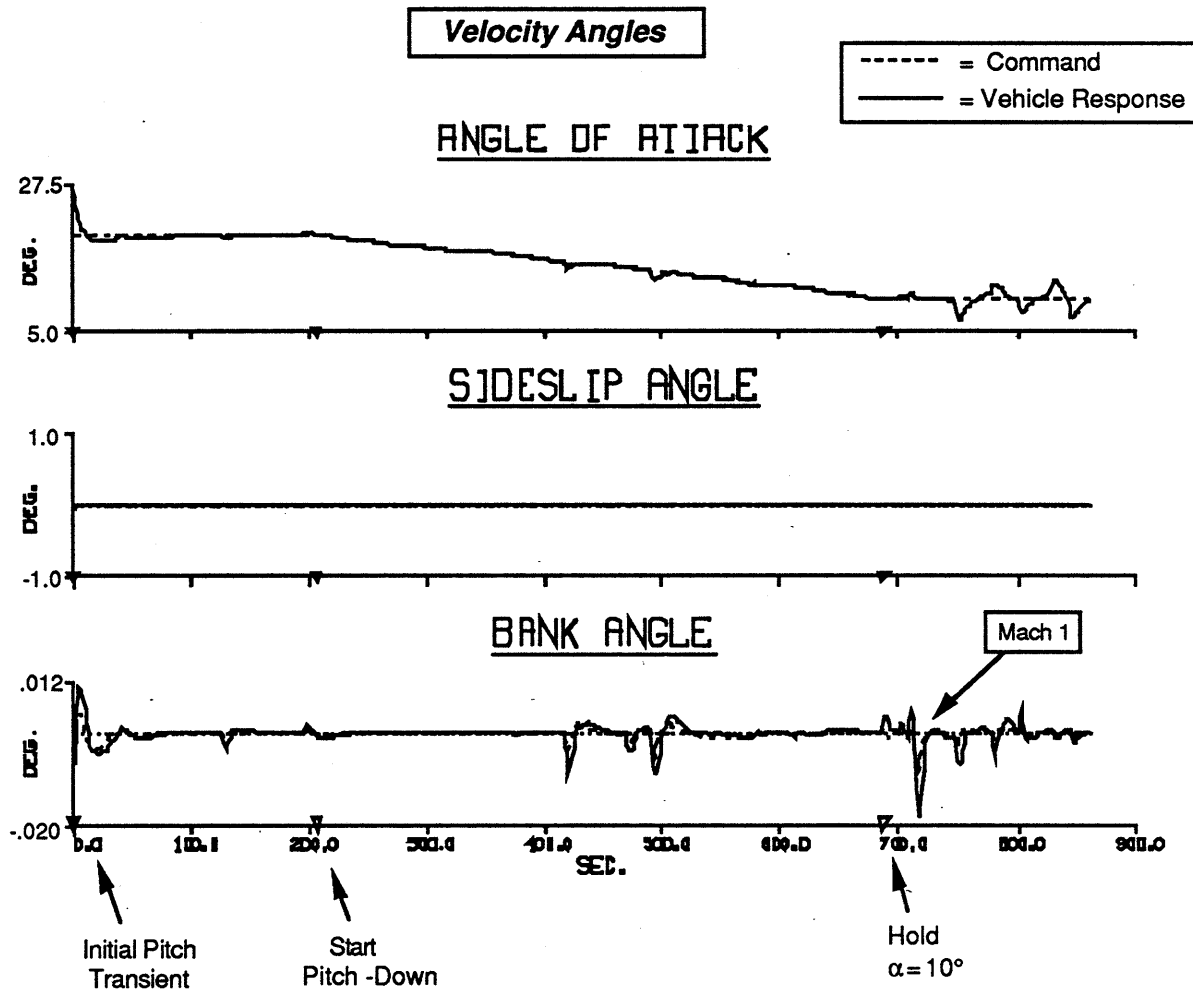


Figure 57

The preceding tests controlled the longitudinal vehicle state primarily through the  $\alpha$ -vs.-Mach# profile of Fig. 22. No feedback of vehicle altitude or airspeed was employed (excepting the limited objective effect introduced in the previous example). All of the remaining examples, however, employ the longitudinal translation controller sketched in Fig. 21 to follow the altitude-vs.-Mach# profile of Fig. 23. The first test in this series is a reference that assumes nominal operation and a well-balanced aerosurface-to-jet cost ratio (ie. similar to the test of Figs. 50  $\rightarrow$  52). No translational control is considered in the objective function. Results are shown in Figs. 60  $\rightarrow$  63. Aerosurface deflections (Fig. 60) are reasonably behaved, with limited canard/rudder activity augmenting yaw and trimming roll from lateral jet firings (Fig. 61) needed to stabilize sideslip & bank at the beginning of the test.

# Example #12: Re-Entry, Schedule $\alpha$ : Translational Objective

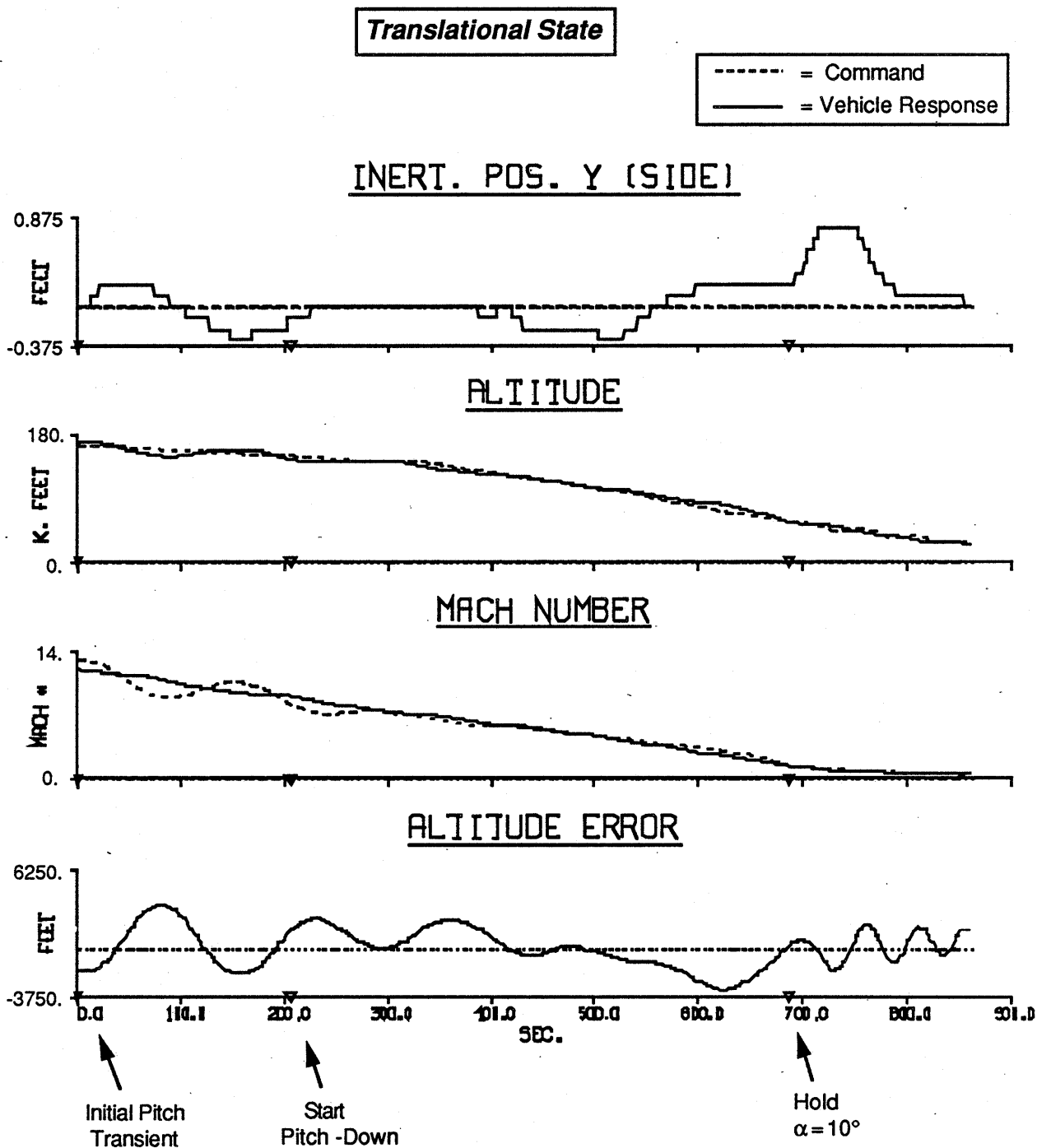


Figure 58

### Example #13: Re-Entry, Schedule $\alpha$ : No Translational Objective

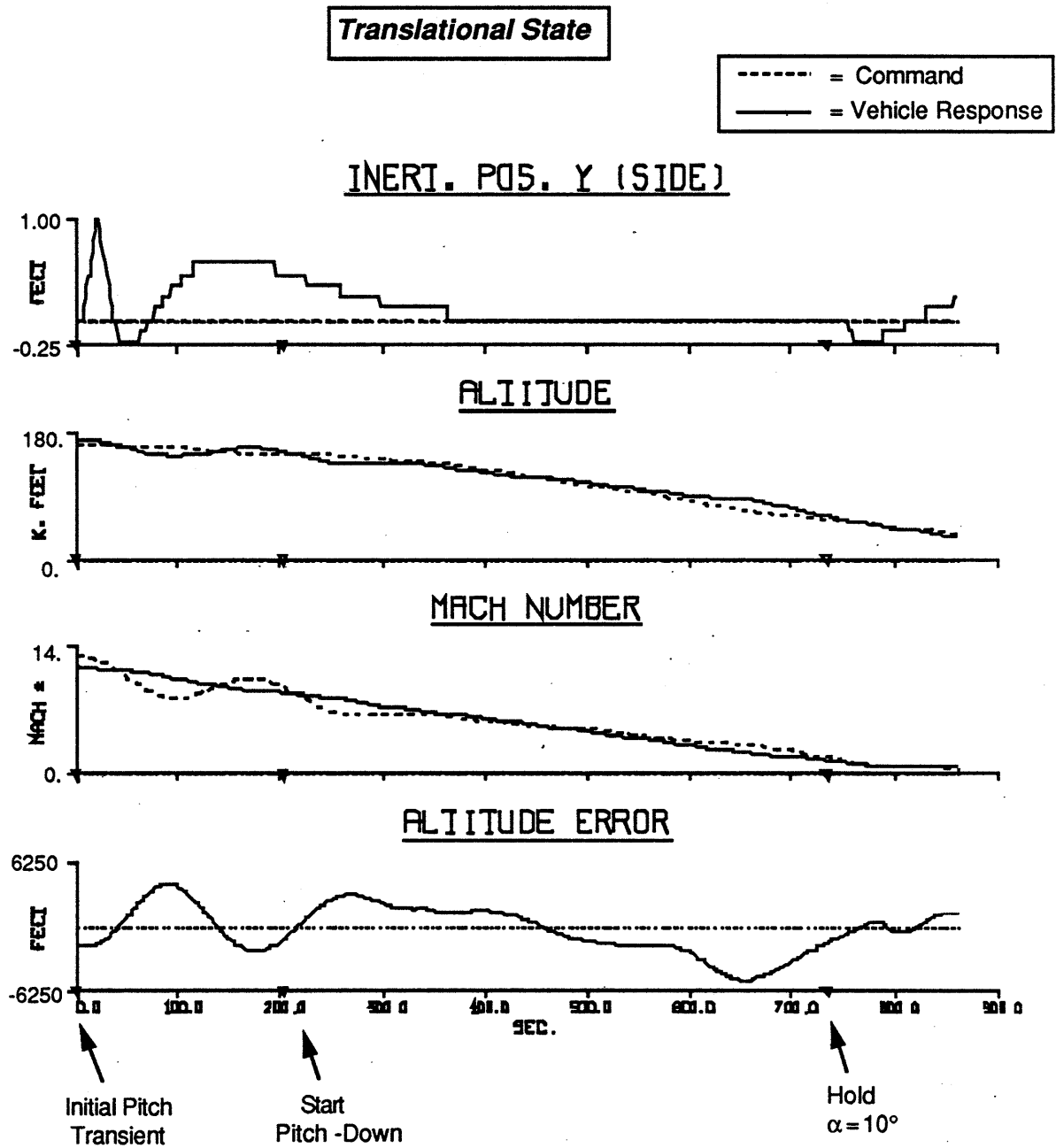


Figure 59

# Example #14: Re-Entry, Full Control: Nominal Case

## Aerosurface Deflections

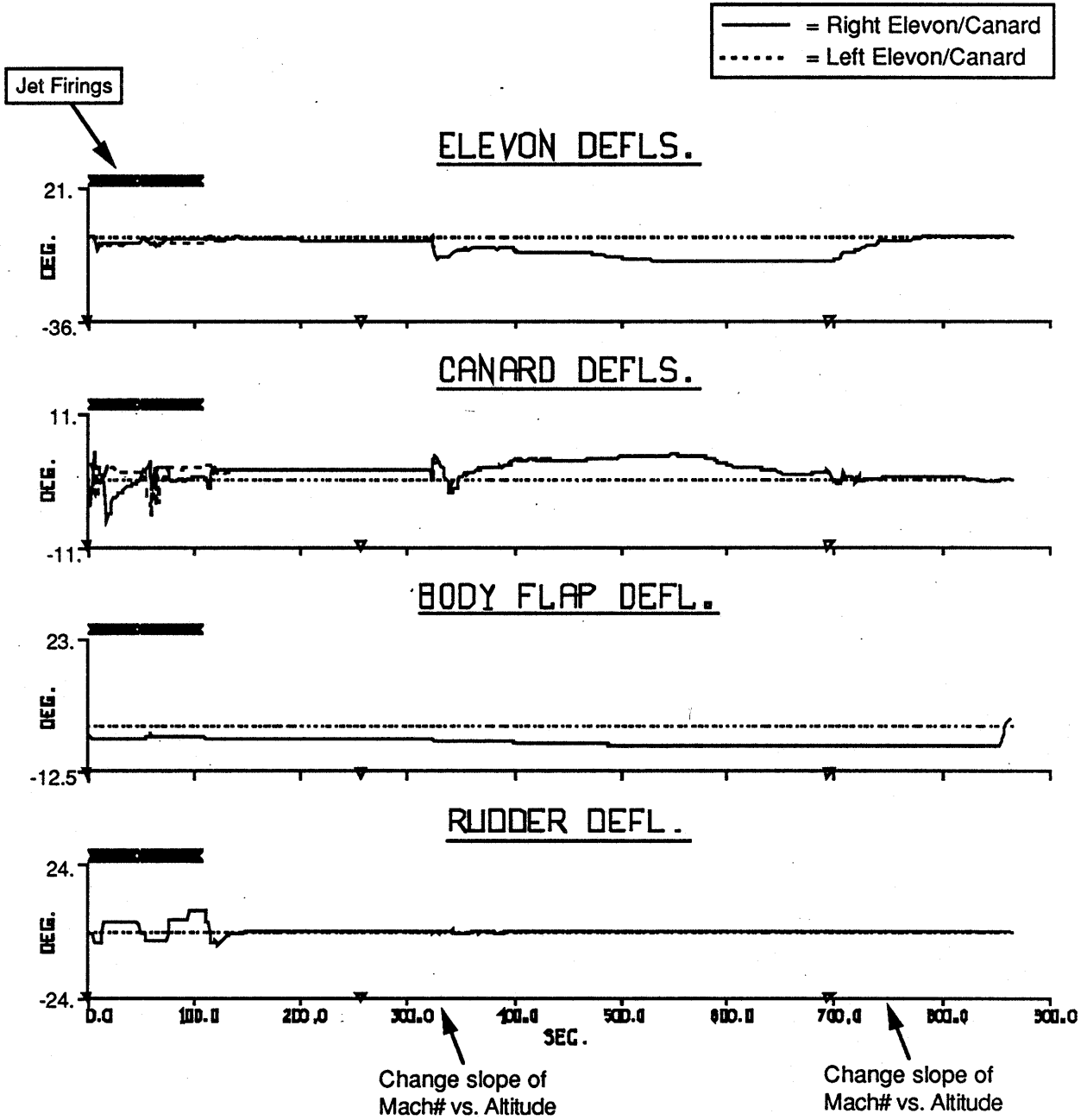
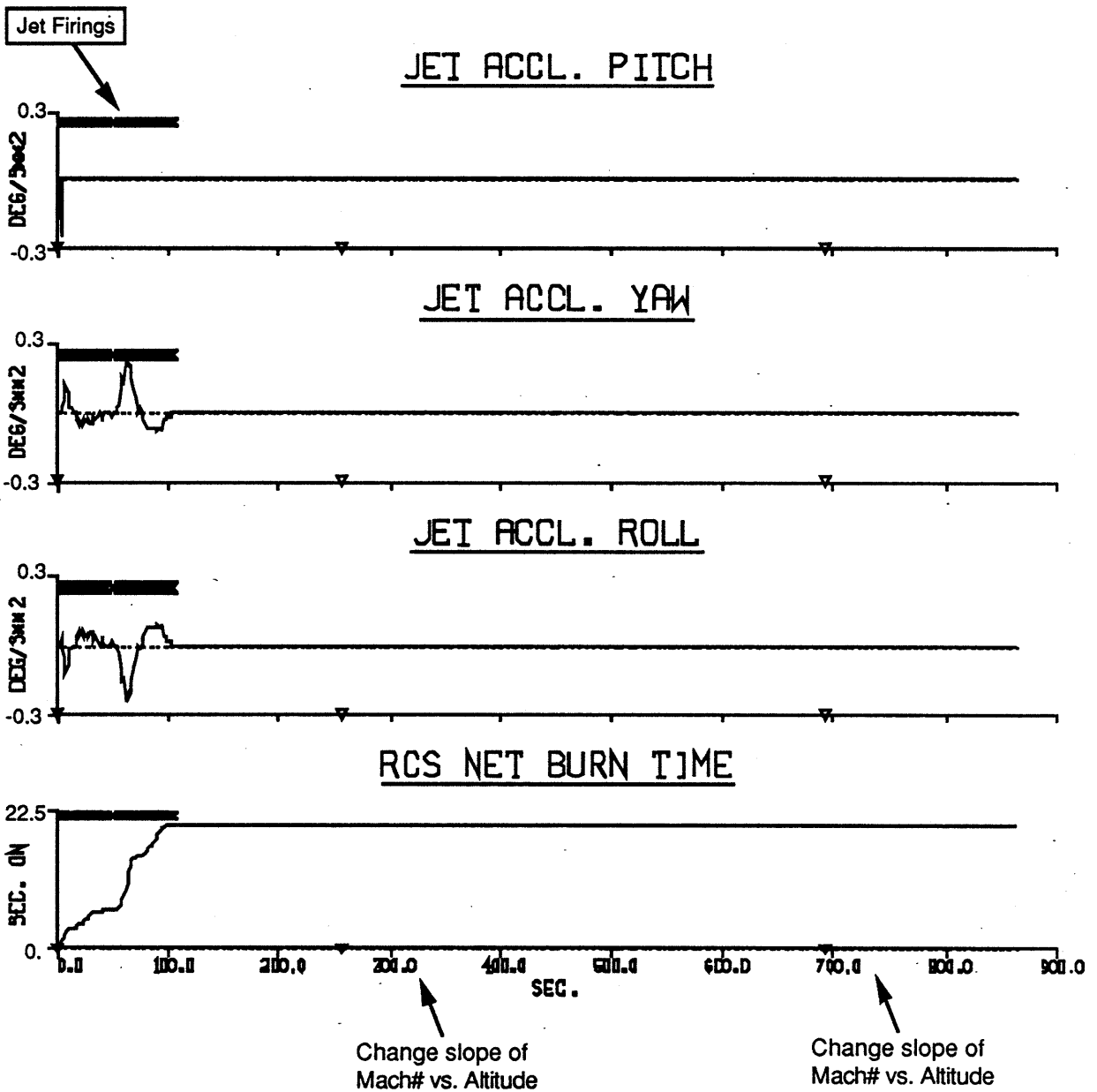


Figure 60

**Example #14: Re-Entry, Full Control: Nominal Case**

**Jet Performance**



**Figure 61**

## Example #14: Re-Entry, Full Control; Nominal Case

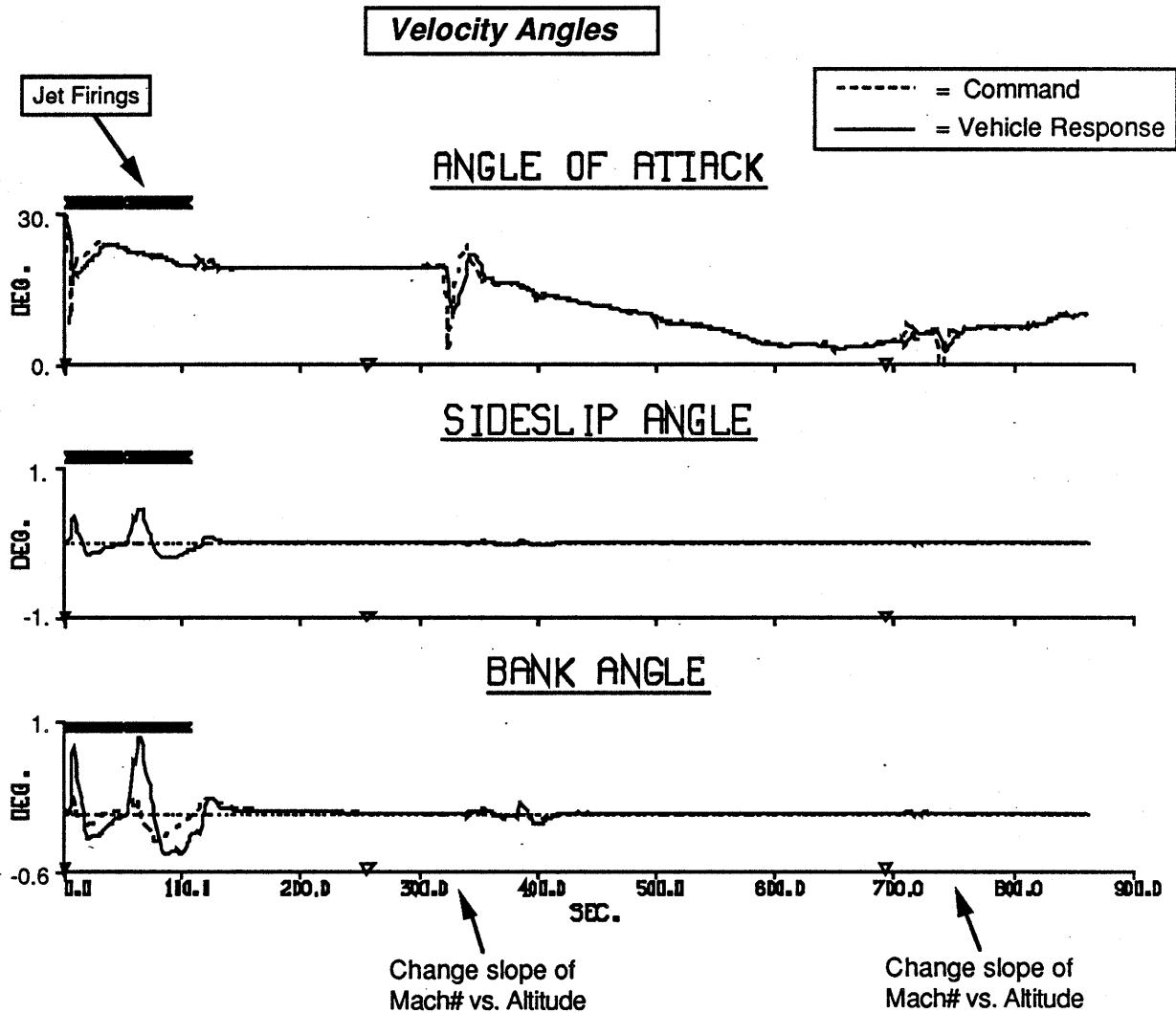


Figure 62

Jets are needed for a significantly shorter segment of this test than encountered in previous examples. This is due to the longitudinal control applied through  $\alpha$ ; as seen in Fig. 62,  $\alpha$  is immediately decreased at the start of the test to drop altitude, causing the rudder to exhibit an earlier increase in authority. Jet firings are discretized to an 80 msec. minimum duration at higher altitudes in these examples; the plotted values in Fig. 61 are averaged over three 320 msec. time steps, however, resulting in an observed dynamic range of 12-to-1, which can appear nearly continuous (the environment nonetheless quantizes jet firings to the minimum intervals).

Angle of attack is seen to track a relatively smooth profile, excepting commanded impulses at the start of the test (where  $\alpha$  is modulated to null the initial altitude & Mach errors), at roughly

**Example #14: Re-Entry, Full Control: Nominal Case**

**Translational State**

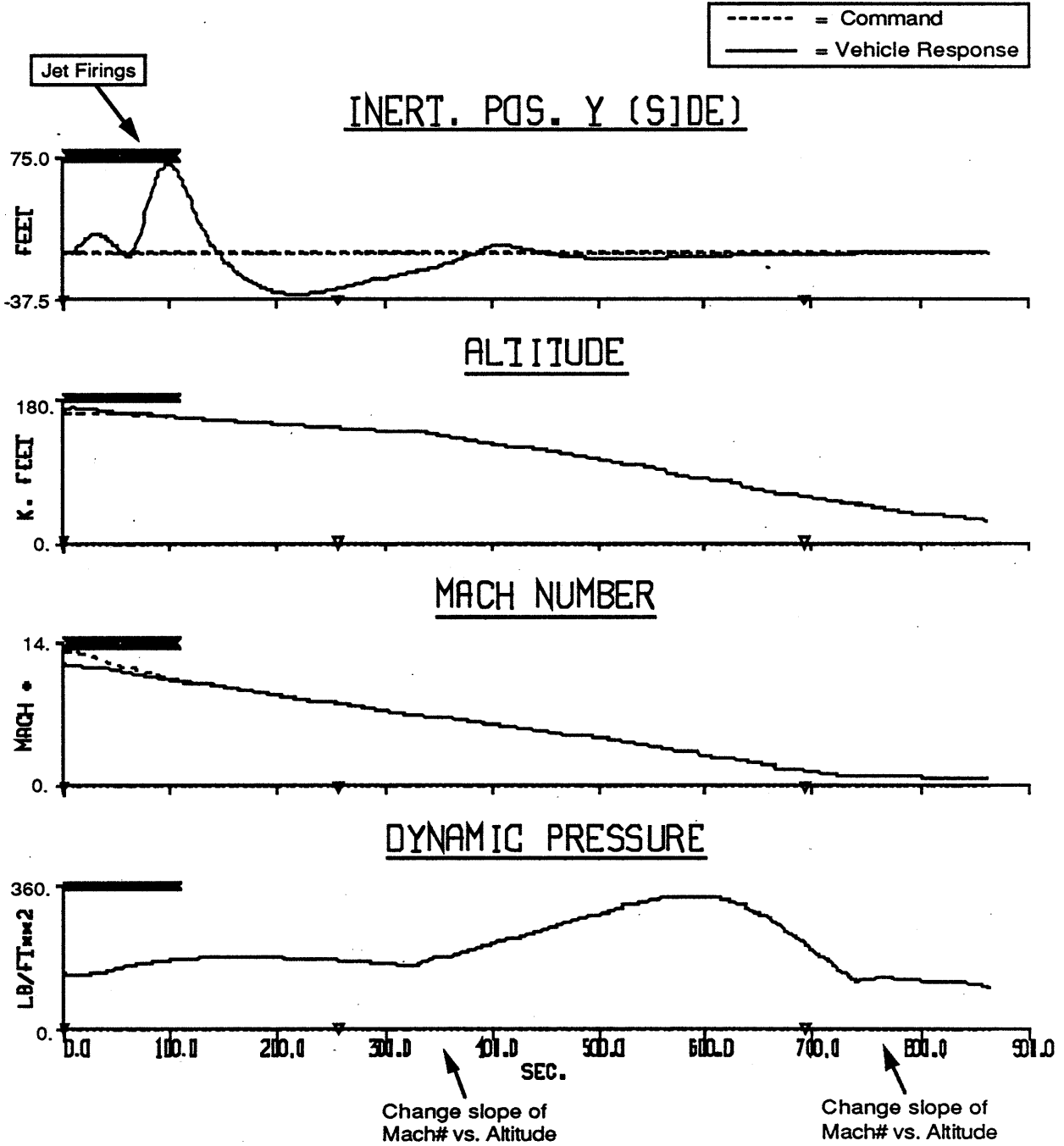


**Figure 63**

350 sec. midway through the test (where  $\alpha$  is pulsed after the vehicle passes Mach 7 to quicken the rate of vertical descent in correspondence with a discrete steepening in slope of the commanded altitude vs. Mach # profile) and at roughly 800 sec. near the end of the test (these impulses are due to disturbances encountered in the passage through Mach 1, together with a commanded flattening in the slope of commanded altitude-vs. Mach # profile). These  $\alpha$ -impulses were not pre-programmed; they result directly from the longitudinal control logic sketched in Fig. 21 responding to translational state errors (dotted line = commanded state). The initial  $\alpha$  impulse was of sufficient magnitude to introduce a brief pitch jet firing, as can be noted in Fig. 61. Sideslip and bank disturbances were kept minimal.

Translational variables are plotted in Fig. 63. The lateral controller is seen to reject disturbances and keep side position near zero. A marked change, however, is noted in the plots of altitude and Mach #; after nulling an initial offset, the desired state (dotted line) is tracked precisely across the entire trajectory. The dynamic pressure history is also presented for this example; it slowly grows up to 360 lb/ft<sup>2</sup>, then tapers off at the close of the test (the discontinuities at 320 & 720 sec. are due to the discrete changes in slope of the commanded altitude vs. Mach # profiles).

The next test demonstrates the action of the deflection minimization and stops avoidance cost contributions (Eqs. 4 & 5). The deflection cost ( $K_A$ ) and the stops cost ( $K_S$ ) are decreased by an order of magnitude. Results are given in Figs. 64 → 67. The deflection histories show considerable aerosurface activity during jet firings (again, encouraged by the lower relative aerosurface cost), with frequent approaches to maximum canard and rudder limits. After the initial firings finish, the canards are left at large deflection, and the body flap is kept near its maximum limit. The longitudinal impulse at approximately 350 sec. eventually moves the aerosurfaces back, although the canards are repeatedly advanced to large deflection later in the test. The deflection & stops cost contribution prevented this behavior in earlier re-entry examples, where maximum limits were generally avoided, and an aerosurface was never left at large deflection due to the large associated expense.

Jet activity (Fig. 65) arises exclusively from aft side-firing jets. The decreased relative aerosurface cost has made large aerosurface deflections more cost effective, thus the initial  $\alpha$  impulse (which resulted in firing of a pitch jet in the previous test) is now accomplished mainly via large canard swings (which produce smaller roll/yaw disturbance than equivalent elevon motion).

Velocity angles (Fig. 66) and translational response (Fig. 67) appear entirely nominal. Dynamic pressure is not plotted for this (and most future) tests, since it is derived from the scheduled altitude-vs. Mach vehicle state, which is now precisely tracked to agree with the results of Fig. 63.

The next example again assumes full longitudinal/lateral vehicle control, but includes an estimate of actuator drag to be minimized in the objective function (as did the analogous constant

# Example #15: Re-Entry, Full Control; Reduced Angle & Stops Costs

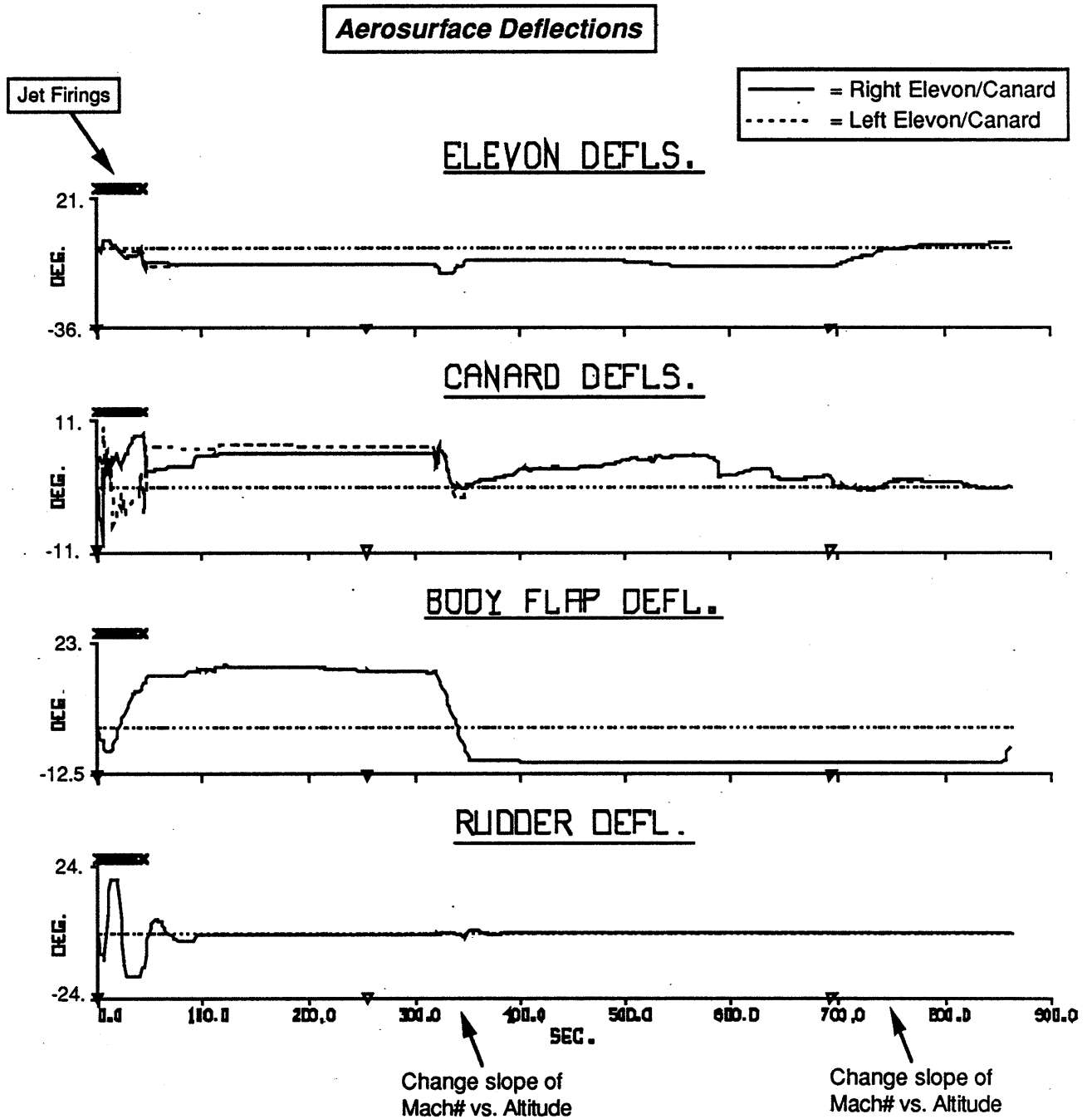
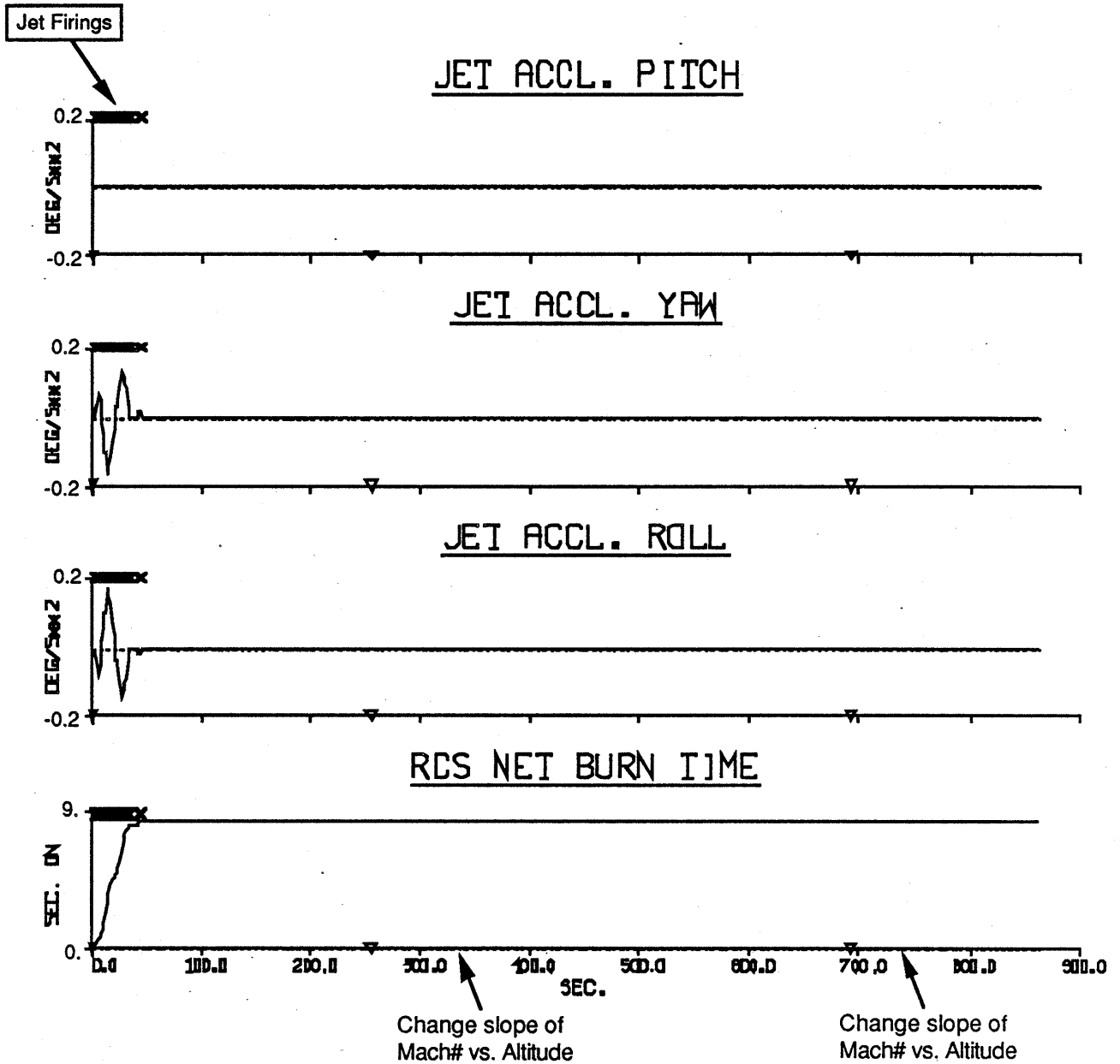


Figure 64

**Example #15: Re-Entry, Full Control; Reduced Angles & Stops Costs**

**Jet Performance**



**Figure 65**

**Example #15: Re-Entry, Full Control: Reduced Angles & Stops Costs**

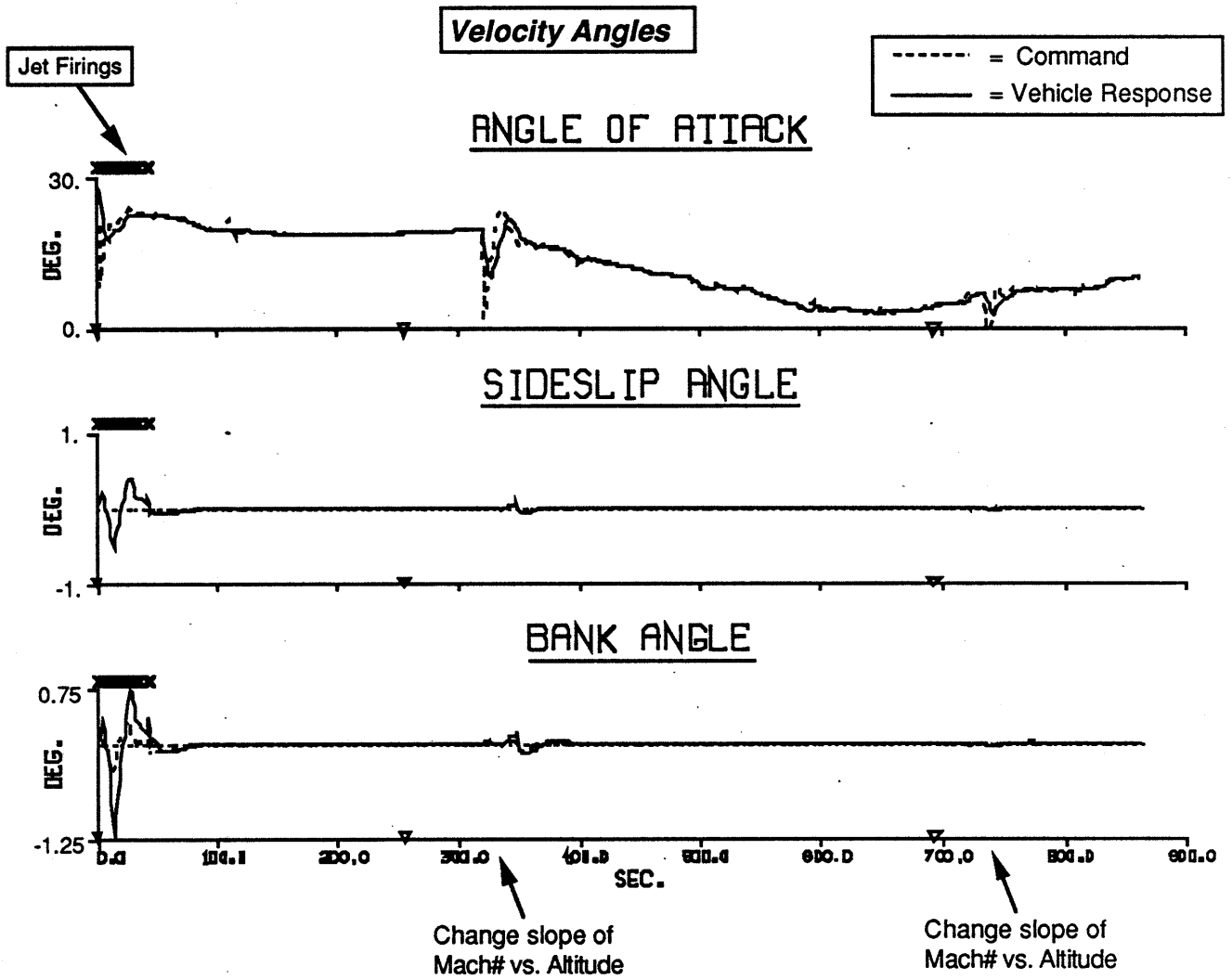


**Figure 66**

altitude test of Figs. 33 → 35). Results are shown in Figs. 68 → 71. A different actuator behavior (Fig. 68) is seen in comparison with the nominal test results (Fig. 60). Elevon and canard deflections are kept negative (up out of the airstream) throughout most of the flight. As the vehicle descends and  $\alpha$  decreases, the canards are deflected slightly positive to balance the changing airframe pitch torque; this does not result in much drag penalty, however, since the canards have a reduced drag coefficient (canards are again brought negative at the close of the test).

**Example #15: Re-Entry, Full Control; Reduced Angles & Stops Costs**

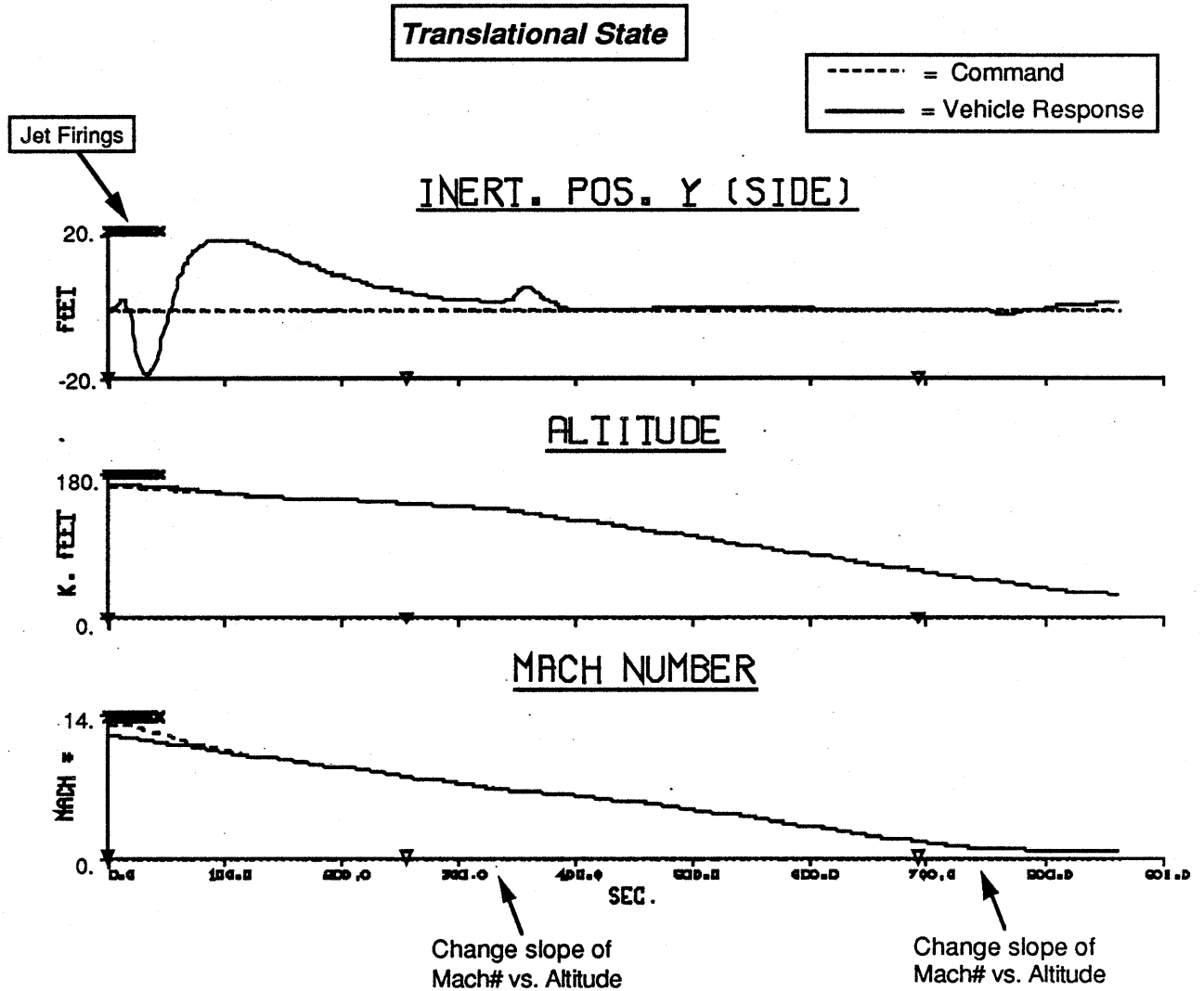


**Figure 67**

If the drag cost contribution is additionally increased, and drag-beneficial activity vectors are allowed to have negative costs (by reducing  $K_{min}$  in Eq. 38), the minimum-drag effect can be made even more pronounced in actuator operation.

Velocity angles (Fig. 70) and translational states (Fig. 71) appear entirely nominal, as interpreted in the results of the previous examples. Jet accelerations (Fig. 69) indicate that aft side-firing jets were used exclusively (no pitch jets were needed to compensate the initial  $\alpha$  transient). The lack of lateral disturbance in this test resulted in a low fuel requirement (4.5 sec. net firing time).

# Example #16: Re-Entry, Full Control; Minimize Drag

## Aerosurface Deflections

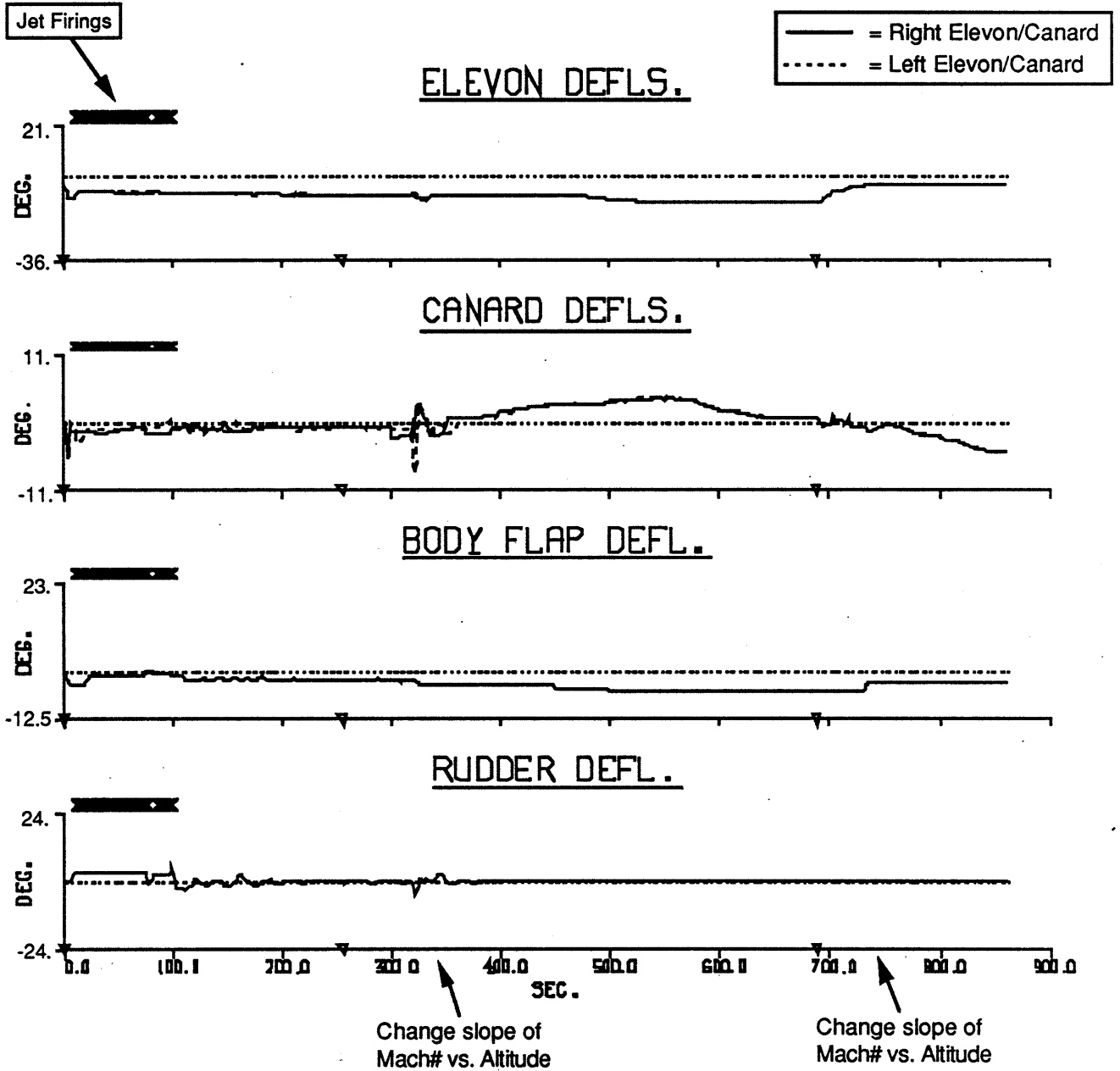


Figure 68

# Example #16: Re-Entry, Full Control: Minimize Drag

## Jet Performance

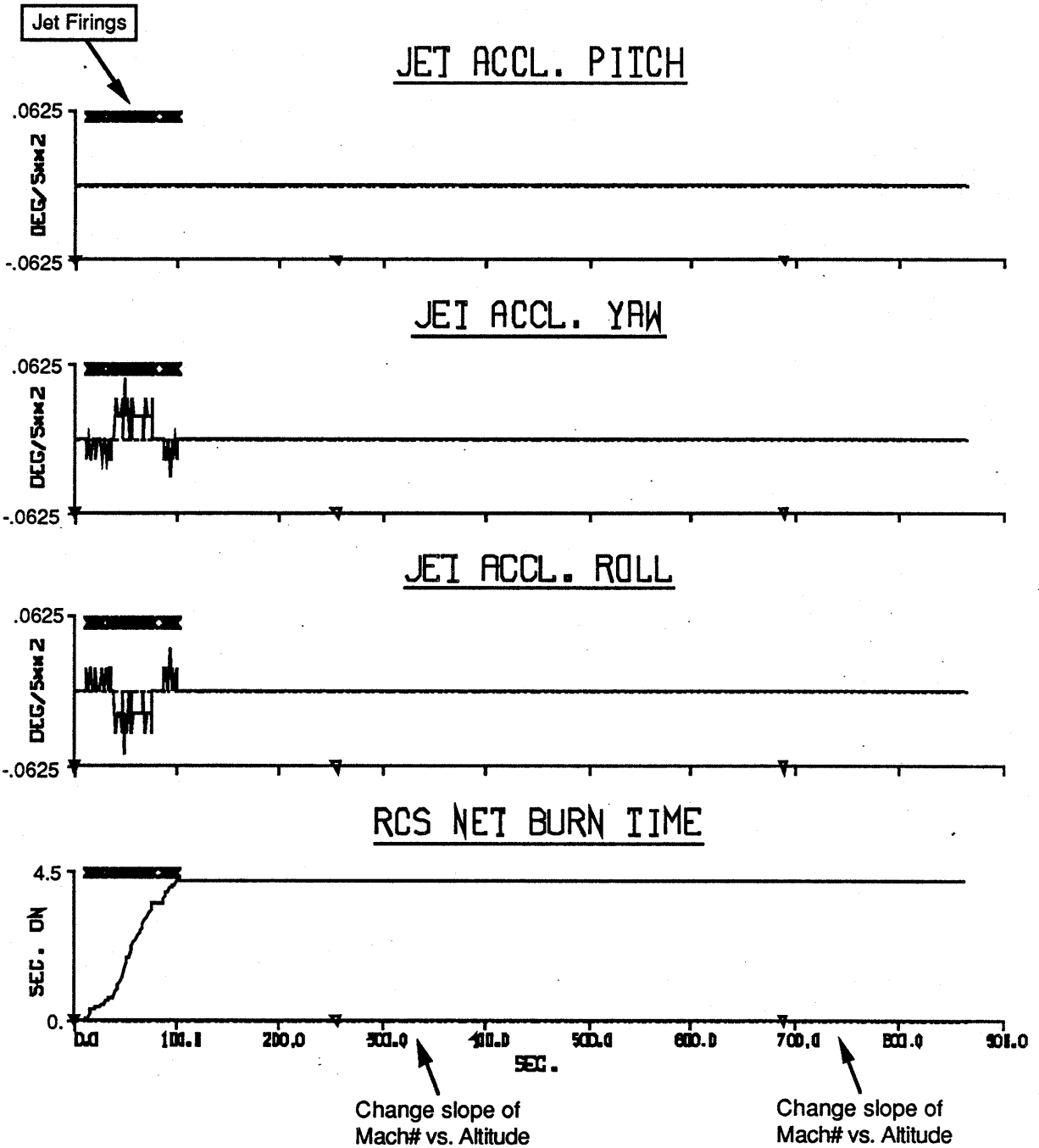
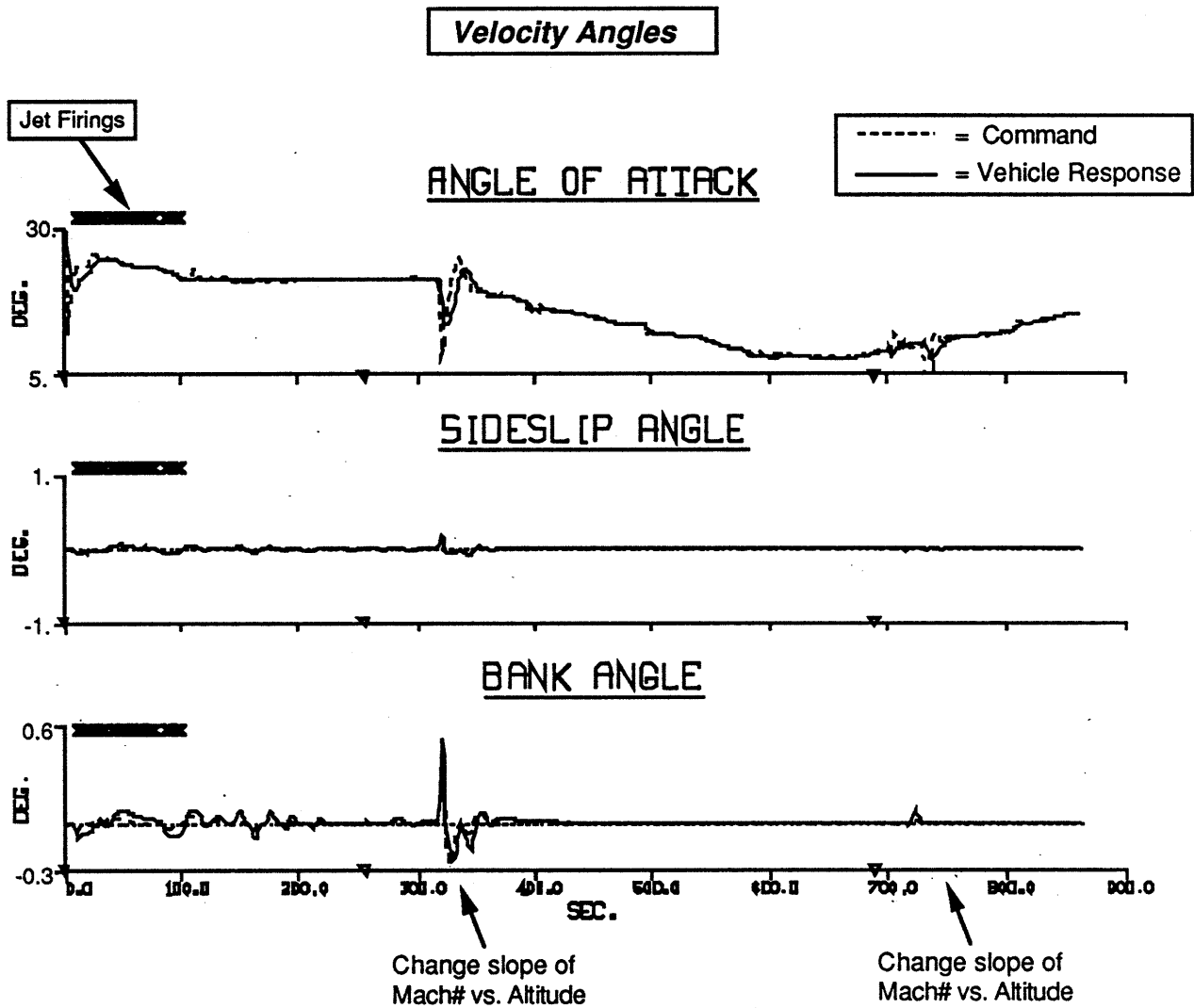


Figure 69

## Example #16: Re-Entry, Full Control: Minimize Drag



**Figure 70**

The next series of tests employ full longitudinal/lateral control and assume a standard objective formulation (re. test of Figs. 60 → 63). The vehicle is now commanded to momentarily displace sideways by 10,000 ft. during the descent.

Results are shown in Figs. 72 → 75. The actuator response (Fig. 72) is nearly identical to that of the standard case (Fig. 60). Exceptions can be noted at roughly 175 sec. and 500 sec. into the run. At both of these occurrences, elevon/canard & rudder activity is evident, which is needed to produce the  $\pm 7^\circ$  bank shown in Fig. 74. This yields the commanded lateral impulse of 10,000 ft., that can be seen to be successfully achieved in Fig. 75. Since the vehicle sideslip tracks zero (as commanded), the lateral impulse is realized by a pair of "perfect" or "coordinated" turns. The

### Example #16: Re-Entry, Full Control: Minimize Drag

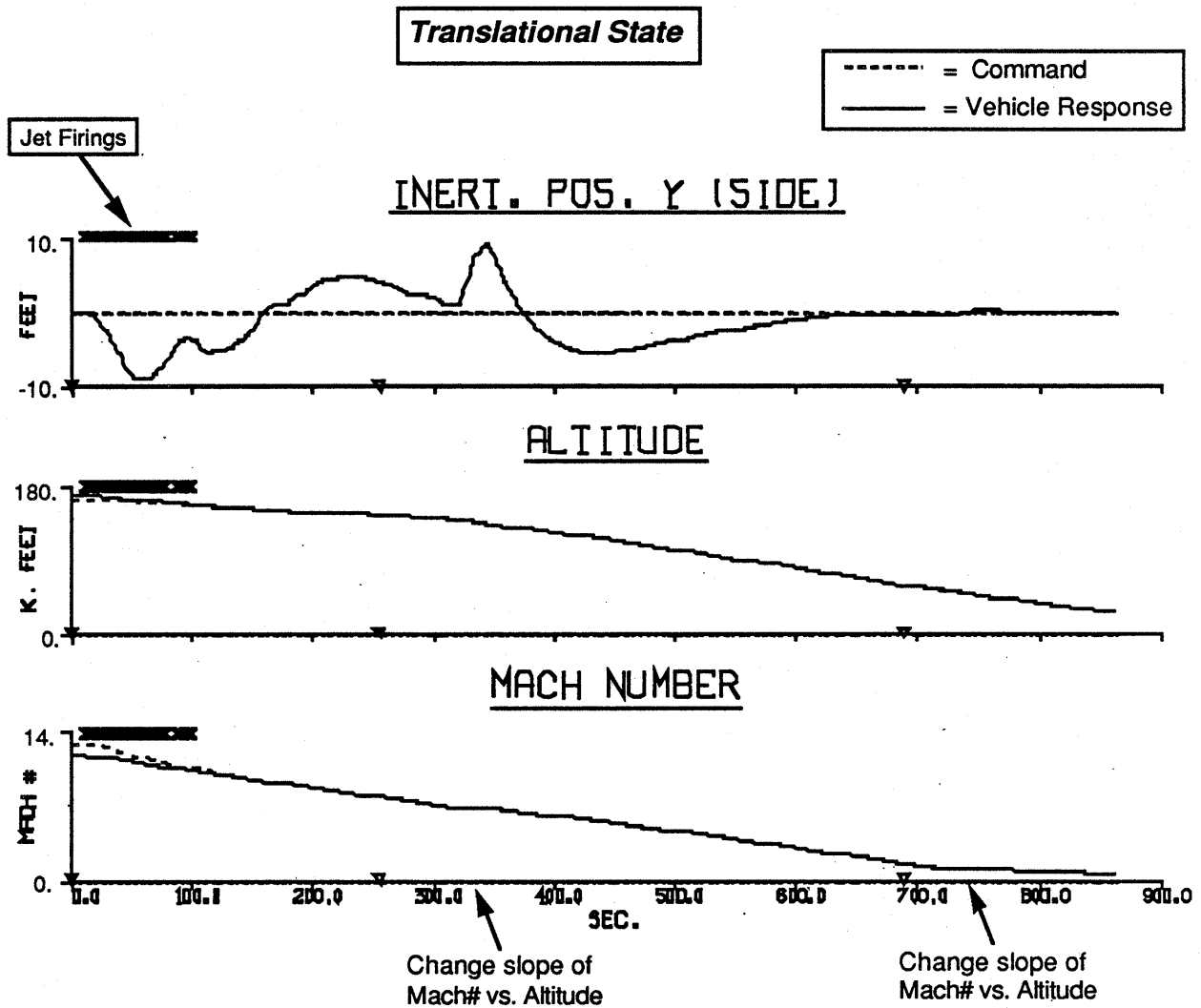


**Figure 71**

longitudinal controller continues to track the commanded re-entry corridor, as is also evident in Fig. 75.

Because of the limited rudder authority at high  $\alpha$ , jets are introduced to assist in the initial bank. These are again side-firing aft jets, as can be noted in Fig. 73. Jets are not needed in the latter bank maneuver, which occurred at significantly lower  $\alpha$ .

The 10,000 ft. lateral position impulse command (and this objective formulation) is retained in future tests; the results presented above (ie. Figs. 72 → 75) can be used as a reference for comparison with all future examples, which mainly examine the effects of hardware failures, vehicle reconfiguration, and modelling errors.

### Example #17: Re-Entry, Lateral Maneuver; Nominal Case

#### Aerosurface Deflections

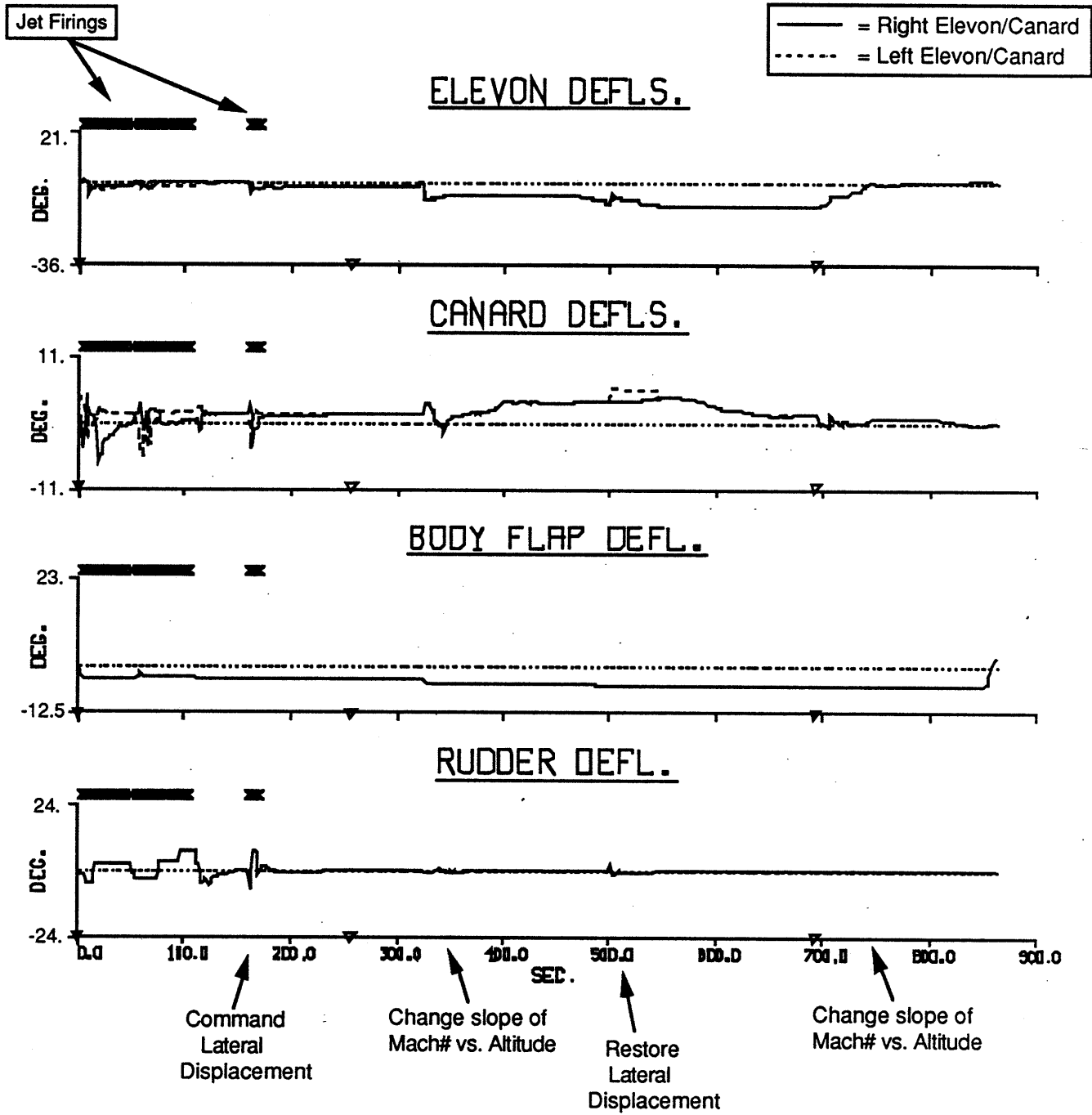


Figure 72

# Example #17: Re-Entry, Lateral Maneuver: Nominal Case

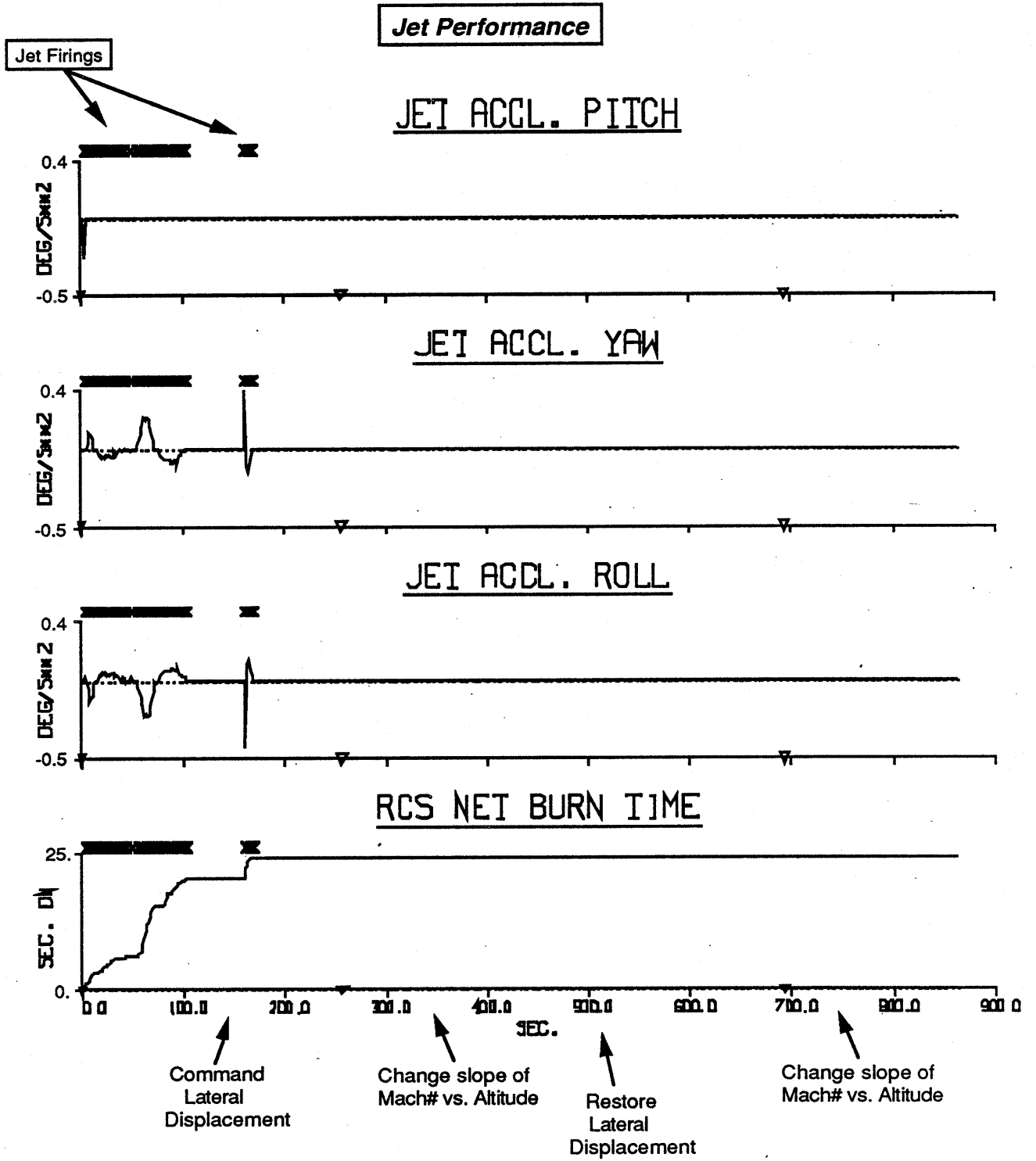
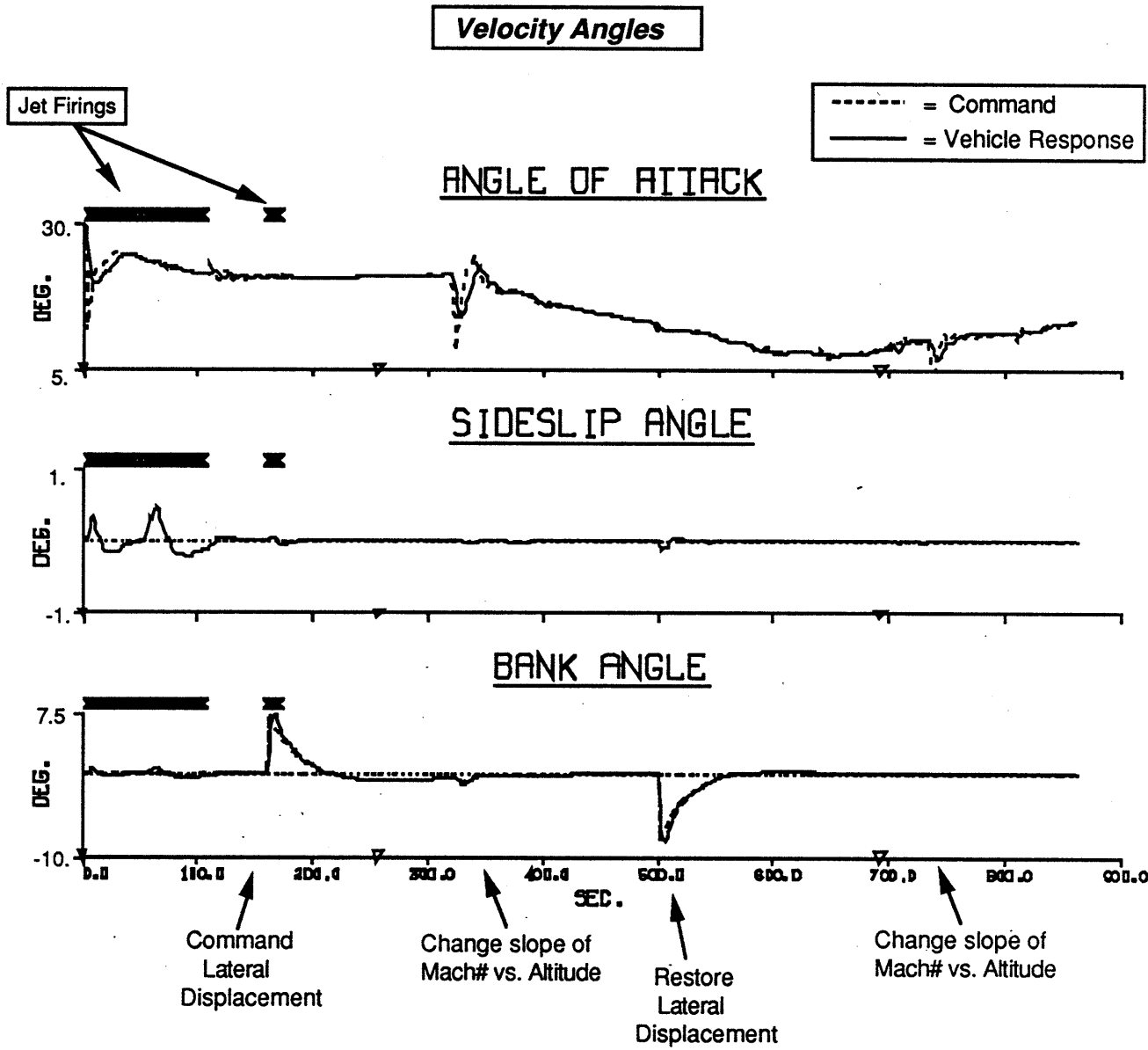


Figure 73

**Example #17: Re-Entry, Lateral Maneuver; Nominal Case**



**Figure 74**

The next example "fails" both left & right elevons (ie. freezes them at constant angle and inhibits their selection) at 45 sec. into the run. Results are given in Figs. 76 → 79.

The elevons were failed shortly after the initial  $\alpha$  correction; at this time, the elevons were slightly scissored to trim roll disturbance (possibly related to jet firings). After failure, they were locked into this slightly scissored position, yielding a secular roll torque. This was compensated by a nearly constant canard scissoring throughout the flight, as is evident in Fig. 76. Because of

## Example #17: Re-Entry, Lateral Maneuver; Nominal Case

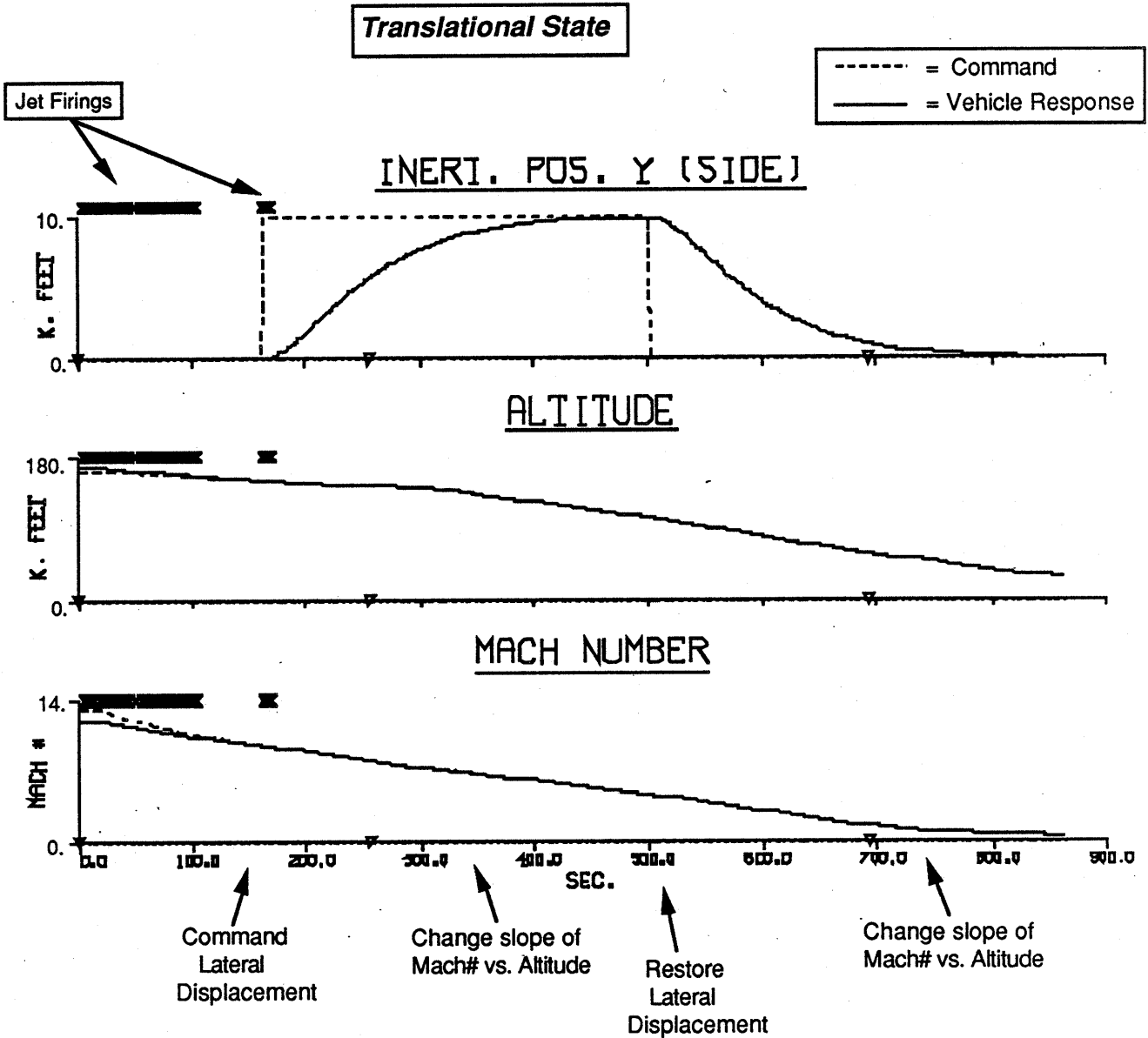


**Figure 75**

the order-of-magnitude reduction in canard roll authorities (relative to the elevons), the canards had to scissor considerably further to compensate the roll error caused by the small elevon-induced aileron deflection.

Considerably greater canard activity can be noted to occur upon issuance of significant attitude commands (ie.  $\alpha$  impulses and bank maneuvers). Jets are needed to assist lateral authority during both banks that form the 10,000 ft. impulse. The situation is indeed interesting in the

### Example #18: Re-Entry, Lateral Maneuver: Fail Elevons

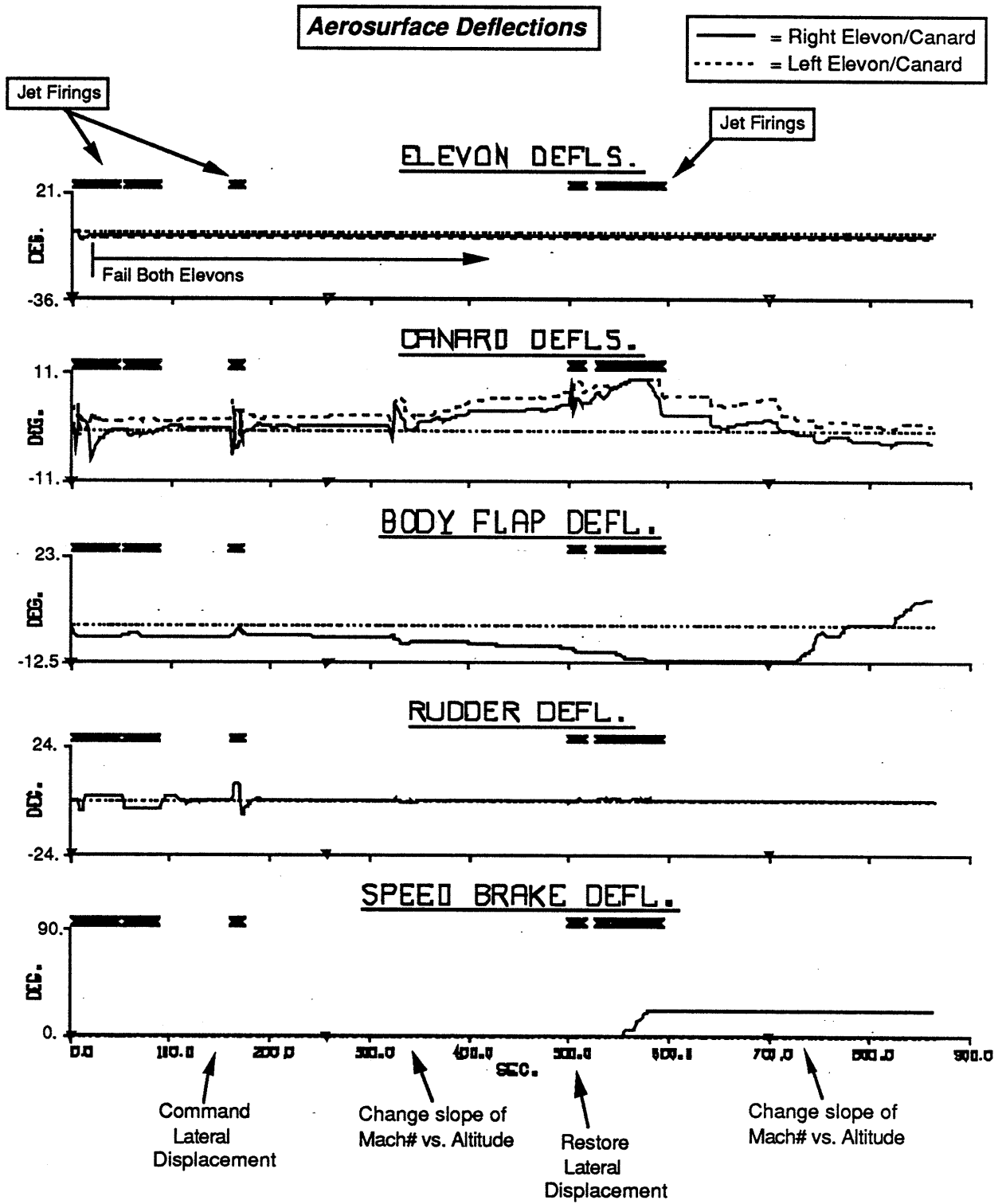
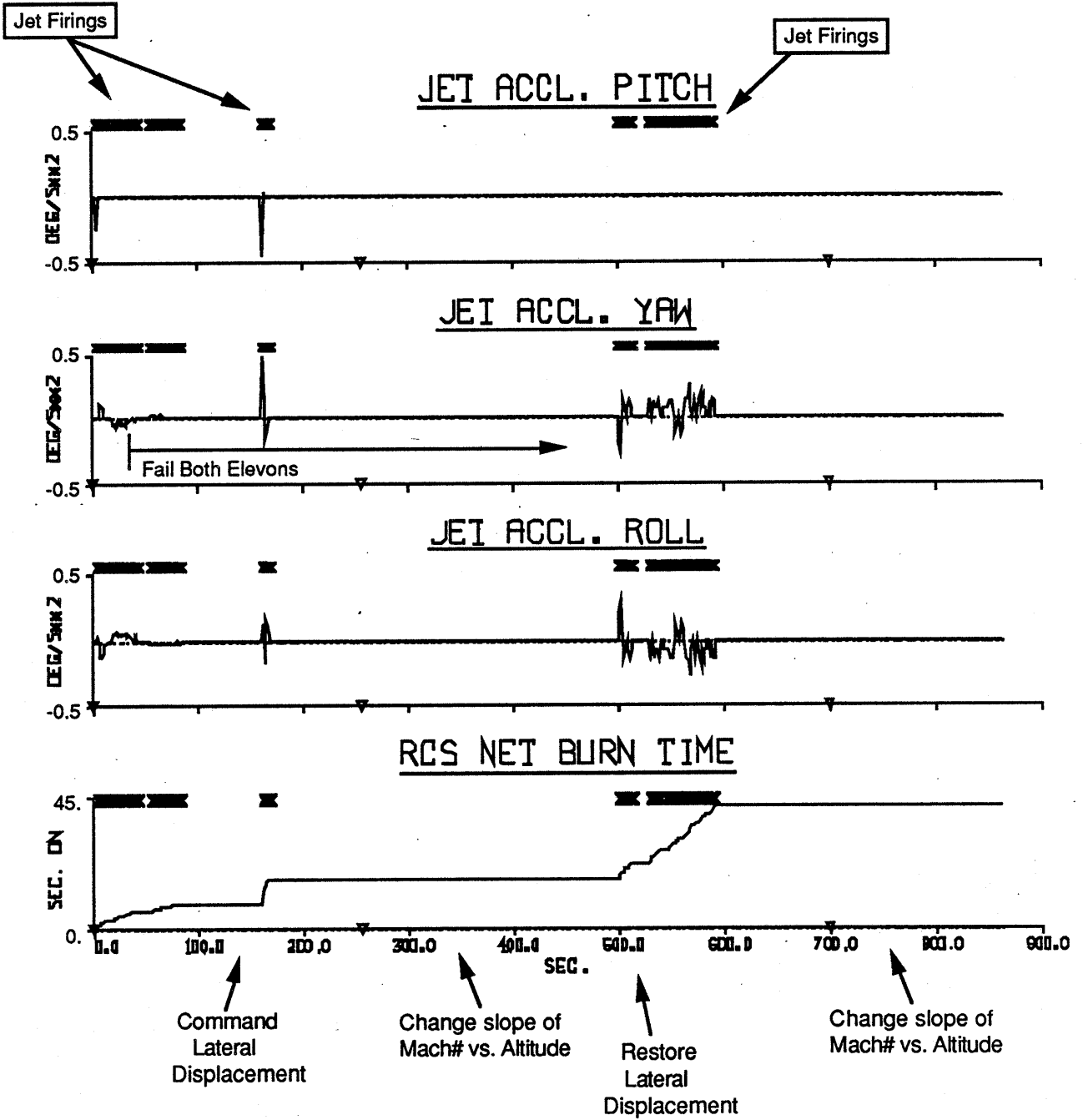


Figure 76

**Example #18: Re-Entry, Lateral Maneuver; Fail Elevons**

**Jet Performance**



**Figure 77**

### Example #18: Re-Entry, Lateral Maneuver: Fail Elevons

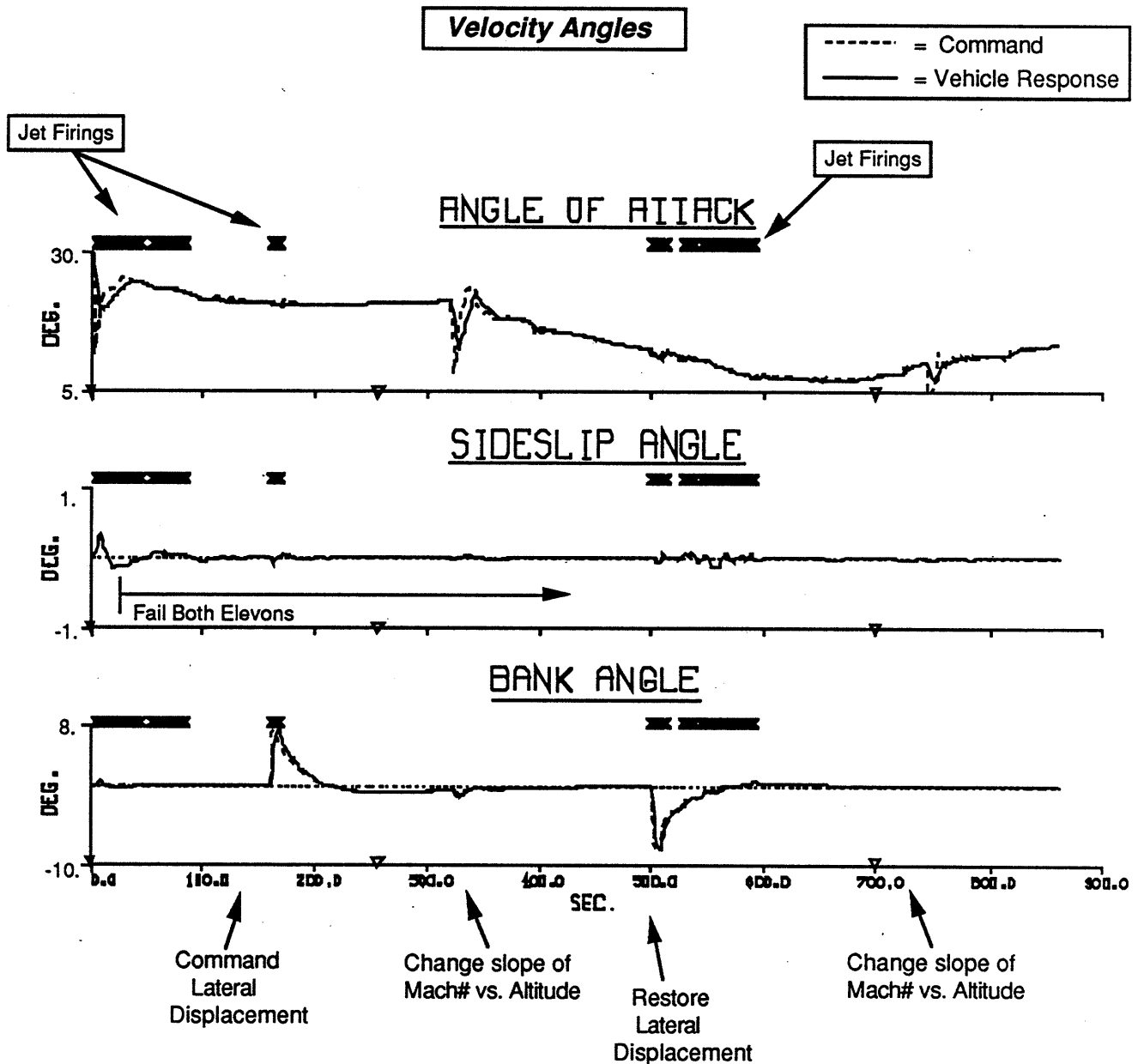
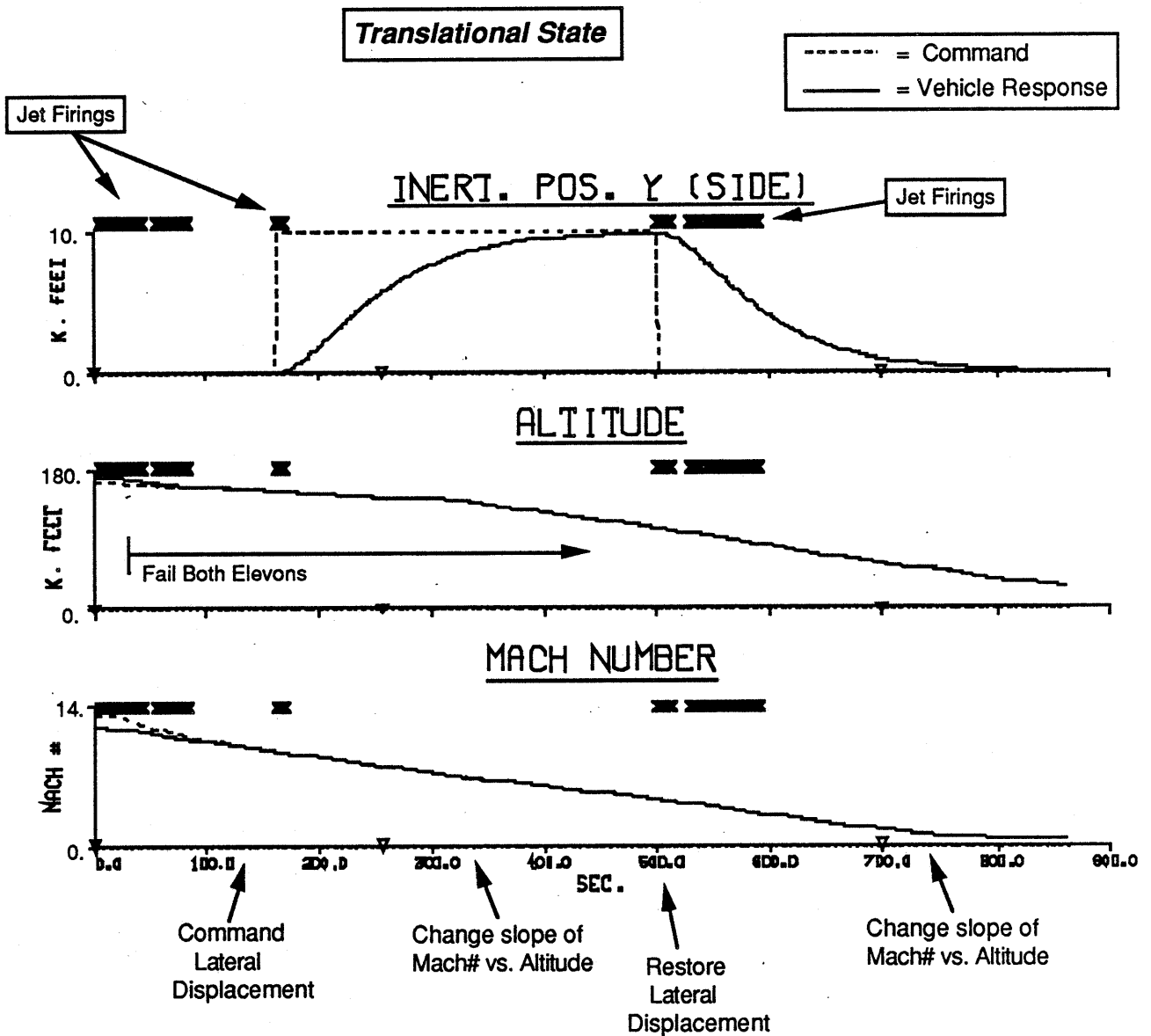


Figure 78

vicinity of the second bank (ie. at 500 → 600 sec.). Here, we see that all pitch actuators (canards & body flap) become saturated to compensate the large pitch torque at lower  $\alpha$ . Since both canards are at their extreme, the already limited roll authority disappears, thus jets are needed for lateral stability (particularly with the constant roll disturbance induced by the "frozen" elevon scissoring). Aft side-firing jets are introduced, as seen in Fig. 77. Note that the latter firings are

## Example #18: Re-Entry, Lateral Maneuver: Fail Elevons



**Figure 79**

needed primarily in negative roll to compensate the secular elevon torque (the brief positive roll impulse at 500 sec. is used to achieve bank for the lateral position maneuver). Vehicle yaw can be easily handled by the rudder during this portion of the test; these firings are needed for roll. Because the required response is much larger, note the increase in magnitude typical of the latter jet firings. This indicates that commanded duty cycles were much larger (or several jets fired simultaneously), resulting in a considerable increase in fuel consumption. The minimum jet firing

**Example #19: Re-Entry. Lateral Maneuver: Fail Canards**

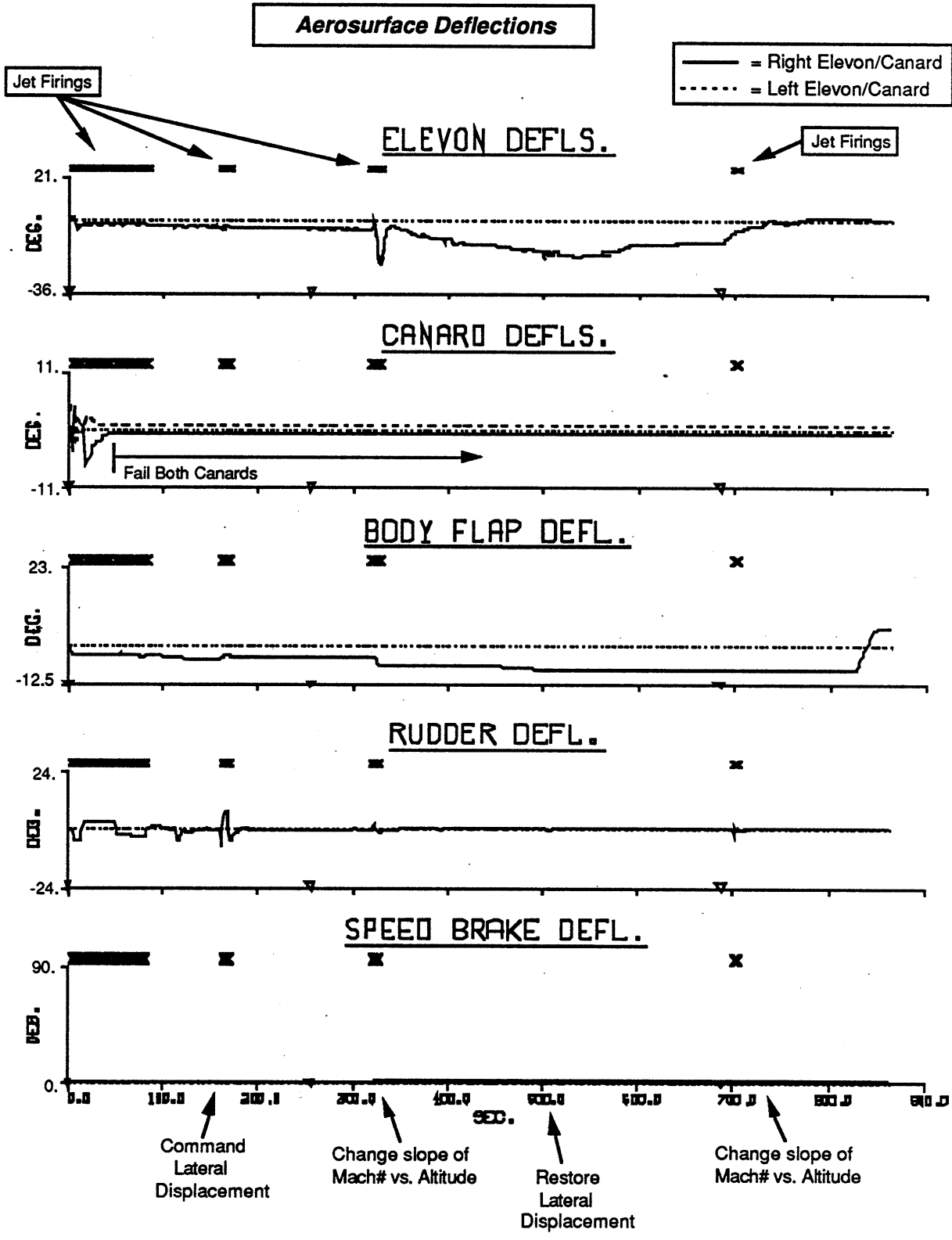


**Figure 80**

# Example #19: Re-Entry, Lateral Maneuver; Fail Canards

## Jet Performance

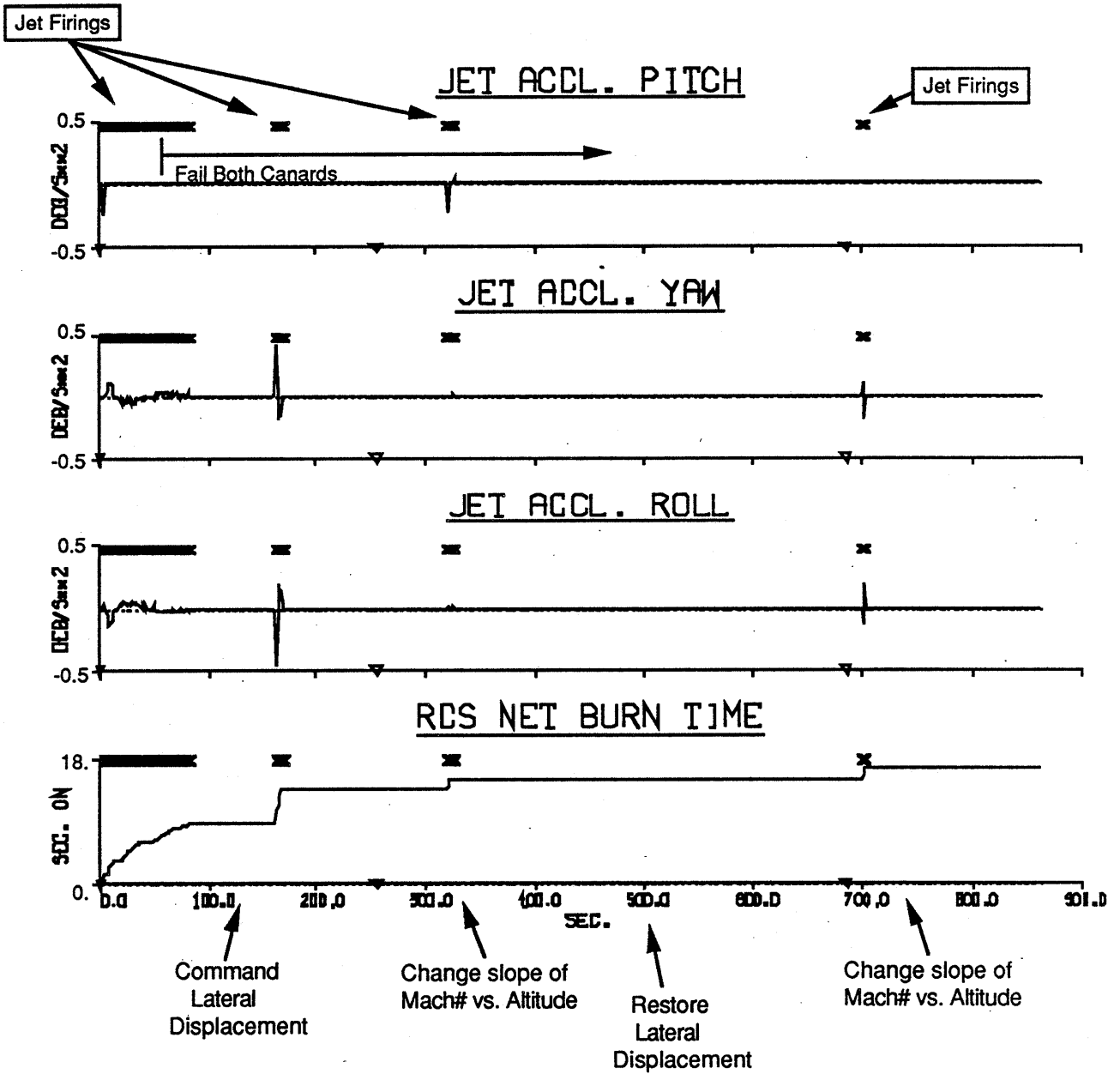


Figure 81

### Example #19: Re-Entry, Lateral Maneuver: Fail Canards

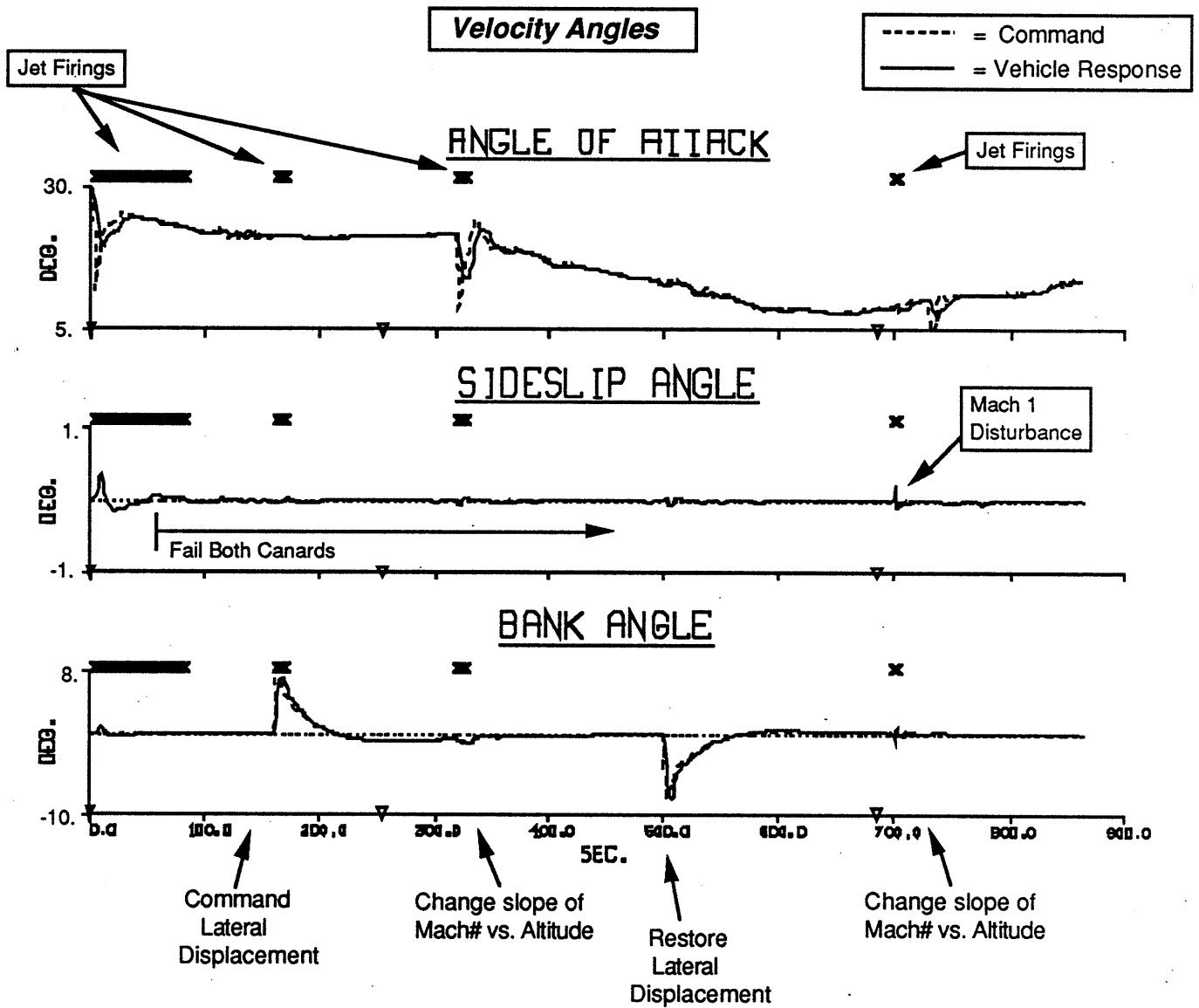


Figure 82

duration is 320 msec. at these altitudes (as opposed to 80 msec. higher up), which leads to increased granularity in modelled jet firings.

Figure 77 indicates that jets were not needed for pitch control while the canards and body flap were pinned against their stops. The additional pitch authority seemed to be derived from the speedbrake, which is seen to deflect appreciably (despite its high cost) during the latter jet firings. A pitch component is evident, however, in the set of firings used to establish the initial bank for the lateral maneuver (at 175 sec.). This did not occur in the previous "ideal" example (Fig. 73), but is

### Example #19: Re-Entry, Lateral Maneuver: Fail Canards

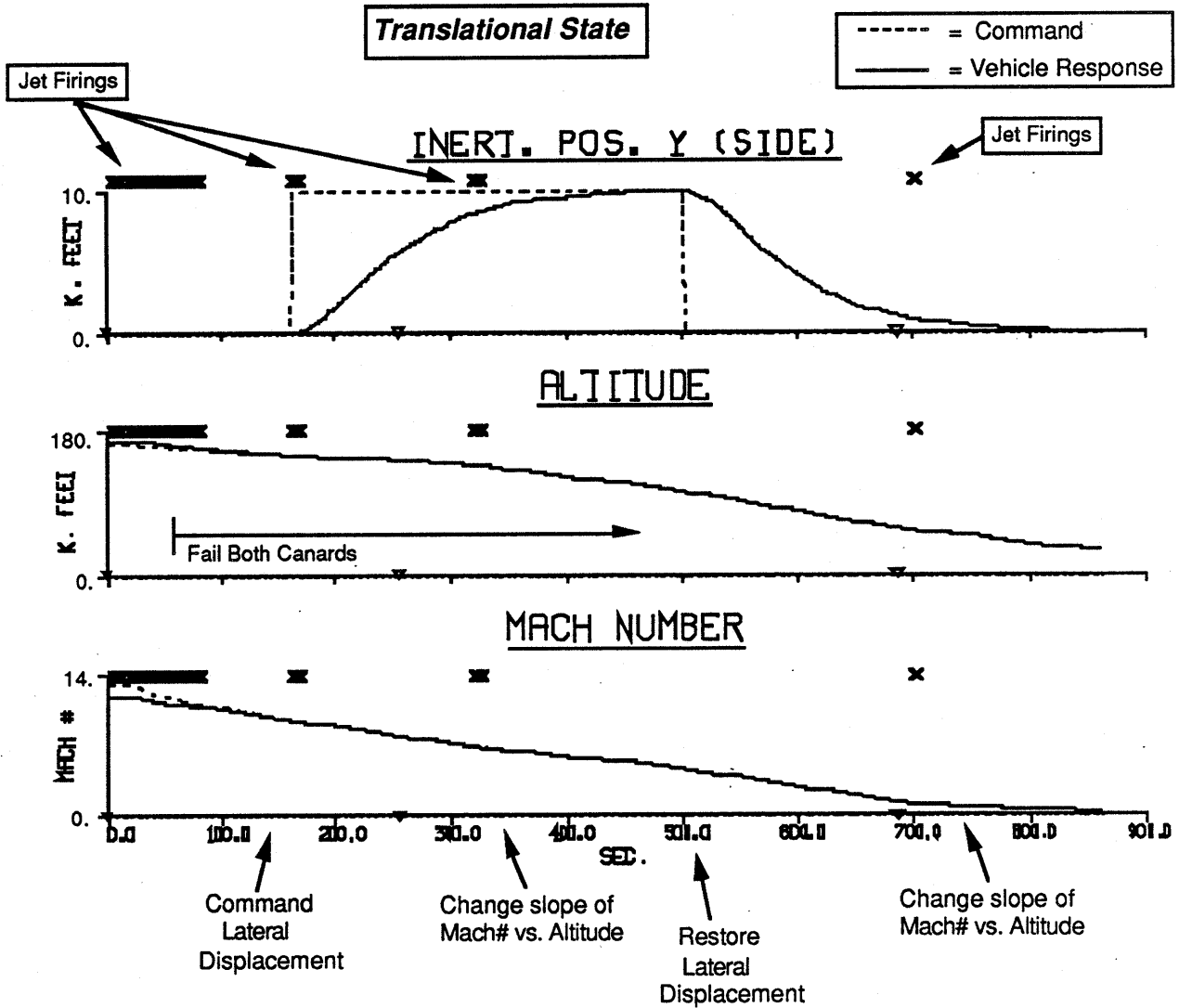


Figure 83

introduced here to compensate for the limited pitch and roll authority available from the truncated actuator set.

Velocity angles (Fig. 78) change as commanded (dashed curves). The lateral impulse is seen to be successfully achieved (Fig. 79), and the commanded longitudinal entry corridor is continuously tracked.

In the next example, the elevons remain active across the entire re-entry. Instead, the left & right canards are failed (ie. frozen) 45 sec. after the start of the test. Results are given in Figs. 80 → 83.

The canards are failed (in Fig. 80) shortly after the initial  $\alpha$  impulse. The elevons are then used to generally manage pitch and roll. Although the canards are failed with significant scissoring, this translates into a minute roll disturbance; very little elevon scissoring is needed for compensation (the situation here is opposite the previous test, where wide canard scissoring was needed to compensate a small elevon misalignment). The first two intervals of jet firings (through  $t = 200$  sec.) are entirely lateral, as seen in Fig. 81 and typical of previous examples. Additional jet assistance, however, is needed to attain the commanded  $\alpha$  impulse after 300 sec. have elapsed. As indicated in Fig. 81, this is a pitch firing; it was introduced to gain extra pitch authority that was formerly accommodated by the canards (this  $\alpha$  impulse is quite rapid, and requires the actuators to produce a fast change in pitch torque). The speedbrake was also slightly deflected here to aid in pitch control, as seen in Fig. 80.

As  $\alpha$  decreases, the elevons are brought negative to combat changing airframe pitch torques. Because of the wider deflection range available (up to  $-35^\circ$ ), the elevons were able to maintain pitch/roll control in the low  $\alpha$  region (the canards are only able to deflect up to  $+10^\circ$ , which limited the potential pitch authority in the previous example). Additional body flap deflection is evident in this region (although it was not saturated, as in the previous test) to aid in compensating the loss of canard-contributed pitch authority. A brief lateral jet firing was introduced to counter disturbance encountered upon approach to Mach 1 later in the test. The limited choice of available actuators made the firing optimal here for 3-axis control; it could probably be suppressed by increasing the mean jet-to-aerosurface cost ratio.

Velocity angles (Fig. 82) and translational states (Fig. 83) were seen to be well-tracked throughout this test, in spite of the canard failures.

In most of the previous examples, canards were brought to positive deflection at the start of the test, and maintained there for nearly the full entry duration. Because of thermal and aerodynamic effects, deflection of aerosurfaces into the airflow may be undesirable during certain flight regimes. This is particularly true of forward surfaces, such as canards, which appreciably perturb the airflow and are subject to extreme thermal loading. The drag-minimization objective was somewhat able to address this concern, as illustrated in a set of previous examples. This method, however, did not impose a hard constraint on allowed deflection; as seen in the example of Figs. 68  $\rightarrow$  71, canards were eventually deflected down (positive) when the selection deemed this action optimal to compensate the changing pitch torque at lower  $\alpha$ . Although increasing the drag minimization cost contribution can aid in its expression, imposing a hard constraint on perilous aerosurface deflection will guarantee that fiducial limits will not be violated. Such constraints will be time-dependent, and will evolve as the aircraft crosses through different flight regimes.

# Example #20: Re-Entry, Lateral Maneuver; Bound Canards

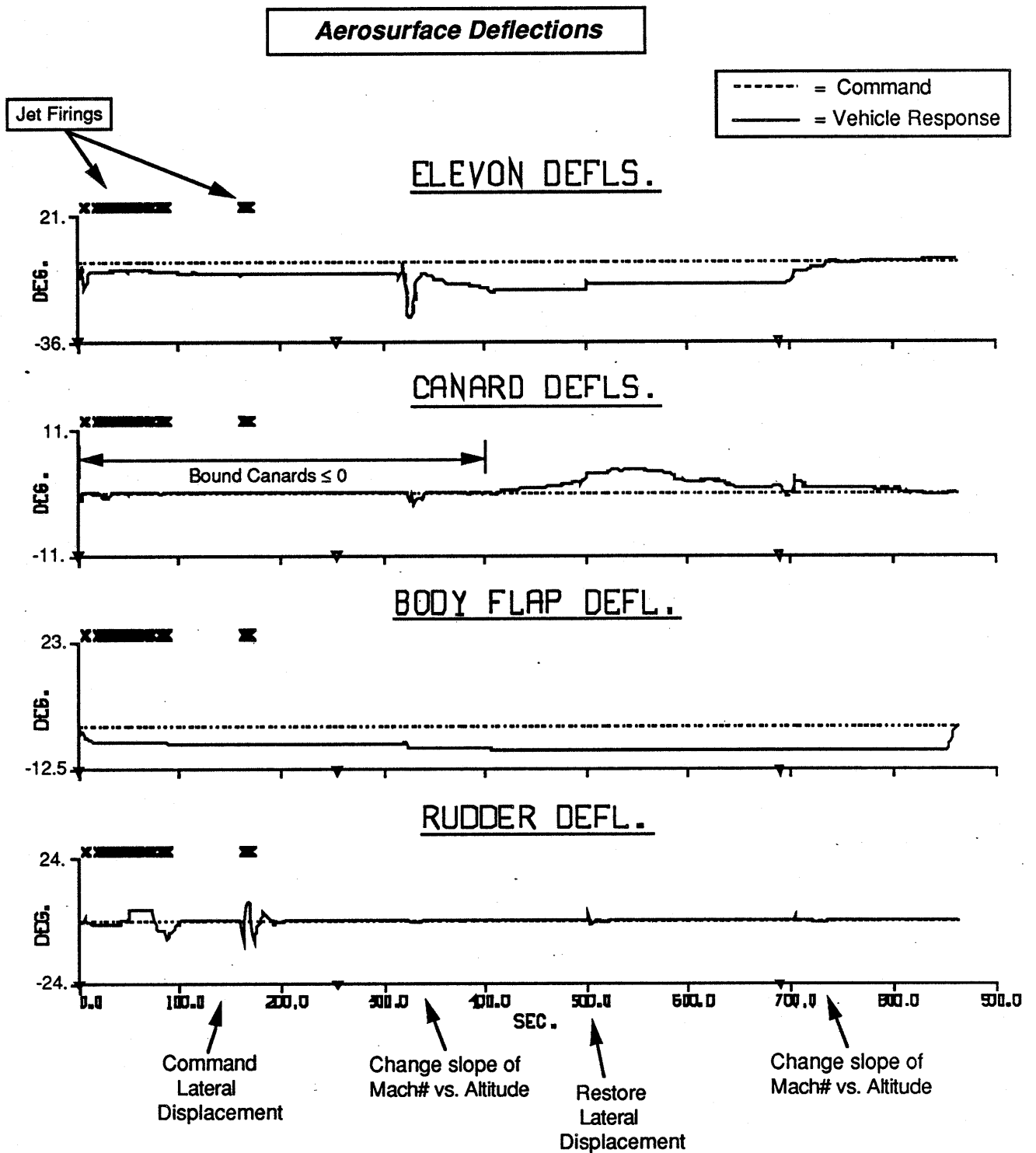


Figure 84

# Example #20: Re-Entry, Lateral Maneuver; Bound Canards

## Jet Performance

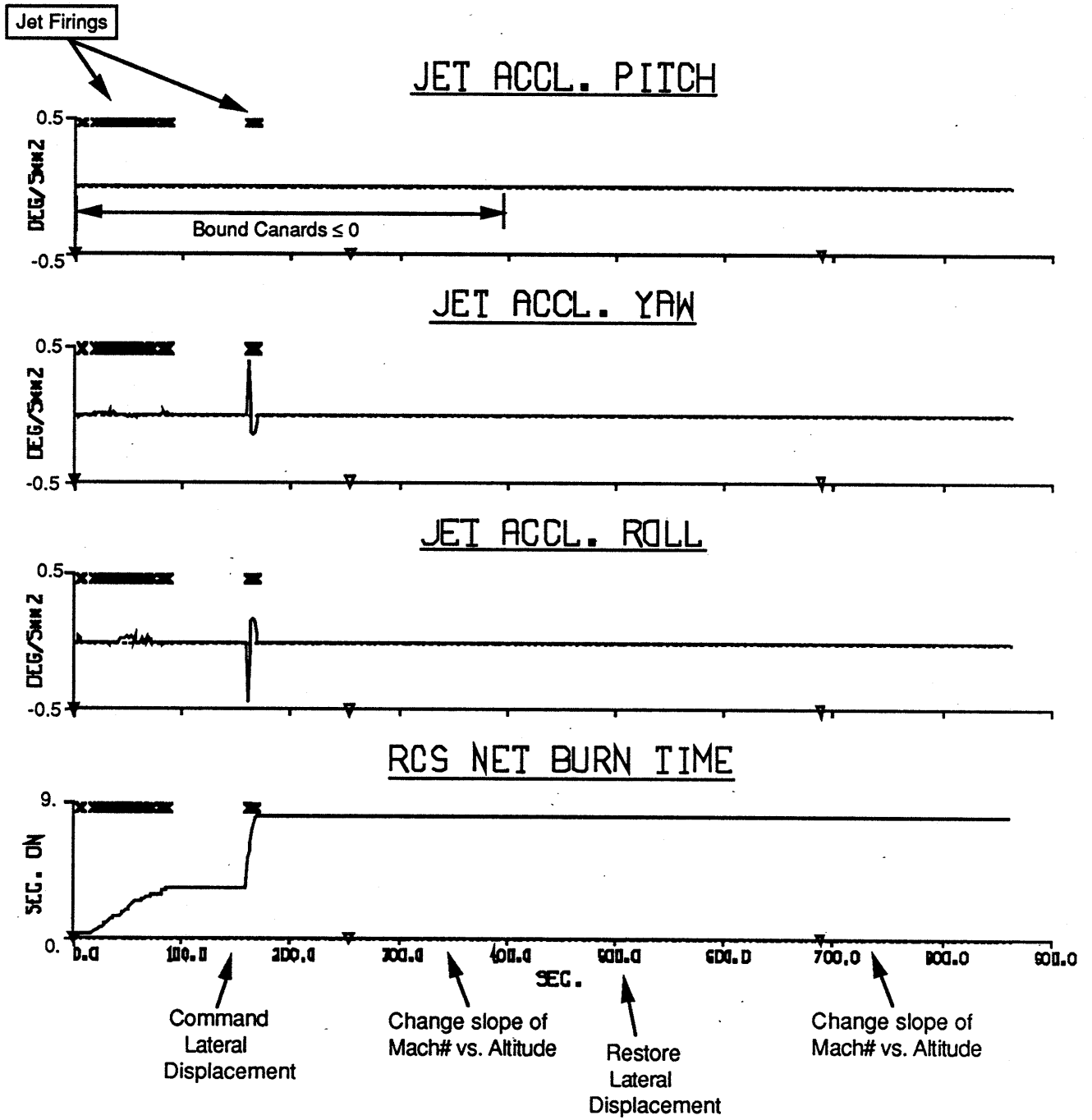
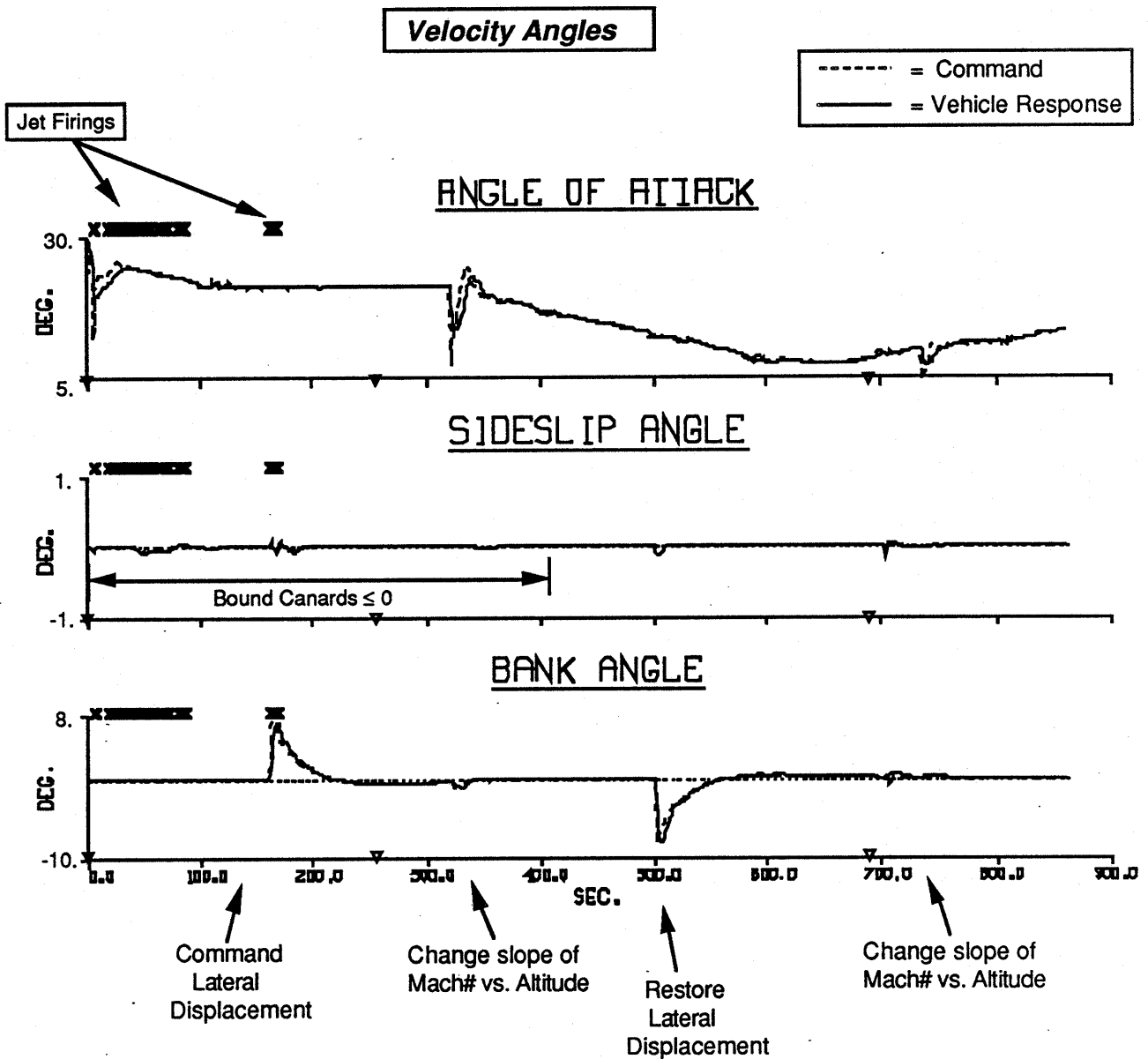


Figure 85

## Example #20: Re-Entry, Lateral Maneuver; Bound Canards



**Figure 86**

This feature is directly addressed in the next example. All aerosurfaces are continually available to the selection throughout the test. The canards, however, are constrained (via their simplex upper bounds) to refrain from positive deflection until 400 sec. into the flight.

Results are given in Figs. 84 → 87. The effect of the canard limit is immediately evident in the plots of aerosurface deflection (Fig. 84; compare with the nominal test results in Fig. 72). In order to balance pitch torque, the canards initially stay mainly at zero deflection and do not violate

## Example #20: Re-Entry, Lateral Maneuver; Bound Canards

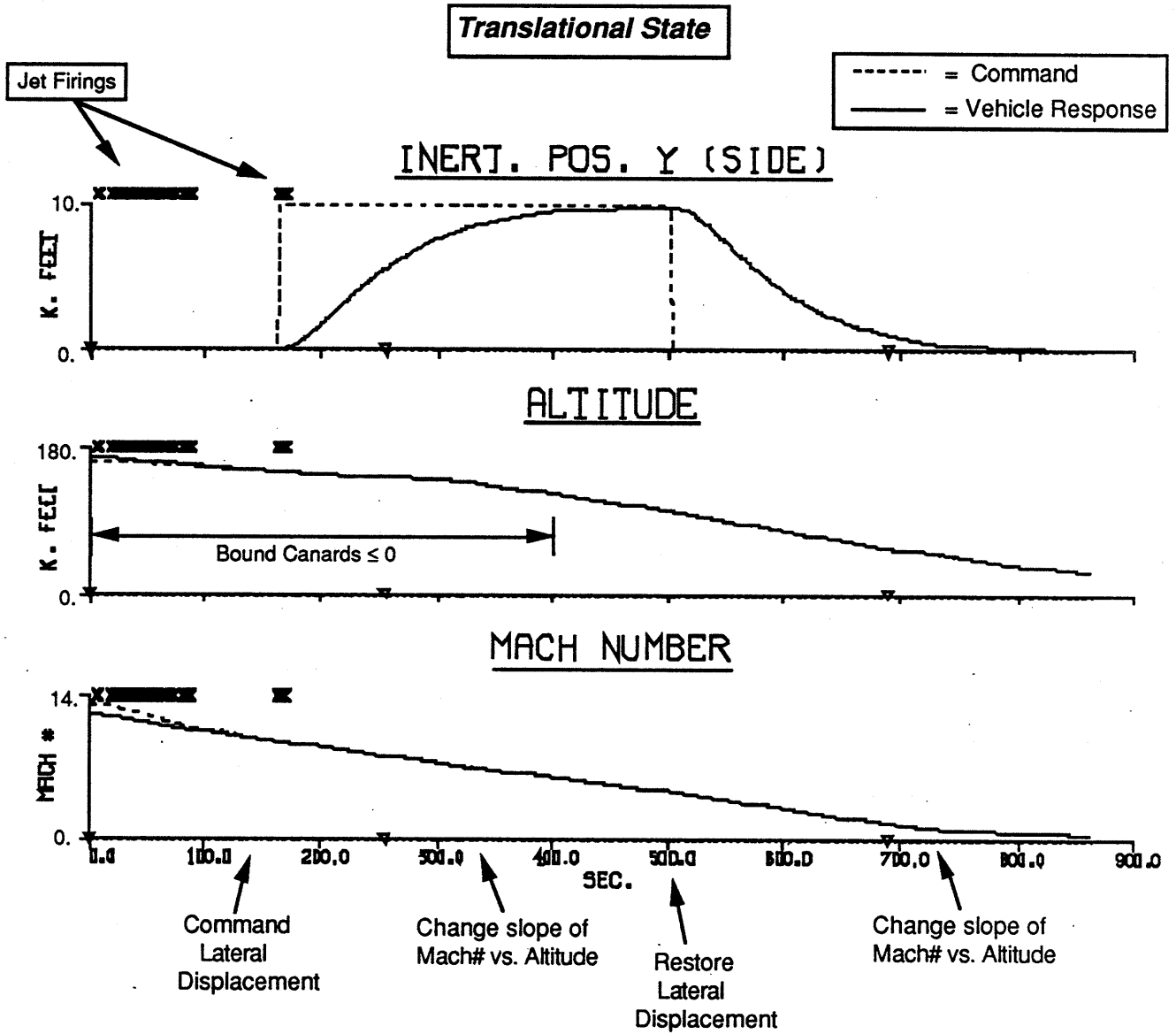


**Figure 87**

the upper bound by deflecting positive (they were positive by a few degrees in Fig. 72). Occasional forays into negative deflection were performed to balance  $\alpha$  impulses and jet disturbances. The elevons are seen to deflect more negative (compared with the nominal case of Fig. 72) to attain the additional pitch authority. After the positive canard bound is restored to its  $10^\circ$  maximum at 400 sec., the canards promptly begin drifting into positive deflection to better assist in balancing pitch torques.

**Example #21: Re-Entry. Lateral Maneuver; Schedule Speedbrake Cost**

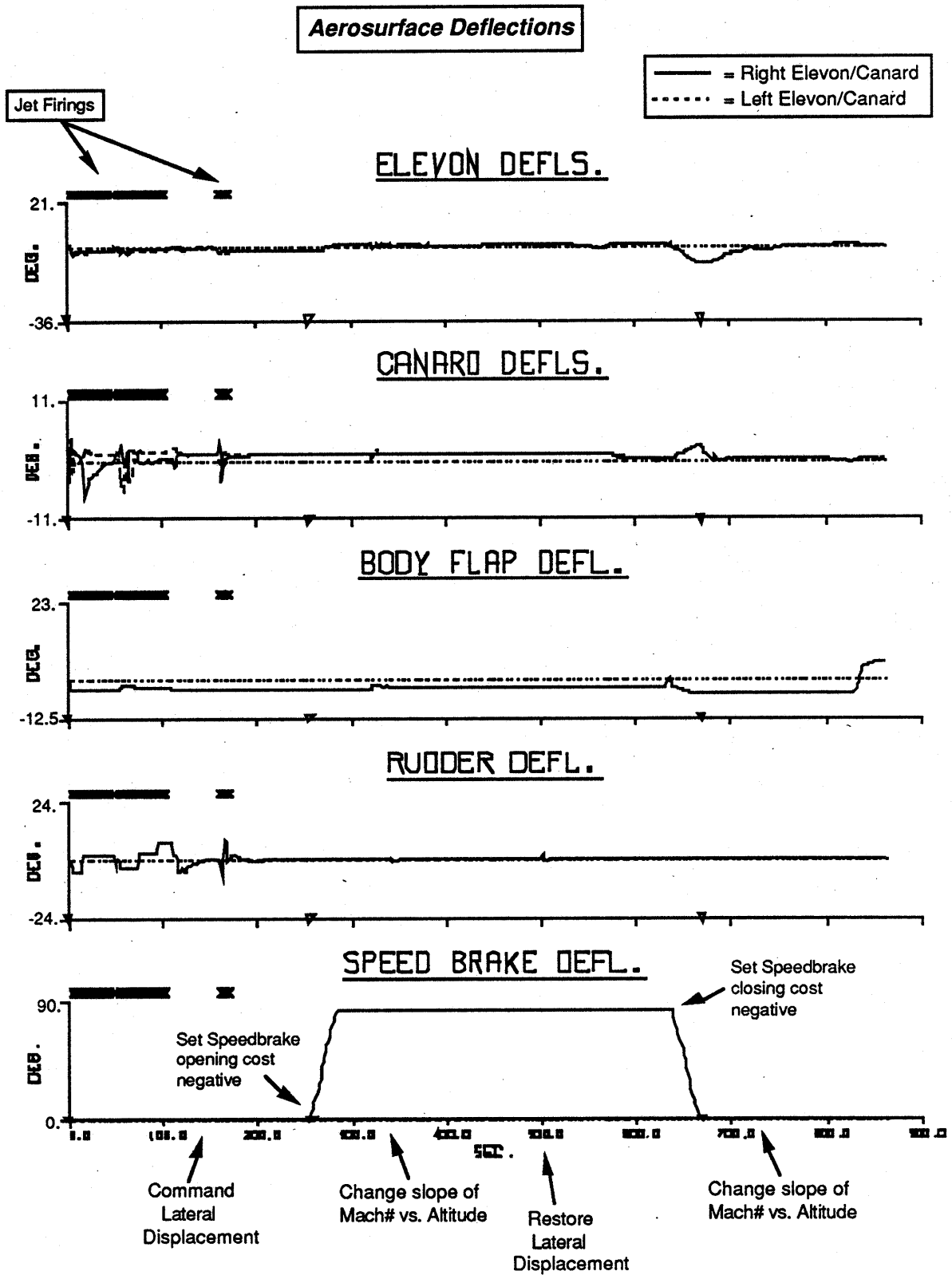


**Figure 88**

## Example #21: Re-Entry, Lateral Maneuver: Schedule Speedbrake Cost

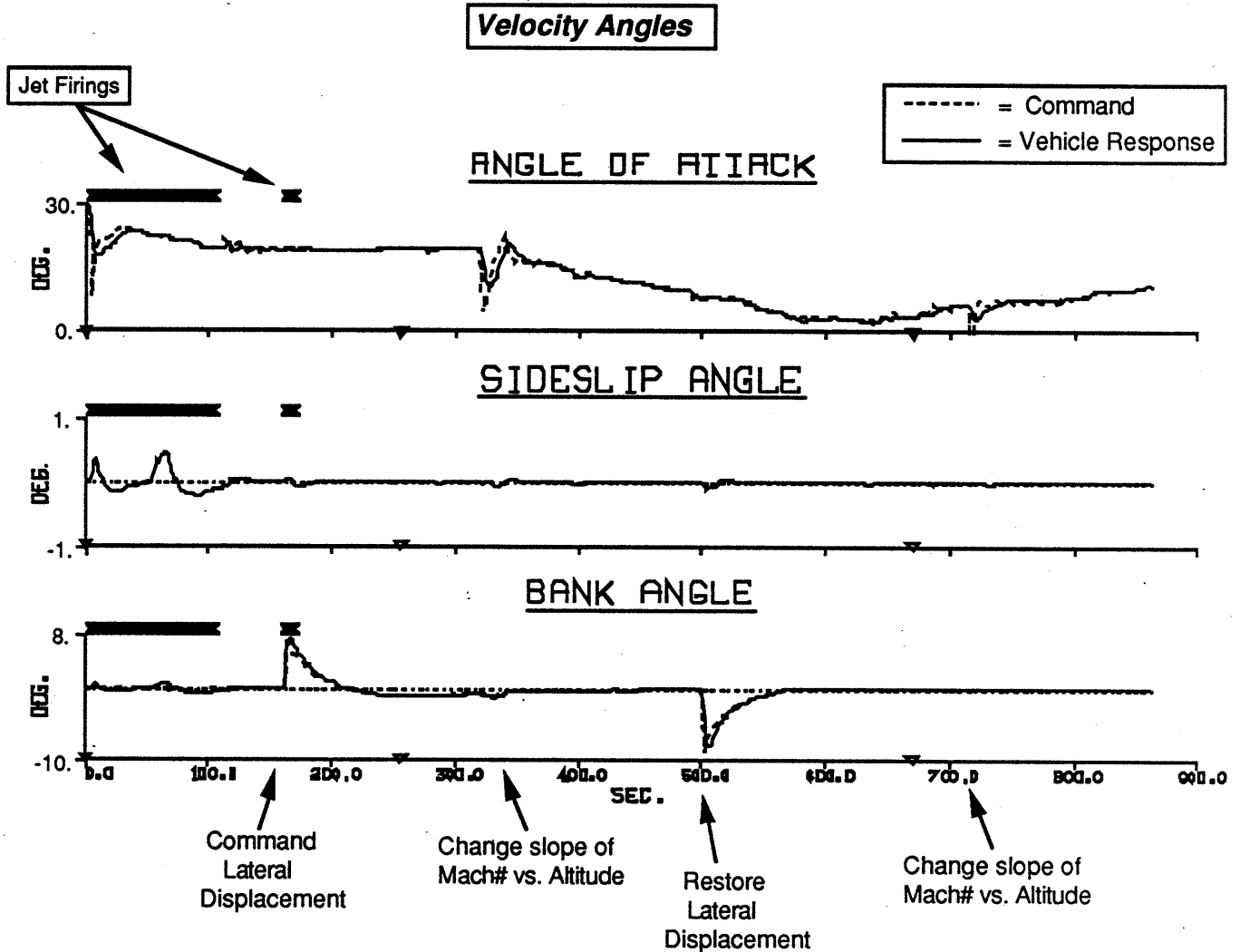


**Figure 89**

The jet firings (Fig. 85) are seen to be purely lateral in this example; the major jet contribution was applied to achieve the needed bank assistance at high  $\alpha$  for the commanded side-position kick. Velocity angles (Fig. 86) and translational states (Fig. 87) were seen to be well-behaved & well-tracked, despite the constrained canard freedom. No speedbrake deflection was commanded in this test, thus its plot was not included in Fig. 84.

Application of the speedbrake was seen to be considerably limited in the previous examples. This is due to the high cost associated with its selection & deflection ( $K_0$  and  $K_A$  respectively in Table 4), and limited control authority, particularly at high  $\alpha$ . It was seen to participate to a certain extent in some tests, but only when the pitch control authority was severely

## Example #21: Re-Entry, Lateral Maneuver; Schedule Speedbrake Cost

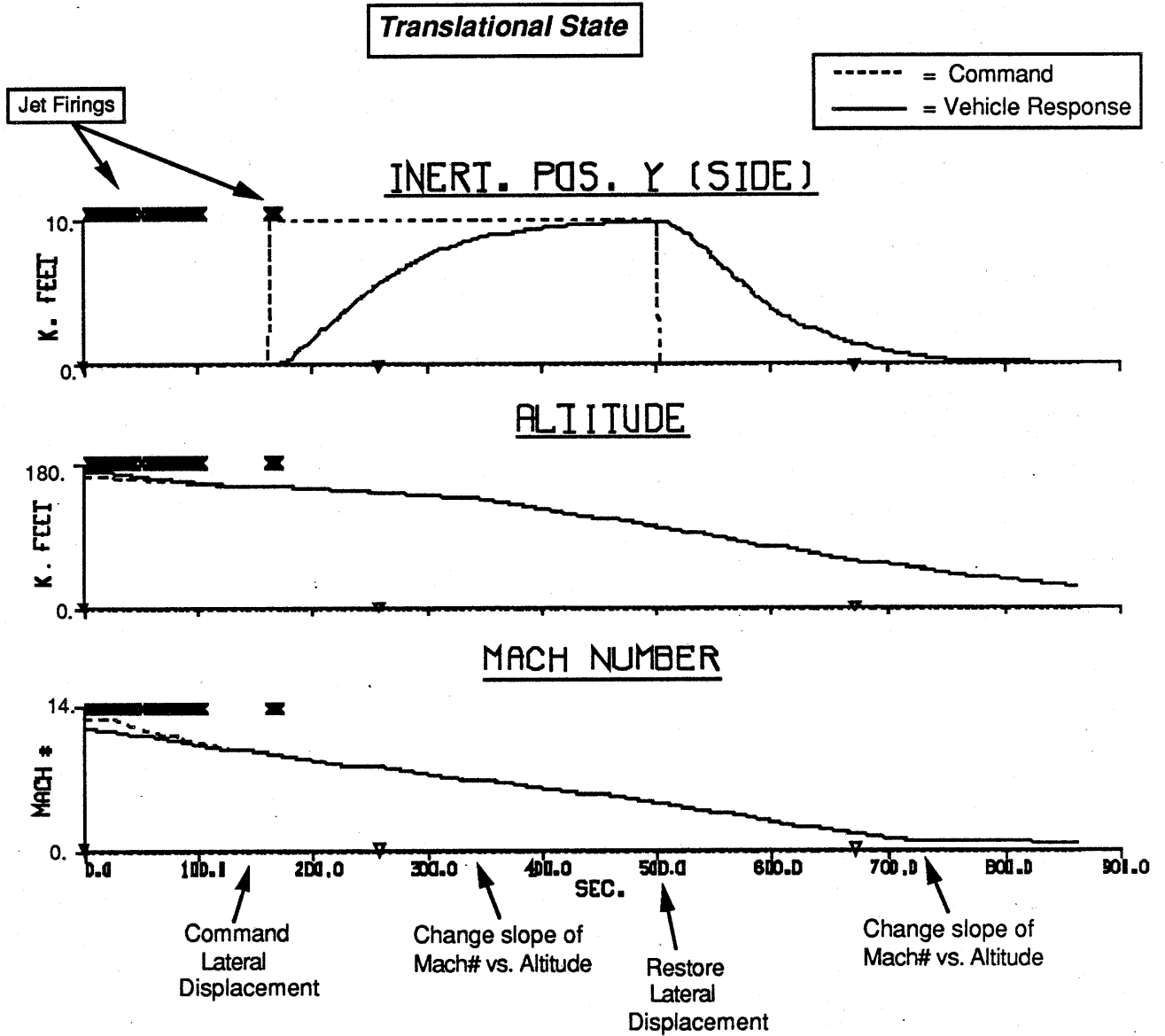


**Figure 90**

stressed (where it was required) or when the objective function was modified to account for translational control (where it was made optimal). In actual Shuttle re-entries (Ref. [29]), however, the speedbrake is commanded to open to maximum during a portion of the entry corridor, as indicated in Fig. 24. The linear programming scenario can be adapted to encourage special behavior of specific actuators through negative costs (as has been done with the body flap in all of these examples). The following series of tests adapt this concept to speedbrake application.

**Example #22: Re-Entry. Lateral Maneuver: Bound Speedbrake**

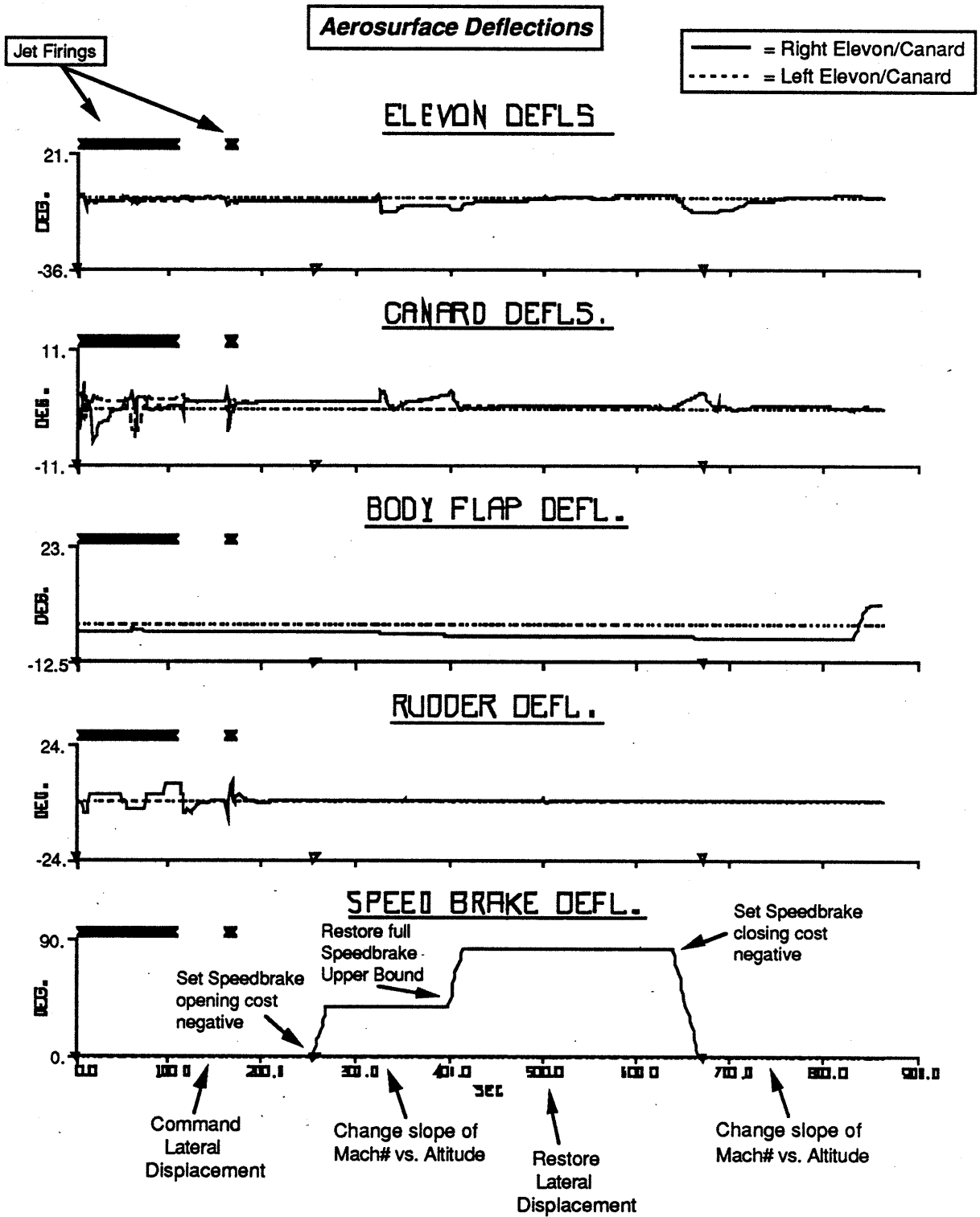


**Figure 91**

## Example #22: Re-Entry, Lateral Maneuver: Bound Speedbrake

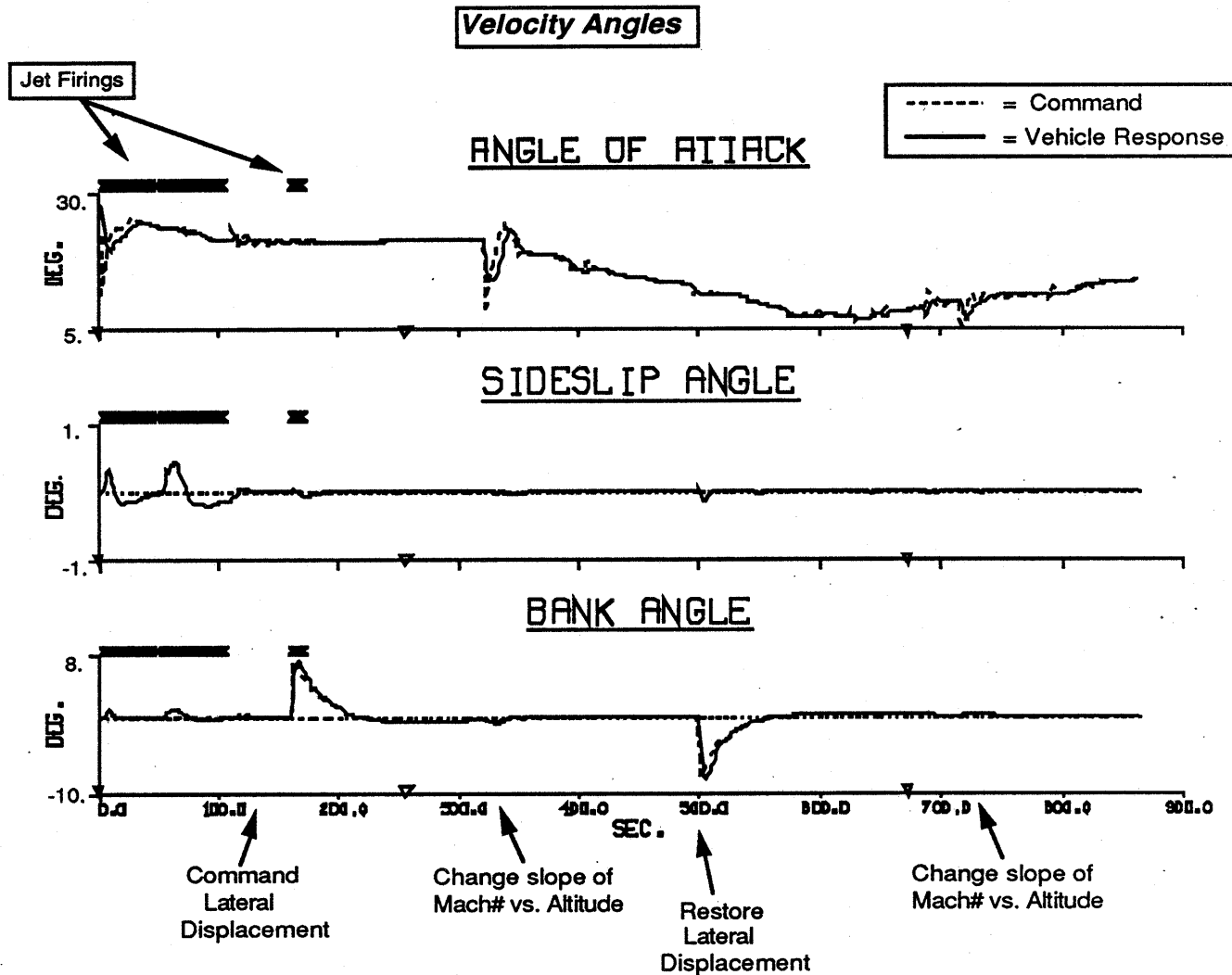


**Figure 92**

The next two examples employ the negative-speedbrake cost scheduling logic discussed in Sec. 4.3 to encourage speedbrake deflection between Mach 8 and Mach 5 (as an approximation to the prescription of Fig. 24). In the first test (Figs. 88 → 90), all aerosurfaces are continually available and allowed to deflect up to stop limits. Looking at the aerosurface deflections (Fig. 88), the initial portion of the test is identical to the nominal case (Fig. 72). As soon as the speedbrake's positive-deflection activity vector attains negative cost (at  $t = 250$  sec.), it is fully deployed at its maximum attainable slew. The elevon and canard deflections are reduced (relative to their profiles in Fig. 72) to compensate the change in pitch torque. When the speedbrake's negative-deflection

## Example #22: Re-Entry. Lateral Maneuver: Bound Speedbrake

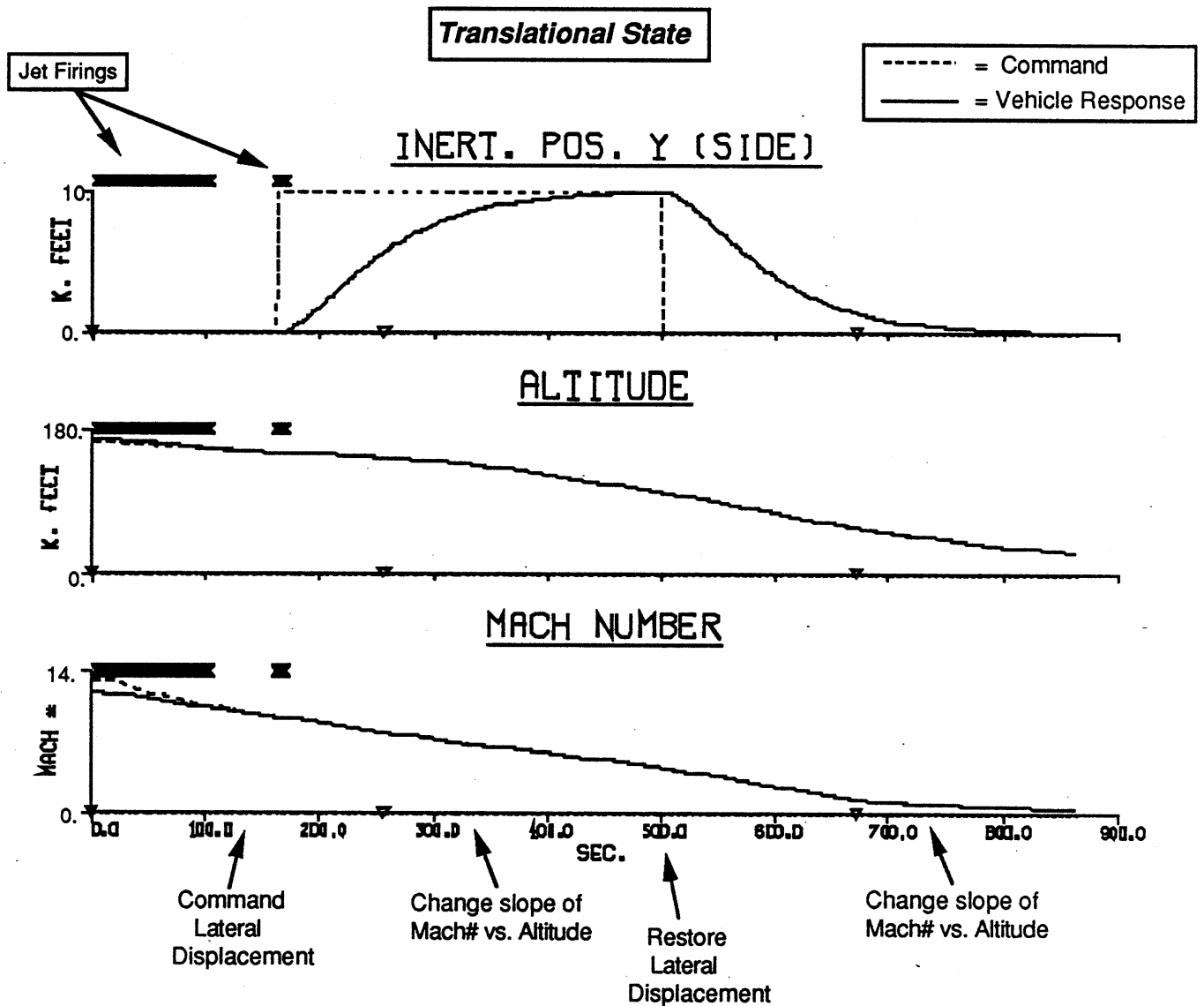


**Figure 93**

activity vector is given negative cost (at  $t = 640$  sec.), it is slewed back to zero deflection, resulting in elevon and canard deflection being needed once more to null pitch torque (as in Fig. 72).

Jet accelerations are identical to those in Fig. 73, thus their plot is omitted for this example. Velocity angles (Fig. 89) and translational state (Fig. 90) are seen to again be well-behaved and appropriately answer commands, indicating that the simplex selection had little difficulty including the speedbrake activity in its selected solutions.

Of course, under actual operation, it may not be desired to abruptly deploy actuators such as the speedbrake to full deflection at maximum slew; it might prove more apt to schedule their activity to conform to the dynamic characteristics of the current flight path. This may be accommodated in simplex by scheduling the negative cost associated with actuator deployment in a more complex fashion; if the negative costs are initially small, the actuator will tend to deploy more slowly.

Another method is available, however, that provides precise control of maximum actuator deflection; the actuator upper bound can be made time-dependent, and varied as the deflection cost goes negative. This is attempted with the speedbrake in the next example. Although the negative cost profile is identical to that used in the previous test, the upper bound on speedbrake deflection is set initially at  $40^\circ$  until roughly 410 sec. have elapsed, then extended to its full maximum of  $87.2^\circ$ .

Results are given in Figs. 91  $\rightarrow$  93. The speedbrake is indeed seen (Fig. 91) to respond to the bounded profile sketched above, and canard/elevon deflections provide appropriate pitch compensation as the vehicle changes  $\alpha$  and the speedbrake is extended. Velocity angles (Fig. 92) and translational parameters (Fig. 93) also appear satisfactory in this example. Jet accelerations are again identical to the nominal case (Fig. 73), thus are not presented here.

## **5.5) Response to Modelling Error**

All previous examples investigated the ability of the linear programming control strategy to adapt through specification of an objective function, upper bounds, and failure flags. The environment was fairly benign; no mismodelling was introduced between the predicted actuator effect (via the activity vectors) and the actual vehicle response (aside from the linearizing assumptions, which, in some cases, can have significant effect). The final group of examples presented here deliberately distort the activity vectors (or environment model) to ascertain the effect of uncertainty on the hybrid control strategy.

This is an extremely cursory approach to this investigation. An actual vehicle will possess an onboard sensor array and estimation logic to track the vehicle environment and predict actuator authority. Although such systems should be incorporated into these simulations to more realistically ascertain the performance of any control scheme, the detailed work required is beyond the scope of this study and remains a topic for future efforts[27]. Instead, the examples presented

# Example #23: Re-Entry, Lateral Maneuver; Smear Jets

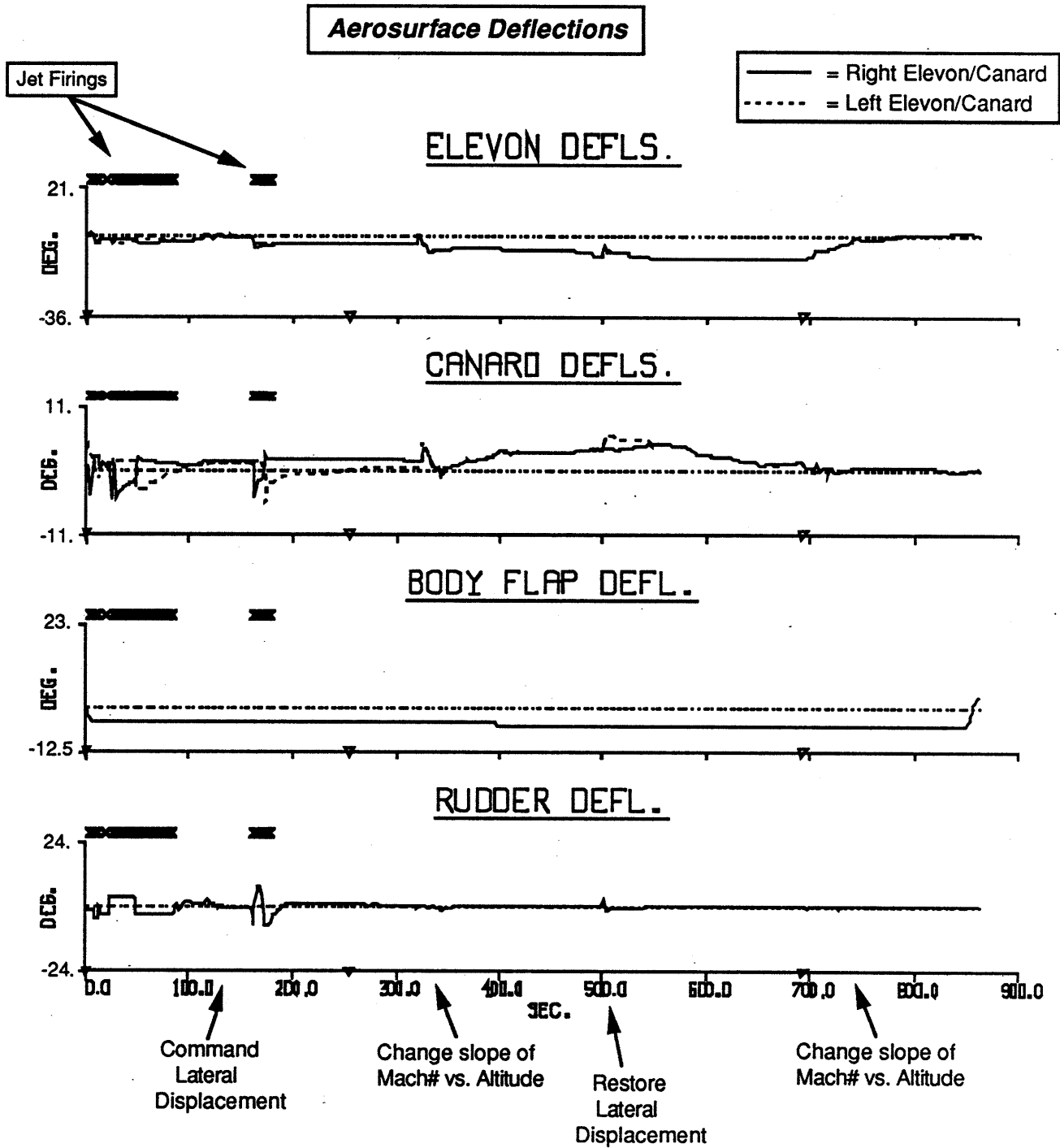
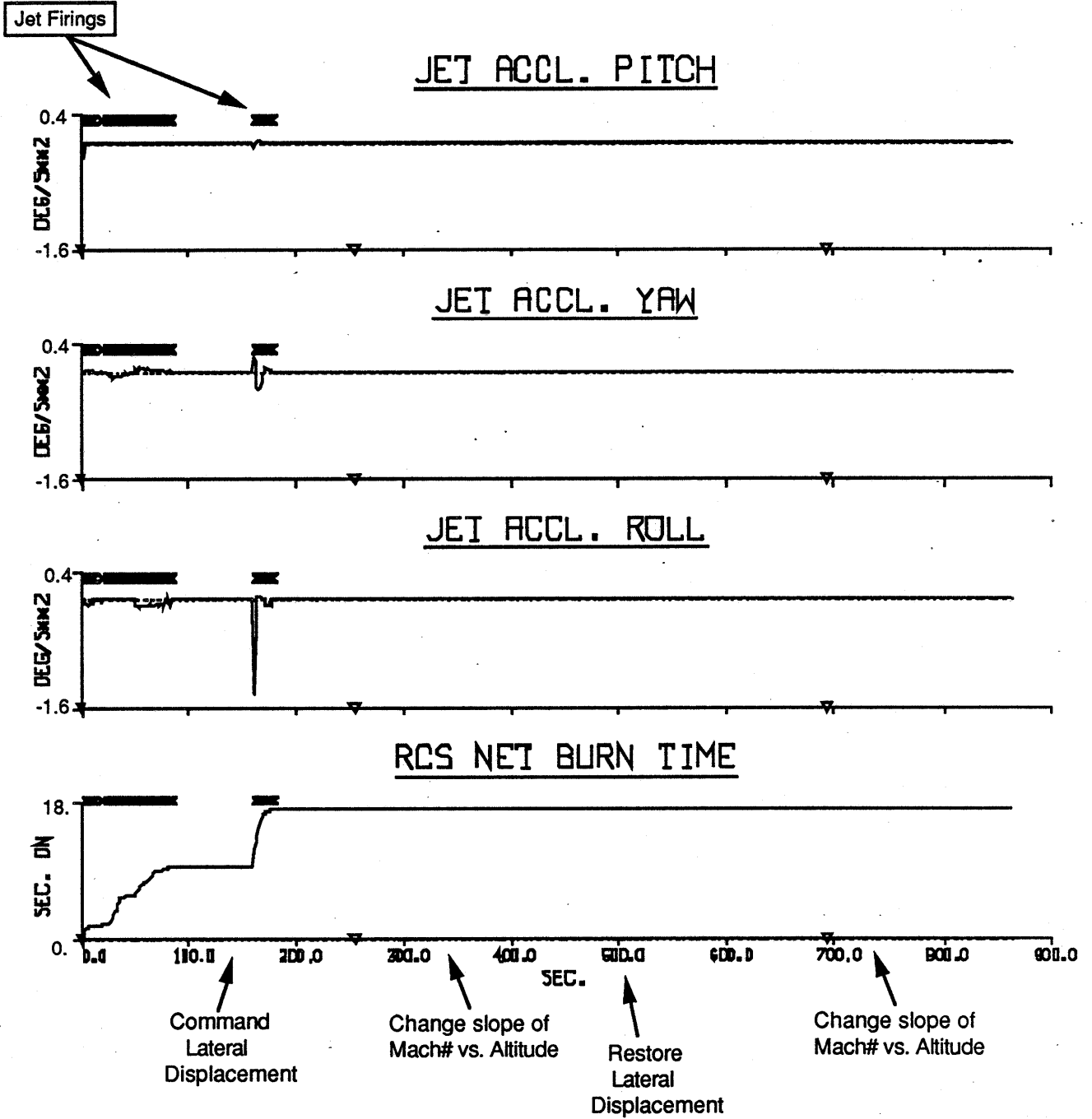


Figure 94

**Example #23: Re-Entry, Lateral Maneuver; Smear Jets**

**Jet Performance**



**Figure 95**

**Example #23: Re-Entry, Lateral Maneuver: Smear Jets**

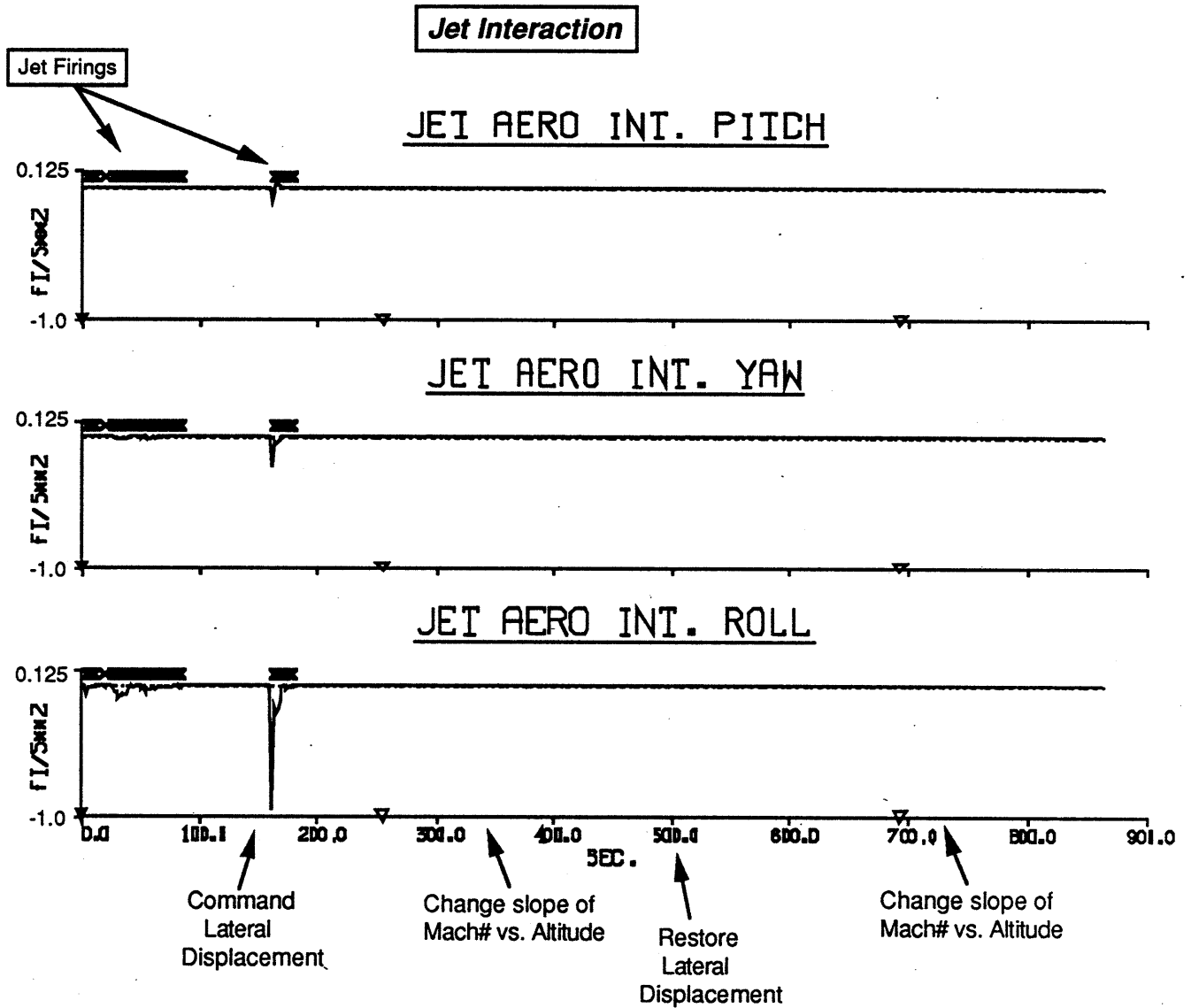


**Figure 96**

here merely perturb aerodynamic quantities and observe the vehicle response; active estimation is not considered.

The first example employs the model of jet aerodynamic interaction that was developed in Sec. 3.4. Jet activity vectors continue to employ vacuum jet accelerations, but their effect on the vehicle environment includes the full interaction perturbation stated in Eq. 25 and the associated discussion. Otherwise, the test is nominal; all actuators are assumed available, upper bounds

## Example #23: Re-Entry. Lateral Maneuver: Smear Jets

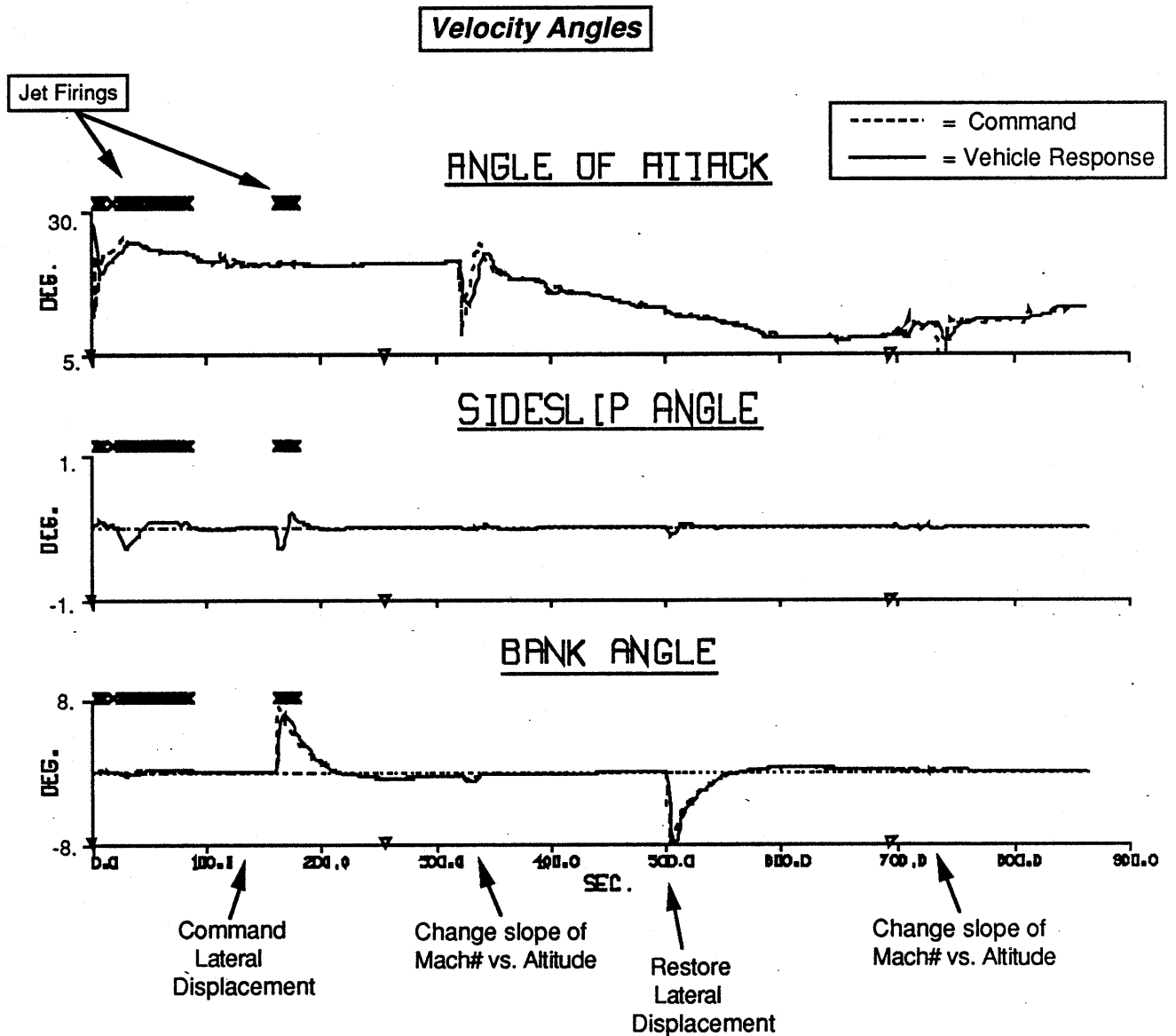


**Figure 97**

extend to the aerosurface stops, the objective function is standard, and the speedbrake is not coaxed with negative costs. Results are plotted in Figs. 94 → 98.

The aerosurface deflections (Fig. 94) do not appear unusual; canard/elevon scissoring is commanded to combat lateral disturbances (and assist in yaw control) during jet firings. The effect of aerodynamic perturbation, however, can be seen in the plots of jet acceleration (Fig. 95) and jet interaction (Fig. 96).

### Example #23: Re-Entry, Lateral Maneuver: Smear Jets

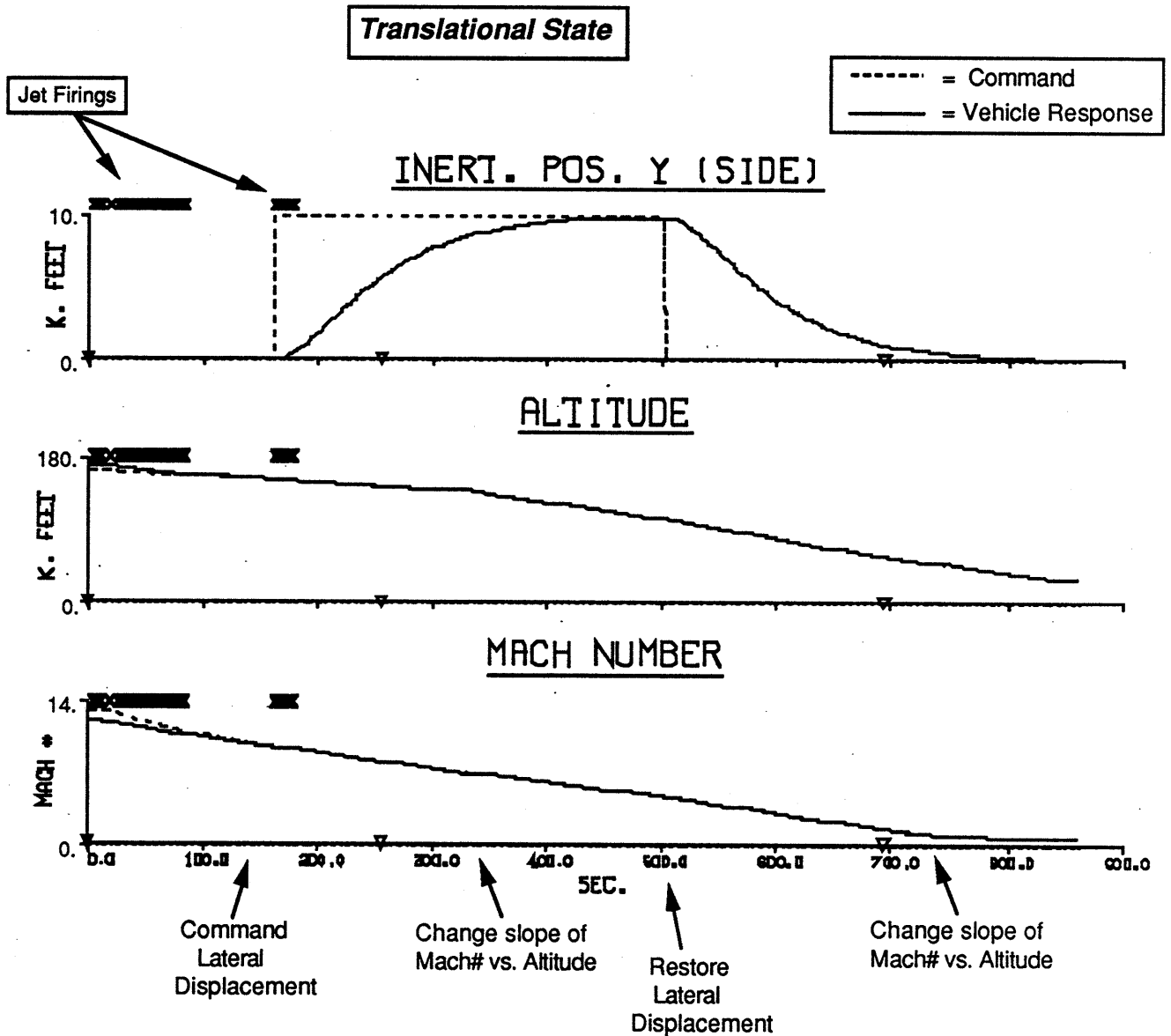


**Figure 98**

The plotted jet accelerations (Fig. 95) include the interaction effects; comparing with the interaction contribution (plotted independently in Fig. 96), one sees that the major interaction influence is along the roll axis. This is the primary phenomenon noted in most tests employing aerodynamic jet interaction; particularly in examples (such as these) using side-firing jets. The roll effect contributed by aerodynamic interaction can often approach or exceed the vacuum roll acceleration, depending on the number of jets firing simultaneously and the value of dynamic pressure (ie. the "momentum ratio" of Eq. 27). This indeed seemed to happen at roughly 175

sec. into the test, where jet assistance was needed to bank the vehicle for the 10,000 ft. lateral impulse. The spike in roll acceleration (Fig. 95) is mainly due to aerodynamic interaction (seen in Fig. 96). Because of the large need for yaw torque, three side-firing jets were brought in simultaneously, yielding a high momentum ratio, and thus large interaction effect.

Because the interaction does not dominate the jet yaw acceleration as it does in roll (although it is nonetheless significant), vehicle control was maintained throughout the test. The elevons and canards (which have plenty of roll authority) were able to cancel any errors arising from the jet interaction roll contribution. The jets are needed for yaw, but the distortion of jet response along this axis was not large enough to obliterate control (some error in jet response is always present from quantization effects). The big lateral firing at 175 sec. also resulted in a small pitch interaction contribution; aerosurface authority is always sizable in pitch, however, thus this had little effect on the vehicle.

Even though the jet authority was mismodelled, the fuel requirement (ie. net jet on-time in Fig. 95) is somewhat lower than the nominal case (Fig. 73). Small differences like this are mainly due to the divergence of state trajectories discussed at the beginning of this chapter. The jet firing policy pursued in the nominal test may have been more accurate (particularly in roll), but nonlinear aerosurface response and jet quantization effects introduced errors leading to larger sideslip & lateral disturbance, requiring additional jet activity. The policy pursued under jet interaction did not produce quite as wide a sideslip error (the distortion in jet firings was not significant enough to create problems), thus less jet activity was required. Again, small differences like these can be path-dependant; larger and more general effects (as seen in some of the other examples) indicate a specific trend in control behavior.

Velocity angles (Fig. 97) and translational state (Fig. 98) are entirely nominal, and show no effect from jet interaction. This example thus indicates that aerosurfaces can compensate for most jet interaction errors, since the major effect seems to be along vehicle roll for aft side-firing jets. In cases involving several jets firing simultaneously, however, the interaction can grow quite large, and should be accounted for in the control and selection procedure. Methods of accomplishing this were suggested in Sec. 3.4; ie. introducing estimation logic or applying constraints to jet firings. It must be noted that the jet interaction effects have been calculated here in a rather crude fashion (data of Ref. [16] were essentially fit by eye). A precise determination of the interaction contribution would require considerable additional effort (and is unneeded for this task).

The next test examines effects of stochastic "gusts" on vehicle performance. Gusts are modelled as random errors in dynamic pressure. Two white noise sources are used, and both are low-pass filtered; one is filtered heavily (with a time constant on the order of seconds), and the other is left with much wider bandwidth. Whenever the low-frequency filtered noise exceeds a pre-set threshold, the dynamic pressure is scaled with the wide-bandwidth noise. This causes

# Example #24: Re-Entry, Lateral Maneuver: Gusts

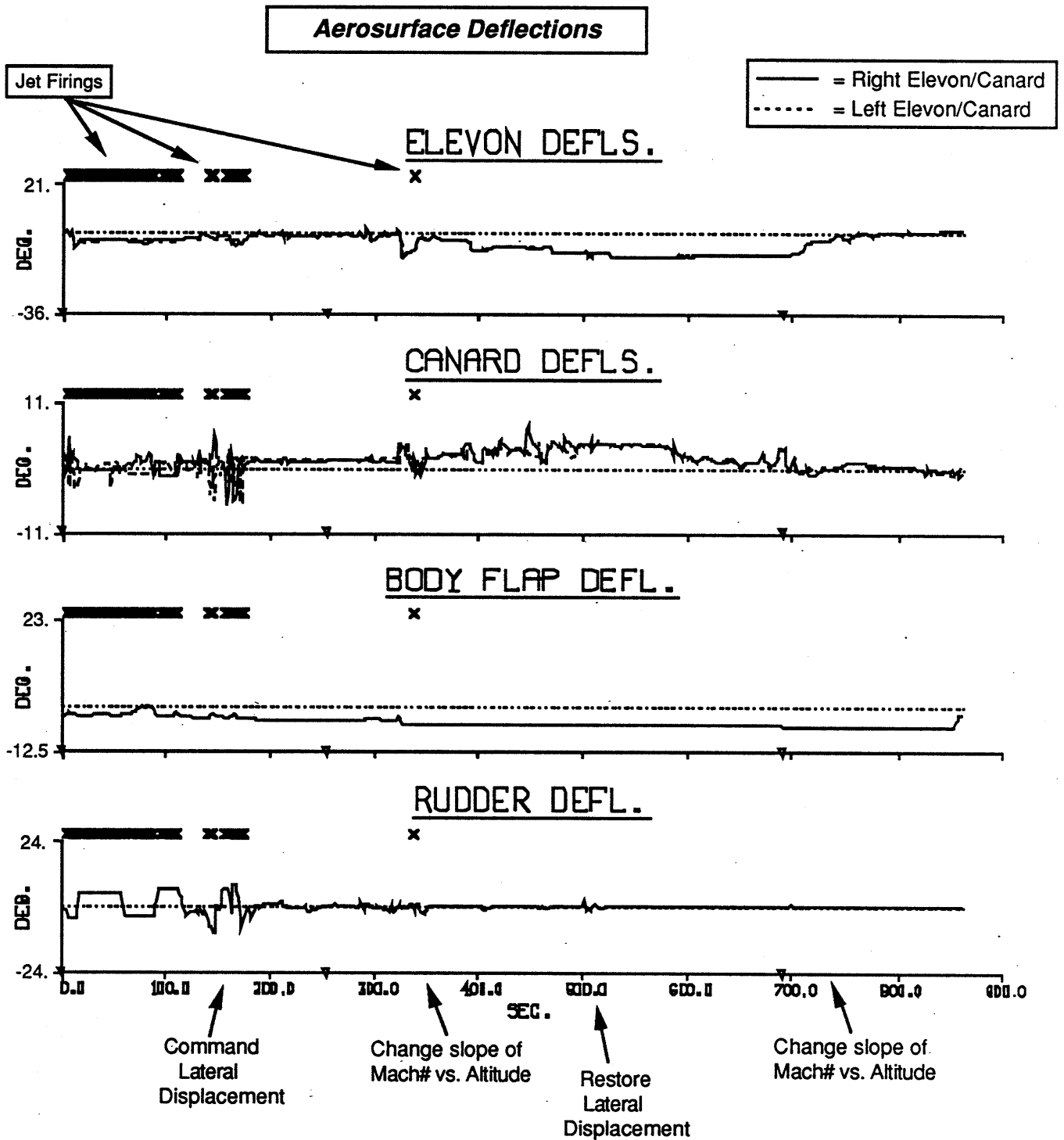


Figure 99

# Example #24: Re-Entry, Lateral Maneuver: Gusts

## Jet Performance

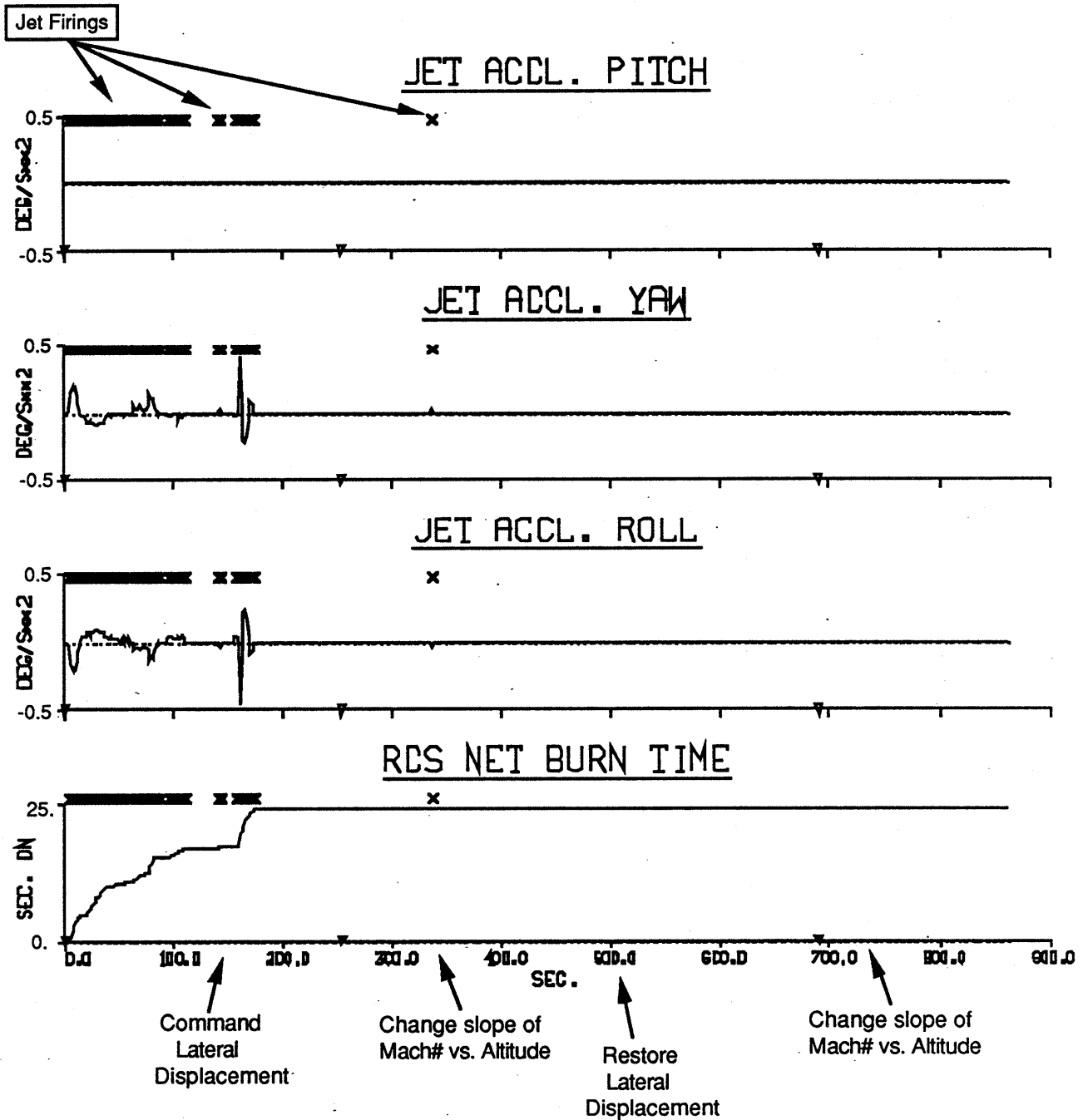
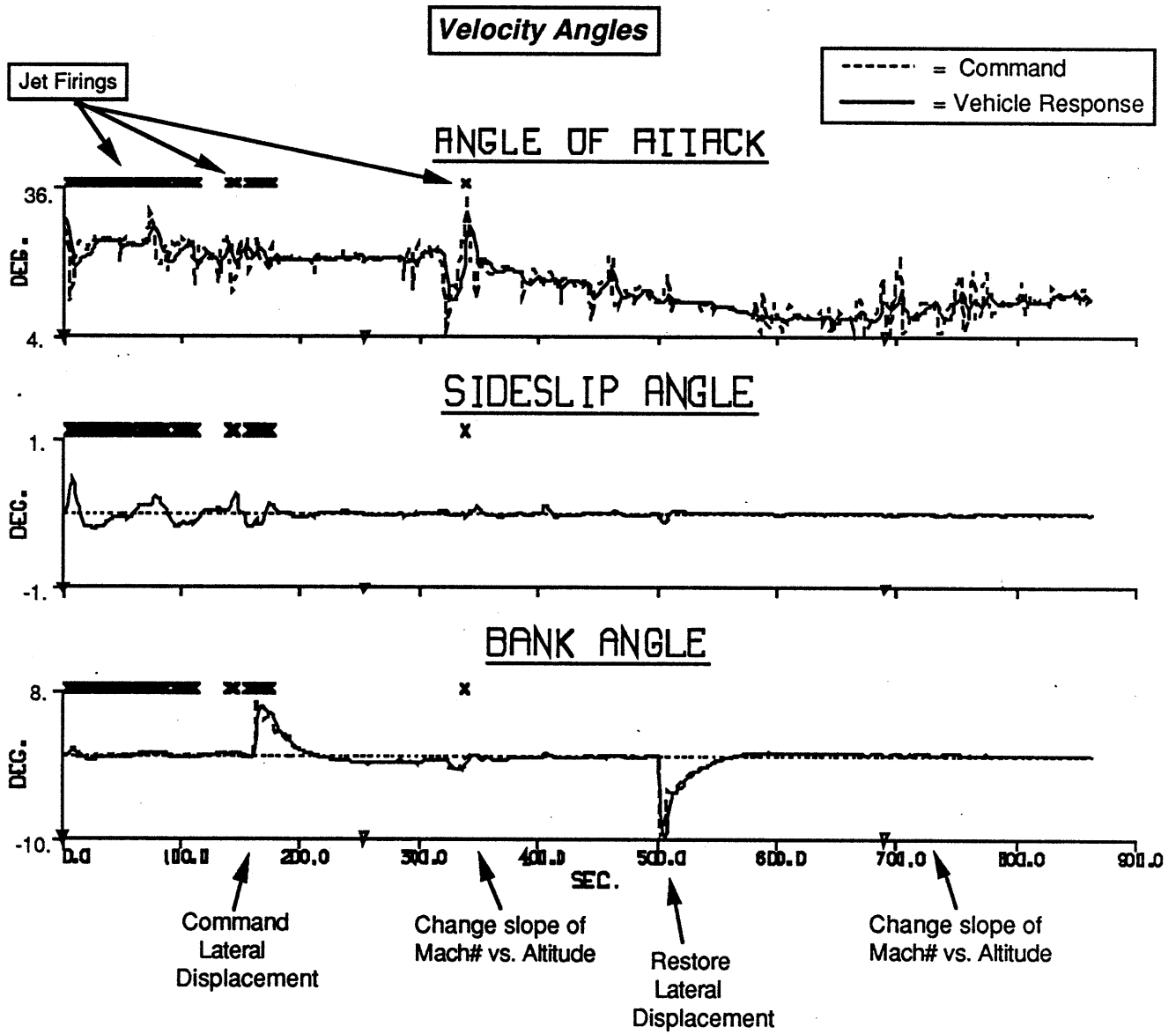


Figure 100

## Example #24: Re-Entry, Lateral Maneuver; Gusts



**Figure 101**

rapidly changing  $\bar{q}$  errors that are clustered into discrete "gusts". Perturbations are only made to the value of dynamic pressure used in the vehicle environment; the activity vector calculation still employs the "ideal"  $\bar{q}$  without added noise. This procedure may be somewhat pessimistic, since sensors and estimation algorithms will continually measure vehicle state and update the dynamic pressure value, but is adequate for assessing general performance.

## Example #24: Re-Entry, Lateral Maneuver: Gusts

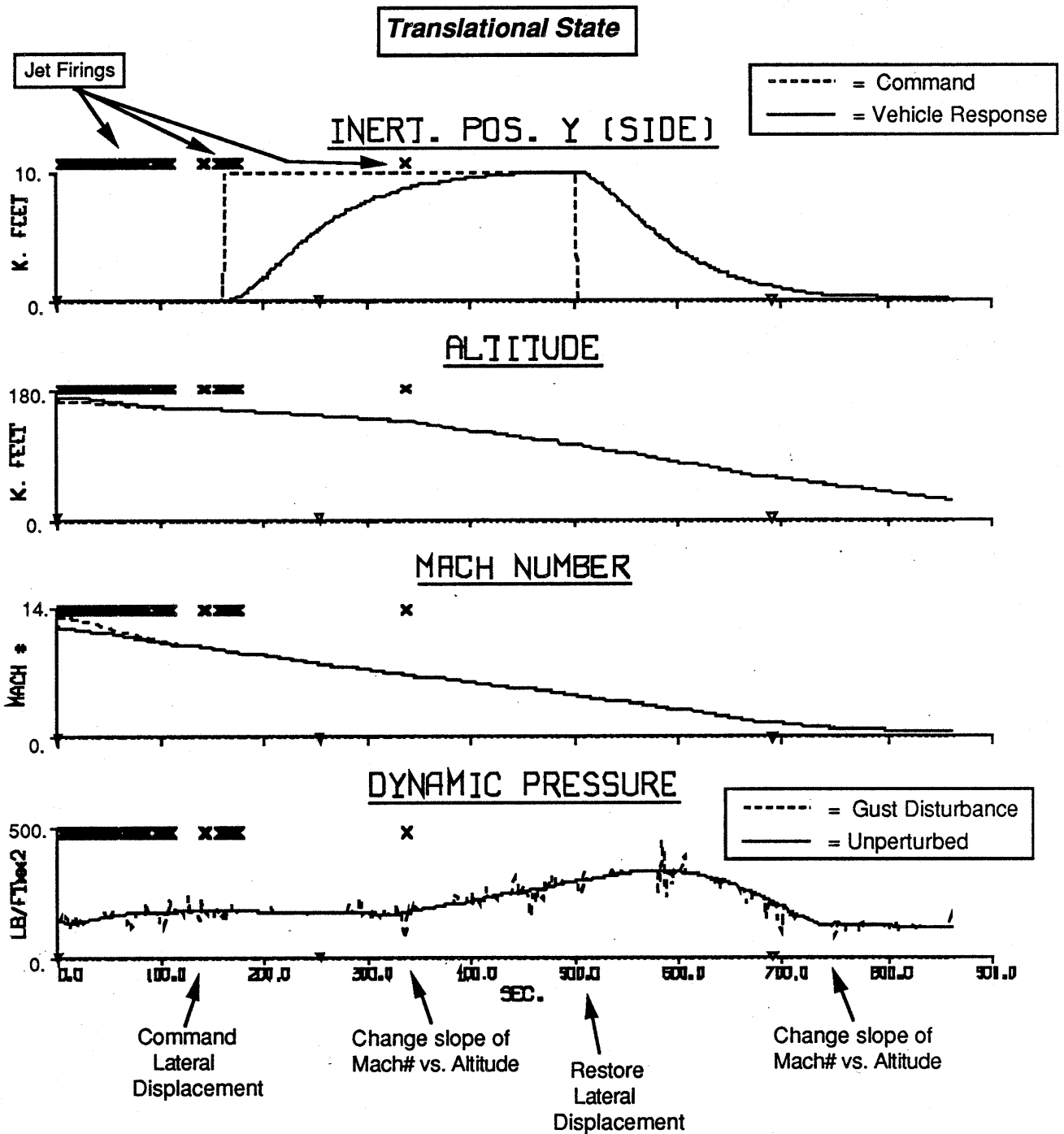


Figure 102

Results are given in Figs. 99 → 102. As before, the actuator and selection setup is nominal throughout the entire flight. Jet interaction is not considered in RCS firings; vacuum accelerations are assumed.

The aerosurface deflections (Fig. 99) exhibit the same general trends noted in earlier examples, as they respond to the standard re-entry profile tracked by the longitudinal controller. A significant increase in high-bandwidth jitter can be noted, however, in aerosurface response (particularly with the faster actuators; ie. canards, elevons, and, to some extent, the rudder). Some of this is introduced to combat the rapid variation injected into  $\bar{q}$  by the gust model. An additional contribution, however, is evident in the plot of velocity angles (Fig. 101). The relatively high gains assigned to the longitudinal controller have induced significant perturbation to the commanded  $\alpha$  profile to compensate for gust-induced errors in longitudinal state (and instigated a corresponding aerosurface response). Although the re-entry corridor is tracked perfectly (re. plots of altitude and Mach # in Fig. 102), this potential  $\alpha$  excitation indicates that the longitudinal controller should be adjusted to produce less  $\alpha$  disturbance. Otherwise, sideslip excursions remain limited and bank follows the commands with minimal error.

The translational vehicle state (Fig. 102) remains well-tracked, despite the variation in dynamic pressure, which is also plotted in Fig. 102 (the solid curve is the ideal profile, while the dashed curve represents the effect of the gusts). Jet accelerations (Fig. 100) are entirely lateral, as usual, and fuel consumption appears very similar to that encountered under nominal operation.

As seen in this example, the feedback control is able to reject random "gust" disturbances and track commanded states, at the potential expense of noisier aerosurface response. The next example examines the vehicle response to systematic modelling error. Figs. 103 → 106 present results of a test that introduces a constant bias into the measured-vs.-actual angle of attack. The value of  $\alpha$  used in activity vector calculation is shifted higher by  $+5^\circ$  from the "actual"  $\alpha$  assumed in the vehicle environment. No gusts or other mismodelling effects are assumed.

The aerosurface deflections (Fig. 103) are again seen to be significantly noisier than under nominal environments, presumably because of the  $\alpha$ -dependent errors in predicted actuator response. Jets are required for a longer interval (thus down to lower  $\alpha$ ), since the positive modelling error in  $\alpha$  reduces the predicted rudder yaw authority, thereby "tricking" the actuator selection into specifying unneeded firings. These firings are purely lateral in nature (Fig. 104), and all of the low  $\alpha$  jet activity is composed of exceedingly brief pulses (due to the small sideslip disturbance); most of these could be readily filtered through imposition of a hysteresis margin in jet activity (or perhaps higher jet costs).

Velocity angles (Fig. 105) appear slightly noisy, but very close to their standard profiles. Much of the  $\alpha$  excitation seen in the last example (Fig. 100) was driven by the random nature of

**Example #25: Re-Entry, Lateral Maneuver: Shift  $\alpha$**

**Aerosurface Deflections**

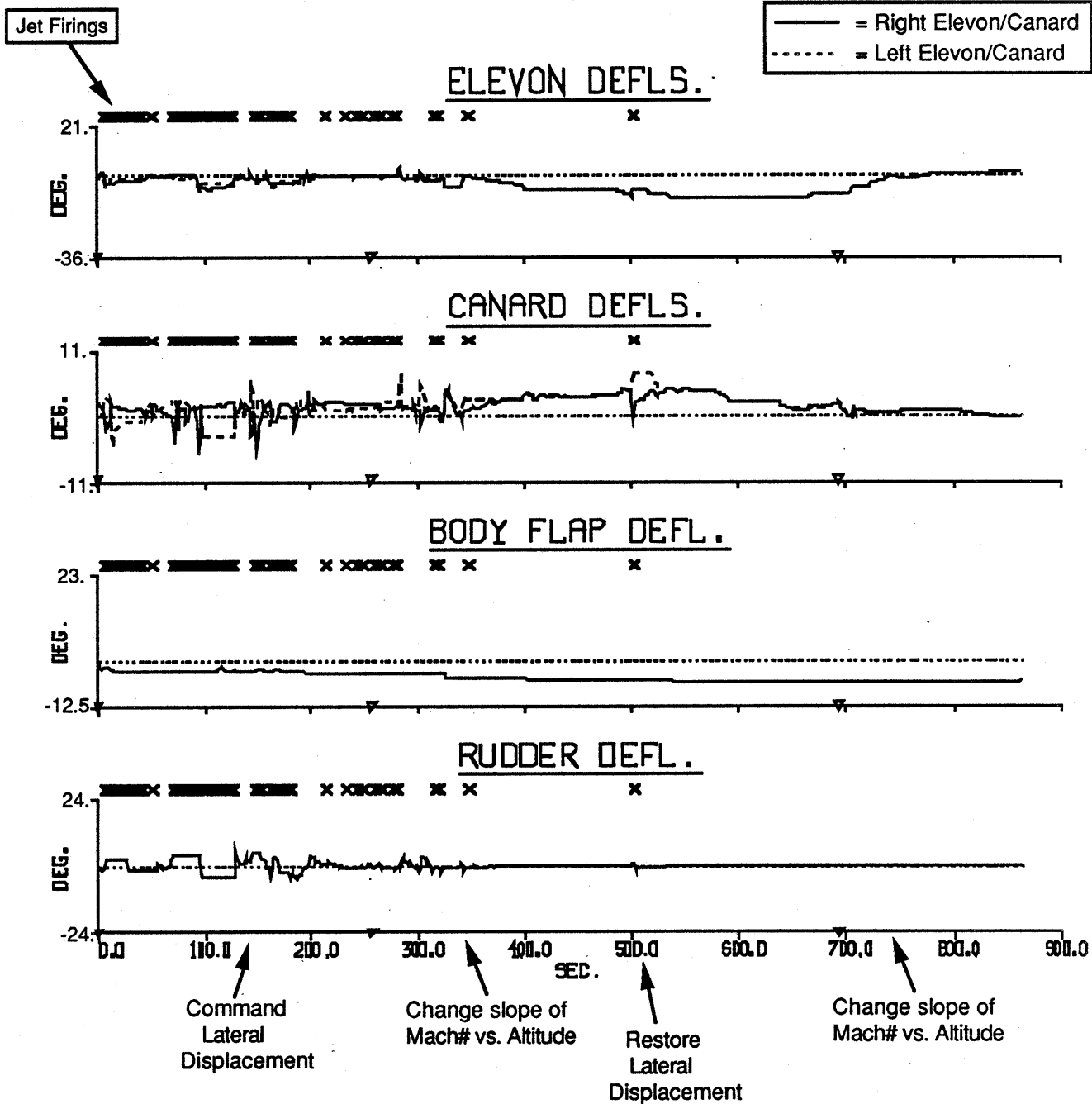


**Figure 103**

**Example #25: Re-Entry, Lateral Maneuver: Shift  $\alpha$**

**Jet Performance**

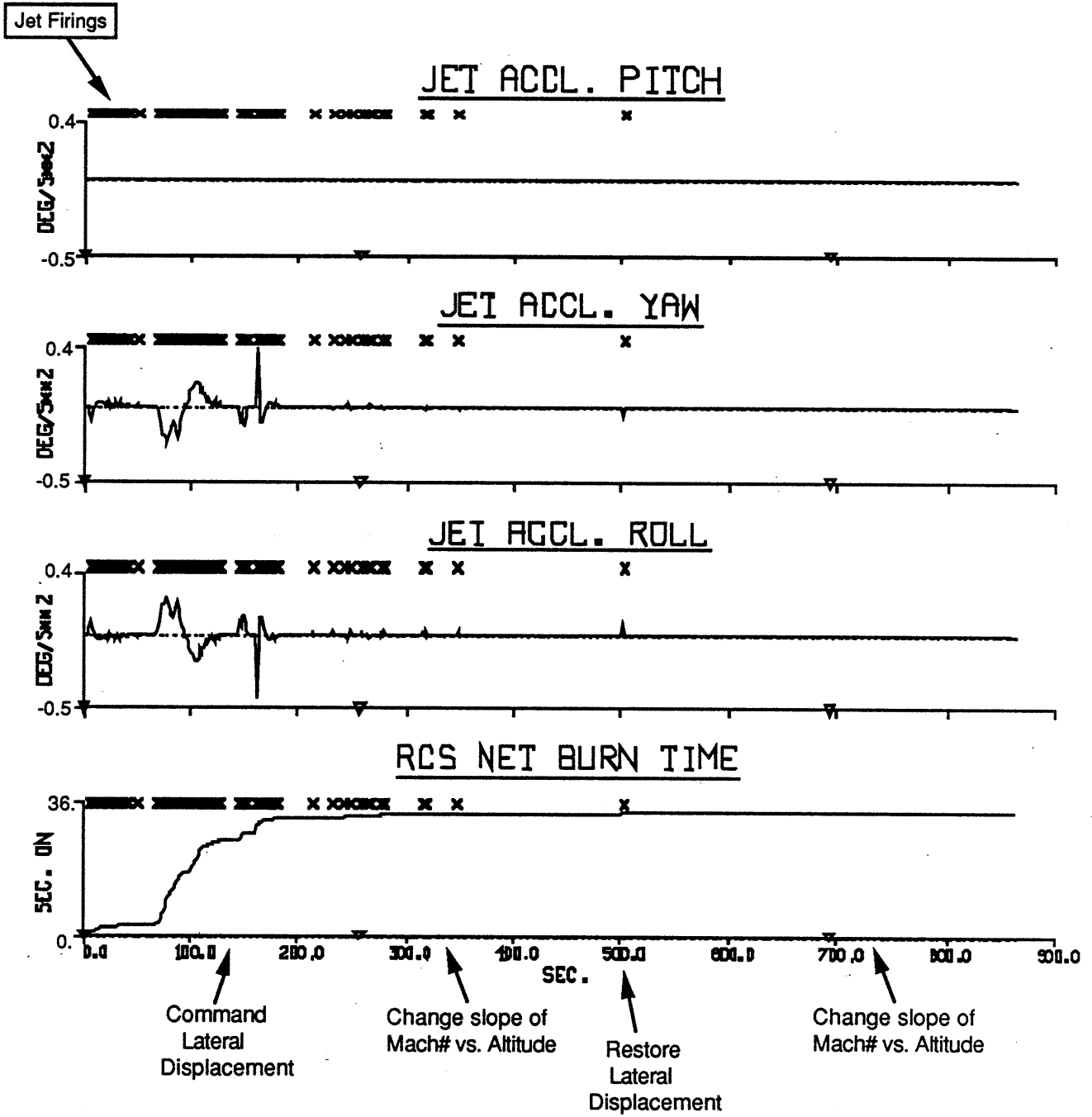


**Figure 104**

**Example #25: Re-Entry, Lateral Maneuver; Shift  $\alpha$**

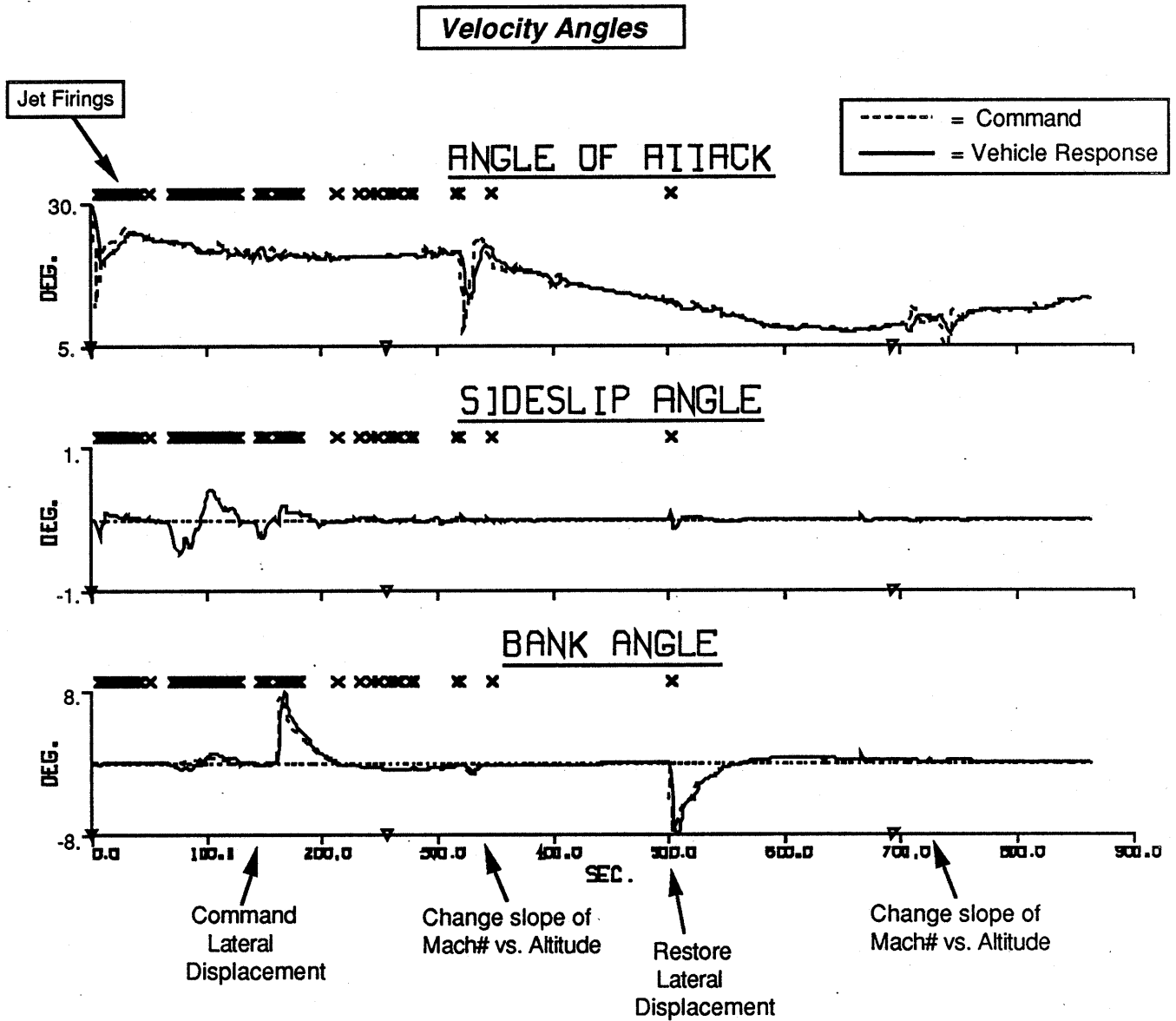


**Figure 105**

the modelled gusts; the systematic error created here evokes much less  $\alpha$  response. The translational states (Fig. 106) are seen to be well-tracked, despite the modelled  $\alpha$  error.

Other tests have been performed to examine the effect of systematic modelling error on different state variables. Simulations that model a  $+5^\circ$  shift in the actual-vs.-predicted deflection of one elevon exhibit particular sensitivity during jet firings. Hybrid activity can drive the system into a sideslip limit cycle, seemingly caused by roll/yaw error in the predicted effect of elevon scissoring. At lower  $\alpha$ , where jets are not employed, results appear nearly entirely nominal. As

### Example #25: Re-Entry, Lateral Maneuver: Shift $\alpha$

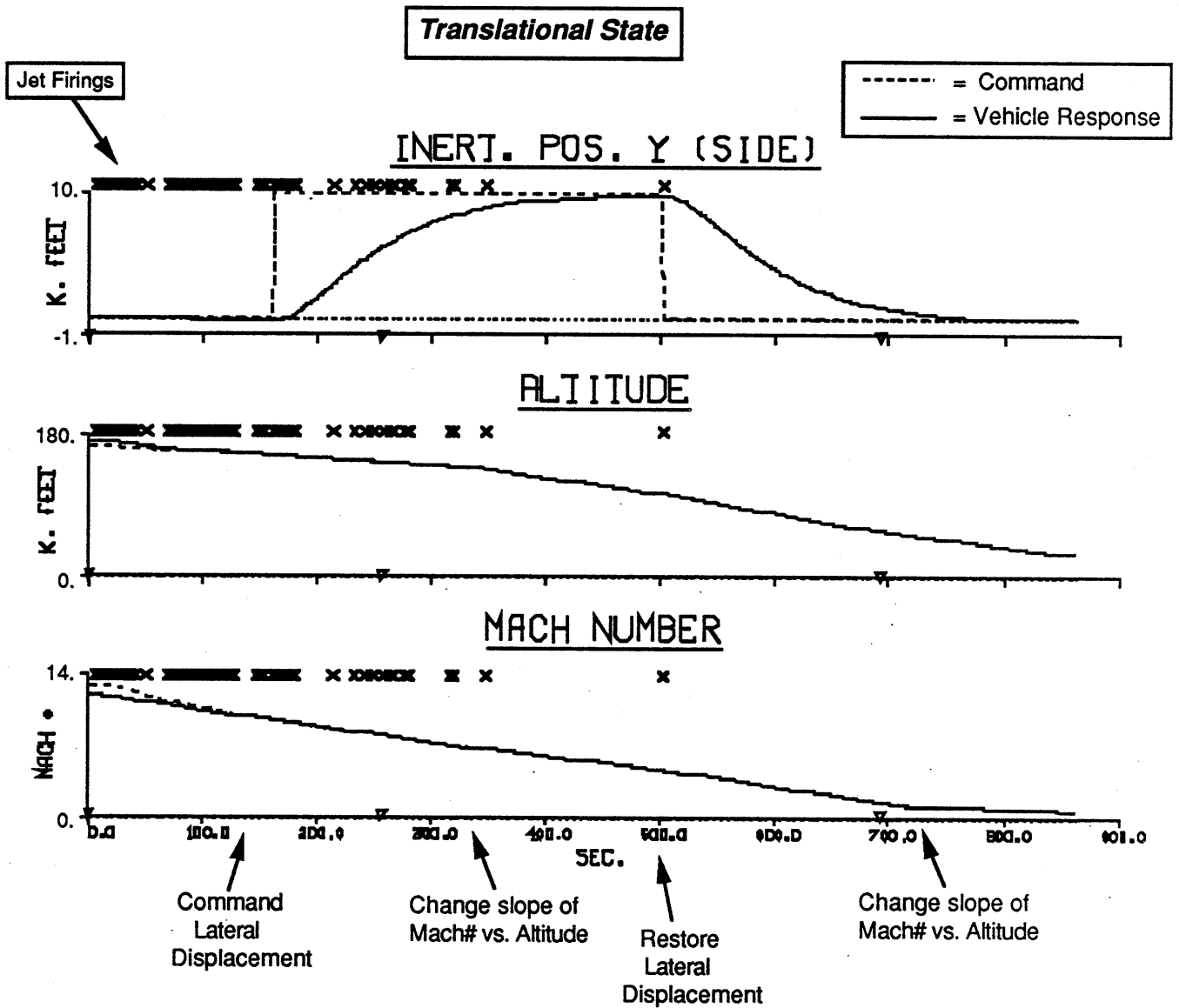


**Figure 106**

noted in former examples, the flight regimes where jets are required can tend to exhibit considerable aerosurface activity to derive any small yaw contribution. Jets are avoided wherever possible, due to their relatively large cost. The  $5^\circ$  elevon mismodelling employed here can significantly disturb any fine aerosurface balance prescribed to produce small yaw torques, leading to the observed sensitivity.

Tests were also performed that shifted the actual-vs.-predicted Mach number. The system did not exhibit any particular sensitivity to airspeed errors exceeding one Mach unit, until the

vehicle approached Mach 1, at which point the induced errors could result in a severe loss of control because of the rapid change in modelled aerodynamic performance (which is essentially unknown to the vehicle controller with a large Mach error in predicted aerosurface effect). Satisfactory control across the entire flight was retained with predicted-vs.-actual airspeed errors of under Mach 0.2.

The examples presented in this section indicate that sensitivities to a range of modelling errors might be manageable under the linear programming selection. A more precise statement requires an increase in the simulation detail (the "linear" interpolation outlined in Sec. 3.3 was adequate for the basic tests presented in this chapter, but should be replaced with a more accurate aerodynamic model) along with incorporation of realistic sensor emulation and candidate estimation schemes (ie. Ref. [27]).

## 6) Conclusions

The effort documented in this report has demonstrated that linear programming promises the potential to answer many of the needs that will appear in future generations of aircraft and aerospace vehicles. Linear programming has been successfully adapted to specify aerosurface deflections and jet firings for control of aerospace vehicles, and a framework has been defined under which thrust-vector control may be incorporated to allow management of an ascent vehicle.

Several simulations have been performed to ascertain the features & utility of the linear programming selection. Space Shuttle aerodynamic data has been adapted in order to simulate the re-entry of a hypothetical vehicle. Tests were performed at both constant altitude (where the aerodynamic properties are static) and throughout a simulated re-entry (where aerodynamic properties evolve continuously across the flight path). The velocity attitude and translational (longitudinal & lateral) vehicle control schemes developed to drive the hybrid selection were seen to adequately track commanded states.

The actuator operation was found to change dramatically with the mean aerosurface-to-jet cost ratio. If this ratio is too high, frenetic aerosurface activity and excessive jet firing will result from the nonlinear aerosurface behavior. If this ratio is too low, the aerosurfaces will move only slightly, and the bulk of the control burden will be realized by the jets (again, leading to potentially excessive firings). This ratio must be adjusted to strike a balance between acceptable jet activity and moderate aerosurface deflection (in regions where jets are required).

It was determined that "hybrid" selections, in which both jets & aerosurfaces are available, could be applied at every control step. There was no need to impose a re-selection protocol as was used with CMGs[5], where only aerosurfaces would be considered unless the system was in saturation, at which point another selection would be made (with revised bounds and objectives) to also consider jets. Jets were seen to be automatically introduced into solutions whenever the input torque-change request was too large for aerosurfaces, or aerosurface authorities were limited due to actuator saturation, low dynamic pressure, or high angle of attack (ie. actuator shadowing effects).

In the latter case (high  $\alpha$ ), aft side-firing jets were selected for yaw control, as favored in the objective formulation.

The minimum-angle and stops-avoidance cost contributions were seen to discourage large aerosurface deflections. Situations can occur, however, where brief impulsive maneuvers can result in large deflections that can only be relieved by continued vehicle disturbance or control requests (without significant commanded input, the simplex procedure will generally specify very small aerosurface deflection changes). This condition may not be significant in an actual vehicle (which is always countering disturbance), and may be relieved via negative cost assignment and effective null motion.

The objective formulation has been successfully adapted to penalize actuator drag or achieve a commanded translational effect. The objective may also be adjusted to account for specific actuator features; ie. the body flap was encouraged to deflect in a direction to unload the elevons & canards, while speedbrake deflection was encouraged to occur during a specific Mach range. Relative actuator application can be adjusted via specification of objective weights; ie. the speedbrake was assigned very high cost in most of these tests, and was seen to be generally applied only when other sources of available pitch torque were limited.

The intrinsic actuator decoupling performed by the linear program was demonstrated in many examples. In most tests, differential scissoring of canards and elevons was automatically selected to generate yaw torque at high angle of attack (where the rudder is ineffective). Translational coordinates can also be directly controlled via available actuators; an example was presented that automatically adjusted aerosurface deflections to maintain constant vertical lift force during a bank maneuver (performing a "flat turn").

The prowess of linear programming in managing vehicle reconfiguration was illustrated in several examples. Various aerosurfaces were failed in different situations; vehicle control was maintained through other aerosurfaces or (where necessary) introduction of jet firings. The ability of linear programming to impose dynamic bounds on actuator response (ie. aerosurface deflection) was also demonstrated in a set of examples.

The hybrid control scheme was seen to tolerate limited systematic discrepancies in the vehicle environment model. Operation under systematically perturbed angle of attack, Mach #, and elevon deflection was possible, but could lead to inefficiency and potential instability for large modelling errors. Stochastic error was introduced into the dynamic pressure calculation to examine performance under random perturbations. The vehicle was seen to maintain control under these conditions; a "noisier" aerosurface response was noticed (following the variations in dynamic pressure), and a sensitivity was detected to angle of attack excitation through the high longitudinal controller gains (the latter effect, however, is unrelated to the performance of the hybrid selection).

Definitive results on the effects of modelling error require incorporation of a sensor model and state estimation scheme.

Aerodynamic jet interaction was seen to have little effect on vehicle performance across the flight envelope considered here. This is due to the fact that the modelled aerodynamic perturbations tend to occur mainly around the roll axis for the jets generally selected (aft side-firing jets were usually preferred), thus any control errors could be readily compensated by the aerosurfaces (ie. elevons and canards). Potential problems, however, can result from large errors caused by simultaneous jet firings and vehicle state dependence of the interaction effect. Dedicated estimation logic and additional constraints on jet firings (and/or the vehicle control & actuator selection schemes) may be necessary to satisfactorily guarantee accommodation of the jet interaction effect; additional study is recommended in this area.

## **Acknowledgements**

I'd like to thank several of my colleagues at the C.S. Draper Laboratory that have assisted this project in various capacities. Special acknowledgement goes to Ed Bergmann for providing helpful advice and suggestions. Our discussions have proven highly valuable in pursuing this project, and Ed's activity was pivotal in initiating the original CSDL IR&D proposal that started this activity. Phil Hattis enabled the various phases of our diverse NASP activities to appear coordinated, and deserves sincere thanks for his advice and assistance in reviewing the results & various reports produced by this project. The effort expended by Phil (as well as Norm Sears and Steve Croopnick) in interfacing with the CSDL IR&D committees and other interested organizations is appreciated. Darryl Sargent is earnestly thanked for interrupting his already saturated schedule on several occasions to provide essential details on the Shuttle Orbiter and SLS simulation. Mike Corvin deserves thanks for our many discussions on aeronautics and Macintosh computing. John Dzielski's assistance with VersaTerm was appreciated, and our many conversations about mathematics, control theory, and generalities were always enjoyable. Owen Deutsch's advice on Microsoft Word and Macintosh software is much appreciated, and indeed aided in the realization of this document. The action of Eli Gai in supporting this project and funding the completion of this document is especially appreciated. Discussions with Larry McWhorter at NASA/Johnson Space Center were very helpful in understanding the characteristics & operation of the Shuttle Orbiter & autopilot during re-entry. Ed Bergmann, Phil Hattis, and John Vullo are thanked for reviewing this manuscript.

This activity has been supported under C.S. Draper Laboratory Independent Research and Development Task 236.

## List of References

- 1) Operational Flight Level C, Functional Subsystem Software Requirements (FSSR); Guidance, Navigation, and Control, Part C, Flight Control Entry--GRTLs, Rockwell/NASA document STS 83-0007.
- 2) Bergmann, E.V., Croopnick, S.R., Turkovich, J.J., Work, C.C., "An Advanced Spacecraft Autopilot Concept," *Journ. of Guidance and Control*, Vol.2, No. 3, May/June 1979, p. 161.
- 3) The OEX Autopilot was flight-tested on Space Shuttle missions STS 51G (June, 1985) and STS 61B (Nov., 1985).
- 4) Paradiso, J.A., "A Highly Adaptable Steering/Selection Procedure for Combined CMG/RCS Spacecraft Control," *1986 AAS Guidance and Control Conf., Keystone CO.*, AAS 86-036, CSDL-P-2653, Feb., 1986.
- 5) Paradiso, J.A., "A Highly Adaptable Steering/Selection Procedure for Combined CMG/RCS Spacecraft Control, *Detailed Report* ," CSDL-R-1835, March, 1986.
- 6) Paradiso, J.A., "Performance & Applications of a Hybrid Jet Selection & CMG Steering Law Based on Linear Programming," CSDL-R-1901, Oct., 1986.
- 7) Paradiso, J.A., "Selection and Management of Magnetically Gimbaled CARES Gyroscopes via Linear Programming," CSDL Division 10C Space Station Memo 86-19, Dec., 1986.
- 8) Raza, S.J. and Silverthorn, J.T., "Use of the Pseudo-Inverse for Design of a Reconfigurable Flight Control System," AIAA Guidance & Control Conference Paper 85-1900, 1985.

- 9) Dzielski, J., Bergmann, E., Paradiso, J., Rowell, D., and Wormley, D. , "An Approach to CMG Steering Using Feedback Linearization," Submitted to *Journal of Guidance and Control*, 1988.
- 10) Smith, G.A. and Meyer, G., "Aircraft Automatic Digital Flight Control System with Inversion of the Model in the Feed Forward Path," *Proc. of the 6'th Digital Avionics Systems Conference, Baltimore, MD*, Dec. 1984.
- 11) Dzielski, J., "A Feedback Linearization Approach to Spacecraft Control Using Momentum Exchange Devices," MIT PhD Thesis, CSDL-T-977, April, 1988.
- 12) Paradiso, J., "Methods of Smoothing CMG Gimbal Rates Calculated by Linear Programming," CSDL Division 10C Space Station Memo 87-20, Nov. 20, 1987.
- 13) Chung, A. Linear Programming, Charles E. Merrill Books, Inc., Columbus, Ohio, 1966.
- 14) Bradley, S.P., Hax, A.C., and Magnanti, T.L., Applied Mathematical Programming, Addison-Wesley Publishing Co., Reading, MA., 1977.
- 15) Brown, L.W., and Montgomery, R.C., "Space Shuttle Separate-Surface Control-System Study, NASA Technical Paper 2340, N84-28801, July, 1984.
- 16) "Operational Aerodynamic Data Book," Volumes 1 & 3, STS85-0118, Rockwell International, Sept., 1985.
- 17) Silver, Leonard W., "ESIM Model Book for the C.S. Draper Laboratory Statement Level Simulator (Revision 4)," C.S.Draper Lab. Report R-776, June 1980.
- 18) Stasiowski, P. and Sargent, D. (CSDL), personal communication.
- 19) The particular data used in the aerodynamic calculation was taken from "SLS REL 9".
- 20) Shuttle Operational Data Book (SODB), Volume 2, "Mission Mass Properties," Revision B, NASA document JSC-08934, Aug. 1980.

- 21) Ferziger, J.H, Numerical Methods for Engineering Application, John Wiley & Sons, 1981.
- 22) Chamitoff, G., "Hypersonic Aerodynamic Calculations for the Aerospace Plane," CSDL Division 10C memo TAV-87-07, July 7, 1987.
- 23) McCormick, B.W., Aerodynamics, Aeronautics, and Flight Mechanics, John Wiley & Sons, 1979.
- 24) CRC Handbook of Chemistry and Physics, *65'th Edition*, CRC Press, Inc., Boca Raton, Florida, 1984/85.
- 25) Shuttle Operational Data Book (SODB), Amendment 211, JSC-08934, Revision D, Oct., 1984.
- 26) Bergmann, E.V. and Weiler, P.S., "Accommodation of Practical Constraints by a Linear Programming Jet Select," *1983 AIAA Guidance and Control Conf., Gatlingburg, Tenn.*, CSDL -P-1704, June, 1983.
- 27) Chamitoff, G., MIT Phd Thesis in progress.
- 28) Zacharias, G.L., "A Digital Autopilot for the Space Shuttle Vehicle," MIT Master's Thesis, CSDL-T-632, Feb., 1974.
- 29) Findlay, J.T., Kelley, G.M., Heck, M.L., and McConnell, J.G., "Summary of Shuttle Data Processing and Aerodynamic Performance Comparison for the First Eleven (11) Flights; Final Report," NASA-CR-172440, N87-10884, Sept., 1987.
- 30) Moon, F.C., Chaotic Vibrations, John Wiley & Sons, 1987.
- 31) Kirkpatrick, S., Gelatt, C.D. Jr., and Vecchi, M.P., "Optimization by Simulated Annealing," *Science*, Volume 220, Number 4598, p. 671, May 13, 1983.